UNIVERSIDADE TÉCNICA DE LISBOA
INSTITUTO SUPERIOR TÉCNICO

COMPARISON OF CALIBRATION OF HYPERSPECTRAL IMAGE-PROCESSING TECHNIQUES FOR ENVIRONMENTAL ASSESSMENT IN S. DOMINGOS MINE, SE PORTUGAL

Lídia Maria Amaral Raposo do Quental

Thesis prepared to obtain the PhD Degree in Engineering Science

Supervisor: Doctor António Jorge Gonçalves de Sousa
Co-Supervisor: Doctor Stuart Harry Marsh

Jury

Chairman: Chairman of the IST Scientific Board

Members of the Committee:
Doctor Eduardo Anselmo Ferreira da Silva
Doctor Henrique José de Figueiredo Garcia Pereira
Doctor António Jorge Gonçalves de Sousa
Doctor Stuart Harry Marsh
Doctor Maria Teresa de Abrunhosa Barata
Doctor Pedro Miguel Berardo Duarte Pina

July 2011

UNIVERSIDADE TÉCNICA DE LISBOA
INSTITUTO SUPERIOR TÉCNICO

COMPARISON OF CALIBRATION OF HYPERSPECTRAL IMAGE-PROCESSING TECHNIQUES FOR ENVIRONMENTAL ASSESSMENT IN S. DOMINGOS MINE, SE PORTUGAL

Lídia Maria Amaral Raposo do Quental

Thesis prepared to obtain the PhD Degree in Engineering Science

Supervisor: Doctor António Jorge Gonçalves de Sousa
Co-Supervisor: Doctor Stuart Harry Marsh

Jury

Chairman: Chairman of the IST Scientific Board
Members of the Committee: Doctor Eduardo Anselmo Ferreira da Silva
Doctor Henrique José de Figueiredo Garcia Pereira
Doctor António Jorge Gonçalves de Sousa
Doctor Stuart Harry Marsh
Doctor Maria Teresa de Abrunhosa Barata
Doctor Pedro Miguel Berardo Duarte Pina

Funding Institutions

FCT Fundação para a Ciência e a Tecnologia
MINISTÉRIO DA EDUCAÇÃO E CIÊNCIA

British Geological Survey

July 2011

For Daniel and Sofia

ABSTRACT

This study addresses the application of hyperspectral or imaging spectroscopy (IS) sensors to environmental concerns related to mining areas and is tested in the old S. Domingos Mine.

To detect for acid mine drainage a multi-source spectral methodology was developed based on distinct spectra: mineralogical libraries, field, and endmembers extracted from the images. A quantitative link is established among them, selecting the highest correlation values as input spectra for the Spectral Angle Mapper algorithm, generating two maps in function of either field or endmembers spectra. The final improved map is the pixel intersection of both, converted to high spectral correlations of mineralogical assemblages indicators of low pH (<3)[copiapite(coquimbite)(smectite-alunite-illite-kaolinite)]. The low pH areas vary in function of the atmospheric corrections and the thresholds selected, but generally assign the same critical hazardous areas in year 2000.

The monitoring capabilities were tested with another IS sensor seven years apart (2007) but the same methodology did not yield significant results, highlighting the complexity of a multi-sensor approach.

The translation of input IS data resampled to a contemporary multispectral image mapped similar areas of low pH and opens good perspectives for multispectral routine application, once at some stage multi-source IS knowledge is available on a site.

KEY-WORDS: Imaging spectroscopy; spectroscopy; multi-source spectra; acid mine drainage; monitoring; multispectral.

RESUMO

A aplicação de sensores hiper-espectrais ou de espectroscopia de imagens (EI) a questões ambientais relacionadas com áreas mineiras é testada na mina de S. Domingos.

Para a detecção da drenagem ácida mineira, uma metodologia espectral multi-fonte é desenvolvida baseada em diferentes espectros: bibliotecas mineralógicas, campo e termos extremos extraídos das imagens. As correlações mais elevadas entre eles são seleccionadas para um algoritmo de Mapeamento de Ângulo Espectral gerando dois mapas em função de espectros de campo ou de termos extremos das imagens. O mapa final é a intersecção dos dois a nível de pixel, convertido em correlações elevadas de associações mineralógicas de baixo pH (<3)[copiapite(coquimbite)(esmectite-alunite-illite-caulinite]. Estas áreas de pH baixo variam em função das correcções atmosféricas e do valor de correlação, mas genericamente definem as mesmas áreas críticas de perigosidade no ano de 2000.

As potencialidades de monitorização foram testadas com outro sensor EI (2007), mas a mesma metodologia não teve resultados significativos, evidenciando a complexidade duma abordagem multi-sensor.

A translação de dados de EI para uma imagem multiespectral contemporânea mapeia áreas similares de baixo pH e abre boas perspectivas para a aplicação rotineira de dados multi-espectrais, uma vez que haja em algum período conhecimento multi-fonte de EI disponível.

PALAVRA-CHAVE: espectroscopia de imagem; espectroscopia; espectros multi-fonte; drenagem ácida mineira; monitorização; multiespectral.

ACKNOWLEDGMENTS

I am grateful to the following persons and institutions for support throughout the development of this research:

- to Prof. Jorge de Sousa, who was as the person responsible for the development of this work, even if in a slightly different direction than foreseen. His suggestions, discussions and incentive were very helpful

- to Prof. Stuart Marsh who embraced this project and provided conditions for its development. He gave important focused directions and every talk and discussion proved to be fruitful and very helpful

- to the British Geological Survey (BGS) for hosting me in the UK. Special thanks to the Remote Sensing Laboratory team for their nice welcome, help and discussions, in particular Claire Fleming and Gisela Ager who also provided logistic and pleasant conditions during my stays in the BGS

- to the National Environment Research Council / BGS and Airborne Remote Sensing Facility (ARSF) who financially supported the SPECIM EAGLE-HAWK data set over the S. Domingos Mine and the European Fleet of Airborne Research (EUFAR) for field funding as well as helping to plan the flight through the HYPMINGEO project

- to Mr. Andrew Wilson from AWK Technologies, responsible for pre-processing SPECIM EAGLE HAWK and for his inputs, highlights and suggestions when analyzing the data

- to Prof. José Cardoso Pereira, on behalf of the Instituto Superior de Agronomia, who allowed the use of ASD FieldSpec and to Dr. João Carreiras who conducted the field measurements in 2007

- to Prof. Maria Manuela Abreu from the Instituto Superior de Agronomia for her collaboration throughout the MINEO project and afterwards on the development of a scientific paper

- to Irene Cadima from the Instituto Nacional de Recursos Biológicos for enlightening discussions and good suggestions concerning remote sensing issues

- to the Foundation for Science and Technology who funded the work developed in the BGS facilities in the UK (BD/17257/2004)

- to my Institution, the Laboratório Nacional de Energia e Geologia (LNEG)/ Laboratório de Geologia e Minas (LGM) for the authorization to carry out this research. The institutional support to develop the thesis has crossed a few precursor institutions: IGM, INETI and presently LNEG/LGM and I acknowledge the authorization and time conceded. In particular, my former heads of department, Mr. Luís M. P. Martins who initially promoted the work and Dr. J. Tomás de Oliveira who provided the conditions to finish off.

— to my colleagues at LNEG/LGM through their suggestions and help, and from releasing me from other tasks. Of these, special thanks to Daniel de Oliveira, who (im)patiently dived into an area very different from his field of expertise to understand my thoughts and correct my English. He gave me valuable suggestions with a sharp critical eye, as first reader of the thesis. Maria João Batista gave me good inputs and helpful discussions. Teresa Pena Silva and Prof. Maria Ondina Figueiredo enlarged my vision with fruitful discussions. Pedro Sousa was responsible for the set up of all GPS field data acquisition in 2000 and 2007 in a very efficient way thereby resolving several logistical and technical issues.

And lastly but most important, this work was only really made possible due to my family's patience and support at all levels, and for placing it on its right spot when the work was overwhelming:

— to Zé Carlos and Maria Lídia for their incentive and comprehension

— to my in-laws and mother, who provided a place of solitude for the children and gave them excellent conditions to overcome their mother's absence

— to Daniel and Sofia for their good humour and sweetness.

TABLE OF CONTENTS

LIST OF FIGURES

LIST OF TABLES

1 INTRODUCTION

1.1 RATIONALE

Remote Sensing is the field of study associated with extracting information about the properties of electromagnetic waves emitted or reflected, without coming into physical contact with the object (Scott, 1997, Campbell, 2007). In a more strict sense, the electromagnetic radiation is usually measured and recorded at different wavelengths by a sensor onboard an aircraft or satellite. From these measurements information may be inferred to identify or characterize these objects, for example, in terms of their physical or chemical properties.

In essence, information is conveyed in remote sensing data by the spatial and spectral distribution of energy that is either reflected or emitted from the Earth (Landgrebe, 1978).

Every remote sensing system can be broken down into several components: I) an energy source, II) the interaction of this energy with particles in the atmosphere, III) subsequent interaction with the ground targets, IV) energy recorded by a sensor as data and V) data displayed digitally for visual and numerical interpretation. The latter may imply several processing algorithms until one can extract reliable information from the raw data, i.e. to generate a useful product to end users.

The characteristics of the sensors that record the energy, including the source, spectral range of the electromagnetic spectrum, field of view, signal to noise ratio (S/N), number of bands and spectral bandwidth, defines the type of images that will be acquired. When considering very narrow contiguous spectral bandwidths and many bands as well as a signal to noise ratio that can be high, the images obtained are in the domain of hyperspectral data or imaging spectroscopy (IS).

With such properties the information that can be extracted from this type of images is very detailed, based on the distinctive absorption features of the materials spectra related to its molecular composition. In this way there is a different spectral response of the materials, whether natural or artificial. When the target material is captured by an IS sensor, the spectral response obtained and processed through adequate algorithms can then be identified at a mineralogical and chemical level.

Thus, a wide span of applications ranging from Earth Sciences such as geology, agriculture, or atmospheric studies, but also medical sciences, chemometrics or space research can take advantage of IS data (Schaepman et al., 2006; 2007; Goetz, 2009).

The increase of environmental concerns and monitoring issues in our planet has found an adequate field of application in IS data, e.g. designing the spatial pattern of pollutants or defining the dispersion of its effects (Swayze et al., 1996; Kemper and Sommer, 2003; Richter et al., 2008), or vegetation stress over time. Medical applications of IS (Cope and Delpy, 1988; Randeberg et al., 2010), or in less evident fields such as indoor air monitoring (Chudnovsky and Ben-Dor, 2008) or control quality of food (Gowen et al., 2007), have implications in our daily life.

The mining and extraction industry, as a result of tight regulatory controls and legislation, is one activity that has been clearly hampered by environmental pressures. This is particularly due to the mining legacy left dating back from pre-historic times as well as by the more recent industrialized phase of mine development (Marsh et al., 2000), where environmental degradation and impact on human health remains in some cases until nowadays.

Although former mining areas are more prone to present environmental problems, due to the different environmental concept and technological issues at the time, the current mining activity can also threaten the environment and provoke substantial damage. This is the case of the technological risks that lead to catastrophic events, such as mine spill accidents recently reported e.g. the sulphide tailings dam spill of Aznalcóllar, Spain, in 1998 (Grimalt et al., 1999) or cyanide contaminated water released in Baia Mare, Romania in 2000 (Dzombak et al., 2006).

These catastrophic events are extremely powerful in contributing to raise the public awareness and negative impact over this type of industry, although long term contamination disseminating pollutants in soils and waters can also damage significantly the areas surrounding the exploitation areas.

Despite the environmental issues and related public concern, the actual trend is towards prevention and monitoring instead of hamper the mining and extraction industry. An elementary concept lies behind it looking at the fact that these activities contribute with about 7% of the gross domestic product of the EU and are the primary source to maintain the high technological standards of living, feeding essential raw materials to all other industries.

Plus, the role of this industry is becoming more relevant in the EU where the independence of the raw materials supply is being promoted, e.g. through the European Technology Platform on Sustainable Mineral Resources (ETP-SMR) (Tiess, 2009) as well as developing innovative and sustainable production technologies, including reuse, recovery and recycling. The aim is to contribute to the sustainable development of the mining industry in the EU, minimizing the environmental footprint.

With this background and a new insight to the extraction and mining industry, innovative tools have been developed and exploited to comply with the legal environmental requirements and controls. The aim is to use not only good environmental practices, but also to substantially reduce costs, time-consuming procedures and improve productivity.

The characteristics referred of the hyperspectral or IS methods and tools, with powerful identification capabilities, provides an adequate technology to meet this demand of environmental data, while contribute with non invasive, relatively low cost and less time consuming procedures. The applicability and relevance of IS has already been demonstrated for environmental assessment and monitoring of mining areas in a diversity of challenging European environments (Chevrel, 2003a; Chevrel et al., 2003b).

Environmental indicators have been derived from the vegetation stress (Kuosmanen et al., 2005), the dispersion of waste mining materials and their potential to be harmful (Quental et al., 2002; 2003), or delineating the Acid Mine Drainage (AMD) directly from mineralogical mapping (Bourguignon et al., 2002; 2003), were important achievements and encouraging results. Hence, some issues were raised to be further investigated when using IS data and tools.

The results obtained with IS methodologies can be framed by EU directives and policies. This includes the Soil Policy Development and Soil Strategy from DG ENV, in particular soil monitoring. Additionally the directive 2006/21/EC on the management of waste from extractive industries, which seeks to minimize the environmental and human health effects of polluted drainage from extractive waste disposal facilities and to prevent or minimize the impact of accidents, provides a legal framework for the sound management of such waste. More recently, the Integrated Pollution Prevention and Control (IPPC, 2008/1/EC) Directive establishes further requirements for industrial and agricultural activities with a high pollution potential.

1.2 OBJECTIVES

Despite being a powerful tool, the IS still presents some constraints that make it difficult to use in a routine procedure. This encompasses issues related to the data acquisition, pre-processing and processing phases.

The aim of this research is to optimize the use of hyperspectral imagery to environmentally assess and monitor mining areas. In this perspective three factors are considered:

I. CALIBRATION/CORRECTION OF IS DATA – Pre-processing issues with the atmospheric corrections comparison of statistical and physical models. The removal of atmospherical components may play a significant role, eliminating, shifting or adding spectral features mismatching the real signal of interest. Commonly used, the radiative transfer modeling is applied to IS data and can be tested using different types of software.

II. IMAGE-PROCESSING ALGORITHMS FOR ENVIRONMENTAL ASSESSMENT AND MONITORING - Amongst the several image-processing algorithms the focus on similarity measures is the one that has been more routinely applied. Some particularities can be emphasized within these types of classifiers, specifically related to the AMD detection.

III. HYPERSPECTRAL VERSUS MULTISPECTRAL - Once demonstrated the application of an IS methodology to assess mining areas, the response provided by a multispectral device can be tested. In this way a quantitative approach following the same methodology or adjusted can have interest under the point of view of economy and time consuming procedures. Plus, large areas can be covered and the repeatability of data acquisition is facilitated.

Concerning these factors some contribution is given and some possibilities were tested providing more understanding of the application of IS data to the mining environments, particularly related to the AMD, and highlighting further developments.

1.3 STRUCTURE OF THE WORK

This work is developed in 7 chapters, with all but the first and the last containing an introduction and conclusion, each one focused on the presentation of the work undertaken (Figure 1.1):

I. Chapter 1 - gives an overview about the work that is developed and some considerations about the objectives of this study and problems related with the use of hyperspectral data.

II. Chapter 2 - provides detailed information about background, concepts, definitions and problems related with the theme of the work, i.e. hyperspectral or IS, mining cycles and legal environmental framework, as well as some constraints on the use of the IS tools.

III. Chapter 3 - deals with the description of the test site, i.e. the S. Domingos mine from the geological, mining history and environmental concerns points of view. The multi-temporal IS data

capture and results are described in the framework of two previous projects: MINEO and HYPMINGEO.

IV. Chapter 4 - describes part of pre-processing and calibration of IS data focused essentially on the use of physical models. The results obtained using a radiative transfer modelling are compared using two types of software when available.

V. Chapter 5 - describes the image-processing algorithms developed, namely a multi-source spectra methodology in order to improve the results. Furthermore, it deals with the testing of this methodology in the study area using different atmospheric corrections. Also, an investigation of the impact of the atmospheric correction techniques on the effectiveness of IS algorithm performance is undertaken and lastly, the trends of environmental evolution of the study area are done comparing with another IS data seven years apart.

VI. Chapter 6 - the environmental retrieval of information obtained through IS data set is tested when converted to multispectral resolution and conclusions drawn on the results achieved as well as the potentialities and limitations.

VII. Chapter 7 - is an overview of the work undertaken, the main achievements and forward developments.

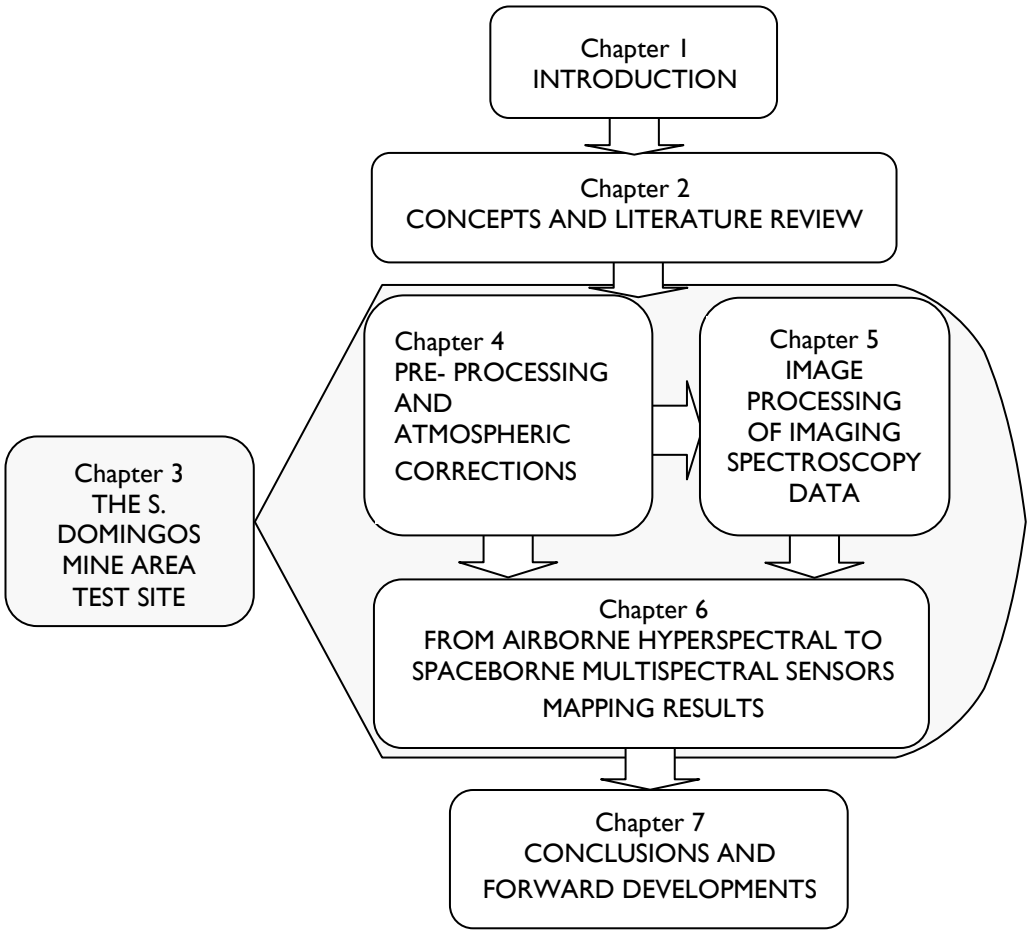

Figure 1.1 Structure of the thesis.

2. CONCEPTS AND LITERATURE REVIEW

2.0 INTRODUCTION

This chapter provides details about background, concepts and definitions related with the theme of the work, i.e. hyperspectral or imaging spectroscopy (IS). The capabilities of IS are shown. The IS data acquisition and subsequent image processing chain required for extraction of information is seen and some of the steps are emphasized. Some advantages and constraints of the use of IS are also highlighted.

The mining environment throughout all its life cycle can take advantage of IS technology, herein particularly related to a major environmental concern i.e. the Acid Drainage issue.

2.1 IMAGING SPECTROSCOPY

2.1.1 BACKGROUND

The concept of dispersion of light was born three centuries ago with Isaac Newton in his 'Treatise of Light' (Newton, 1704) indicating that white light can be dispersed in continuous 'colors', using prisms. The corpuscular theory proposed and developed by Newton was gradually succeeded over time by the wave theory, resulting in Maxwell's equations of electromagnetic waves (Maxwell, 1873). But it was only in the early 19th century that quantitative measurement of dispersed light was recognized and standardized by the discovery of dark lines in the solar spectrum by Joseph von Fraunhofer (1817) and their interpretation as absorption lines on the basis of experiments by Bunsen and Kirchhoff (1863) (Schaepman et al., 2006; 2009).

The term spectroscopy, first used in the late 19th century, is the study of light as a function of wavelength that has been emitted, reflected or scattered from a solid, liquid, or gas. The light in any form, i.e. the electromagnetic radiation (EMR), can be described in terms of a stream of photons or quanta, which are massless particles each traveling in a wave-like pattern and moving at the speed of light. Each photon has a wavelength determined by its energy level. Hence, the EMR can be distributed in terms of continuous wavelength as depicted in Figure 2.1, designated by electromagnetic spectrum. Or, the EMR can be expressed in terms of energy (in units of ergs, joules, or electron volts) or frequency of the photons according to Planck`s quantum equation1.

[1] ($E=h\nu=hc/\lambda$ where h=Planck's constant, ν= [Hz] is the frequency, λ [m] is the wavelength and c =speed of light=2.998×108 ms-1 NM,KL9IJ

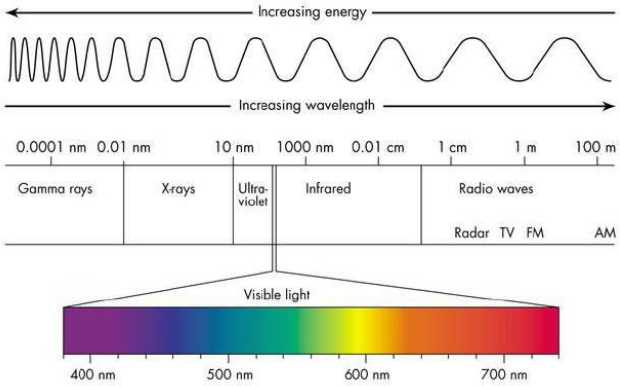

Figure 2. 1 The distribution of the continuum of all radiant energies as a function of wavelength (electromagnetic spectrum), with the visible region expanded to the colours detected by human vision.

The generation of an EMR is attributed to atomic motion, i.e. whenever an electric charge is accelerated, or more generally, whenever the size and/or direction of the electric (E) or magnetic (H) field is varied with time at its source (Campbell, 2007; Short, 2009). These atomic motions are variable along the electromagnetic spectrum, as depicted in Table 2.1.

Table 2. 1 The electromagnetic radiation (EMR) and the atomic motion involved. Miscellaneous source: Short (2009); Campbell (2007); Elachi and Van Zyl (2006).

EMR	Processes of Interaction mechanisms with matter	ATOMIC MOTION RELATED	REMOTE SENSING APPLICATIONS
Gamma-rays	Atomic	Disruption of atomic nuclei during nuclear fission or fusion reaction	Mapping of radioactive materials
X-rays		Atoms within the source that are bombarded by high energy particles that cause the source electrons to move to an outer orbit and then revert to one further end (back to the ground state).	
Ultra-violet	Electronic	Transitions of outer electrons to a higher metastable energy level	Presence of H and He in atmospheres
Visible	Electronic, and vibracion molecular Vibracional, vibrational-rotacional		Surface chemical composition, vegetation cover, and biological properties.
Infrared		Inter- or intra-molecular vibrations and rotations	Thermal infrared
Radio waves	Scattering, conduction, ionospheric effect	Rapidly oscillating electric current in a conductor	Surface physical properties, subsurfdace sounding, ionospheric sounding / atmospheric constituents, surface temperature, atmospheric precipitation

The EMR concerned herein is related with the Visible and Near-infrared (VNIR, 400-1350 nm) and the Short-Wavelength Infrared (SWIR, from 1400 to 2500 nm, considered the upper limit for this study). In these, the dominant interaction mechanisms with the matter are electronic processes detailed in Burns (1993) such as the shift of electrons between orbital shells and vibrational processes detailed in Farmer (1974) from the subtle movement of molecules or bonded atoms which generate spectral features in the Infrared region1400-4000 nm (Hunt and Salisbury, 1970).

As photons enter a mineral, some are reflected from grain surfaces, some pass through the grain, and some are absorbed. Those photons that are reflected from grain surfaces or refracted through a particle are said to be scattered. Scattered photons may encounter another grain or be scattered away from the surface so they may be detected and measured. Photons may also originate from a surface, a process called emission. Emitted photons are subject to the same physical laws of reflection, refraction, and absorption to which incident photons are bound (Clark, 1999).

Photons are absorbed in minerals by several processes. In the domain of electronic processes the most important are crystal field effects and charge transfer absorptions, although others exist such as conduction bands and color centers (Clark, 1999; Lau, 2004; Pinet et al., 2006; Short, 2009). In the vibrational processes, energy is associated with relative displacements between equilibrium center positions within diatomic and polyatomic molecules. These translational motions may be linear and unidirectional or more complex varying within a 3-axis coordinate system. Specific transitions are produced by distortions of bonds between atoms as described by such terms as stretching and bending modes. There is one fundamental energy level for a given vibrational transition, and a series of secondary vibrations or overtones at different, mathematically related frequencies (yielding the n orders mentioned above), as well as combination tones (composed of two or more superimposed fundamental or overtone frequencies (Short, 2009).

The variety of absorption processes and their wavelength dependence allows the extraction of information about the chemistry of the minerals from its reflected or emitted light. The wavelength dependency, at definite values, derives from the characteristics of crystal lattice, such as coordination number, nature of ligands and nature of the central ion. Coordination number and ligands define the electric field exerted on the central ion and, thereby, the order of magnitude of electronic or vibrational processes (Hunt and Salisbury, 1971a; b; Pinet et al., 2006).

2.1.2 CONCEPTS

The concept behind Remote Sensing lies on the basis of measuring the varying energy levels of the photons as tied to the parameter wavelength. When any target material is excited by internal processes or by interaction with incoming EMR, it will emit or reflect photons of varying wavelengths whose radiometric quantities differ at different wavelengths in a way diagnostic of the material.

The continuous sequence of electromagnetic energy of a material arranged according to wavelength or frequency is a spectrum. It can be measured in terms of spectral radiance or reflectance. The former, which is the radiant energy per unit wavelength or frequency interval per unit solid angle per unit of projected area of the source, is usually expressed in $W \cdot sr^{-1} \cdot m^{-2} \cdot nm^{-1}$. The spectral reflectance, being the ratio of energy reflected from a surface in a given waveband to the energy incident in that waveband is usually expressed as percentage of maximum. Further details are given in Chapter 4**.**

For any given material, the amount of solar radiation that it reflects, absorbs, transmits, or emits plotted in a spectrum, the connected points produce a curve called the material's spectral signature which is the spectral response curve. (Figure 2.2).

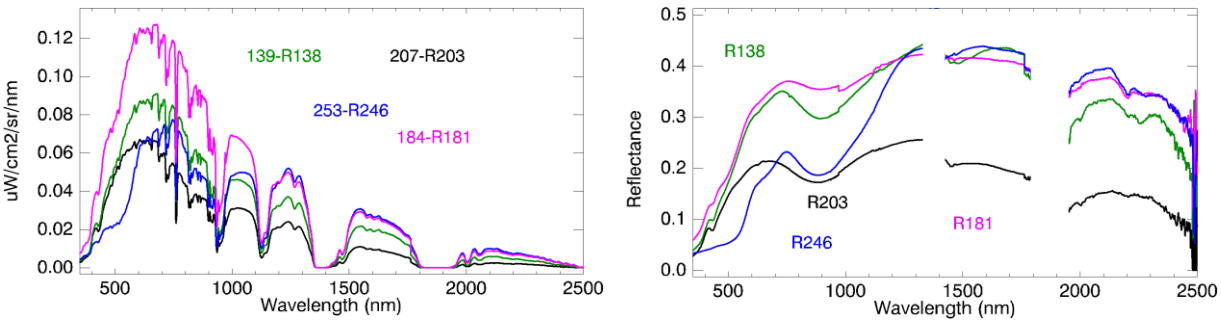

Figure 2. 2 Spectra of waste mining materials and soils in an abandoned mining area (Chapter 3). On the left are radiance measurements with the key (R) for equivalent reflectance measurements on the right.

Although the term spectral signature is frequently used and the term suggests being unique in Nature, in fact, is used in a broader sense within the remote sensing community. The variations in material composition often cause shifts in the position and shape of absorption bands in the spectrum. Thus, with the vast variety of chemistry typically encountered in the real world, spectral signatures can be quite complex and sometimes unintelligible (Clark, 1999). The term "spectral response patterns" has been suggested (Lillesand et al., 2004) as being more rigorous.

Grain size and roughness of the surface are the major physical properties that affect the spectral response. Subtle variations in the chemical composition imply modifications in the spectral response or signature of the target considered. Then, the absorption features detected in minerals spectra serve as diagnostic indicators. The causes of absorption bands in minerals and diagnostic features are given in Hunt and Salisbury (1970), Hunt (1977; 1980; 1982), Gaffey et al. (1993); Clark (1999) and Montero et al.(2005) and (references therein), for the visible and near-infrared.

Mineral identification according to spectral absorption features is feasible for minerals containing molecules or anions like H_2O, OH^-, SO_2^-, CO_3^{2-} or CH. This includes phyllosilicates, most sorosilicates, the hydroxides, some sulphates, the amphiboles and the carbonates. The dominance of the ferrous and ferric ion in the spectral range between 400 and about 1000–1300 nm is due to their large distribution on the Earth's surface, with the frequent occurrence of silicates, and their ability to replace many other ions (e.g., Mg^{2+}, Al^{3+}, Si^{4+}, and Mn^{2+}) in various minerals (Pinet et al., 2006). Thus, iron oxides and sulphates are predominantly identified in the VNIR, and some phyllosilicates, while the latter and also carbonates are identified in the SWIR range.

The detailed research developed in the spectral features of minerals for the above mentioned authors among others, lead to the development of spectral libraries measured in laboratory. Examples of these are the JPL (Grove et al., 1992) and USGS (Clark, 1993; Clark et al., 2007) spectral libraries.

In the literature, the terms "imaging spectroscopy", "imaging spectrometry" and "hyperspectral imaging" are often used interchangeably. Even though semantic differences might exist, a common definition is: simultaneous acquisition of spatially coregistered images, in many, spectrally contiguous bands, measured in calibrated radiance units, from a remotely operated platform (Van der Meer, 2001; Schaepman et al., 2006; Goetz, 1985, 2009) (Figure 2.1.2).

Spectrometry is derived from spectro-photometry, the measure of photons as a function of wavelength, a term used for years in astronomy, and more recently also to indicate the measurement of non-light quantities, such as in mass spectrometry (Clark, 1999; Ball, 2007).

Hyper refers to "excessive in extent or quality" (Gove, 1976). This "excess" information results from the high spectral resolution (i.e., narrow bandwidths) and the wide range of spectra that are recorded, which together

enable users to extract subtle differences in spectral signatures. There is no absolute definition of how many bands are needed or how narrow the bandwidths need to be to make imagery "hyper," although most sensors that are called hyperspectral have 48 or more bands with spectral resolutions of 20 nm or smaller (Aspinall et al., 2002).

Also scientific terminology and definitions evolve with time. The original definition of imaging spectrometry given by Goetz et al. (1985) was "the acquisition of images in hundreds of contiguous, registered, spectral bands such that for each pixel a radiance spectrum can be derived." In particular, it sets this type of spectral remote sensing apart from "multispectral imaging" by requiring the bands to be contiguous, in actuality overlapping, so that no gaps occur through which precious information might slip undetected. The requirement for "hundreds" of spectral bands is not critical and detracts from the much more important "contiguous" in describing the spectral bands (Goetz, 2009).

Although initially the term hyperspectral was more identified with the tool due to its heavy use in military related applications, the term imaging spectroscopy is becoming more used. Plus, the term spectroscopy focuses more directly with the capabilities of this technique by its older use, and expansion from a point spectroscopy to a spatial dimension. Adding to this, the fact that "hyper" is connoted with excessive and following the advance of knowledge it may not be, i.e. the mathematical solutions for the complexity found in real world may require these "excess" (Clark,1999), IS seems a preferable way to describe the technology.

Put in another perspective than the one referred above, IS can be described as the technique for obtaining a spectrum in each position of a large array of spatial positions so that any one spectral wavelength can be used to make a recognizable image (Clark, 1999). Essentially, this is the application of reflectance/emittance spectroscopy to every pixel in a spatial image.

Thus, IS combines the spatial and spectral information capture techniques into a common technique to obtain spatial information matched (or corregistered) with the corresponding multi band spectral information. Visually, the IS data is expressed through an "image cube" or "data cube", i.e. a stack of images over a spectral range, in a 3-D dimensional array where two spatial dimensions give the coordinates of each pixel and the third dimension is wavelength, as the example depicted in Figure 2.3.

In this, an RGB image shows the spectral slice of the top row and far-right column in a perspective view. This image shows color coded pixel values measured for each pixel along the top and right edge of the image and provides two spatial dimensions X and Y, while Z depicts the wavelength with radiance recorded at each point in the cube.

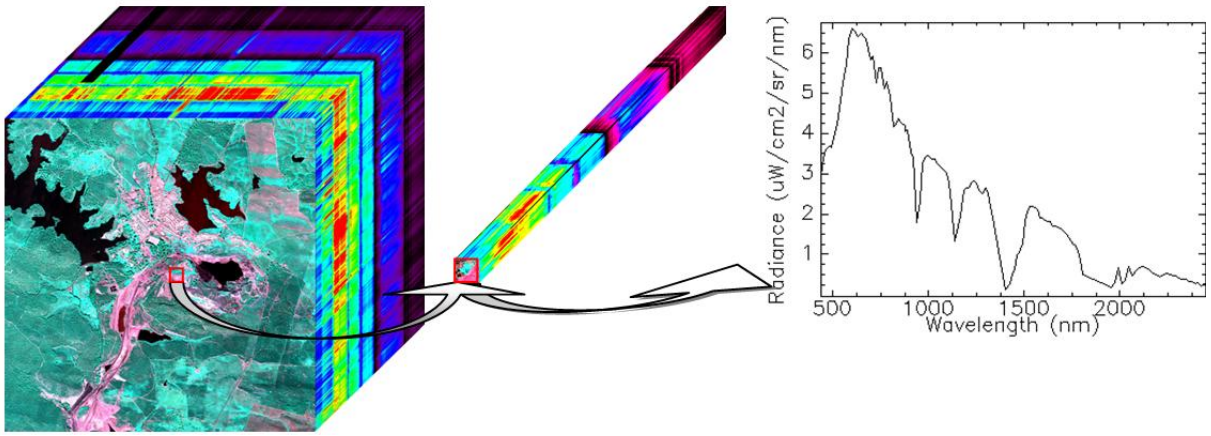

Figure 2. 3 Images collected in many contiguous spectral bands result in a continuous radiance spectrum for each pixel. Detail of a small area of 3-D data cube and visualization of spectral response.

The IS data acquisition is undertaken with a sensor, i.e. an electronic device for measuring intensity of radiation absorbed or reflected by a material as a function of wavelength. The major elements of the electro-optical scanner are the optical system, the detectors and the signal processor (Short, 2009). In this work are only considered passive sensors that detect EMR from an external source, e.g. the Sun, instead of a built–in source of radiation like in active sensors.

Depending on the principal parameter measured, i.e. spectral, spatial or intensity, then the device has a specific name, as depicted in a triangle diagram in Figure 2.4. In this way it is possible to gather information at different levels, in a point spectroscopy, with intensity and spectral information, or then to the imaging spectrometers or imaging radiometers with spatial information.

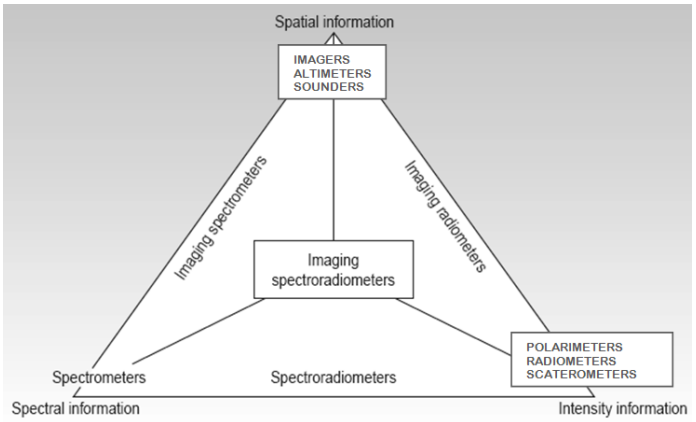

Figure 2. 4 Interrelationship of spectral, spatial, and radiometric information in different measuring devices (adapted from Elachi, 1987 and Short, 2009).

The hyperspectral data capture ranges from laboratory and field measurements to airborne or spaceborne dimensions. The simplest way, a point dimension, is to have a spectral measurement in a laboratory where it's easier to control external factors such as light. This is critical because light interacts with all matter, in absorption, reflection, and emission modes.

A spectrometer records the photons in the instrument field of view that strikes the detector. The photons are collected at particular wavelengths using some form of dispersive element or filter mechanism. When using a spectrometer in a natural environment, the signal obtained is a real spectral response of the target materials (Figure 2.5), but with limited control of external factors.

An imaging spectrometer expands the concept by using an array of detectors. The photons are captured from each subregion in a larger area onto individual detectors, resulting in an image of the area which is digitally recorded.

By enlarging the envelope of the field of view, the dimension is then spatial generating a hyperspectral image (Figure 2.6). The image acquired is dependent of some parameters of the imaging spectrometer such as spectral range, spectral bandwidth or spectral resolution, bandpass spectral sampling, swath width, signal to noise ratio and instantaneous field of view (IFOV) (Aspinall et al., 2002; Clark, 1999; Short, 2009).

Spectral range is important to cover enough diagnostic spectral absorptions to solve a specific problem, spanning the most used for geological and environmental applications from 400 to 2500 nm. The thermal emitted energy starts from 2500 to 3000 nm peaking near 10000 nm decreasing afterwards, and is also important on the aforementioned applications.

Spectral resolution is the measure of the narrowest spectral feature that can be resolved by a spectrometer. One of the more common ways to characterize spectral resolution is to determine the bandpass profile, Full Width at Half Maximum (FWHM), of an instrument's response to a monochromatic signal. Spectral sampling

Figure 2. 5 Field measurements with an ASDFielspec spectrometer (BGR) (Chapter 3). Right-measurements under high temperatures.

Interval is the spacing between sample points in the spectrum. Sampling is independent of resolution and in the case of ASD spectrometers is between 2 and 5 times per FWHM.

Signal-to-noise ratio (S/N) is the mean signal level divided by one standard deviation of the fluctuations of the signal. Sampling interval (SI) is the spectral distance between the centers of adjacent spectral channels sampled along a spectrum. Further definitions are given in the section 2.1.3.

2.1.3 DATA AQUISITION

The capture of IS data over large areas, i.e. in a small scale, is done in an airborne or spaceborne platform as depicted in Figure 2.6. The imaging spectrometer collects data along a swath. The longitudinal extent of the swath is defined by the motion of the instrument with respect to the surface, whereas the swath width is measured perpendicularly to the longitudinal extent of the swath. The ways the sensor collect the spectral information in a motion along or across the flightline or overpass satellite establish the pushbroom or whiskbroom mode respectively.

In a pushbroom sensor, the instrument consists of a line of sensors arranged perpendicular to the flight direction of the aircraft or spacecraft. This allows the simultaneous parallel observation of a cross track line of spatial resolution cells, where the total field of view (FOV) is covered, meaning the full swath width. Different areas of the surface are imaged as the instrument moves forward.

In a whiskbroom sensor, only a linear detector array is required. A scanner is used to project an image of the fligthline of scene in the cross-track direction, one pixel at a time. It only needs to cover the instant field of view (IFOV). A spectrometer disperses the incoming radiation, forming multiple images of the pixel, at all

wavelengths, on the linear array. A mirror scans across the path, reflecting light into a single detector which collects data one pixel at a time. The mechanical scanning makes this type of sensor expensive and more prone

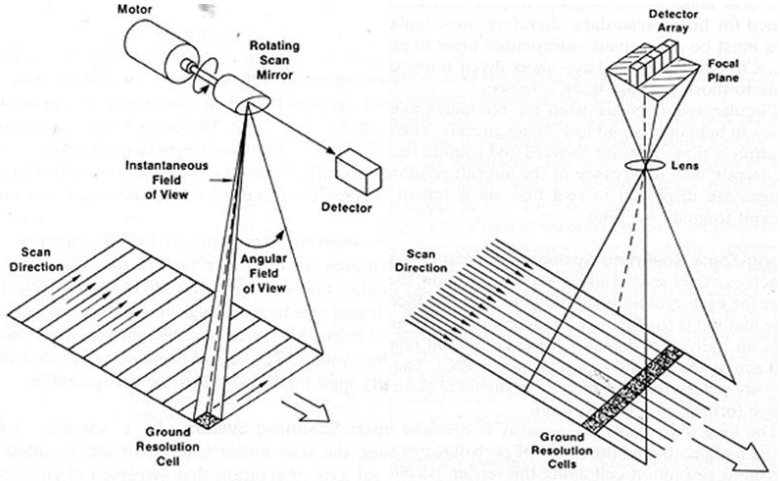

Figure 2. 6 Hyperspectral data capture schema and scanning directions according to wiskbroom (left) or pushbroom (right) scanners in a swath (after Sabins, 1999, in Short, 2009).

to wearing out. However, there are fewer distortions at the swath edge when compared to pushbroom sensor (Kramer, 2009). The latter, can gather more light due to a longer exposure of an area than their whiskbroom counterparts.

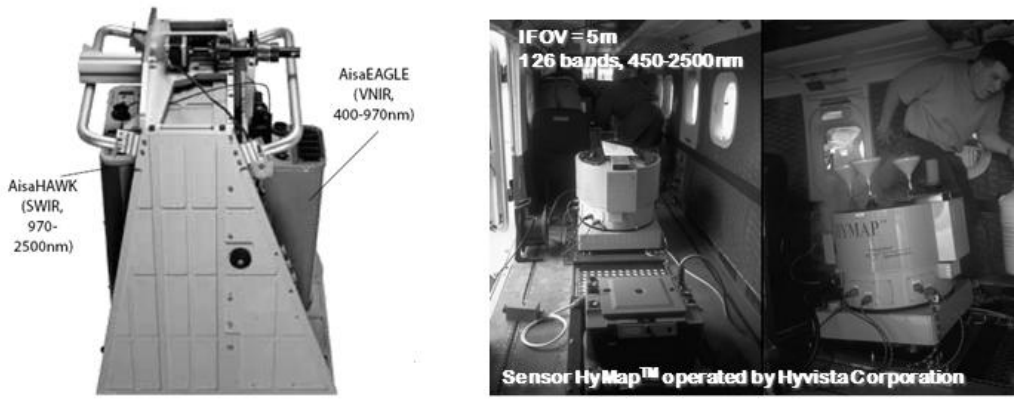

Figure 2. 7 A pushbroom (EAGLE-HAWK) and a whiskbroom sensor (HyMap™).

The developments related to IS sensors has increased significantly since the eighties of the XX century. In fact, the beginning of IS is rooted in spaceborne Landsat-1(MSS), launched in 1972, and effectively a "low resolution imaging spectrometer". The comparison of field data with MSS promoted the development of field spectroscopy, with portable field reflectance spectrometer, as a requirement to interpret the images. This lead to the inclusion of "additional" bands in Landsat for the detection of hydrothermal alteration minerals and to the development of the Shuttle Multispectral Infrared Radiometer (SMIRR), flown on the second flight of Shuttle in 1981, and justified the beginning of imaging spectrometer development (Goetz et al., 1982; Vane et al., 1983; Goetz, 2009).

The advances in IS sensors are closely linked to the advances in digital electronics and computing capabilities (Goetz, 2009; Kramer, 2009; Schaepman, 2009). Presently, there is a significant number of available IS sensors,

as depicted in Table 2.2. Other recent airborne instruments had their first flight campaign, such as ARES in 2008, while APEX (Itten et al., 2008) had it in 2009.

Table 2. 2 Examples of operational and planned hyperspectral imaging sensors. Miscellaneous source: Dalponte et al., 2009; Guelman and Ortenberg, 2009; Kruse et al., 2011).

SENSOR Platform: Satellite (S) Aerial (A)	Manufacturer	Maximum number of bands	Maximum spectral resolution (nm)	Spectral range (nm)
Hyperion on EO (S)	NASA Goddard Space Flight Center	220	10	400–2500
MODIS *(S)	NASA	36	40	400–14385
HyspIRI	NASA	Up to 210	(?)	380-2500 plus TIR
CHRIS Proba (S)	ESA	Up to 63	1.25	415–1050
EnMAP (S)	German Consortium (DLR Space Agency)	200	20	420-2450
AVIRIS (A)	NASA Jet Propulsion Lab	224	10	400–2500
HYDICE (A)	Naval Research Lab	210	7.6	400–2500
PROBE-1 (A)	Earth Search Sciences Inc.	128	12	400–2450
CASI 550 (A)	ITRES Research Limited	288	1.9	400–1000
CASI 1500 (A)	ITRES Research Limited	288	2.5	400–1050
SASI 600 (A)	ITRES Research Limited	100	15	950–2450
TASI 600 (A)	ITRES Research Limited	64	250	8000–11500
HyMap (A)	Integrated Spectronics	126	17	400–2500
ROSIS (A)	DLR	84	7.6	430–850
EPS-H (A)	GER Corporation	133	0.67	430–12500
EPS-A (A)	GER Corporation	31	23	430–12500
DAIS 7915 (A)	GER Corporation	79	15	430–12300
AISA Eagle (A)	Spectral imaging	244	2.3	400–970
AISA EagleT (A)	Spectral imaging	200	3.3	400–1000
AISA Hawk (A)	Spectral imaging	320	8.5	970–2450
AISA Dual (A)	Spectral imaging	500	2.9	400–2450
MIVIS (A)	Daedalus	102	20	430–12700
AVNIR (A)	OKSI	60	10	430–1030

Comparatively to airborne sensors, the spaceborne sensors have the advantage of capturing near global coverage repeated at regular intervals. However, spaceborne hyperspectral imaging is still in the development stage, even if, from the very few available such as EO-Hyperion and CHRIS Proba are providing data since 2000 and 2001, respectively. Among the upcoming spaceborne imaging spectroscopy sensors is the Environmental Mapping and Analysis (EnMap) (Stuffler et al., 2009), developed in Europe and now scheduled to be launched in 2014. The Hyperspectral Infrared Imager (HyspIRI) is a proposed NASA satellite remote sensing system to be launched in 2015. These sensors can significantly increase the amount of available IS data in the near future.

2.1.4 IMAGE PROCESSING CHAIN

IS data collected facilitates quantitative and qualitative characterization of both the surface and the atmosphere, using geometrically coherent spectral measurements. This result can then be used for the mostly unambiguous direct and indirect identification of surface materials and atmospheric trace gases, the measurement of their relative concentrations, and subsequently the assignment of the proportional contribution of mixed pixel signals (e.g. spectral unmixing), the derivation of their spatial distribution (e.g. mapping), and finally their evolution over time (multi-temporal analysis) (Schaepman et al., 2007; 2009). However, before one reaches this valuable information, several procedures have to be carried out.

Once obtained from an airborne or spaceborne sensor the IS data slots into an image processing chain, which is variable according to the objective of data capture. This may encompass the steps, even if in a different order, of the generic processing chain depicted in Figure 2.8.

Calibration refers to the process of quantitatively define the system responses to known and controlled signal inputs. Generally, IS instrument should undergo different calibration processes: i) the spectral calibration, defining the centre wavelength of a detector spectral channel, ii) the geometric calibration, defining the spatial response of a detector pixel and, iii) the radiometric calibration, defining the relationship between the recorded digital numbers (DN) and the measured spectral radiance (Dell`Indice, 2010).

The spectral and radiometric calibration of a sensor is usually performed in a laboratory (preflight calibration) and repeated afterwards due to variations during data capture. In particular, spectral shifts and channel broadenings are very likely to appear in detector arrays mounted in the focal plane of imaging sensors. Thus, post launch calibration campaigns are often conducted to check the accuracy or stability of the laboratory calibration (Guanter et al., 2006).

ATMOSPHERIC CORRECTIONS

The IS radiance data cube contains not only the spectral response of the materials but also complex interactions of light during the radiation´s way from the sun to the ground and back to sensor that masks the signal recorded. These interactions have an increased impact when leaving from the controlled laboratory environment to airborne and spaceborne platforms, and with the target to analyze kilometers away from the instrument. Varying atmospheric conditions (e.g. meteorological conditions), differences in the sun geometry (sun zenith and azimuth angles) and topographic effects strongly influence the spectral signal (Figure 4.1, Chapter 4). To obtain the target features, these variable sources must be removed from the data cube, leaving only the spectral response of interest.

The objective of an atmospheric correction is the elimination of atmospheric and illumination effects to convert the data from at sensor radiance to reflectance. This is particularly required when the objective is change detection through multi-temporal analysis or for quantitative analysis to derive a physical parameter. If the analysis is one-off image classification then it is feasible to use raw data as DN values, with no conversion to any physically meaningful units. However, there are some advantages when analyzing values of reflectance instead of radiance (Figure 2.2). The subject of atmospheric corrections is dealt in detail on Chapter 4.

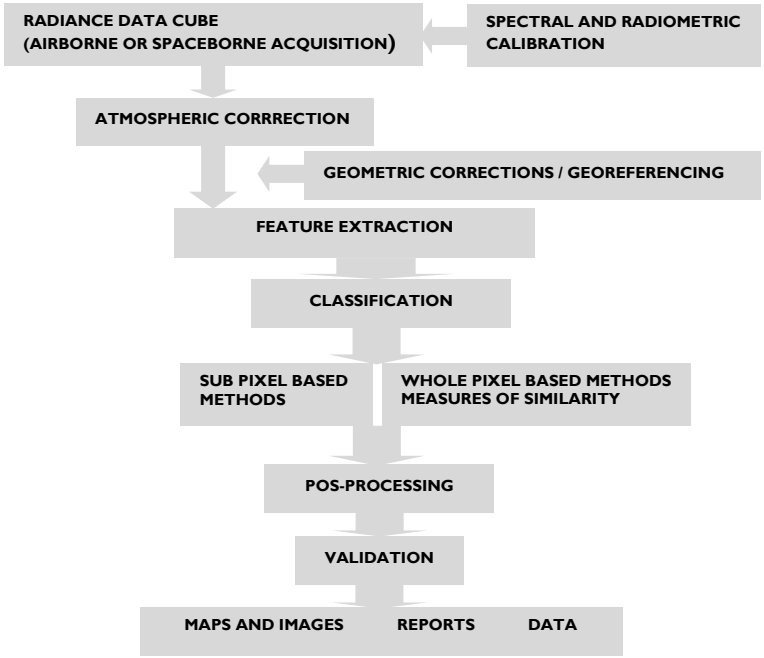

Figure 2. 8 Generic hyperspectral image processing chain.

GEOMETRIC CORRECTIONS

The sources of the geometric errors that occur in the data are two-fold, i.e. systematic and non-systematic distortions. The former are independent of flight or terrain conditions. Non-systematic errors involve altitude and attitude (roll, pitch and yaw) variation of the platform in which is mounted the sensor, and effects of topographic elevation.

Geometric rectification is a process by which points in an image are registered to corresponding points on a map or another image that has already been rectified. By this procedure, the image elements are put in their proper planimetric (x and y) positions. For hyperspectral data simpler nearest-neighbor resampling schemes may be preferred because these do not distort spectral characteristics (Kempeneers, 2007) (Figure 3.8, Chapter 3). Dedicated software for geometric correction such as PARGE (Schläpfer, 2006) exactly reconstructs the scanning geometry for each image pixel using position, attitude, and terrain elevation angle. Additionally, corrections for geographic relief are applied if a digital terrain model is available. The geometric rectification is done by direct georeferencing to a map projection or latitude/longitude grid. The positions and attitude data are measured in real time during data acquisition, using a GPS and Inertial Measurement Unit (IMU) onboard.

Some authors prefer to make the spectral analysis of the data cube prior to georeferencing, to avoid degradation of spectral information in an image by spatial re-sampling and mixing (Kruse et al., 2004; Stark et al., 2009). Thus, this approach is maintained whenever georeferencing is not a pre-requisite.

FEATURE EXTRACTION AND ENDMEMBERS

Feature extraction is generally defined as the process of reducing the data to a lower dimension without significant information loss. By definition, IS is a high dimension data with a vast volume leading to excessive computing time and data complexity for transmission and storage.

Feature extraction is a general term used to create a feature (sub)set from the vector of available spectral bands. It creates new features by transforming the data in a new feature space, for example as a linear combination of the spectral bands.

Another characteristic of IS data is that adjacent bands are very highly correlated, whereas the interband (spectral) correlation tends to be higher than the intraband (spatial) correlation. So, data reduction is effectively a necessary and challenging problem. This characteristic provides us with the probability to compress the hyperspectral images by making efficient use of this spectral correlation (Zhang and Desai, 2000).

Feature extraction has been investigated in two aspects: I) effective feature extraction for dimensionality reduction and classification, and II) reliable spectral signatures discovery for target identification. It is worth nothing that specific feature extraction algorithms should be related with hyperspectral remote sensing data and application objectives (Du et al., 2009).

Several algorithms have been developed for IS data, although some are still rooted in the multispectral data analysis. As an example, the statistical data reduction Principal Component Analysis (PCA)(Jollife, 2002), applied in a routine way, has been succeeded by the Minimum Noise Fraction (MNF). The former relies in finding components (features) that are optimal (in a least-squares sense) for representing the data with a reduced feature set. The features are constrained to be linear functions of the input variables. The components are ordered according to the amount of variance explained in the original signal. The first principal component is the linear combination that accounts for the largest amount of variance.

The MNF algorithm developed by Boardman and Kruse (1994) and implemented in a modified version from Green et al. (1988) in ENVI software (ITT, 2010), is essentially two cascaded PCA transformations. The first one decorrelates and rescales the noise in the data while the second one is a standard transformation of the noise-whitened data. For further spectral processing, the inherent dimensionality of the data (Boardman, 1995) is determined by examination of the final eigenvalues and the associated images. The data space can be divided into two parts, one part associated with large eigenvalues and coherent eigenimages, and a complementary part with near-unity eigenvalues and noise-dominated images. By using only the coherent portions, the noise is separated from the data, thus improving spectral processing results.

The IS data can be cast as a scattering of points in an n-dimensional Euclidean space, where n is the number of spectral channels. Each spectral channel is assigned to one axis of the space, all being mutually orthogonal. Every pixel in an IS data set has a point associated with it in the n-d space, its Cartesian coordinates defined by the values in each spectral channel (Boardman, 1995). If the n is the number of channels (wavelengths), an equivalent number n of scatterplots is required to contain all the information. It is the shape of the n-d scatterplot, the patterns within it and the configuration of its exterior that can be used to understand and analyze the spectral information in the data.

The upwelling radiance from multiple materials within a given pixel field of view is conveyed into a single observed spectrum. Thus, the information obtained can be considered as linear combination of the spectral response of the "purest" materials or endmembers within the data set. The endmember concept, as described in Boardman (1995) is a pixel spectrum that lies at the vertices of the image simplex, the "purest", or any component of a mixture, in the case of a 2-D-dimensional space (Figure 2.9).

The location of a spectral point, associated with a mixed pixel, within an n-d mixing simplex is completely determined by the fractional abundances of the n+1 mixing endmembers. Pixels that are pure, only containing one endmember material, will be found at the vertices of the simplex. Pixels that are equal mixtures of all endmembers will exist at the centroid of the simplex. A spectral endmember is the "purest" spectrum or just a spectrum that is a constituent part of a spectral mixture. Thus, if a spectrum does not mix with anything it is not a useful endmember. At remote sensing scales is expected virtually that all pixel spectra to consist of

mixtures of the spectra of the materials that can be measured on the ground. Thus, endmembers that are defined from pixels of training areas are not pure when viewed from a field perspective, but they may be relatively pure at image scale (Adams and Gillespie, 2008).

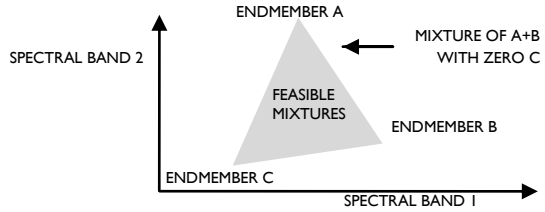

Figure 2. 9 Example of 2-D simplex with three component endmembers. The feasible mixtures lie inside the vertices (adapted from Boardman, 1995).

Several methods have been proposed in the literature to extract endmembers from the IS data cube (Winter, 1999), being one of the most successful approaches the Pixel Purity Index™ (PPI) (Boardman et al., 1995). This algorithm is based on the geometry of convex sets, which finds the "purest" pixels in the scene through a series of repeated projections on to randomly oriented lines in N-dimensional space. The PPI is run in a MNF space. The potential endmember spectra are loaded into an n-dimensional scatterplot and rotated in real time until a trained analyst selects extremities in the data cloud that likely correspond with scene endmembers. This procedure is widely accepted, available in the commercial software system ENVI, but it is time-consuming and highly interactive (Plaza et al., 2001).

To overcome some of these time consuming procedures, an automated function was developed in ENVI. In this, the PPI function is typically run in the MNF space, according to previous defined parameters, e.g. number of MNF bands to use and PPI iterations (Figure 2.10), as well as threshold values (ITT, 2010).

Other methods than PPI, include endmember selection tool (MEST) (Bateson and Curtiss, 1996), N-FINDR (Winter, 1999), optical real-time adaptive spectral identification system (ORASIS), the endmember optimization method of Tompkins et al. (1997), convex cone analysis (CCA) (Ifarraguerri and Chang, 1999), iterative error analysis (IEA) (Neville et al., 1999), automated morphological endmember extraction (AMEE) (Plaza et al., 2002), iterated constrained endmembers (ICE) (Berman et al., 2004), and vertex component analysis (VCA) (Nascimento and Dias, 2005), (Plaza et al., 2002; Rogge et al., 2007).

With the exception of AMEE, the above methods select endmembers by discriminating between pixels using their spectral characteristics. This is done independently of neighbouring pixels, the spatial distribution of endmembers, and the characteristic spatial mixing relationships between endmembers. Another algorithm (SSEE) combining a spatial–spectral endmember extraction was developed by Rogge et al. (2007).

The establishment of endmembers, as well as its level of acquisition, is a key-issue when analyzing IS data. The endmembers can be determined at different levels, i.e. from laboratory, field or images.

Some researchers have taken the approach of constructing spectral libraries of pure elements that can be matched with every spectrum in a hyperspectral image in order to classify the scene (Roberts et al., 1999). This processing is suitable when pure materials, contained in the library, are on the ground, but in real-world situations, since materials are spatially or intimately mixed, only the strongest features are matched. As a result, the most widely used technique is to determine endmember spectra directly from the image (Plaza et al., 2001).

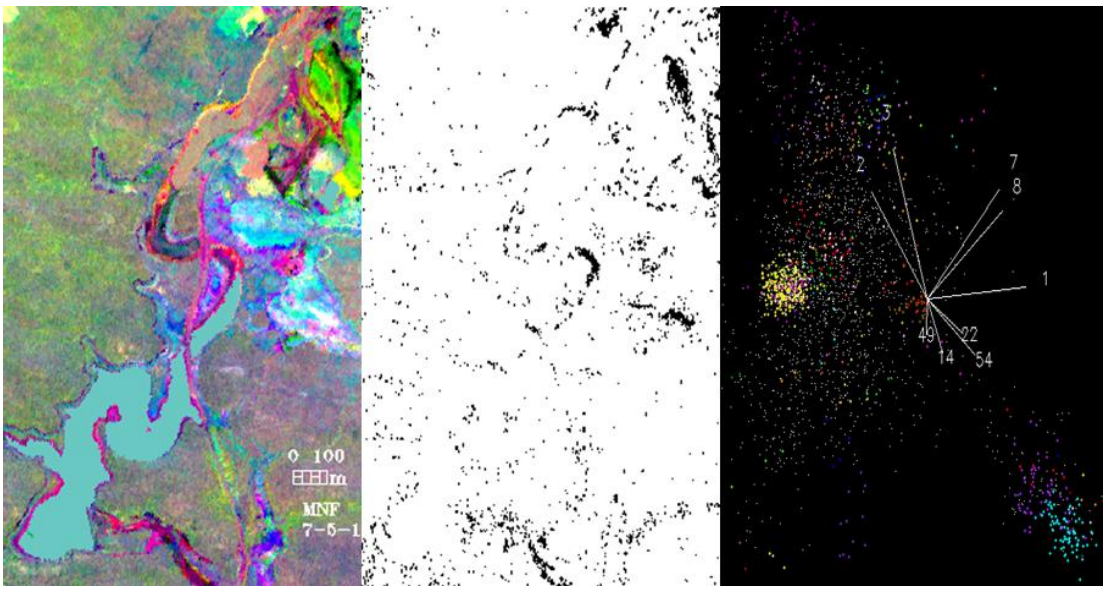

Figure 2. 10 Sequence of Minimum Noise Fraction (MNF), Pixel Purity Index (PPI) and n-D Visualizer leading to the extraction of endmembers. Detail from an old mining area (Chapter 3).

Endmember spectra determined from images have benefits over the use of spectra measured in the field. In fact, library and field spectra are rarely acquired under the same conditions as airborne or satellite data; and they may not adequately represent all important endmembers. On the other hand field and laboratory spectra are usually collected from surfaces one wants to map, and thus, they have direct physical meaning for mapping purposes. Imagery may provide similarly meaningful endmembers that can be considered "pure", or relatively "pure" spectra, meaning that little or no mixing with other endmembers has occurred within a given pixel (Rogge et al., 2007). However, recent trends on algorithm development for the endmember identification tend to make the assumption of images without "pure" pixels. This subject has been dealt with recently by Plaza et al. (2011) where an attempt to compare different algorithms for the endmembers identification is made.

CLASSIFICATION

On a possible imaging processing chain of IS, e.g. Figure 2.8, once features or endmember spectra are identified it is necessary to recognize their spatial dispersion, associations and abundances, which is tackled by using an adequate processing technique according to the objective of the study.

Recent advances in processing techniques as described in Plaza et al. (2009), focuses on the design of techniques able to deal with the high dimensional nature of the data, and to integrate both spatial and spectral information (Plaza et al., 2008).

Two major approaches widely used on classifiers for IS data can be defined at pixel level, whether it's a full pixel technique or a sub-pixel analysis, both relying on spectral information. However, this is merely a descriptive point of view and an oversimplification, given the very active research area related to IS technique analysis (Plaza et al., 2009, Dópido et al., 2011; Martín et al. 2011; Villa et al., 2011) and encompassing very different mathematical formalisms (Plaza et al, 2009).

FULL PIXEL TECHNIQUES

The underlying assumption governing full pixel techniques is that each pixel vector measures the response of one predominant material at each site in a scene. The basis is the spectral similarity between the pixel vector and the reference spectra.

Full pixel includes the standard supervised classifiers such as Minimum Distance (Richards and Jia, 1999), pattern recognition-based approaches such as statistical linear discrimination (Du and Chang, 2001), quadratic multivariate classifiers (Chen and Tu, 1996) and neural networks (Martinez et al., 2002) (Plaza et al., 2004).

A considerable number of dedicated algorithms have been developed for the IS data from which two widely known are the Spectral Feature Fitting (SFF, Clark et al., 1990; 1991; Crowley and Clark, 1992; Swayze and Clark 1995) and the Spectral Angle Mapper (SAM, Kruse et al., 1993).

The SFF matches targets and pixel spectra by examining specific absorption features in the spectra. SFF is a detection algorithm that uses least squares methods to compare the fit of image spectra to selected reference spectra.

This approach is done using a specific range of wavelengths within which a unique absorption feature exists for the chosen target. Reference endmembers are scaled to match the image spectra after continuum removal (Kruse et al., 1985; Clark et al., 1987; Kruse et al., 1993), which is a convex hull fit over the top of a spectrum utilizing straight-line segments that connect local spectra maxima, from both data sets. The pixel spectra are then compared to the target spectrum using two measurements. The first is the depth of the feature in the pixel, related to the material abundance, which is compared to the depth of the feature in the target. The second is the shape of the feature in the pixel, which is compared to the shape of the feature in the target using a least-squares technique.

An advanced example of this method, called Tetracorder, has been developed by the U.S. Geological Survey (Clark et al., 2003). The U.S. Geological Survey (Denver Office), has been instrumental in the successful implementation of variations of the SFF for their applications (Clark, 1999).

One of the first developed algorithms, SAM, is an algorithm which is a physically-based spectral classification that uses an n-dimensional angle to match pixels to reference spectra (Kruse et al., 1993). The algorithm attempts to find target pixels by simply calculating the angle $\theta(Xi,T)$ between image pixel Xi and the given T target signature where:

$$\theta(Xi,T) = \cos^{-1}\left(\frac{\left|\langle Xi,T\rangle\right|}{\left\|Xi\right\| \bullet \left\|T\right\|}\right) \quad \text{Eq. 2.1.}$$

Many users, including in ENVI software (ITT, 2010) implementation of SAM just skip the inverse cosine. Since the latter is (decreasing) monotonous on the interval (0, π), it just results in a (inverse) rescaling. The SAM algorithm tends to work well in relatively easy scenes, where the target is fully illuminated and large enough to fill entire pixels. In these cases, the measured pixel will contain only the desired target, and thus the image spectrum should be close (small angle according to the Eq.2.1). However, it is known that SAM does not do well in scenes that contain mixed pixel targets. This can occur when the target is too small, relative to the sensor ground sampling distance, or when the target itself is not clearly visible. In such cases the measured spectrum will be an additive mixture of both the target and some non target signature, such as the background or "shadow" spectrum. The addition of the non-target material can lead to the measured image spectrum to be pushed away from the library spectrum, increasing the angle between them. This is frequent in the real-world imagery. As a consequence, to identify the target pixels, either the angular threshold must be increased (leading

to increase in the number of false alarms) or the mixed pixels targets will not be identified (leading to an increase in missed detections (Chang, 2007).

In order to address the problem of the mixed pixels in the SAM algorithm, a modification of the algorithm has been proposed by Gillis and Bowles (2004) including a linear mixing model (section below) to define a new set of coordinates using endmember spectra of the target spectrum.

The SAM algorithm when applied on calibrated reflectance data is relatively insensitive to effects of illumination on the target material because changes in light will impact the magnitude but not the direction of the vector. A poorly illuminated target will cause the points to be plotted closer to the origin (Clark, 1999).

MIXED PIXEL TECHNIQUES

The underlying assumption governing mixed pixel techniques, also called spectral unmixing (Boardman, 1989b; 1993) or spectral mixture analysis (SMA), is that each pixel vector measures the response of multiple materials at each site. Thus, the technique relies on the calculation of the quantity of target materials in each pixel. The disadvantage of subpixel analysis is the number of false detections that occur when precise spectra measurements are attempted within a limited amount of information.

The SMA can overcome some of the weaknesses of full pixel approaches by using linear statistical modeling and signal processing technique. They are inherently either nonlinear techniques or linear techniques. Nonlinear mixed pixel analysis involves a detailed knowledge of multiple scattering effects that may arise due to the intimate association of components residing inside each pixel (Borel and Gerstl, 1994) (Plaza et al., 2004).

Examples of mixed pixel analysis methods include complete linear spectral unmixing (CLSU, Boardman, 1993) and matched filtering or partial unmixing (MF, Harsanyi and Chang, 1994; Boardman et al., 1995). In both, a pixel value in the output image is proportional to the fraction of the pixel that contains the target material. In CLSU it is required to know all the endmember spectra inside the pixel. A linear combination in this context can be thought of as a weighted average, where each endmember weight is directly proportional to the area the pixel containing that endmember. If the spectra of all endmembers in the scene are known, then their abundances within each pixel can be calculated from each pixel's spectrum.

MF performs a partial un-mixing of spectra to estimate the abundance of user-defined endmembers from a set of reference spectra. The algorithm does not require knowledge of all the endmembers within an image scene and can also be used to identify single feature types (Aspinall et al., 2002).

A method that builds on the strengths of MF and spectral unmixing is the mixture tuned matched filtering (MTMF, Boardman, 1998), combining the ability to map a single known target without knowledge of all endmember signatures with the leverage of mixed pixel models including constraints on feasibility. MTMF also reduces the incidence of false positives (Aspinall et al., 2002).

VALIDATION

One of the most important post-processing steps is the validation of the results obtained, as the way to assess how reliable they are. To any map resultant from classification or estimated parameter is required to know its accuracy. This is the objective of validation, or accuracy assessment.

Accuracy can be defined as the closeness of the estimated label or value to the truth. The reference data has often been referred as "ground truth" data. It should be noted that reference data are assumed to be more correct than the map is being used to assess, it is by no means true that these data are perfect or represent "the truth" (Congalton and Green, 2009). That's the reason why some authors prefer to not to use the term

"truth" (Khorram et al., 1999; Bird et al., 2000; Congalton and Green, 2009) in the context of accuracy assessment.

A more careful definition for accuracy measure is used by McCloy (2006) "estimate of closeness of the estimated value to the best estimate that can be made of that value". Reference measurement techniques are far from perfect. In most cases, only a relative accuracy is obtained, comparing the results from remote sensing to reference methods e.g. in situ measurements (Kempenneer, 2007).

There are two types of map accuracy assessment, i.e. positional and thematic. The former is related to the accuracy of the location of map features, whilst the latter deals with the labels or attributes of a map (Congalton and Green, 2009). They are both important and interrelated, once the IS data may also be of high spatial resolution, and reference measurements on the ground require high positional accuracy. Despite this interrelationship, the focus here will be on thematic accuracy, and the higher complexity that can reach.

In the accuracy assessment it has to be taken into account the specific type of results to which concerns. Plus, in the case of IS data the collection and processing of ground "truth" and image data requires users to address a number of issues that are familiar to remote sensing researchers. This ranges from collection of appropriate ground "truth" data to calibration and removal of error from the imagery to validation of classification results. At the same time, the data collection and image processing for IS mapping and analysis are substantially different, lie a number of less obvious problems that result from the difficulty of acquiring IS data, the geometric and calibration constraints imposed by the fine spectral and spatial resolution of the data, and problems in applying classical validation techniques when the imagery may map the environment with greater accuracy than can be obtained by field crews or maps produced by other methods then remote sensing (Jacquez et al., 2002; Aspinall et al., 2002; Foody, 2008).

Aspinall et al. (2002) and Marcus (2002) discuss how this dilemma poses a serious challenge to accepted methods for accuracy assessment and suggest that new approaches are required for evaluating maps and modelling results from IS.

Particularly when tackling with IS data the theme to map plays a relevant role in the validation procedures. Independently of the accuracy achieved, when mapping e.g. land cover or an urban environment is possible to compare with ground reference maps or photos and follow routine procedures. These routine procedures reports to principles of ground "truthing" and accuracy, well established in remote sensing literature (e.g. Congalton and Green, 1999; 2009).

Three critical or fundamental steps are identified in the accuracy assessment: I) designing the accuracy assessment sampling, II) collecting data for each sample, and III) analyzing the results (Stehman and Czaplewski, 1998; Congalton and Green, 2009).

It's worth noticing that generically in remote sensing the realm is to extend the results for an entire area, whilst only a few reference measurements are obtained. By knowing the few reference measurements, the true value for the entire area can be estimated, but is not known. This problem has been studied thoroughly in statistics, where is needed to estimate an unknown parameter from a large population, for which only a limited sample is available (Kempenner, 2007).

Most of accuracy assessment methods rely on statistical tools. Root Mean Square Error (RMSE) is a standard measure for positional accuracy, where is computed as the sum of the square of the differences between the position of the point on one data layer as compared to the position of the same point on another data layer (often the ground) using the same data that were used to register the layers together. This measure is, therefore, not an independent measure of positional accuracy (Congalton, 2005).

For thematic accuracy assessment, building up an error or confusion matrix, also referred to as error or contingency matrix, has been the most used procedure as the way to quantitatively compare the results obtained.

The error matrix consist of a square array of numbers or cells set out in rows and columns, which expresses the number of sample units assigned to each land cover type as compared to the reference data. The columns in the matrix represent the reference data (actual theme) and the rows represent assigned the mapped theme. The major diagonal of the matrix indicates agreement between the reference data and the interpreted land cover types.

An error matrix is a very effective way to represent map accuracy in that the individual accuracies of each category are plainly described along with both the errors of inclusion (commission errors) and errors of exclusion (omission errors) present in the classification. Each and every error is an omission from the correct category and a commission to a wrong category. In addition, other accuracy measures can be computed from the error matrix, such as overall accuracy, producers accuracy an user´s accuracy (Congalton and Green, 2009; Congalton 2005).

The error matrix can be applied to IS data when the theme or target to identify is, e.g., land cover including urban mapping or any type of vegetation, when the "truth" can be easily accessed by another independent data type. However, as shown in previous sections, IS mapping capabilities go far beyond the capabilities of the human eye. If we consider as a theme a mineralogical or a chemical map, the design of an accuracy assessment is farther more complex. In fact, even if ground reference data exists, with another analytical tool results such as X-ray diffraction or chemical analysis, it might not correspond to a global signature of the pixel. Otherwise, for a global pixel validation it would be required an extensive field work and analysis, somehow difficult to achieve even if at pixel level.

An exception to this is when the pixels analyzed are dominantly covered by a mineral, e.g. a salt mine or a sulphur area in volcanoes, where a field map can be obtained. Thus, excluding some of the themes mentioned above, the error matrix in IS has been essentially used to compare methods, e.g. as in Kruse (2002); Plaza et al., (2002), instead of the validation of a final product.

Then, the validation of IS data tends to rely on other type of indicators, more subjective, that can give a relative measure of the results obtained, based on the data used. Examples of this include the comparison of the areal extent of spectral classes to a point spectrum, i.e. a field spectroradiometric measurement (Quental et al., 2002a, Chapter 3). This relative assessment does not take into account the locations at which class labels have been assigned, due to the fact that the point collection may not be representative of the pixel even if it looks at such by human vision. This "relative" type of measure is not independent of the image processing system, thus not as an adequate accuracy assessment should be (Congalton, 2005).

Another example of a relative assessment of the results can be done trough a statistical parameter, the variation coefficient, whereas is shown the variability of pixel spectral values (Chapter 3 and 5).

Congalton and Green (2009) emphasize that no single recipe exists for accuracy assessment and every aspect of a mapping project should be considered in order to design and implement the best possible assessment given the strengths and limitations for each mapping project.

2.1.5 ADVANTAGES AND CONSTRAINTS OF IMAGING SPECTROSCOPY

The capabilities of Imaging Spectroscopy (IS), as described previously, make it an extremely powerful tool over a wide span of applications. This ranges from Earth Sciences such as geology, agriculture, or atmospheric studies, but also medical sciences, chemometrics or space research which can take advantage of IS data

(Schaepman et al., 2006, 2007; Goetz, 2009). Examples coming from areas such as control quality of food (Gowen et al., 2007), health (Cope and Delpy, 1998, Randeberg et al., 2010,) or environment related have implications in our daily lives.

Davies (1987), recognizing the importance of IS based on Wetzel (1987) who consider it as "sleeping technique", made an analogy considering that it was "Time for the Giant to wake up". Nevertheless, and despite the fact that presently there is a huge amount of hyperspectral related interested and use (Schaepmann et al., 2009), still the development concerning this tool is below expectations.

In order to promote an improved access to IS data across Europe, an European specific Support Actions project HYperspectral REmote Sensing in Europe (HYRESSA) undertook a strategic planning tool which is used to evaluate the Strengths-Weaknesses-Opportunities and Threats involved in a project (SWOT). A SWOT evaluates the external factors and internal situation facing a project, in this case the access to IS data. Strengths and weaknesses are internal aspects and sequentially can be influenced within the project. Opportunities and threats are external aspects. These are aspects of the environment influencing the project and cannot be changed, but can be anticipated (Steiniger, 2003).

The results of the SWOT analysis from HYRESSA are depicted in Table 2.3, give an overview for items related to IS such as campaigns, sensors, processing and applications.

Table 2. 3 SWOT concerning IS (adapted from Holzwarth and Heldens, 2006; Reunsen et al., 2007).

HYPERSPECTRAL CAMPAIGNS	
STRENGTHS	WEAKNESSES
1. Increased availability of airborne and ground instruments 2. Increasing effectiveness and efficiency 3. More than 10 years of data provision in Europe	1. High costs for aircraft and mobilization in a scientific environment 2. Restricted windows of opportunities for campaigns 3. No operational hyperspectral satellites available
OPPORTUNITIES	THREATS
1. Increase the education and training of end users and potential users 2. Open up to semi-commercial (administration) end-users 3. Manage the (end-) user's expectations	1. Financers are not convinced (restricted future funding) 2. There is a lack of education 3. Lack of transfer of knowledge
HYPERSPECTRAL SENSORS	
STRENGTHS	WEAKNESSES
1. IS is developing from experimental to operational services 2. Increased understanding of physical measurement 3. There actually are calibrated and maintained sensors	1. Sensor stability, repeatability and reproducibility are difficult 2. Quality assurance often lacking 3. Calibration information is lacking
	(cont.)
OPPORTUNITIES	THREATS
1. Define standards on traceability, calibration, terminology 2. Provide documentation of calibration and maintenance data. 3. Define minimum calibration standards	1. Decision makers don't understand the importance of calibration and validation. 2. Lack of agreed standards 3. Calibration costs higher than data acquisition costs
DATA PROCESSING	
STRENGTHS	WEAKNESSES
1. Tools for geometric and atmospheric correction exist. 2. Detailed understanding of involved factors exists. 3. Geometric and atmospheric corrections combined.	1. No real capability to define the accuracy right now. 2. Validation processes are missing. 3. Lack of (agreed) standards.
OPPORTUNITIES	THREATS
1. Develop algorithms for thermal sensors 2. Define standardized products which include data analysis 3. Describe standards for data format, metadata description	1. Hard to understand contribution of noise to the analysis 2. Lack of precise DEM's 3. Processing too slow for commercial oriented customers
APPLICATION	
STRENGTHS	WEAKNESSES
(Cont.)	

(Cont.)	**APPLICATION**
STRENGTHS	WEAKNESSES
1. Some features can only be derived from IS data 2. Spectral information can be used for almost everything 3. IS is (semi-)operational for Geo-applications	1. Little understanding of added value of IS data 2. Knowledge is scattered 3. Data is not efficiently used
OPPORTUNITIES	THREATS
1. Perform temporal data takes 2. Exploit full spectral coverage in greater extent 3. Intensify interdisciplinary collaboration	1. People are reluctant to switch from multispectral to IS 2. Applied science is preferred but basic science is needed first

Despite these general conclusions about the advantages and constraints of IS, a few points can be stressed as IS advantages. One, still in the generic domain, is the unique capability of mapping at chemical and mineralogical level with a non-destructive character. The spectral response of minerals yields information about grain size, abundance and chemical composition, including ion substitution in minerals, degree of crystallinity or temperature of formation. Subtle differences in the reflectance spectra of minerals can indicate major differences in chemistry or some physical parameters.

Another advantage is that IS is sensitive to both crystalline and amorphous materials, unlike some diagnostic methods, like X-ray diffraction (Clark, 1999).

The acquisition of the contiguous spectrum for each image pixel over a selected wavelength interval makes it possible not only to identify surface materials by their characteristic reflectance or emittance spectrum but also allows the intervening atmosphere to be characterized to the level required for removal from the measured radiance signal (Clark, 1999). The possibility to model the atmosphere at very fine spectral detail retrieves reflectance with much more accuracy than ever possible. Thus, there is an increased possibility to extract other types of parameters. In addition, this allows a more subtle characterization of the spatial heterogeneity using spectral mixture analysis techniques Plaza et al. (2004), required for certain applications.

The huge data volume is a considerable threat leading to time consuming processing, too slow for commercial oriented customers. However, it's worth noticing that the major advances in remote sensing are closely linked to technological developments (Kramer, 2009). Thus, can be expected, despite of contribution to data reduction, that technology will play a key-role in solving this issue. Another contribution to satisfy time-critical constraints in specific applications, rely on parallel implementation which has already been successful for some algorithms (Plaza et al., 2009).

2.2. MINING ENVIRONMENTS

In modern societies, it is easy to overlook the fact that a large proportion of the total economy continues to rely on the extraction and utilization of geological resources.

The raw materials that are extracted are essential for the sustainable functioning of modern societies. Sectors such as construction, chemicals, automotive, aerospace, machinery and equipment which provide a total value added of € 1 324 billion and employment for some 30 million people all depend on access to raw materials (EC-DG, 2008).

The modern mining industry refers to the exploration for and removal of raw materials from the earth, economically and with minimum damage to the environment. Fuel, non-fuel minerals and non energy minerals are types of raw materials mined. There are significant differences in the mining techniques and environmental effects of mining metallic, industrial, and fuel minerals.

Particularly for this work the focus is on metallic minerals, which are also non-fuel minerals, usually combined in nature with other materials as ores.

2.2.1 THE MINE LIFE CYCLE

Minerals are non renewable resources. Thus, the life time of a mine is finite and corresponds to a temporary use of land. The mine life cycle typically comprises the following phases: I) exploration and feasibility, II) planning and construction-development, III) extraction and processing-operations, and IV) mine closure (Durucan et al., 2006; ECPMM, 2009).

During the mine life cycle, associated activities may include the items depicted in Figure 2.11, which are described below based on ECPMM (2009). Exploration is the work involved in determining the location, size, shape, position, and value of an ore body using prospecting methods, geological mapping and field investigations, remote sensing (aerial and satellite-borne sensor systems) drilling, geophysics and other methods. A feasibility study is a decision tool, based on a financial analysis, whether to abandon or develop the property.

The phase of development includes planning and construction. Items such as designing the mine, permits, and environment and social issues as well as a closure plan are dealt in the planning stage. The construction phase involves the development of the infrastructure where is established the underground or surface mine workings to provide direct access to the ore body. The overburden, i.e. the surface material above the ore deposit that is devoid of ore minerals, is typically stockpiled if it is suitable for later use in mine reclamation. All the mine infrastructure are built up such as transportation, ore handling and processing, mine waste disposal, power infrastructure, vehicle storage and maintenance, fuel supply and storage, explosives storage, as well as shops, offices, warehouses and accommodations. Particular attention is given to water management and wastewater treatment systems, water supply, potable water treatment and distribution system and sewage and waste disposal.

The operational phase includes the removal of the ore by surface or underground mining, or in situ mining, as well as ore processing and associated activities. The typical activities are depicted in Figure 2.12.

The closure of a mine refers to cessation of mining at that site, when the equipment is removed and the dismantling of facilities. It involves completing a reclamation plan and ensures the safety of areas affected by the operation. A reclamation plan outlines the "combined process of land treatment that minimizes water degradation, air pollution, damage to aquatic or wildlife habitat, flooding, erosion and other adverse effects from surface mining operations, including adverse surface effects incidental to underground mines, so that mined lands are reclaimed to a usable condition which is readily adaptable for alternate land uses and create no danger to health or safety". A reclamation plan, which in fact occurs at all stages of a mine life cycle, involves earth work and site restoration including revegetation of waste rock disposal areas.

The final stage is monitoring, which includes environmental testing and structural assessments that commonly continue long after the mine is closed.

The duration of mine life cycle is extremely variable depending on several factors, some of them inherent to the resources mined such as its dimension and type. Others are related to the options undertaken during the management of the mine and the technology available. Additional exploration may lead to the discovery of additional mineralization that conducts to the expansion of the operation thereby increasing the life of the mine. At some sites, the mine operations phase may extend continuously over a period of several years to decades while at other sites, the mine operations phase may include short or extended periods of inactivity due to changes in market conditions.

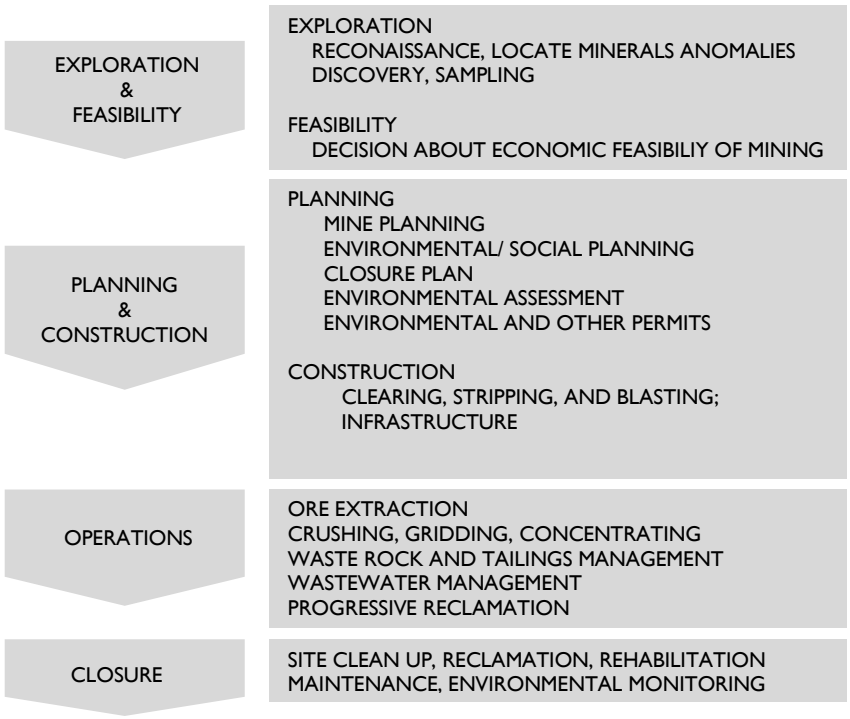

Figure 2. 11 Steps in the mine life cycle (adapted from ECPMM, 2009).

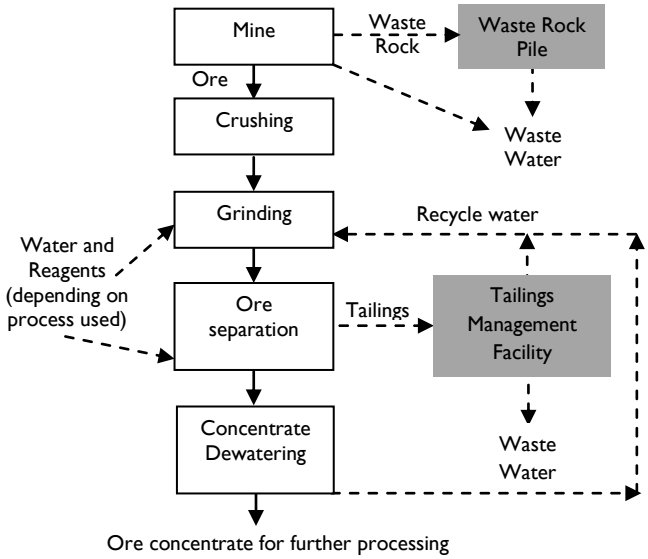

Figure 2. 12 Typical activities of the mine operations phase (adapted from ECPMM, 2009).

2.2.2 ENVIRONMENTAL CONCERNS

The environmental responsibility of mining operations is the prevention and control of environmental releases to air, water and land. This is assessed and controlled through the Environmental Impact Assessment (EIA) and Environmental Management Plans (EMP).

Throughout all mine life cycle there is an interaction with the environment, which may leave a more or less evident imprint if not adequately managed. The most striking effects are related to the operation phase, although the other phases may also interact with the environment. Examples of non-operation phase include building access roads to a drilling site during exploration or in preparation phase by excavation of the deposit to remove overburden. Mostly, they are short-term impacts in the environment.

Potential environmental concerns associated with mining include (ECPMM, 2009):

- wastewater runoff from the site, mining and ore processing, and mine wastes;
- release of airborne particulate matter and air emissions from engine operations and other processes;
- effects on terrestrial ecosystems, including wildlife;
- effects on aquatic ecosystems, including fish;
- effects on local and regional surface water quality and groundwater flow;
- noise;
- planned and accidental releases of pollutants;
- aesthetic impacts, such as alteration of landscapes;
- social impacts, such as unemployment, and people migration from mine adjacent activities and leisure activities sport or subsistence fisheries

The environmental management is significantly different if it is an open pit or an underground mine. This includes variations on waste rock disposal, tailings, area of surface disruption, reclamation, land subsidence, blasting effects, truck noise and mine water.

ACID DRAINAGE

A major environmental concern is related with the presence of sulphide minerals on surface, which form the ore minerals for many VMS base metal deposits. Pyrite (FeS_2), chalcopyrite ($CuFeS_2$), galena (PbS) and sphalerite [(Zn, Fe)S] are ubiquitous in these type of ore deposits. Sulphides may also occur in the host rock and their importance from an environmental perspective lies in the fact that in contact with water and oxygen, they oxidize and generate an acidic leachate that can act as an agent carrying heavy metals, trace elements and dissolved salts. This process is commonly known as acidic drainage s.l. (AD) and may also be differentiated in Acid Mine Drainage (AMD) or Acid Rock Drainage (ARD). The latter may even occur without mining activity and constitute a natural occurrence for, e.g., volcanogenic massive sulphide deposits.

AMD can be the result of underground mine drainage, runoff and seepage from the waste-rock dumps on surface, and from percolation in the waste bedrock interface (Walder and Schuster, 1998), and also from tailings pond areas, waste-disposal areas and haulage roads. Hence, whenever there is any type of waste mining materials with high sulphide content which interact with water and oxygen, they are considered as a primary source of AMD (Singer and Stumm, 1970; Nordstrom and Alpers, 1999; Espãna et al., 2005) and thus are potential acid generating materials.

The extent of environmental trace element contamination associated with AD is related with the extent of the oxidation of the sulphide-containing materials, the type of gangue material, ore host rocks, mine waste dispersion, mining infrastructures (e.g. dams, channels, ore mills, mine landfills), the hydrology and the hydrogeology of the area.

Iron, Cu and As sulphides, and sulphosalts in the ores make them especially sensitive to weathering and subsequent AMD producers (Abreu et al., 2010).

The weathering of pyrite, as an example of one of the most abundant sulphides, can be used to demonstrate the global reaction that explains the low pH, and the high concentrations of, at least, iron and sulphate ions, in the oxidizing environments near the sites containing sulphide minerals (Abreu et al., 2010). These reactions are well documented (Singer and Stumm 1970; Gray, 1997):

$$FeS_2(s) + {}^{7}/_{2}O_2(g) + H_2O(l) \rightarrow Fe^{2+}(aq) + 2SO4^{2+}+(aq) + 2H^{+}(aq) \quad \text{(Eq.2.2.)}$$

$$4Fe^{2+}(aq) + O_2(g) + 4H+(aq) \rightarrow 4Fe^{3+}(aq) + 2H_2O(l) \quad \text{(Eq.2.3.)}$$

$$Fe^{3+}(aq) + H_2O(l) \rightleftarrows Fe(OH)^{2+}(aq) + H^{+}(aq) \quad \text{(Eq.2.4.)}$$

$$Fe(OH)^{2+}(aq) + H_2O(l) \rightleftarrows Fe(OH)^{2+}(aq) + H^{+}(aq) \quad \text{(Eq.2.5.)}$$

$$Fe(OH)^{2+}(aq) + H_2O(l) \rightleftarrows Fe(OH)^{3\,0}(aq) + H^{+}(aq) \quad \text{(Eq.2.6.)}$$

The highly acidic aqueous solutions can promote the dissolution of both ore and host rock materials originating solutions with a high specific electrical conductivity. In the presence of oxygen and water, the Fe^{2+} ions are also oxidized to Fe^{3+} leading to the precipitation of various insoluble iron bearing minerals. A possible pathway to explain the formation of several Fe^{3+} minerals is shown in the following scheme (Williams, 1990; Hammarstrom et al., 2005; Abreu et al., 2010):

$$n\text{Fe(OH)}^{3\,0}(aq) + mH_2O(l) \rightarrow \text{ferrihydrite } (5\ Fe_2O_3{\cdot}9H_2O \text{ or } Fe_2O_3{\cdot}2FeOOH{\cdot}2.6\ H_2O) \quad \text{(Eq.2.7.)}$$

$$\text{ferrihydrite} \rightarrow FeOOH(\text{goethite, akaganeite, lepidocrocite, feroxyhyte}) + zH_2O(l) \quad \text{(Eq.2.8.)}$$

$$2FeOOH(s) \rightarrow Fe_2O_3\ (\text{hematite, maghemite}) + H_2O(l) \quad \text{(Eq. 2.9.)}$$

Other possible pathways exist depending on the water and iron content, which in turn is connected with pH values. If pH is less than 3.5, significant quantities of Fe^{3+} can exist in solution. At pH>2.5, precipitation of ion ferrihydrate will remove Fe^{3+} from solution. If the sulphate concentration is sufficiently high, ferric ion may also be removed from acidic solutions by precipitation of iron-sulphate minerals like jarosite, coquimbite, and kornelite, however, these iron-sulphate minerals have high solubility.

The ferrous ion may oxidize to form ferric ion and precipitate as ferrihydrate (or goethite, jarosite, schwertsmannite) following the reactions:

$$4Fe^{2+} + O_2 + 4H^{+} = 4Fe^{3+} + 2H_2O \quad \text{(Eq.2.10.)}$$

$$Fe^{3+} + 3H_2O = Fe(OH)_3(s) + 3H^{+} \quad \text{(Eq.2.11.)}$$

The acidic leachate is partly neutralised by hydrolysis reactions with the surrounding materials as the solution flows away from the active oxidation points leading to the accumulation of Fe sulphates, oxyhydroxides and oxides in a spatial and temporal sequence that represents the buffering of the acidic solution as it moves away from its source (Swayze et al., 2000, Montero et al., 2005). The accumulation of specific type of minerals is function of the pH values and the chemical content of leachates. Copiapite $[Fe^{2+}Fe^{3+}4(SO_4)_6(OH)_2 \cdot 20(H_2O)]$ and jarosite $[KFe_3(SO_4)_2(OH)_6]$ form at pH values <3, and precipitate near sources of acidity that are also sources

of iron and trace elements (Nordstrom and Alpers, 1999; Smith et al., 2006). However, jarosite may occur precipitating at higher values of pH waters, i.e. 3.8 as referred in Bigham et al. (1996). Goethite [α -FeOOH] forms at pH values generally less than 6 from the dissolution of previous minerals, including early-formed goethite, and precipitates farther from contaminant sources. Hematite [α -Fe_2O_3] accumulates even farther from the sources of acidity after forming in a pH dependent process that may involve the dehydration and transformation of earlier precipitates, such as those of goethite and ferrihydrite (Montero et al., 2005). The latter usually occurs at pH 6.5 or higher (Bigham et al., 1996) (in Quental et al., submitted, Chapter 5).

The complexity and diversity of the composition of AMD solutions is reflected by the variety of solid phases that can be formed under different conditions. It is not easy to explain the formation of the secondary solid phases, but some authors (Hammarstrom et al., 2005; Montero et al., 2005), based on previous studies, present general possible reaction pathways indicating the conditions (solutions composition, temperature and atmospheric relative humidity) for the crystallization of some secondary sulphate minerals from the oxidation of the primary ores (Abreu et al., 2010).

The climate is an important control on mineral formation and mobilization of metals due to the high solubility of many of the efflorescent sulphate minerals. In wet climates, salts are ephemeral unless they develop in sheltered areas. In arid climates, or during prolonged dry periods in humid climates, thick crusts of salts can form by evaporative processes, where upward migration of water by capillary action is the dominant process (Olyphant et al., 1991; Dold, 1999). The cycling of metals and acid by the precipitation and dissolution of efflorescent salts is an important process at mine sites (Hammarstrom et al., 2005).

The result of AMD, with the generation of metal-laden effluents of low pH, if not carefully managed can contaminate soils, waters and groundwaters and derived impact on ecosystems. This can occur during all mine life cycle and also after closure of the mine. The AMD is more evident in old mining areas due to the different environmental concept at the time and technological issues, which were not able to prevent or control the associated damage.

Europe has a history of mining activity that dates back to prehistoric times. Whole regions are affected by the results of this activity, as well as by the more recent industrialized phase of mine development. Increasingly, rather than exploration for new prospects, the key issue being addressed by many European geological surveys is how to manage the waste products of mining activity (Marsh et al., 2000). However, some mine waste has shown its usefulness and it has been recognized since the beginning of mining and smelting. Changing economic circumstances may turn a particular waste into a valuable asset, either because the economic extraction of resource ingredients may now be possible using improved technology or a market has been found for the previously unwanted material. In summary, yesterday's waste can become today's resource (Lottermoser, 2007).

The European Union (EU) has developed a few environmental directives that have imposed a legal pressure and frame of mining related issues, and the emergency to develop the innovative approaches to deal with. Among the key directives is the Environmental Impact Assessment (EIA) 85/337/EEC, Landfill (1999/31/EC), the Water Framework (2000/60/CE), the management of waste from extractive industries (2006/21/EC), and the Integrated Pollution Prevention and Control (IPPC, 2008/1/EC) Directives. Hence, long term repetitive site characterization mining related areas is required at all the mine life cycle as well as after closure to detect contamination extension and modelling its evolution. This will in turn mitigate its damage to the environment, with adequate remediation or safety measures.

Monitoring usually involves chemical analyses of samples of soil and organisms taken close to the mine site as well as far away from the mine site. Hence, it is often necessary to establish a relatively large number of

sampling stations, and to analyze a large number of samples to assess the level of pollution and the delineation of areas affected by pollution.

The repetitiveness of the regulatory controls will lead to choose the less expensive and time consuming methods in order to forecast the pollution dissemination processes, the level and the areas affected by pollution. This implies to minimize field–sampling density and analysis.

2.2.3 APPLICATIONS OF IMAGING SPECTROSCOPY

With the capability to detect subtle changes in the chemistry and/or structure of a material, IS constitutes an excellent tool for environmental assessment of mining areas, mineral mapping and exploration. In particular IS provides synoptic spatial coverage with associated high spectral resolution and it has a non-destructive character.

The development of the technology has started with geological mapping and its commercial role in mineral exploration (Cocks et al., 1998). In this it worked as an important tool to recognition of hydrothermally altered rocks that may be associated with mineral deposits (Hutsinpiller, 1988; Henkle et al., 1993; Crowley and Zimbelmand, 1997; Scott et al., 1998; Clark, 1999; Lorchert, 1999; Yang et al., 1999).

The IS methodologies have been used previously in mining environments in arid or sparsely vegetated environments in the USA (Superfund programme of EPA-USGS[2], using the AVIRIS sensor) and in Australia (studies made by CSIRO[3] and HyVista Corporation with Hymap™ sensor) and in Europe in a diversity of mining environments (MINEO and HyVista Corporation with Hymap™ sensor, Chapter 3).

If the mineral exploration has been the driving force in the development of mining related IS, the environmental concern has also been increasing, also to comply with EC regulations and Directives.

Thus, studies related to environmental indicators as assessment and dispersion of pollutants (Kemper and Sommer, 2003; Mars and Crowley, 2003) have been developed. The detection can be done through a mineralogical mapping or chemical correlation on materials targeted. The developed knowledge of mineralogical mapping for geological applications was naturally extended for mapping secondary minerals related to AD for environmental applications (Ong et al., 2003). Other environmental parameters mining related have been established based on vegetation stress (Kuosmanen et al., 2005).

As aforementioned, one of the major sources of pollution is the AMD generating metal-laden effluents of low pH. The detection of AMD using IS can be addressed in several ways:

1. Through mineralogical assemblages, such as Fe-bearing sulphates, oxides, and oxyhydroxides, which are identifiable through specific spectral ranges, due to their chemical and structural properties. Valuable studies have assessed (Montero, 2002; Montero et al., 2005; Swaze et al., 1996; 2000; Dalton et al., 1998) and monitored (Riaza et al., 2007; Riaza et al., 2009) areas affected by AMD and consequent release of hazardous elements. Using imaging spectroscopy principles it is possible to identify the unique spectral absorption characteristics of iron secondary minerals (Clark 1999) from hyperspectral images. Further details on the basis for spectral interpretation and mineral identification are given in Montero et al. (2005) and Crowley et al. (2003). Thus, the mineralogical mapping of an area based on specific minerals, particularly

[2] EPA-USGS (Environmental Protection Agency-United States Geological Survey)

[3] CSIRO – (Commonwealth Scientific and Industrial Research Organisation)

Fe-bearing minerals, as described previously, can indicate pH values at the time of their generation and subsequently their acid generating potential. Highlighting AMD hot spots, the mineralogical mapping provides valuable information for prioritization related to remediation procedures or safety measures.

II. Quantitative physiochemical maps from airborne hyperspectral data transfered from spectral prediction of pH from laboratory analysis (Ong et al., 2003a; Zabcic et al., 2005). The former consider that the mineralogical maps for characterizing and assessing the risks or hazards at contaminated mine sites are only shown on single "snap shots" taken on specific dates. However, traditional methods of assessing and monitoring AD conditions rely on chemometric measurements and to deliver a product that is aligned with industry standards, there is value in providing these physiochemical parameters directly. Secondly, it is necessary to demonstrate that it is possible to derive these measurements accurately and repeatedly. The method relies on the use of relationship between IS data and pH measurements using field data obtained from environments affected by AD. A predictive model is generated from this laboratory analysis based on a statistical technique, called partial least squares (PLS) and with a final regression coefficient (FRC) based on linear combinations of channels. The ability to transfer this predictive capability to produce quantitative physiochemical maps from airborne hyperspectral imagery is demonstrated, as well as is multi-temporal capabilities. Zabcic et al. (2005) apply the same methodology to the Spanish Iberian Belt, demonstrating its usefulness in a distinct environment.

III. Spectral Mixture Analysis with a classification approach based on fraction maps of major mine tailings-related surface materials and hence generates a surface map separating green vegetation, transition zones, dead vegetation, and oxidized tailings, and calculates the extent (superficial area) of each of the zones. The four zones are correlated with the extent and degree of vegetation cover affected by tailings material, and is interpreted to span respectively from very low to medium, high, and very high AMD pollution. (Richter et al., 2008). This method determines by areas, scene-based reference spectra and not by spectral libraries. It combines constrained spectral mixture analysis and threshold based classification. The relationship with the AMD is performed indirectly.

IV. Through dispersion of contaminants such as in mining spills, e.g. the accident in Spanish Aznalcóllar Mine (Kemper and Sommer, 2003). A spectral mixture modelling approach applied to field and airborne hyperspectral data was implemented to map residual contamination after a mining accident where heavy metal bearing sludge from a tailings pond was distributed over large areas of the Guadiamar flood plain. A Variable Multiple Endmember Spectral Mixture Analysis (VMESMA) tool was used providing possibilities of multiple endmember unmixing, aiming to estimate the quantities and distribution of the remaining tailings material. A spectrally based zonal partition of the area was introduced to allow the application of different submodels to the selected areas. Based on an iterative feedback process, the unmixing performance could be improved in each stage until an optimum level was reached. The sludge abundances obtained by unmixing the hyperspectral spectral data were confirmed by the field observations and chemical measurements of samples taken in the area. The semi-quantitative sludge abundances of residual pyritic material could be transformed into quantitative information for an assessment of acidification risk and distribution of residual heavy metal contamination based on an artificial mixture experiment.

Any of the methods is a valid contribution of IS applied to mining environments. It is worth noticing that in sustainable mineral resources operations, IS derived information is an advantageous assessment and monitoring tool. Thus, throughout the mine life cycle and in long term post-mining, IS contribution can be extremely useful. It's an appropriate method to comply with the demand of environmental data required by legal framework and with repeatability capabilities to constitute a major component of environmental monitoring systems related to mining areas.

2.3 CONCLUSIONS

Imaging spectroscopy (IS) or hyperspectral is an invaluable tool relying on spectroscopy principles established in the 19th century (Schaepman et al., 2009). The spectral response given by an IS sensor allows the expansion of a point spectroscopy to a spatial dimension providing the capability of gather spectral information over wide areas.

The absorption features obtained by an IS sensor facilitates the quantitative and qualitative characterization of both the surface and the atmosphere. The acquisition of spectral data can be undertaken at several scales, in laboratory, field or airborne or spaceborne platform. Once obtained, several procedures have to be addressed on IS data before obtaining a map of an area for specific themes. This may include the atmospheric and geometric corrections, as well as feature extraction and endmembers. The spectral measurement of materials in laboratory and gathered in standard spectral libraries to compare with imagery data is frequent.

The classification can follow distinct pathways, whether considering the full or mixed pixel approach both relying on spectral information. Recent trends, however, focus on the integration of both spatial and spectral information (Plaza et al., 2009). Also, the processing techniques may encompass very different mathematical formalisms.

The application of classical validation or accuracy assessment to IS data presents a few constraints and limitations, once the imagery may map the environment with greater accuracy than can be obtained by field crews or maps produced by other methods then remote sensing (Jacquez et al., 2002; Aspinall et al., 2002; Foody, 2008). Several other constraints and advantages exist when using IS data related to items such as campaigns, sensors, processing and applications.

In a mining environment, a mine life cycle typically comprises the following phases: I) exploration and feasibility, II) planning and construction-development, III) extraction and processing-operations, and IV) mine closure. In all, environmental concerns occur, although in some phases are more emphasized then others, and has to comply with legislation requirements.

With the capability to detect subtle changes in the chemistry and/or structure of a material, IS constitutes an excellent tool for environmental assessment of mining areas, mineral mapping and exploration. Thus the application of IS can occur throughout all mine life cycle, and in a particular environmental concern in the case of Acid Drainage several approaches have already been demonstrated for its detection, whether in assessment or monitoring.

IS is an appropriate method to comply with the demand of environmental data required by the legal requirements, by minimizing costs of density sampling and analysis. Jointly with repeatability capabilities, IS can constitute a major component of environmental monitoring systems related to mining areas.

3. THE S. DOMINGOS MINE AREA TEST SITE

3.0 INTRODUCTION

This chapter describes the test site, following essentially the main structure as in Quental et al. (2002a), adapted and updated with new studies. Some general characteristics are described, as well as geology, history of exploitation and related environmental problems of the test site.

The Imaging Spectroscopy (IS) data capture in 2000 over this test site, objectives and results, are presented in a broader framework of an EU research project, the MINEO (5th FP, 2000-2003) as well as the lessons learnt and foreseen scientific developments.

For the S. Domingos area, a new capture of IS data took place in 2007 in the framework of the HYPMINGEO project funded through EUFAR (6th FP of the EU) and the acquisition and ancillary data is described.

3.1 GENERAL CHARACTERISTICS

The now abandoned S. Domingos mining area is located in SE Portugal (Figure 3.1) within the Baixo Alentejo Province some 60 km SE of the city of Beja, close to the Spanish border. The climate of the region is, according to the Thornthwaite classification, semiarid mesothermic with no excess water and small thermal efficiency in the hot season, and it can be divided in two distinct periods, a wet period from November to March and a dry period from May to September The annual average air temperature is 17.6 °C, and annual precipitation is 559 mm (Abreu et al., 2008).

The population density is currently low nowadays although it has reached nearly 5000 persons whose main activity was related with the extraction of massive sulphides.

Most of the area is covered by thin soils, and natural rock outcrops are abundant.

In the S. Domingos Mine, pre-roman and roman mining works are known to have exploited Ag, Cu and, Au, mainly in the gossan resulting from the oxidation of the sulphide mass. Modern exploitation started in the XIX century, both in the gossan and massive sulphide orebody that besides Cu also contained some Zn and Pb, and ended in 1966 due to exhaustion of the ore. As a result of the mining activities several on-site facilities were developed, including a village (S. Domingos, Figure 3.1), water reservoirs, cementation tanks, a sulphur factory, network channels for acid water evaporation, and a railway and harbour (Pomarão) for ore transportation and shipping. It is estimated that from the beginning of pre-roman times until 1968 the Mine produced 25 Mt of ore, and mine waste material in the area is estimated at several hundred thousand tons.

In this context, important environmental problems are associated, which are visible within an area around 50km^2. Although correlated, these problems can be summarized as related to waste material and their pollutant content, acid waters and associated dispersion, as well as landscape disruption.

3.2 GEOLOGY

REGIONAL GEOLOGY

The Iberian Pyrite Belt (IPB) extends from Spain along southern Portugal. It constitutes one of the most important metallogenic provinces for Volcanogenic Massive Sulphide deposits, and within which occurs the S. Domingos Mine (Appendix 1, Figure 3.1).

The general geology of the Mine area consists of the outcropping Volcanic Sedimentary Complex (VSC) rocks that consist of acid and basic lithologies of Tournaisian age (Appendix 1).

Webb (1958) described the area as being underlain by Paleozoic sediments, "comprised mainly of clay-slates with interbedded grits, quartzites and occasional tuffaceous horizons". Recent studies identified these Paleozoic sediments as: in the northern part, older formations from the Pulo do Lobo Antiform [Gafo Formation (schists, silts, greywackes, acid and basic volcanism) and the Represa Formation (schists, silts, greywackes and quartzwackes)] of Upper Devonian age, while to the south, in the mine area outcrops the Phylite-Quartzite Formation (phyllites, silts, quartzites and quartzwackes) and the Barrranco do Homem Formation (phyllites, silts and greywackes) of the same age (Oliveira and Silva, 1990). With the Hercynian compression the sedimentary assemblage was intensely folded and the more incompetent beds marked with a strong flow cleavage, dipping at steep angles to the NNE. The strike direction of both cleavage and bedding is 110-125°.

Locally, quartzites can occur in large extents. At intervals along regional strike, sediments are intruded by dykes ranging from acid (porphyries) to basic (diabases) in composition, which recently were interpreted as belonging to the VSC of Tournaisian age (Oliveira and Silva, 1990). To the south, a large area is covered by the Mértola Formation (Lower Carboniferous) that consists of a turbiditic sequence of pelites and greywackes. The VSC, host to polymetallic massive sulphides of IPB, orientated WNW-ESE, is represented by two structures, the alignment of the S. Domingos and Pomarão anticlines. In the flanks of these structures representative outcrops are marked by three episodes of acid volcanism, separated by sedimentary cycles. Within the Pomarão anticline outcrops the Eira do Garcia Member [silts and pelites and greywackes (PQ)] and the Upper Devonian Nascedios Member (grey pelites with thin interbedded limestones); the Pomarão Harbour being located in its inverse flank. Above the VSC, there is a turbiditic sequence that can reach four thousand meters in thickness and is composed of alternating schists and greywackes (Baixo Alentejo Flysch).

MINE GEOLOGY

An irregular tract of superficial iron-staining and gossan extends southeast from the orebody and lies in part on the slopes of a shallow to moderately incised valley which drains southeast from a point about 500 m from the mine.

The volcanic sequence in the mine is not well exposed and the structure is geologically complicated. The upper volcanic levels are covered by a thick turbiditic sequence (Flysch Group) and the allochthonous Phylite Quartzite (PQ) group caps the volcanic pile. The outcropping area was formed by a unique vertical mass of cupriferous pyrite associated with zinc and lead sulphides, elongated in an E-W direction. This orebody was exploited to a depth of 120 m below the topographic surface as an open pit mine and from this depth down to

420 m. Mining accesses consisted of wells and galleries. The mapping of level 240 m and geological section of the massive sulphide are shown in Figure 3.2. The intense wall-rock alteration surrounding the orebody is typically hydrotermal, and comprises argilitisation (kaolinite and allunite), sericitisation, chloritisation and silicification.

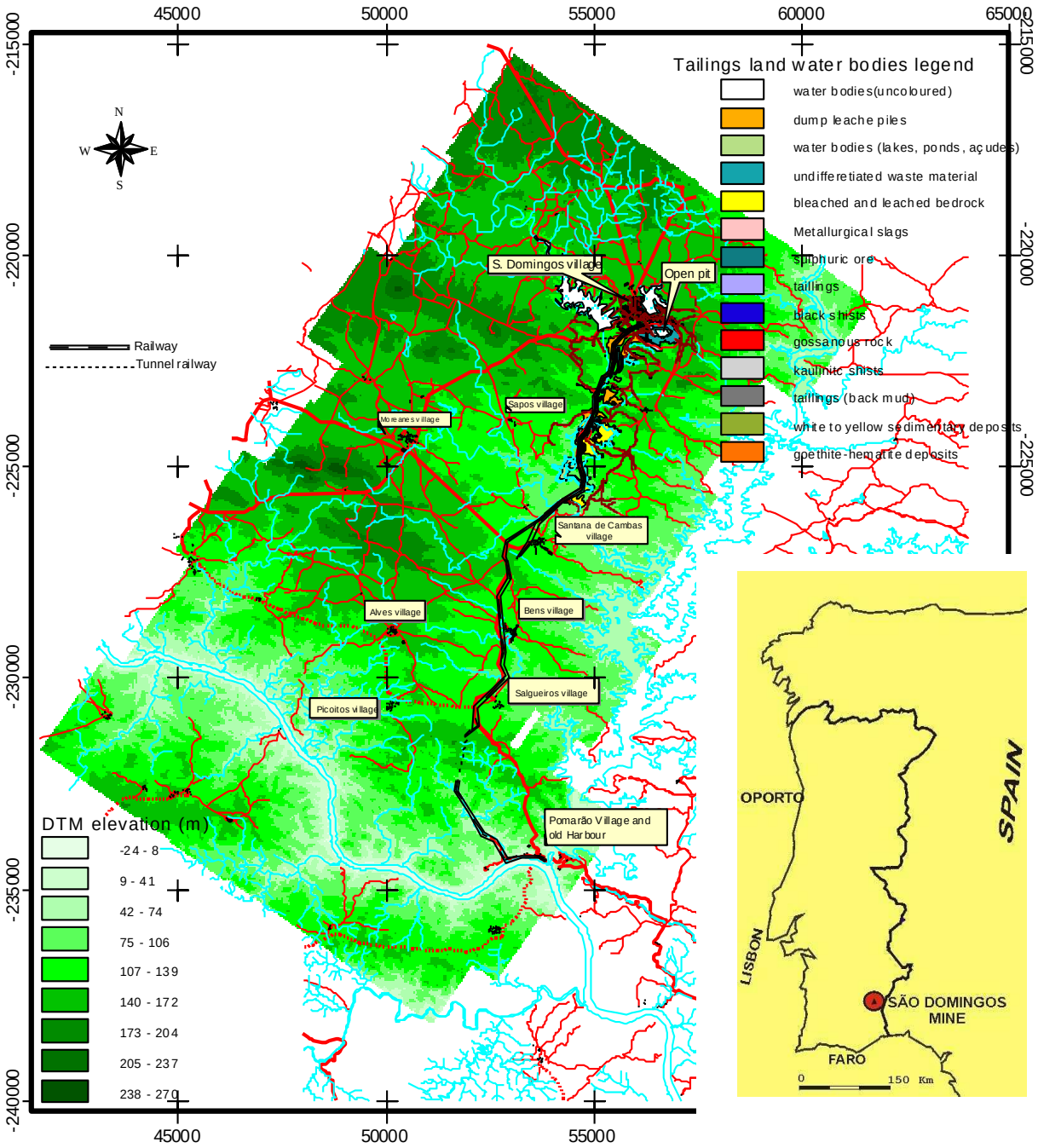

Figure 3. 1 Framework of the S. Domingos mine location and main characteristics (in Quental et al., 2002a).

The reddish-brown gossan extending southeast from the orebody is probably an erosional relict of transported iron oxides and hydroxides that accumulated during the original weathering of the ore, which is almost completely eroded. The deep residual gossan results from a weathering process of the exposed orebody, due to eventual uplift and peneplanation.

The northern side of the open pit mining walls show relicts of ancient roman galleries for exploitation of gold, silver and copper in the gossan. From W to E, along the open pit wall levels, the white coloured alteration zones of the black shales are clearly identified, the extremely silicified felsic tuffs, host rocks of the stockwork feeders, and the basic lithotype, represented by green coloured rocks possibly due to hydrothermal alteration below the stockwork, chloritisation (Silva et al., 1997). Anastomosing veinlets, vein networks (feeder channels) and disseminations of sulphides that grade into massive sulphide lenses make up the stockwork mineralisation by coalescence of veins and replacements.

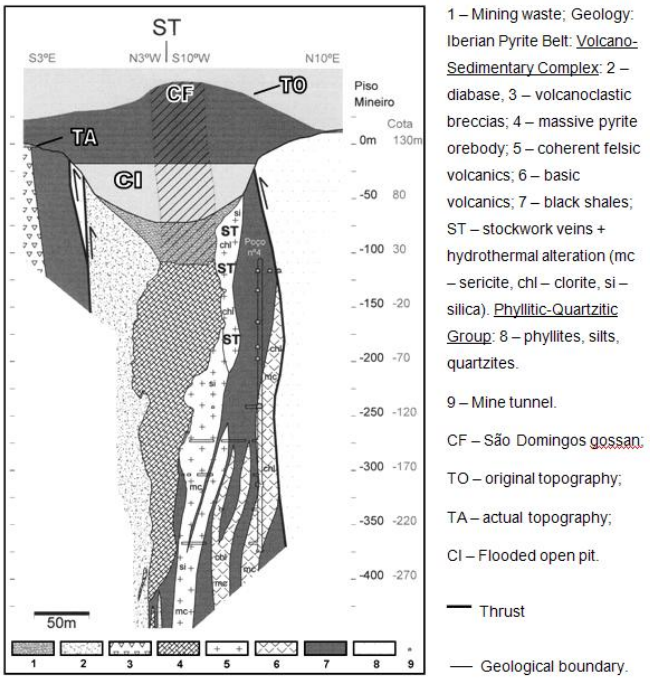

Figure 3. 2 S. Domingos mine open pit, geological cross-section (ad. Oliveira and Matos 2004; Matos et al., 2006).

Stockworks generally occur in highly silicified and chloritised footwall volcanic rocks (Barriga and Carvalho, 1983, in Silva et al., 1997).

3.3. HISTORY OF EXPLOITATION

Based on the work of Batista (2000), the exploitation at the S. Domingos test site, ranging from pre-roman activity to the 1960´s, can be summarized as follows:

PRE-ROMAN PERIOD

Almost every archaeological study in the Volcanogenic Massive Sulphide mines within the Iberian Pyrite Belt (IPB) show evidence of pre-roman exploitation of precious metals and copper in the superficial ore bodies, as a

result of their concentration by supergene alteration. Despite there being no specific studies in S. Domingos, the evidence of works nearby, and the arguments supported by Allan (1965), related to the huge amount and nature of waste material found, and also the presence of megalithic structures, suggests that mining and metallurgy took place (Gaspar, 1998).

ROMAN PERIOD

During this period the existent literature shows that at S. Domingos the underground works went below the hydrostatic level. The Romans exploited gold from the gossan, and small contemporaneous galleries are still recognizable. These ancient mining activities were largely confined to the oxidized ore near the surface (Webb, 1958).

Based on the volumes of ancient waste piles and the respective chemical composition phases, several authors have estimated the volume of Roman works in more than 150 000 m^3, which corresponds to 300 000 t of slags, considering both mines of S. Domingos and Aljustrel (Sequeira, 1884, in Gaspar, 1998).

POST-ROMAN PERIOD

After the roman expulsion by the Visigoths, around 405 A.D., a period of almost no mining activity followed in Iberian Pyrite Belt except maybe at Aljustrel and in one or two mines in Spain until 1492 during the Islamic occupation of the Iberian Peninsula. Irrelevant activity probably occurred after that, but only in the XVIII century, and more intensively in the XIX century, were the exploitation works again economically significant.

XIX CENTURY

The interests of French industrialists, in particular Ernest Deligny, technical director of a few mines in Spain who sent people to do exploration in Portugal, started the process that led to the concession of the S. Domingos Mine. Nicolau Biava is recognized as the legal discoverer of the orebody at S. Domingos and obtained a temporary concession that was transferred in 1855 to Ernest Déligny, Luis Decazes and Eugène Duclerc, who had founded the company La Sabina in 1855.

A permanent license was given in 1859 when Diogo Mason took charge. Mason and Barry, Ltd., was constituted later, to whom La Sabina rented the exploitation concession. The mining exploiters carried out the construction of a typical mining village, whose typology characterizes the classical industrial period. They created rigorous urban planning and the village was almost autonomous with farms, orchards and even with its own police force (Alves, 1997).

The mining plan began in 1859 but the underground and surface mining only began in 1863. Due to the fluctuation of copper grades, only the richest ore were sent to England where incineration processes were used to extract sulphuric acid. This extraction process was experimental in closed ovens, in order to avoid environmental problems that occurred in an open environment, nearby in Rio Tinto, which produced gases rich in SO_2, As, Sb and Ti, provoking disastrous effects locally in fauna and flora that persist today.

In S. Domingos, the first products extracted by incineration processes were separated and the richest nodules were submitted to a fusion process. The leaching of the poor products was carried out in cementation tanks but this process was abandoned in 1868 due to technical difficulties and high costs. When copper prices dropped, the material was leached in a raw state making the recovery more efficient.

The method utilised in the treatment of the ore can be summarised as follows:

1. separation of Cu>2% from Cu <2% into four piles, fines and poor material;

II. crushing of the richest and coarse-grained material into pieces of more or less 5 cm in size;

III. accumulation of Cu<2% in piles with interior channels made of gravel material for easy circulation of the air, sandstone chimneys to control the temperature of the process as this process was strongly exothermic;

IV. the leaching of the piles with water controlling the temperature to avoid spontaneous combustion of the mined material and excessive formation of sulphuric acid that could make a poor cement and raise the iron consumption (Gaspar, 1998).

The ore was exported for sulphuric acid production; the leaching products had 14% of Cu and were led to the tanks to decant particles and sent to cementation tanks. The iron used in the process was about 20 000 t a year. From the 4 Mt of copper mineralization extracted from 1870 until 1887, 334 575 t were transported to the treatment facilities in Achada do Gamo and 378 320 t of washed product and 85 046 t of copper concentrate were exported.

A railway was built in 1858, linking S. Domingos Mine to the Pomarão Harbour, in the Guadiana River, from where the ore was shipped downriver to the Atlantic Ocean and eventually on to the UK. In Swansea part of the material was treated to obtain copper and part to obtain gold and silver (Gaspar, 1998).

The first exploitation plan dates from 1858 and plans for the underground exploitation of the orebody in all it's extension following old works with longitudinal galleries (parallel to the orebody axis) and cross cuts, distributed over several levels with connecting wells and supporting rock piles in the exploitation areas. In 1863-65 27 vertical holes had already been built for mining circulation and sewage waste (Rego, 1996) and in the same period the sulphur smelting facilities were built in Achada do Gamo.

In 1866-67, during a copper price downturn, the mine opted for a cheaper open pit type mining although continuing the underground extraction.

The first exploitation of the open pit started in 1868, causing a progressively strong impact in the landscape leaving an open area with 122 m depth when the extraction was abandoned, continuing only the underground works. Dikes were constructed to support the mining works and the water supply of populations in 1871-73.

Acid effluents from mining, estimated at 2 hm/year were diverted to a network of channels and reservoirs to improve the quality of effluent by increasing settling, to reduce its quantity by natural evaporation and infiltration. It was also a process to control its discharge into the main nearby river, the Chança, during flood periods (Pereira et al., 1995). The total area of evaporation surfaces created in this system was 97 ha (Mason and Barry, 1878).

XX CENTURY

In the early XX Century the worldwide evolution of the sulphuric acid industry favoured its extraction from pyrite, which resulted in an increase in exploitation in the S. Domingos Mine. From 1913 to 1932, S. Domingos produced 3 445 533 t of copper ore and from 1923 to 1932, 3616 t of Cu cement with average grades of 72,33%. At the end of 1960, a new crisis caused by competition within the native sulphur market extracted from sulphur ores of low degree (by hot water pressure) and the external market gave place to internal consumption of sulphides by the sulphur acid factories. As an example, as much as 430 000 t of acid was produced in factories like QUIMIGAL and SAPEC, most of it being used to produce fertilisers. The global ore produced in the XX century in S. Domingos is estimated at 9 882 722 t (Gaspar, 1998).

Mined ore was crushed in a mill located near the open pit. Three kilometres south of the mining area (at Achada do Gamo, Figure 3.1) the crushed ore was smelted to obtain high level grades of copper ore and sulphur products, which were widely used in the chemical industry until the 50's.

Average grades of the exploited material range from 1,25% Cu (10% Cu maximum), 2-3% Zn and Pb (14% Zn and Pb, maximum). Massive pyrite grades average in the range from 45-48% in sulphur, and in addition to pyrite there are subordinate amounts of chalcopyrite, sphalerite, galena and other rare sulphides (Webb, 1958).

The Mine was closed in 1966 presumably due to exhaustion of the ore although some authors think that the ore extends deeper (Gaspar, 1998, Oliveira, V. pers. com., 1999). The open pit has since become flooded.

From the beginning of pre-roman times until 1968, the Mine produced 25 Mt of ore (Carvalho, 1979 in Gaspar, 1998).

On 30th July 1972, the company La Sabina, took possession of mining facilities of the S. Domingos mining concession, after the complex process of bankruptcy of Mason and Barry Limited. In 1984 La Sabina, financed by German capital, lost the historical concession maintaining however the rights acquired in the lands and buildings covered by the mining concession.

This area has not been submitted to any remediation process, although some information and protection around the most endangered areas, i.e. the open pit and Achada do Gamo (Figure 3.1), took place in 2005 as well as some beneficiation of the building of the former railway station of Pomarão. Removal of dump material continues and is used for several purposes, namely construction and pavement, spreading potentially harmful materials, if related to AMD signature.

3.4. RELATED ENVIRONMENTAL PROBLEMS

The type of ore, treatment, processing and transportation, as described in Section 3.3 caused important environmental problems, some of which already reported in the XIX century, and with direct economic consequences for the exploitation company.

The specific problems associated with the S. Domingos test site, can be summarised as follows:

WASTE MINING MATERIAL AND ASSOCIATED CONTAMINATION

Waste mining material such as slags, heap dumps and tailings, either concentrated or dispersed in the area, are still enriched in hazardous elements such as Zn, Pb, Sb, Cu, As, Hg and Cd. These waste materials leached by rainwater and stream waters can have highly acid generating potential, due to sulphide oxidation and Fe-hydrolysis, which increases dissolution and mobility of elements. They constitute hot spots for waters, soils and plant contamination (Figure 3.3).

ACID WATERS AND DISPERSION OF ELEMENTS

The Acid Drainage s.l. (AD), mainly from Acid Mine Drainage but also from Acid Rock Drainage, is the main vehicle for the dispersion of elements in waters, soils and sediments, which covers significant areas in this test site. Water pH in the S. Domingos River can reach values below 2 (Batista et al., 2003).

The network system of channels developed for evaporation of acid waters from mining works strongly affected soil constitution in some areas.

LANDSCAPE DISRUPTION

The open pit with an area of 0.25km^2, ponds, water dams and waste mining material (slags and dumps), concentrated or spread out, have a striking imprint in the area. The presence of unvegetated slopes due to leaching by acid waters still remains, particularly in the margins of S. Domingos river, S of Achada do Gamo.

Slags and dumps are still being moved nowadays by human action, which alters topography and the existing chemical equilibrium conditions within the dumps. This disequilibrium favours acid drainage in a continuous process. The remnants of mining infrastructures distributed in the area present several degrees of degradation and consequent hazard (Figure 3.3).

Figure 3. 3 Example of acid waters channels, unvegetated slopes due to acid drainage and waste mining materials at Telheiro (upper) and Achada do Gamo (lower) (Figure 3.6).

3.5. BASELINE OF IMAGING SPECTROSCOPY DATA: THE MINEO PROJECT

The Project Assessing and Monitoring the Environmental Impact of Mining in Europe using Advanced Earth Observations techniques (MINEO) was a three year Research and Technical Development project funded by the 5th FP of the EC (IST-1999-10337). The Consortium joined seven geological surveys, two mining companies, one environmental research institute and the European Commission's Joint Research Centre. It was coordinated by the *Bureau of Research Geologique et Miniére.* It ended in 2003. The Portuguese coordinator was LNEG (ex-IGM) together with the IST, FCTUNL and ISA universities.

The MINEO project aimed to test hyperspectral remote sensing as a tool to help solve some of the environmental issues related to mining areas within a variety of European environments, through developments of:

I. Innovative methods for the extraction of information and knowledge from Earth Observation (EO) data, which will be required in the future in order to provide the European Community and users (industry, decision makers) with new and regularly updated thematic layers for an environmental database related to mining areas, active, planned or abandoned, and to develop operational tools for preparing and updating these layers;

II. Key components of the decision making tools necessary to exploit EO information and knowledge in environmental management systems and facilitate their use in sustainable information systems to locate and monitor environmental risks related to European mining sites, and thus to aid the environmental management decision processes.

To achieve these objectives the same methodological steps have been followed over six test sites, despite some variations due to site characteristics, as depicted in Figure 3.4. This included (MINEO Consortium, 2003):

I. Hyperspectral airborne data acquisition campaign, carried out during summer 2000, including the simultaneous acquisition of field reference spectra for image calibration and reference target measurements;

II. Spectral identification of contaminated areas during extensive field spectroradiometric campaigns, using various field spectrometers. This led to the development of reference spectral libraries of the contaminated and/or impacted areas and their surroundings, and the generation of the MINEO Spectral Library (MSL). Meanwhile, relevant site environmental data have been collated;

III. Development and verification of specific image processing techniques for discrimination of contaminated or impacted areas, in view of the generation of dedicated "generic" procedures and algorithms for mapping contamination and/or impacts from hyperspectral imagery. Attention was also paid in testing and using commercially available algorithms, and

IV. Integration of the resulting output maps with other site-environment relevant data for GIS modelling of pollutant dissemination, impact assessments, change detection, re-vegetation process in view of the production of examples of EO and GIS-based models for environmental management.

To undertake these steps, six mining areas, five within Europe (Portugal, United Kingdom, Germany, Austria, and Finland) and one in Greenland were been selected for investigation, showing the European climatic, geographic and socio-economic environment diversity (Chevrel et al., 2002; Marsh et al., 2000).

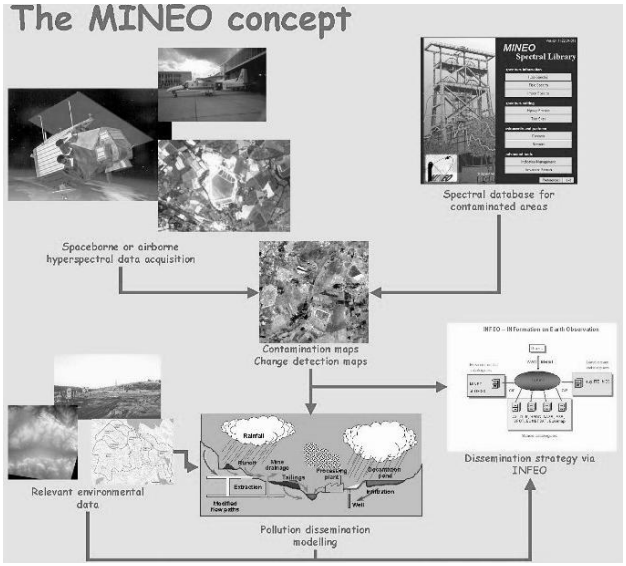

Figure 3. 4 The conceptual methodology of MINEO (in MINEO Consortium, 2003).

SCIENTIFIC ACHIEVEMENTS

Very encouraging results have been obtained in the contribution of airborne imaging spectroscopy for the study and monitoring of mining environments, despite the very challenging but problematic abundance of vegetation characterizing in most of the European environments analyzed. IS has proven capabilities in mapping mining-related contamination and/or impacts. Promising results have been obtained in combining those resulting maps with other relevant information under GIS for modelling contamination, pollution risk, site rehabilitation or change detection (Ditmann and Vosen 2002; Grösel and Belocky, 2002; Tamstorf et al., 2002, Kuosmanen et al., 2002; Cotton and Tongue, 2002; Quental et al., 2002a).

The possible generic character of the procedures and algorithms used has been examined, in particular through site cross-validation approaches, in view of their applicability and reproducibility in Europe and other parts of the world. Despite being based on only six test sites, this large diversity of results and approaches show that imaging spectroscopy can bring an invaluable contribution to very diverse environmental concerns, in a large variety of mining environments and in different morpho-climatic contexts. This opened large encouraging perspectives in meeting the ultimate objectives of the project described above, despite it is clear that this very innovative method still is to be matured before reaching a real operational status (MINEO Consortium, 2003).

A specific spectral database application (MINEO Spectral Library or MSL) has been developed in the course of the project. Fed with more than 1500 representative spectra from either laboratory spectroscopy of field samples, or field spectroradiometry, or hyperspectral image endmembers, MSL constitutes now an innovative extensive spectral library of contaminated or impacted areas from the six test sites. MSL has functionality that facilitates the management, comparison, search and retrieve of spectra, according to spectral characteristics, type of surface feature or target investigated location, climatic conditions, etc. Spectra can be directly displayed into the image-processing software environment for immediate use in IS image processing for environmental impact mapping. It could be used in other similar projects for contamination and impact mapping. The application can also be used in IS projects to create their own-related spectral database. Although a very important product generated, some Intellectual Properties Rights issues were not unblocked in subsequent years in order to make it publically available as foreseen.

Products of the project included spectral libraries of contaminated materials, image processing algorithms for highlighting contamination, methods for modelling pollution migration and generic, low-cost approaches to environmental management using EO data (Marsh et al., 2000; Chevrel et al., 2004). A further benefit was the development of a more widespread European expertise and experience in the use of hyperspectral data ahead of the deployment of satellite systems in the years to come.

SOCIO-ECONOMIC RELEVANCE AND POLICY IMPLICATIONS

The European mining and extractive industry, contributing with 7% of the gross domestic product in Europe, is facing increasing environmental pressure and regulatory controls. Industrialists and decision-makers need innovative and cost-effective tools for environmental data acquisition and processing that provide the sound basis for a dialogue with organisations in charge of environmental control and regulation enforcement ensuring the sustainable economic development of the mineral industry.

Though not producing such a system, MINEO fits into the environmental risk and emergency management system requirements as it intends to develop system of elements such as tools and methods to provide data for assessing environment baseline and monitoring ongoing processes along with generic GIS tools and models for pollution-dissemination (contamination), pollution risk, site rehabilitation or change detection monitoring and forecasting.

Therefore, the MINEO outputs are a contribution for some EU directives and policies. This includes the Soil Policy Development and Soil Strategy from DG ENV, in particular soil monitoring. A few years later, the directive 2006/21/EC on the management of waste from extractive industries, which seeks to minimize the environmental and human health effects of polluted drainage from extractive waste disposal facilities and to prevent or minimize the impact of accidents, provides a legal framework for the sound management of such waste. More recently, the Integrated Pollution Prevention and Control (IPPC, 2008/1/EC) Directive establishes further requirements for industrial and agricultural activities with a high pollution potential.

3.5.1 LESSONS LEARNT

The project and its outputs have shown the potential of IS in remotely mapping mining-related impact over vegetated environments, either by direct mapping of potentially contaminating minerals and/or rocks or by indirect mapping through the stress on vegetation.

MINEO has produced results, which can be used in the process of acknowledging this innovative technology to environmental authorities and regulatory bodies as well as the extractive industry.

Despite the technique still needing maturity, it opens new perspectives towards regular mapping and monitoring of large parts of the territory to regularly update thematic layers for environmental database related to mining areas. These updated layers can be further used in the regular monitoring and control of mining environments by regulatory bodies, but also serve mining companies conducting Environmental Impact Assessments (EIA) and Environmental Management Plans (EMP).

Eventually, MINEO constitutes a good starting point for further RTD projects in the frame of a growing interest for IS in environmental studies and initiated an increasing interest of the international scientific community for mining-related remote sensing studies.

The MINEO project can also be seen as the initial point for forming an EU-wide reclamation task force responsible for rapid risk assessment by independent European experts, development and preparation of site-specific reclamation scenarios.

The possible generic character of the procedures and algorithms used has been examined, in particular through site cross-validation approaches, in view of their applicability and reproducibility in Europe and other parts of the world. Despite based only on six test site, this large diversity of results and approaches show that IS can bring an invaluable contribution to very diverse environmental concerns, in a large variety of mining environments and in different morpho-climatic contexts. This opens large encouraging perspectives in meeting the ultimate objectives of the project described above, despite it is clear that this very innovative method still is to be matured before reaching a real operational status (MINEO Consortium, 2003).

However, further developments were not concretely defined for a while (Chevrel, 2005), although projects related to this subject were launched in 2010 in the EC funded FP7. This is the case of the Earth Observation for Monitoring and Observing Environmental and Societal Impacts of Mineral Resources Exploration and Exploitation (EO-MINERS). This project will, as the name suggests, use current knowledge and data, along with existing and new technological and scientific EO-based methods and tools, including IS, to monitor mineral resources exploration and mining from concept to closure and observe, monitor and provide information to manage its impacts on the environment and society. Another project is the Impact Monitoring of Mineral Resources Exploitation (ImpactMIN), aiming also to develop new methods and a toolset for impact monitoring of mining operations using EO and in-situ data, it points towards a future wherein decision making is based on coordinated, comprehensive and sustained EO and information, which is the main objective of the Global Earth Observation System of Systems (GEOSS). ImpactMin will address the need of the provision of timely data and products for policy makers, thereby harmonising observations, real- or near real-time monitoring, integration of information from in situ and airborne and satellite observation through data assimilation and models.

3.5.2 MINEO FOR THE S. DOMINGOS TEST SITE

The conceptual methodology of the MINEO project, as depicted in Figure 3.4, has been adapted to the S. Domingos mining area, the Portuguese test site as representative of Southern European Environment, according to the works proposed. The work developed in this test site is shown in Figure 3.5, where the relationship among the data set is established, the type of software used and the outcome as well as a relative validation.

The results obtained in this test site are described more in detail in Quental et al. (2002; 2003); Batista et al. (2003) and Tavares et al. (2008).

It's worth noticing the development of a conceptual environmental model for this test site, the establishment of subareas for detailed study, and the validation/demonstration of these subareas with contamination patterns based on geochemical data and further modelling. Also the support that this provides to the works developed on image processing.

Concretely, the area under study in the MINEO project comprises approximately 70 km^2 (Figure 3.6). Within this area, six subareas (S. Domingos-SD, Tapada-TA, Achada do Gamo-AC, Telheiro-TE, Pomarão N-PN and Pomarão S-PS) have been selected for data collection (soils, sediments, waste materials, waters and vegetation), for correlation and validation of hyperspectral data (spectroradiometric measurements, geochemical analysis, and parameters of environmental interest).

Previous knowledge based on the lithologic variability and aspects related to mining and vegetation (Table 3.1), helped in the definition of these sub areas expecting to assess different levels of contamination.

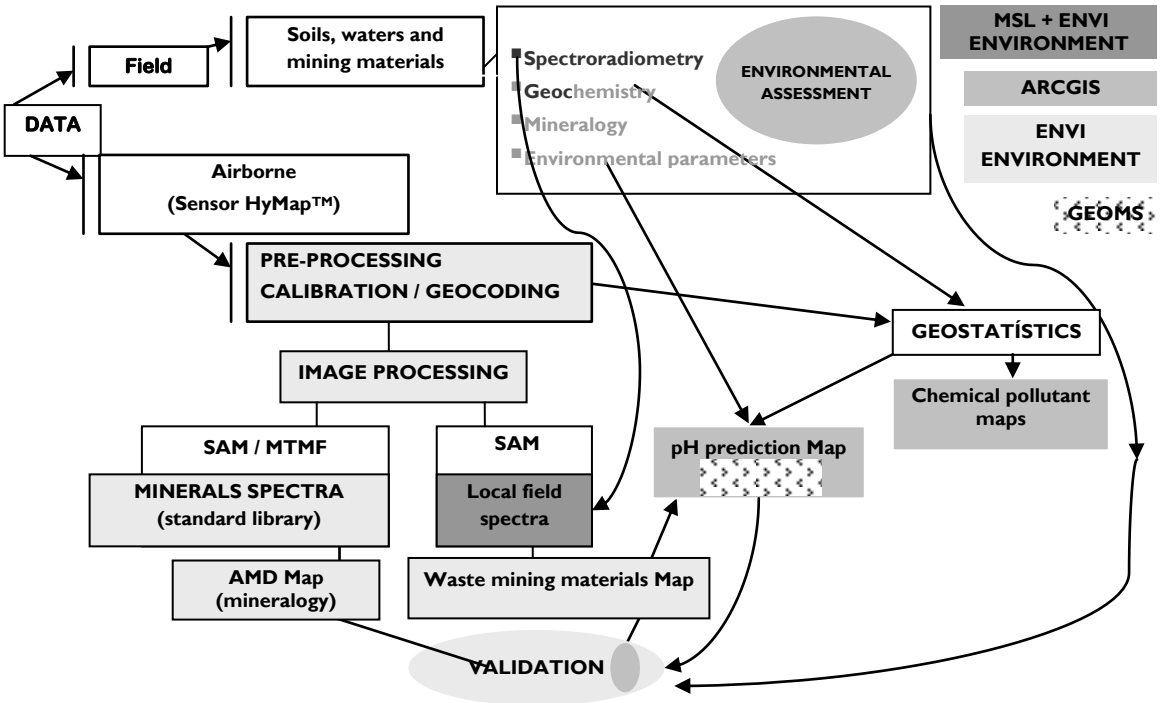

Figure 3. 5 Workflow of the work developed in the framework of the MINEO project for the Portuguese test site, the S. Domingos mining area. Upper right – indicates software environment.

The data collected during field surveys, and subsequent treatment and interpretation, confirmed the main focus of pollutants as the S. Domingos open pit area and Achada do Gamo (sulphur factory), where the lowest pH values were obtained, while Telheiro is contaminated by Acid Mine Drainage (AMD) derived from the

S.Domingos open pit area upstream. The Pomarão Harbour is locally contaminated in the ore shipping area. The Pomarão N and Tapada, the other two subtest areas, were validated as reference areas i.e. uncontaminated.

This work allowed the conception of an environmental model for this mining area, which was fundamental in the approach developed for Image Processing, either using field data (spectroradiometric measurements) either for validation (geochemical and mineralogical data, and waste field mapping) of the image classification results produced. Here are described the main steps and achievements of image processing, as it is subject to further processing.

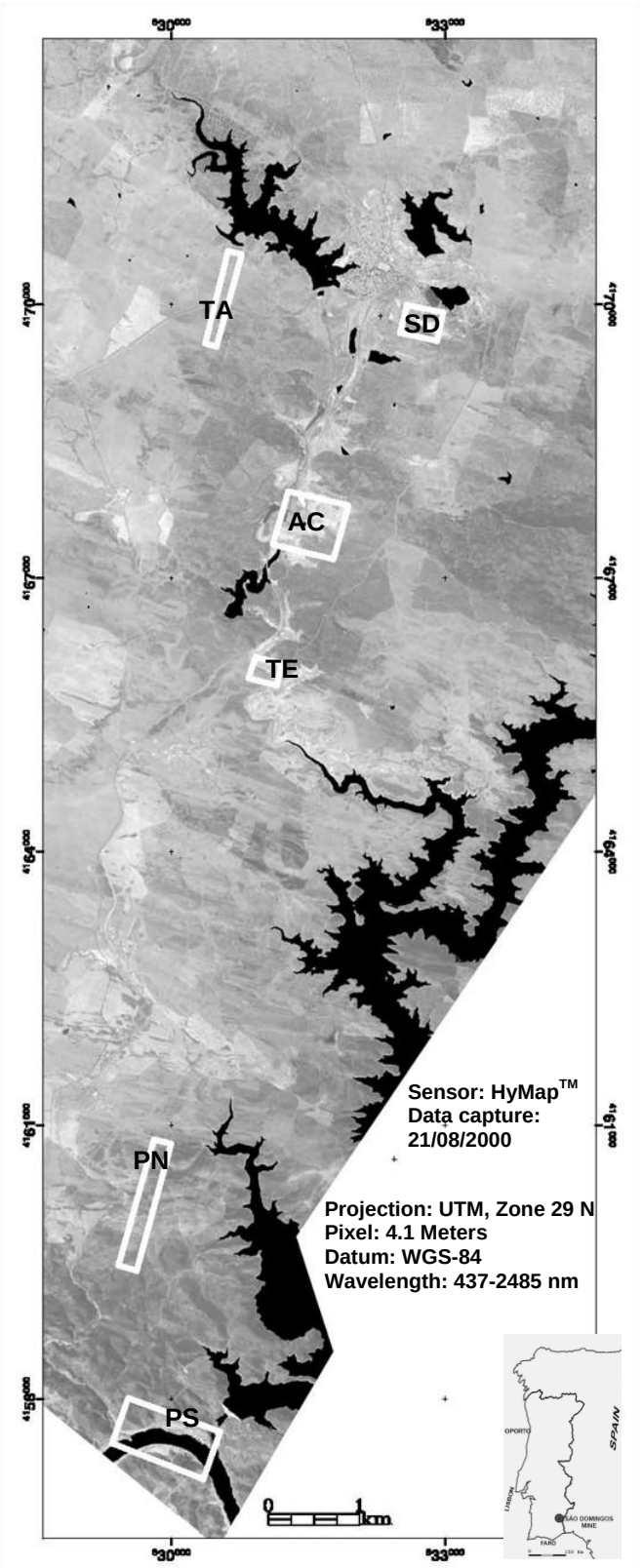

Figure 3. 6 Study area and sub test sampling areas, overlaid on HyMap™ mosaic. Details in Table 3.1.

Table 3. 1. Definition of subareas for validation. NC reports to "expected non-contaminated", while C corresponds to "expected contaminated". Adapted from Quental et al. (2002b).

Itens / *Subareas*	Sampling points	Geological Formations represented Pyrite Belt (PB) Flysch Group of Baixo Alentejo (FGBA)	Dominant Vegetation	Mining Infrastructures or absence thereof
Tapada-TA (NC)	34	Volcano Sedimentary Complex (PB) Phylite Quartzite Formation (PB) Represa Formation (Chança Group)	Lavandula sampaiana Herbs	Proximity of clean water reservoirs developed for mining works
S. Domingos-SD (C)	23	Slags, dumps Volcano Sedimentary Complex (PB)	Erica australis or andevalensis/ Cystus ladanifer /Lavandula sampaiana	Exploitation area, open pit
Achada do Gamo-AC (C)	35	Slags piles, heap dumps Mértola Formation (FGBA) Volcano Sedimentary Complex (PB) Phylite Quartzite Formation (PB)	Cystus ladanifer, Erica australis and/or andevalensis Herbs	Sulphur factory rejects of processing
Telheiro-TE (C)	39	Mértola Formation (FGBA)	Eucaliptus camaldulensis/ Genista polyanthus/ Erica australis and/or andevalensis /Herbs	Confluence of mining effluents/ uncontaminated waters, barren slopes due to AD
PomarãoN-PN (NC)	30	Mértola Formation (FGBA) Volcano Sedimentary Complex (PB) Phylite Quartzite Formation (PB)	Cystus ladanifer Herbs	E of railway for ore transportation
PomarãoS-PS (C)	18	Volcano Sedimentary Complex (PB) Mértola Formation (FGBA)	Rosmarinus officinallis Herbs	Harbor, shipment of the ore

3.5.2.1. IMAGING SPECTROSCOPY (IS) OBJECTIVE

The most important contribution expected from hyperspectral data at the S. Domingos test site will be to detect evidence of superficial Acid Mine Drainage (AMD) (Chapter 2, Section 2.2.2 and 2.2.3). This can be done using two different approaches concerning the imaged ground, one based on waste mining materials and other based on AMD minerals:

I) WASTE MINING MATERIALS

Some waste mining materials when leached by rainwater and stream waters, can have high acid generating potential due to sulphide oxidation and Fe hydrolysis, which increases dissolution and mobility of the enclosed polluting elements (Zn, S, Pb, Sb, Cu, As, Hg and Cd). They constitute hot spots for water, soil and plant contamination, being the present source of AMD. As described in Section 3.4, materials from the mining waste are easily identified in the S. Domingos test site and reflect complex chemical systems that can be seen far away from the primary source. Mapping these materials using IS data can highlight the spread/dispersion of potential pollutants related to AMD according to their acid generating potential.

II) AMD MINERALS

Traces of AMD can be detected through mineralogical data, where specific mineral assemblages define different degrees of acidity, as already highlighted by previous studies with hyperspectral data (Swayze et al., 1999). Fe-bearing minerals such as copiapite, jarosite, hematite and goethite reflect haloes with different degrees of AMD. Some clay minerals also indicate AMD under certain conditions. Mapping these specific minerals will be indicative of the contamination potential related to AMD.

Buffering minerals such as carbonates and silicates, with large surface areas and permanent charges such as smectites, have a very small expression on this test site.

The two potential contributions from hyperspectral data in this test site for AD detection will only be able to give the dispersion of the superficial AMD. However, for a reliable environmental assessment, the interface with other relevant data in a GIS is required, thus allowing a global understanding of the problem. After superficial contamination mapping based on IS processing, GIS tools can highlight the pollutant dissemination pathways, inducing soils and water contamination, and define their direction and extension. This can be achieved based on drainage system and topography data.

DATA ACQUISITION SURVEY

The HyMap™ sensor owned by Hyvista Corporation (HVC), covers the spectral range 450 to 2500 nm, with a spectral bandwidth varying between 10-20 nm and with a signal to noise ratio bigger than 500/1 (Cocks et al., 1998). Further details are given in Table 3.4. This sensor, operated by HVC, covered the S. Domingos area using an aircraft Dornier 228, on 21st of August 2000. The Deutsches Zentrum für Luft und Raumfahrt (DLR) were responsible for the aircraft operations as well as acquisition of aerial photography with a Zeiss-RMK A 15/23 camera. The ground instantaneous field of view (GIFOV) is 4.3 m. Average altitude was 2280 m and average velocity was 277 km/h.

The area covered 726 km^2 corresponding to 11 fligthlines, with 126 bands, from which 8 have been partially selected (11, 10, 9, 8, 7, 6, 5, and 4) for detailed study. 397 aerial photos were acquired for generation of a Digital Terrain Model, performed by British geological Survey (BGS).

The HyMap sensor started at 12h 37m (GMT time) and the last fligthline used in the mosaic started at 14h30m (GMT time).

The data set was provided on radiance by HVC, and also calibrated to reflectance. The reflectance fligthlines were geocoded in UTM, WGS84 datum using DGPS data flight. An overview of the area of interest is given by the mosaiced fligthlines in Figure 3.6.

DATA QUALITY

The delivered data set presented some anomalies related to negative and saturated numbers on radiance data, which lead the contractor HVC to reprocess the data at IGM´s request. The reprocessed data was delivered at the end of June 2001, with additional reflectance data and geocorrection files. According to the explanatory report provided by HVC, the radiance data negative numbers from S. Domingos images could arise due to the following 3 factors:

I. Dark current correction: result in small radiometry errors when dark current correction is applied to the data. This error is likely to be small but could lead to some additional negativity;

II. Saturation of the detectors - if the detectors are subjected to high levels of radiation, large negative values result after dark current correction;

III. Warming of the detectors - detector arrays for IR modules are cooled by liquid nitrogen. If the operator misjudges the timing in terms of refilling the liquid nitrogen, errors in dark current could occur and there can be a rapid and non-uniform increase in the dark current. The onset of this detector warming is rapid and slightly unpredictable.

Further statistical analysis undertaken by the Portuguese team discriminated which of the four detectors were affected by either saturated or negative numbers which lead to the following conclusions:

NEGATIVE PIXELS

Negative pixels are distributed with major importance in atmospheric bands (i.e. near strong water vapor absorption bands). However, fligthlines 7, 9 and 11 present negative data along the whole VIS and part of the NIR region, maybe due to changes in detectors cooling conditions and influence of flight direction illumination. Globally negative pixels occurrence is less than 1% for each total image, except in band 6, where it reaches 1.55% of total image pixels.

SATURATED PIXELS

All fligthlines but one have saturated pixels, being 7, 9 and 11 the ones with highest number of saturated pixels, but less than 0.004% of total image. These pixels are mainly distributed in SWIR1 and SWIR2 spectral regions, however, for fligthlines 7, 9 and 11 is increased the saturated data along the whole VIS and part of the NIR region, again, maybe due to variation of detectors temperature conditions and due to the influence of flight direction.

The occurrence of anomalous pixels is more relevant along water bodies, probably due to specular reflectance, and on the top of buildings. To reduce the effect of anomalous pixels, spectral atmospheric bands where removed from each image, and spatial masks for water bodies where applied to the whole image datasets. Some problems were reported with non-refill of liquid nitrogen in the explanatory HVC report (Quental et al., 2002a), and the quality reported led to exclude fligthline 6 due to a problem of the sensor. From all the fligthlines, fligthline 8 where is located the former sulphur factory, does present neither negative numbers outside the water vapour bands, nor saturated pixels but to the strong water vapour bands seems to have the most balanced data. In opposition, fligthline 10 including the open pit presents high values of saturated data, as well as negative numbers, that is also related to the water bodies present on this area.

Field spectroscopy data, to validate the airborne IS and to obtain the signature of the relevant materials in order to fill the Mineo Spectral Library were undertaken with three spectrometers, a PIMA II, a GER MARK V and an ASD FIELDSPEC (Table 3.2). The PIMA II, collected by BRGM staff, as it uses only SWIR, has not been used for further processing concerning airborne IS data. From the other two, collected by the BGR team, ASD FieldSpec (Figure 2.1.4) collected the most reliable signatures. This portable system works in the spectral range 350-2500 nm, with three detectors, VNIR 350-1050 nm, SWIR1 1000-1800 nm and SWIR2 1800-2500 nm. It acquires reflectance, radiance or irradiance spectra in 100 milliseconds, with less than 10 nm spectral resolution. Examples of mining waste targets are depicted in Figure 3.7.

Dataset has been collected mostly in reflectance mode, but radiance has also been obtained in some of the targets. Unfortunately due to very high temperatures and pavement conditions at the time of data capture, the most relevant spectra related to AMD have not been obtained in radiance mode.

Table 3. 2 Field spectrometers used in S.Domingos in the MINEO framework.

YEAR (August)	SPECTRO-RADIOMETERS	NUMBER OF SPECTRA	TARGETS S-soils, V-vegetation, R-rock, W-mining waste, C-calibration	AREAS (Figure 3.6): SD-Sdomingos, TA-Tapada, AG-Achada do Gamo, TE-Telheiro, PN-Pomarão N, PS-Pomarão S, O-other
2000	GER MARK V	60	S, V, R, W, C	SD, TA, AG, O
2000	PIMA II	300	S, R	SD, TA, AG, TE, PN, PS
2001	ASD FieldSpec	200	S, V, R, W	SD, AG, TE, PN, PS, O

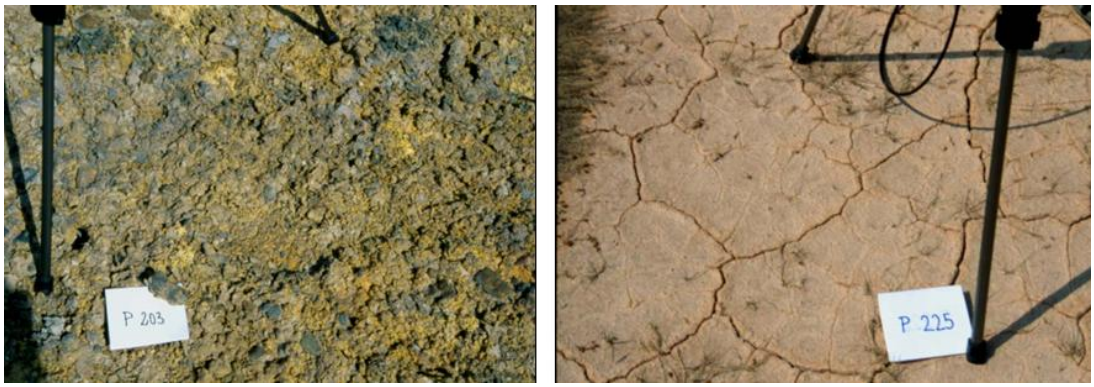

Figure 3. 7 Waste mining materials targets measured by ASD FieldSpec, at Achada do Gamo (AC, 203) and S. Domingos (SD, 225).

DATA PROCESSING

As mentioned previously, the data set was provided on radiance by HVC, and also calibrated to reflectance using HyCorr software, which is a modified version of the ATmospheric REMoval (ATREM) (Gao et al., 1999) and with an Empirical Flat Field Optimal Reflectance TransformationTM (EFFORT) polishment implemented on ENVI software (Chapter 4). The ATREM algorithm is an operational code for retrieving "scaled surface reflectance" from spectral imaging data collected by hyperspectral sensors, using image data. These two software, HyCorr and ATREM, seem to produce similar results according to the work performed by GBA MINEO partner (Groesel et al., 2002), who applied both to the Alpine Europe environment test site. Afterwards, HVC executed an Empirical Flat Field Optimal Reflectance Transformation™ (EFFORT) program. This program determines and applies mild adjustments to ATREM (in this case to HyCorr) apparent reflectance data so the spectra appear more like spectra of real materials, and improving the accuracy of the apparent reflectance without field measurements (ITT, 2010).

As illumination variations remain evident across the fligthlines of reflectance data, additional corrections have been performed, before mosaicking. To all the fligthlines concerning the data selected for the MINEO project, a Cross-Track Illumination Correction, available in the ENVI software, was performed to remove these variations. Along-track mean values are calculated and a polynomial function, in this case of order 1, is fitted to the means. The reflectance data is divided by the fitted polynomial, removing the most striking illumination variations. An example can be seen in Figure 3.8, where on the left side image there is no illumination correction, while on the right image the reflectance data has been divided by a fitted polynomial similar homogenising the fligthline. The Figure 3.8 also shows the geometric correction. In fact, the geometric correction has been done using additional data that reconstructs the scanning geometry of each image pixel using information from the sensor geometry and aircraft attitude (Differential GPS data flight), provided by HVC. These data are Input Geometry Map file (IGM) and Geographic Look Up Table file (GLT) generated on ENVI software.

The IGM file contains map information stored in two bands, one for X coordinates (e.g., latitude or easting) and one for Y coordinates (e.g., longitude or northing). This file itself is not geocorrected, but does contain the geolocation information for each original raw pixel. The IGM file is used to create a Geographic Look-up Table (GLT) file that contains the information about which original pixel occupies which output pixel in the final product and can geocorrect any band or derived product through a simple lookup table procedure. Each fligthline of hyperspectral reflectance data set has been geocoded, using GLT files, into rotated UTM system,

datum WGS84, Zone 29N, reducing or eliminating significant distortions related to flight disturbances (Figure 3.8). Geocoded fligthlines from 04 to 11 were mosaiced (Figure 3.6), resulting in a pixel size of 4.1m.

The identification of the surface environmental impact was done using image processing techniques mainly based on algorithms such as Spectral Angle Mapper (SAM)(Chapter 2, Section 2.1.4). The contamination algorithms obtained used reference spectra from field measurements and standard libraries in two different types of approaches: waste mining material and mineralogical, both taking into account the acid generating potential of the features mapped (Quental et al., 2002a; b, 2003a;b, Appendix II).

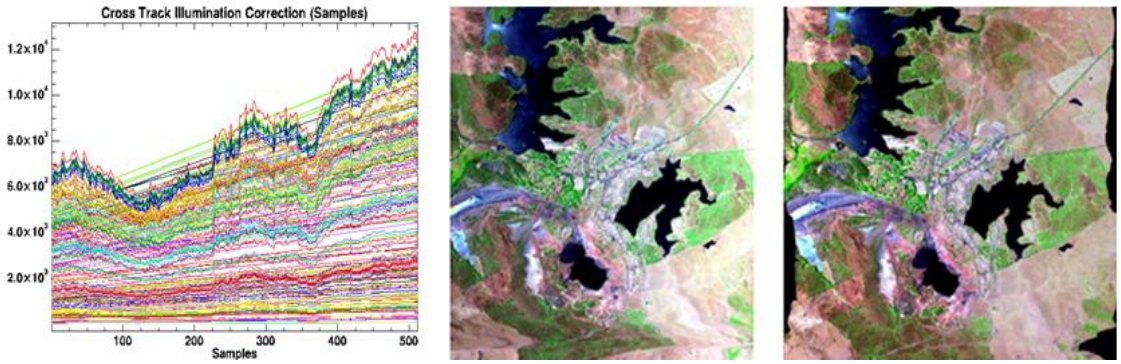

Figure 3. 8 Example of the effects of fitted polynomial on Cross-Track illumination Correction and also of geometric correction in the image.

ACID MINE DRAINAGE WASTE MATERIAL

According to the preliminary data set analysis, statistical, spatial and spectrally, a few steps were performed, before proceeding with contamination mapping itself:

I. Exclusion of some bands related to noisy signatures e.g. 1, 126, and to strong water vapour absorption bands, others that still have a high number of negative pixels and effects that still seem related to water vapour bands. Therefore, the data set selected for subsequent treatment corresponds to 114 bands (2-61, 67-91 and 97-125)

II. Masks on water bodies have been applied due to some anomalies observed (Section 3.2)

III. A vegetation index, where the image data set is transformed into a single band that shows the vegetation distribution, has been applied. The standard algorithm Normalised Difference Vegetation Index (NDVI, ENVI, 1999) was the one used, and very clear and fresh vegetation areas have been masked applying a threshold to the vegetation image

The decision to use both VNIR and SWIR bands is due to the fact that the waste mining materials show spectral signatures of interest that cover all this range or they are excessively flat to select a specific range.

The procedures developed for AMD waste material contamination mapping are summarized as follows:

I. Analysis based solely on image information using spectral algorithms

II. Selection of target area based on expert information

III. Using field data for classification

IV. Enhancement of classified image

These procedures and their relationship are specified in the flow diagram of Figure 3.9.

The part I) of the procedure analyses the image taking into account information solely based on image data, using automatic standard procedures (MNF, PPI). This is essentially a top-down approach (Chapter 5, Section 5.1) The endmembers retrieved on this analysis corresponds to n=48 and are considered as reference spectra for the next step, using the SAM classifier to match the spectra in the image.

Part II) of the analysis of SAM results shows that several classified areas are known to be non-contaminated or even affected by mining works. To facilitate the next processing steps, minimize the data set size and concentrate in the area of interest, the HyMap data set 1 has been masked (subset) of these classified areas, leading to HyMap data set 2.

Although not depicted in Figure 3.9, another mapping algorithm as been tested: Matched Tunned Matched Filtering (MTMF, chapter 2, Section 2.1.4). However, this classification method gives obscure results, probably due to incomplete removal of illumination effects.

Part III) is involved a careful observation and analysis of spectroradiometric field signatures. Based on this observation, some spectra were selected (Figure 3.10) which takes into account ancillary data (geochemical or mineralogical) when it exists. Even if some signatures are similar they have been also included, due to their importance and for eventual merging at the end. Others are not shown, once they are clipped at the final classification.

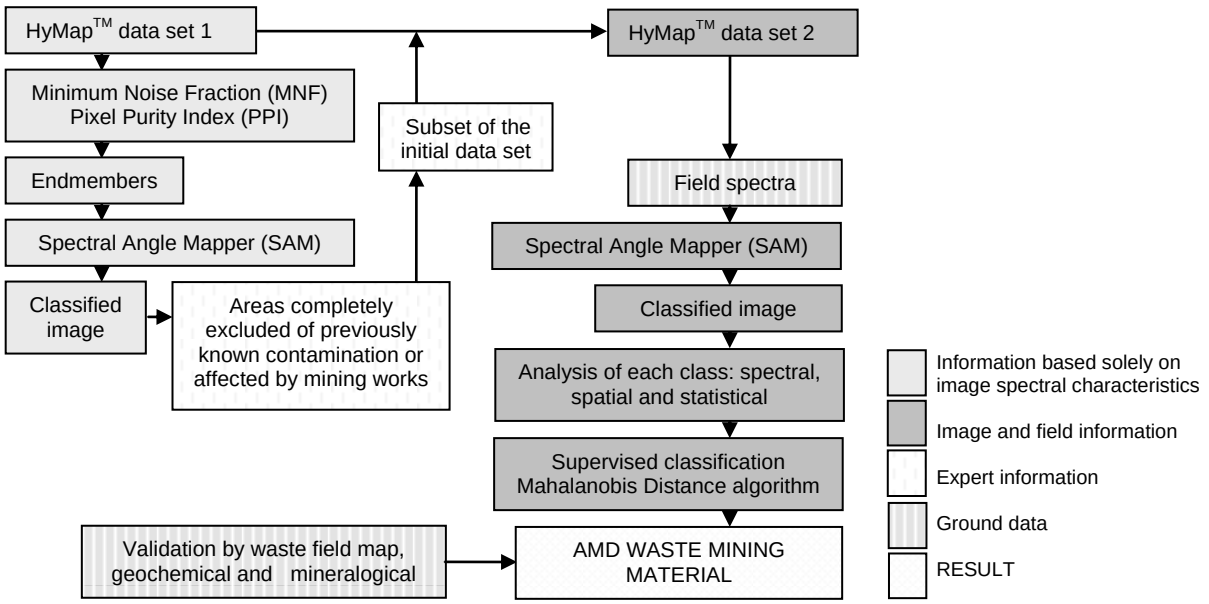

Figure 3. 9 Flowchart of the Imaging Spectroscopy processing on reflectance data developed in the S. Domingos former mining area (adapted from Quental et al., 2002a).

The maps obtained by Quental and Brito (2002) are displayed in Appendix II, a and b. The results are split into two maps, avoiding fligthline 6 which has been masked, showing detail over some of the subset areas.

The extension of AMD waste material was achieved using local field spectra signatures as reference spectra. The developed methodology can be synthesized as using mainly the combination of two classification algorithms. The SAM algorithm was followed by the application of supervised Mahalanobis distance algorithm, to avoid class mismatch in cases where spectra of materials present clusters with some differences not distinguishable by the former.

Some extra experiments were performed using MTMF algorithm, however final results were not satisfactory. Therefore, SAM arises as more robust algorithm for classifying images that present illumination effects, showing however some limitations by different spectra that cannot be distinguished.

The use of field spectra signatures together with image spectra allowed the accurate identification of type and extension of the following mining materials over the study area: *Mixed sulphur materials, Metallurgical slag and leached rock, Fine material associated to metallurgical slag, Yellowish ferricrete, Reddish ferricrete, Whitish leached rock, Red rock dump, Contaminated soils and sediments, Contaminated soils with shale fragments and Mixed leached fragment rocks.*

Although they generally represent materials with significant content of pollutants such as S, Zn, Pb, Sb, Cu, As, Hg and Cd, the first five classes correspond to the highest contents registered in local chemical samples, associated to high acidic potential. Therefore, they are crucial in detecting main dispersion of pollutants, and highlight the potentialities of imaging sensors for discriminate chemical differences in imaged ground surface.

Taking into account the validation issues related to Imaging Spectroscopy analysis (Chapter 2, section 2.1.4) a partial validation of output results was obtained by comparing different data source. In general, the field spectra and spectra of classified image match well (Figure 3.10).

An evaluation of post-classification results and comparison of relative distribution of spectral data from thematic classes per band, a statistical parameter coefficient of variation (CV) was calculated for each class according to the formula:

$$CV = \frac{\sigma}{aver} \qquad \text{Eq. 3.1}$$

where σ -standard deviation and aver-average of data distribution

Generally, a value of CV<1 means: distribution has low data variability and probably absence of anomalous data; 1<CV>1 existence of variability on data distribution; CV>2 high data variability, presence of outliers. The results obtained for IS classification are illustrated in Figure 3.11 (Quental et al., 2003a).

In average, class material types present a CV around 0.3 (0.29), much lower than 1, which implies that the classified features are represented by homogeneous pixel spectral values, with low variability and probably without anomalous spectral data. The highest CV values (around 0.6) reports to the class *Fine material associated to metallurgical class,* however still lower than 1, meaning that statistically the spectral data present for this class is acceptable as a low variability one and, probably, without outlier spectral value.

Waste material field mapping was also compared with other field data results of mineralogy and geochemistry, when available, showing coherent results (Table 3.3).

ACID MINE DRAINAGE MINERAL MAPPING

The extension of AMD minerals was achieved using the standard laboratory measurements of USGS spectral libraries included in ENVI software. This work was performed by BRGM (Quental et al.2002a). It's worth noticing that the original Hymap™ mosaick used was different than the one for waste mining material mapping, i.e. there was no illumination correction before thematic processing.

Based on Mixture Tuned Map Filtering (MTMF) and Spectral Angle Mapper (SAM) algorithms it was possible to delineate the spatial location of soils containing copiapite, jarosite, goethite, hematite and alunite. Both algorithms were used separately and then intersected. Characterizing and mapping jarosite and alunite thus enables to retrieve areas exhibiting pyrite, secondary salts (sulphates) deposition and efflorescent crusts which

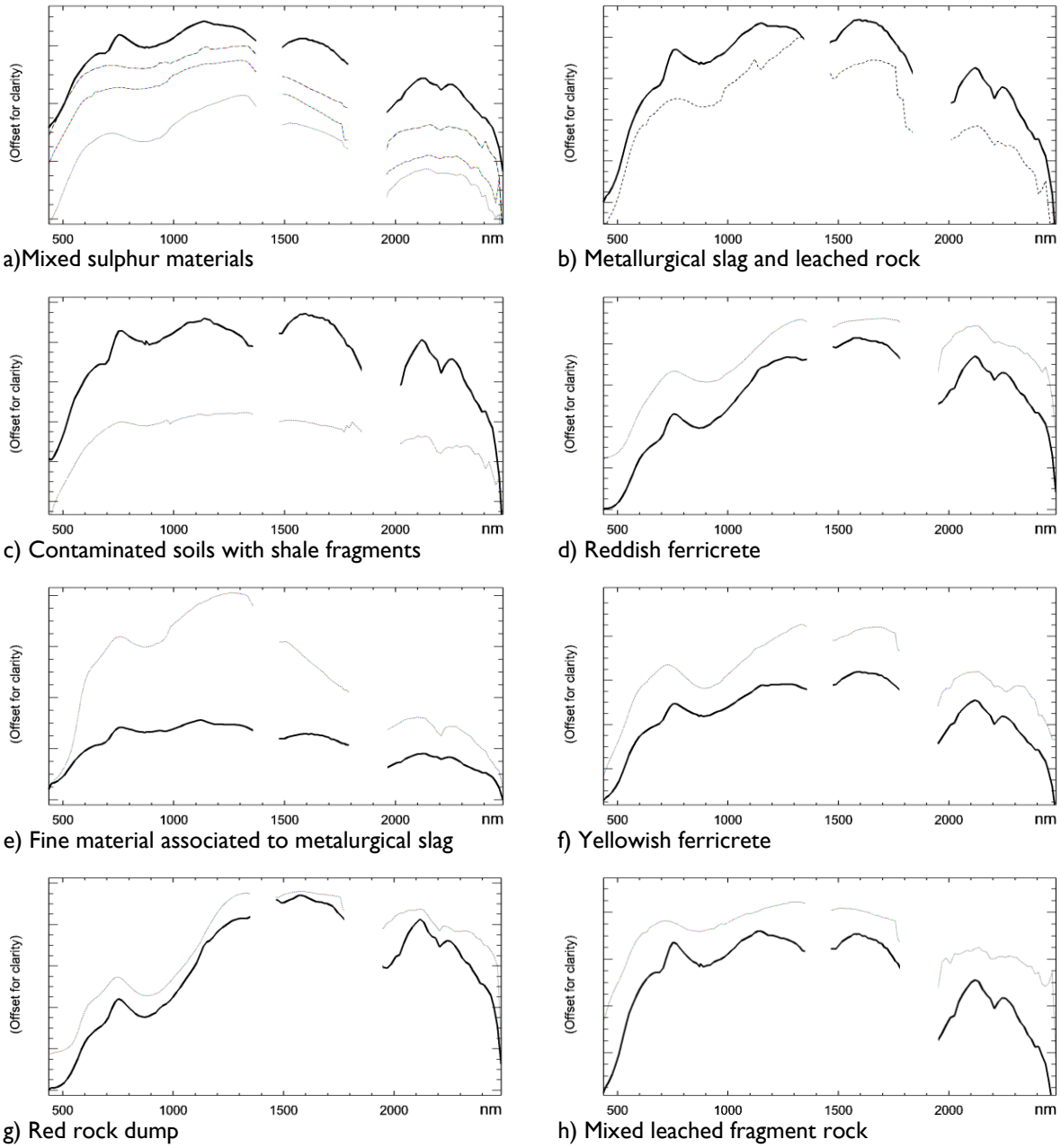

Figure 3. 10 Examples of most important spectra of the HyMap classification image (solid dark line) and respective field spectra (dotted light).

are still very active in acid drainage production. The combined classification results show global class separability in the spectral feature space.

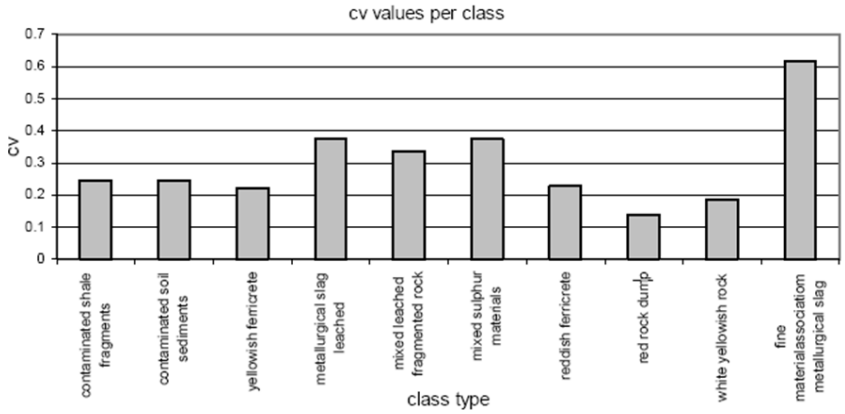

Figure 3. 11 Coefficient of variation per class of WASTE MINING MATERIAL MAP.

Table 3. 3 Main characteristics and comparison of the WASTE MINING MATERIALS map with other field data.

CLASSIFI-CATION RESULTS	Main characteristics *validated by partial field checking	Main field waste map units	Mineralogical results X-ray Diffraction (soil clay fraction and salts)	Classified areas (2,172,776,4 of 7,446,191.2m²)
Mixed sulphur materials	High acidic potential, systematically map surrounding tailings ponds and dams, highligths other unknown areas	Sulphidic ore, tailings (including black mud), dump leach piles, metallurgical slag	Jarosite, goethite, mixture of mcomplex hydrated sulphates of Pb, Cu, Zn, K, Al, As, Fe and Ca, mixtures of copiapite and rumerite (vestigial)	83,243.116 (3.83%)
Metallurgical slag and leached rock	Metallurgical slags (high acidic potential) and leached rocks, the 2nd most important cover (Mahalanobis alg. not yet included for separation	Metallurgical slag, Dump leach piles and bleached and leached bedrock	Complex mixtures	570,027.072 (26.23%)
Fine material associated to metallurgical slag	Essentially related to metallurgical slag, surrounding or overlaying some piles of these materials	Metallurgical slag, bleached and leached bedrock	Complex mixtures	19,818.989 (0.91%)
Yellowish ferricrete	Significant spread in the area, particularly associated to areas affected by AMD	Tailings (including black mud), dump leach piles, leached and bleached rocks	Goethite, heamatite	246,955.698 (11.37%)
Reddish ferricrete	Gossanous materials around open pit and other areas	Gossanous rock, goethite/heamatite bodies	Heamatite, goethite	44,176.678 (2.03%)
Mixed leached fragment rocks	Heterogeneous materials of several grain sizes and colours	Dump leach piles, Metallurgical slag	Illite, kaolinite, quartzo	159,459.652 (6.76%)
Whitish leached rock	Variation from previous, mostly located at higher altitude.	Bleached and leached bedrock, Dump leach piles	Illite, jarosite, interstratified vermiculite-smectite, goethite, quartz	146,784.913 (0.23%)
Red rock dump	Particularly distributed around open pit area	Gossanous rock, undifferentiated waste rocks	Hematite, goethite	5,059.810 (7.35%)
Contamina-ted soils and sediments	Spread over the area, including the village and part of dump leach piles, correspond to contaminated field spectra signature	White to yellow sedimentary deposits, Kaolinitic schist, Dump leach piles, kaolinitic schist	Kaolinite, illite, jarosite, natrojarosite, sulphur (vestigial)	876,322.067 (40.33%)
Contamina-ted soils with shale fragments	A variation from the previous, with a more heterogeneous grain size and less dispersed	Bleached and leached rocks, Dump leach piles	Illite, kaolinite, quartz, jarosite	20,928.449 (0.96%)

Validation of classification results with AD field mapping and mineralogical field result concluded that mineralogical content of materials can be mapped using IS sensors together with standard libraries.

LESSONS LEARNT

Globally, both mapping results obtained either in AMD waste material or in AMD minerals were able to detect mineralogical/chemical characteristics of imaged ground data, validated by field data. IS sensors appear as potential tool when applied to mining environments for environmental assessment. Observations derived during image processing highlight some decisions concerning future work, either concerning field spectra collection either image processing.

The data treatment of hyperspectral images, in spite of several time consuming procedures related to data quality analysis and taking into account that corrections done were not the initial envisaged, has shown high potentialities for remotely assessing mining related environment.

The mapping of waste mining materials and related contamination patterns of the area highlighted the high discrimination level by IS sensors of these materials, which had shown other differentiation that could also be depicted in the field and contributed to detailed field cartography (Matos et al., 2006).

Concerning AMD detection the MINEO project raised also some questions related to different climatic conditions and the characteristics of waste mining materials under evolution. The case study of the S. Domingos test site, showed some particularities when compared to the other MINEO European environments. This was translated by a very low vegetation density and a climate that highly controls the mineral formation and mobilization of metals related to waste mining materials, due to the high solubility of many of the efflorescent sulphate minerals. Hence, there is a very complex geochemical dynamic that develops equally complex mineral mixtures in materials with high variability concerning colour, granulometry, rate of weathering and water content. These complex mixtures, even if processed with mixed pixel analysis, e.g. spectral mixture analysis or unmixing, usually contain minerals that are not present in standard spectral libraries.

The fact that different types of atmospheric correction were foreseen and not undertaken is still an issue to compare and test the implications on mapping results when focused on AMD indicators.

3.6. UPDATE OF IMAGING SPECTROSCOPY DATA: THE HYPMINGEO PROJECT

The European Fleet of Airborne Research (EUFAR) is an Integrating Activity of several Framework Programs of the European Commission. Particularly in the 6th FP, as an Integrated Infrastructure Initiative, EUFAR brought together 24 leading European institutions and companies involved in airborne research, as well as more than 30 instrumented aircraft. Within this framework a project was submitted to acquire IS data over S. Domingos test site denominated Hyperspectral images applied to environmental monitoring of mining areas, optimised using geostatistics (HYPMINGEO). However, although approved, the final flight was supported by the National Environment Research Council (NERC)/British Geological Survey (BGS), with EUFAR funding for the field campaign.

The aim of the HYPMINGEO research was to monitor the S. Domingos area with respect to contamination patterns derived from waste mining materials and related Acid Mine Drainage (AMD) based on hyperspectral imagery and spectroradiometric field measurements. More specifically the objectives were:

I. The acquisition of a new hyperspectral dataset seven years later using an IS sensor similar to the one used over the S. Domingos test site in 2000 (HyMap^{TM}) to allow the definition of evolutionary patterns for contamination through multitemporal analysis,

II. An optimization of pre-processing steps was expected using geostatistical methods, and

III. To test the utility of a new, lower cost hyperspectral sensor in comparison to the established benchmark of HyMap™.

DATA ACQUISITION SURVEY

The airborne dataset capture took place over the S. Domingos area, with a SPECIM EAGLE-HAWK IS sensor on 21st of May 2007. The dataset were collected by the National Environment Research Council (NERC)/ARSF (Airborne Research and Survey Facility) on behalf of the British Geological Survey (BGS) using a Dornier 228 aircraft. Simultaneously, a field campaign took place for Global Positioning System (GPS) precision measurements and field spectral measurements for ground reference data.

The average height of data capture was 1690 m, with no clouds and clear conditions and average velocity of 267kmh^{-1}.

Composed of two sensors EAGLE and HAWK, the SPECIM EAGLE-HAWK instruments have the characteristics depicted in Table 3.4. SPECIM also offers a dual sensor system that would allow data acquisition in 393-2451 nm spectral range. This is achieved by putting Hawk and Eagle sensor head side-by-side to simultaneously collect data.

Table 3. 4 Characteristics of SPECIM EAGLE - HAWK sensors compared to HyMap™.

SPECIM EAGLE HAWK (as collected in 2007) * generic for sensor characteristics		HYMAP™ (as collected in 2000) * generic for sensor characteristics
VNIR (393-988nm)	SWIR (962-2451nm)	VNIR-SWIR (437-2485nm)
▪ IFOV –0.075 degrees ▪ FOV –34.69 degrees (953 pixels) ▪ GIFOV – 2m ▪ Swath width - 0.43*altitude ▪ SNR 450:1* (peak) ▪ 12 bits (per pixel?) ▪ Spectral resolution–2.9nm ▪ 252 bands	▪ IFOV –0.075 degrees ▪ FOV –23.78 degrees (320 pixels) ▪ GIFOV – 2m ▪ Swath width - 0.43*altitude ▪ SNR 800:1* (peak) ▪ 14 bits (per pixel?) ▪ Spectral resolution–8.5nm ▪ 237 bands	▪ IFOV - 2.5 mr along track, 2.0 mr across track ▪ FOV - 61.3 degrees (512 pixels) ▪ GIFOV - 3 – 10 m (typical operational range) – 4.3m in this case ▪ Swadth 2.3 km at 5 m IFOV (along track) SNR 500:1 * ▪ 11-?bits per pixel ▪ Spectral resolution –18nm (average)
489 bands		126 bands
PUSHBROOM		WHISKBROOM

The fligthlines collected were more extensive than the area used for image processing (Figure 3.14) and were delivered in radiance data from level 1B to 3A (geocoded as individual fligthlines) on June 2009. According to remote sensing conventions, level 1B is data where the platform/sensor exterior orientation is enhanced using GPS base station information, allowing for a full radiometric, atmospheric and atmospheric correction. In level 3A the fligthlines are ortho-rectified, with the position accuracy generally matches the spatial resolution of the original data.

The total number of fligthlines is different for both sensors, being of 13 for EAGLE and one less due to a failure of the HAWK sensor (Figure 3.12). The pixel size is 2 m.

The objectives of the field campaign were:

I. To set up a GPS base station for accurate post-processing positions in the field during data capture

II. To collect spectral reference data a) on calibration targets and b) on selected potential contaminated materials related to AMD and also collect samples for further analysis (X-Ray Diffraction, geochemical, etc).

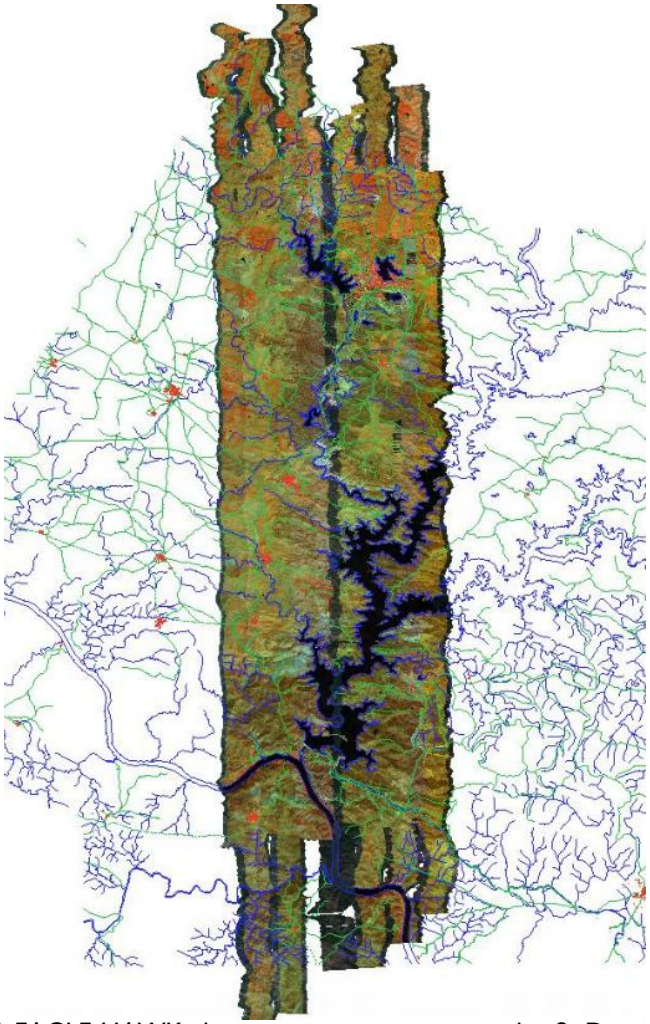

Figure 3. 12 Area of SPECIM EAGLE-HAWK data capture encompassing the S. Domingos study area. The mosaic is overlaid by ancillary topographic layers.

The FieldSpec®3, the spectroradiometer from the Analytical Spectronic Devices, Inc. (ASD), has a spectral range from 350 – 2500 nm, a variable spectral resolution (3 nm @ 700 nm; 10 nm @ 1400/ 2100 nm), a sampling interval from 1.4 nm to 2 nm, and a scanning time of 100 milliseconds. The data was collected in reflectance mode. Five measurements were undertaken at each sampling point and averaged. Further details about equipment and field team are given in Quental et al. (2011).

The targets for reference data acquisition are depicted in Figure 3.13. The reflectance spectral measurements were mainly focused on calibration targets during the overflight. From these, the majority was on the whitish target, one of the playing fields covered with artificial pavement, in S. Domingos village, due to higher variation and fewer nearby, more homogeneous, on the dark target made of plastic. Targets were selected previously taking into account calibration issues and unchanged areas for assessment of the 2000 HyMap^{TM} spectral data to minimize errors.

Climatic conditions on the day of the flight were very windy, which made it difficult to set up the base station for the GPS measurements and complicated some spectral measurements in more exposed areas. This condition eliminated also one of the dark target possibilities, a clean water dam due to intensive rippling in this area.

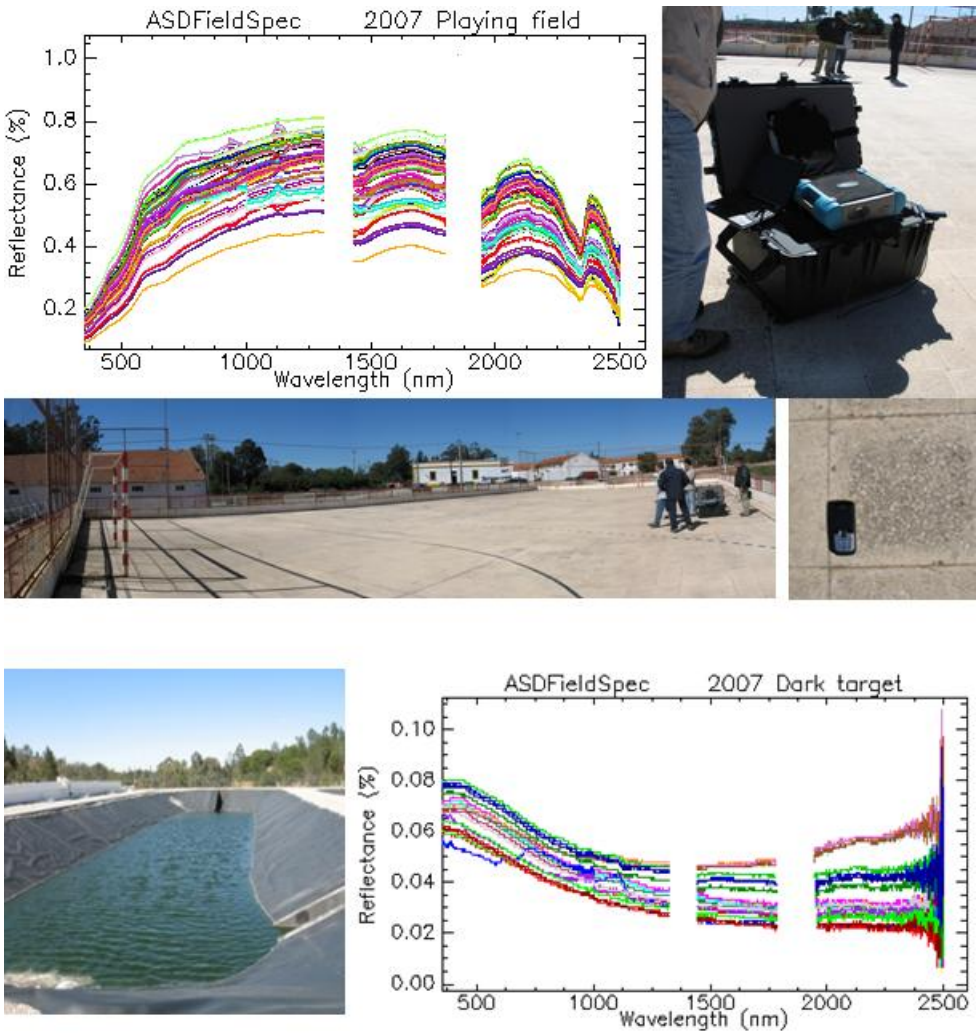

Figure 3. 13 Reference targets measyured by ASDFieldSpec3, owned and operated by ISA. Playing field as a whitish target n=127 and black plastic target n= 25.

Other measurements were mainly concentrated on waste mining materials based on previous spectral knowledge of the area that highlighted areas of acid generating potential, e.g. SD, AG and TE (Figure 3.6). In the Pomarão harbour, the ground had been recently covered with new mining waste material in March 2007, therefore significantly varying the conditions in relation to the 2000 scenario.

DATA QUALITY

Following information related to the pre-processing before data delivery, the ARSF flying was not sequential to cover the core area of interest. All flightlines have needed changes to the scan time, and independently, the scan attitude time, and height variations to get the correct flightline width, with some residual errors being reduced

by changes to the instrument view vectors (roll, pitch, heading) as required. Every flightline of EAGLE and HAWK have required as many as 20 iterations to best match to each other and the vector overlays. There are still some discrepancies due to what appears to be an accumulating time error along flightlines. All these procedures were time consuming.

The basic statistics for the radiance (3A level) mosaick show no negative numbers in radiance dataset. A few saturated numbers occurs. As aforementioned there is one less fligthline of HAWK sensor. This is due to a failure of this sensor that was not reflown. The latter presents also a few gaps in the data depicted in Figure 3.14. In this, a general overview of the mosaiced area, on the left image for radiance EAGLE data, while the right image the missing data of the HAWK sensor in displayed in red. Part of this can be explained by lost pixels due to saturation or specular reflectance.

Other gaps can be explained by the different swath width of both sensors as depicted in Figure 3.15 for an individual fligthline. When mosaicking, part of the geocoded fligthlines can gather only the EAGLE data, i.e. only the dark areas, therefore leaving a no data area for HAWK. From these no data areas, one encompasses the playing field where the field spectroradiometric measurements for ground reference data were undertaken (Figure 3.15). Thus, in the range 962-2451nm the reference ground measurements reports to a very small area derived from the next fligthline.

Typical of pushbroom scanners is a variation across the elements of the detector array (Chapter 2, Section 2.1.3), which frequently results in a strong stripping along flight lines (Larsen, 1997). This is clearly detected when moving to higher numbers of MNF factors as depicted in Figure 3.16. In fact, the MNF factors can easily depict the spatial patterns delineated by stripping, whether across or along fligthline direction.

This stripping along swath is more evidenced in HAWK sensor, although a smooth stripping is also detected in EAGLE sensor. In the latter is also seen stripping across swath. Again, they are more evidenced when analysing MNF factors.

The Signal to Noise Ratio (SNR) is considered generically as depicted in Table 3.4 and has not been specifically calculated for these images, bearing in mind some of the constraints that can arrive for its estimation. Specifically, that the noise estimate varies with individual and land cover type and that a single estimate of noise (or SNR) from a single land cover type is insufficient to represent a remotely sensed image (Atkinson et al., 2005; Asmat et al., 2010).

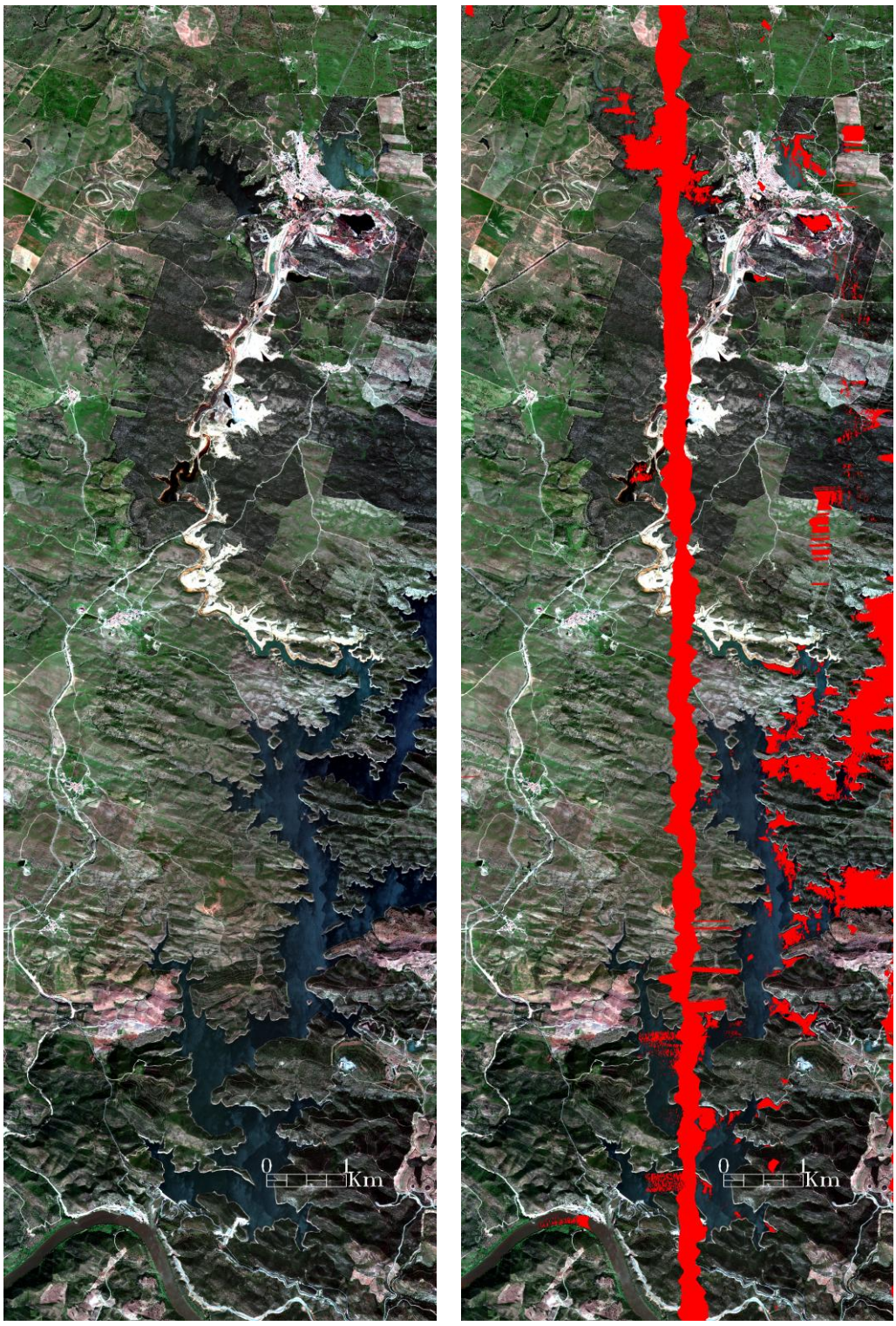

Figure 3. 14 Comparison of missing data on HAWK sensor, red on rigth, with the EAGLE on the left image for the same spatial area and displayed in RGB: 671, 550 and 490 nm.

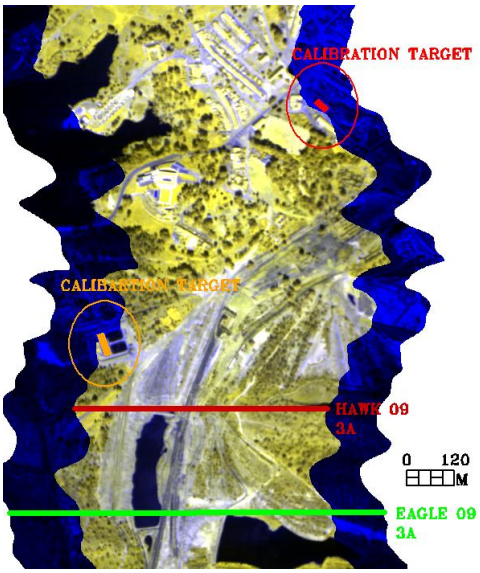

Figure 3. 15 Different swath width for EAGLE and HAWK sensors determines exclusion of the most of the red calibration target when mosaicking fligthlines.

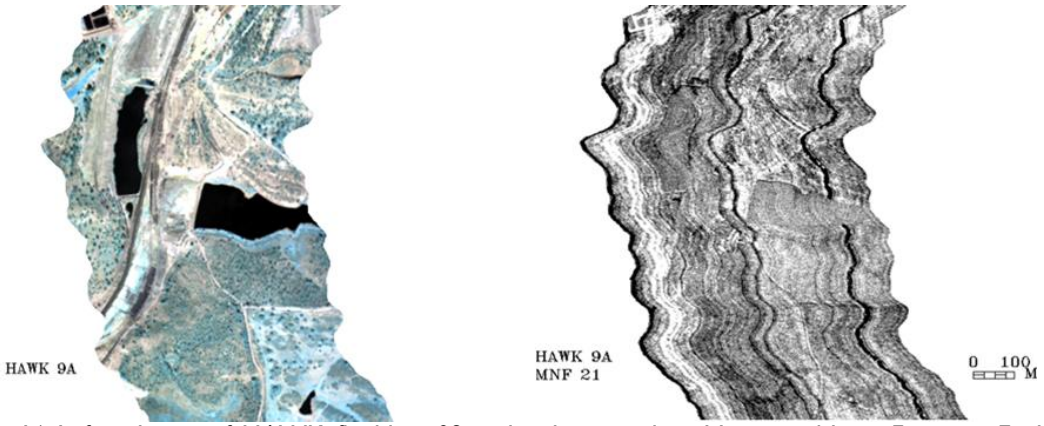

Figure 3. 16 Left-radiance of HAWK fligthline 09 and right-equivalent Minimum Noise Fraction. Evidence of stripping effect due to pushbroom scanning system.

3.7. CONCLUSIONS

The S. Domingos area is enclosed within the Iberian Pyrite Belt, wich constitutes one of the most important metallogenic provinces for Volcanogenic Massive Sulphide deposits. The mining history dates back from pre-roman and roman times, where Ag, Cu and Au were exploited mainly in the gossan resulting from the oxidation of the sulphide mass. The modern exploitation started in the XIX century, both in the gossan and massive sulphide orebody that besides Cu also contained some Zn and Pb, and ended in 1966. The type of exploitation and processing, main products and by-products has been variable during overall mining activity.

Related environmental problems, part of which derived from a different or inexistent environmental concern at the time, can be sinthetised as: I) waste mining material and associated contamination, II) acid waters and dispersion of elements, and III) landscape disruption.

The way to environmentally assess this area has been undertken testing the use of hyperspectral or imaging spectroscopy (IS) data, in the framework of the MINEO project. The IS airborne and ground spectral data gathered allowed the mapping of waste mining materials. The latter highligthed the areas where the Acid Mine Drainage (AMD) could be developed due to the acid generating potential of specific waste mining materials and related contamination patterns. Another way to detect the AMD was achieved using USGS mineralogical standard spectral libraries. Both mapping results were able to detect chemical/mineralogical characteristics of imaged ground data. A relative validation, following related issues described in Chapter 2, with ancillary data was obtained. Hence, IS appear as a powerful tool to be applied in mining environments.

Concerning AMD detection in S. Domingos some questions were raised related to different climatic conditions and the characteristics of waste mining materials under evolution. This area has a very low vegetation density and a climate type that highly controls the mineral formation and mobilization of metals related to waste mining materials, due to the high solubility of many of the efflorescent sulfate minerals. Hence, there is a very complex geochemical dynamics that develops equally complex mineral mixtures in materials with high variability concerning colour, granulometry, rate of weathering and water content. These complex mixtures contain minerals that are not present in standard spectral libraries. Another point to stress is that the different types of atmospheric correction foreseen and not undertaken is still an issue to compare and test the implications on mapping results when focused on AMD indicators.

The upadte of IS data, in the framework of HYPMINGEO project, occurred seven years appart from MINEO (2000) and with different IS sensors. Among others, the main purpose was to detect the evolutionary trends related to AMD dispersion. By this way, it can be demonstrated the IS capabilities for mining related monitoring purposes. The simultaneously spectral data measurements that occurred for ground data calibration were not completely successful when translated to the airborne IS data. The different swath width of both sensors excluded one of the ground reference calibration data in the range 962-2451nm. A few other gaps occur in this range, including a fligthline in the middlle of the study area, which encloses part of the contaminated areas of AG and TE. Stripping effects along the swath are more visible in noisy bands of MNF factors and in the 962-2451nm wavelength.

Globally, the preliminary assessment of data quality is good concerning saturated and negative pixels the data. These IS sensors will then be tested to demonstrate the routine application of IS based tools as key data for change detection over time.

4. PRE-PROCESSING AND ATMOSPHERIC CORRECTIONS

4.0 INTRODUCTION

This chapter addresses the pre-processing procedures, particularly the atmospheric correction / calibration in Imaging Spectroscopy (IS) and the related factors. An overview of the approaches to deal with image calibration/atmospheric corrections is given.

For the two IS data sets collected in the S. Domingos area, i.e. the HyMAP^{TM} and SPECIM EAGLE-HAWK, the pre-processing procedures are referred. Both are atmospherically corrected using a radiative transfer modelling, comparing in the case of HyMAP^{TM} two different types of software as well as post atmospheric corrections.

For a comprehensive understanding of the implications of the corrections performed, a few experiments were undertaken in different reflectance products concerning the AMD detection and mapping. This took into account the multi-source mapping approach developed in Chapter 5.

The evaluation of different options while modelling the IS data and results obtained were statistically compared through average spectral values.

The results obtained were compared in multi-temporal / multi-sensor global image mosaics and also in detailed local targets, both for atmospheric corrections (HyMAP^{TM}) and for change detection (HyMAP^{TM} and SPECIM EAGLE-HAWK).

The data set were processed in ENVI from ITT Visual Solutions (ITT, 2010).

4.1 FACTORS RELATED TO ATMOSPHERE CONTROLLING SPECTRAL SIGNAL RESPONSE

Due to the thick atmospheric media, there is significant attenuation along the sun–surface–sensor pathway. Thus, the "true" spectral response of the surface target is heavily "contaminated" by atmospheric and solar signals, as well as by other factors including sub-pixel mixture, sensor geometry and optics, adjacency and topographic effects (Ben-Dor et al., 2004).

The atmosphere can have a significant effect on, among other things, the intensity and spectral composition of radiation available to any sensing system. These effects are caused mainly through the mechanism of atmospheric scattering and absorption (Lillesand et al., 2004; Gao et al., 2009; Short, 2009).

The components on the system sun-surface sensor are depicted in Figure 4.1 for the solar region, i.e. in the 350-2500 nm. The total radiation signal L received at the sensor consists of three components (Richter, 2010):

I. Path radiance, L1, i.e. the photons scattered into the sensor´s field of view, without having ground contact.

II. Reflected radiation, L2, from a target, and directly or diffusely transmitted (global flux) to the sensor

III. Reflected radiation from the neighbourhood, L3, scattered by the air volume into the current instantaneous direction, the adjacency radiance. This consists of two components (atmospheric backscattering and volume scattering)

Only component 2 contains information from the currently viewed pixel. The task of atmospheric correction is the calculation and removal of components 1 and 3 and the retrieval of ground reflectance from component 2.

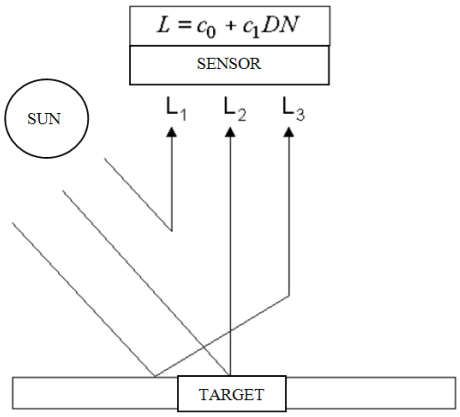

Figure 4.1 Interaction between atmosphere and target in the signal received at sensor (adapted from Richter, 2010).

This, for the simplest case, is where a flat terrain is considered, therefore excluding the role of other factors such as topography, opposing facing hills that reflect radiation to the target pixel. Other factors depend if the media is ground or water; the latter having a few other specificities such as Fresnel reflections off the water surface (Mustard et al., 2001).

In S. Domingos, due to low altitude variations within the study area, i.e. ranging mostly in the 100-150 m interval, the topography factor is neglected (Figure 3.1, Chapter 3).

It is usually considered in the current atmospheric corrections programs that the target to analyze has a Lambertian reflectance, i.e. a perfectly diffusing surface where the brightness of a point is independent of the viewer direction. In fact, the reflectance of real surfaces is represented in function of illumination geometry and viewing angle [through Bidirectional Reflectance Distribution Function (BRDF)]. Further details about BRDF as well as definitions of reflectance are detailed in Schaepman-Strub et al. (2006). A Lambertian reflectance of the target is adopted because real data typically don´t have enough information to make a topographic correction. The final result of the atmospheric correction is called "scaled surface reflectance" or "apparent reflectance", which can be converted to surface reflectance if the surface topography is known (Kruse, 2004).

The particular wavelengths (or frequencies) detectable by visible/infrared sensors depend in large measure on the extent to which the waveband radiation is absorbed, scattered, or otherwise modified by the atmosphere ("windows of transparency" concept). The radiation measured from space platforms is usually secondary in that it is reflected or emitted energy generated from molecular interactions between incoming radiation (irradiance) and the Earth material being sensed. Common primary energy sources include the Sun or active radiation-

generating devices such as radar; sensed thermal radiation from the Earth´s surface results from both internal heat sources and the heating effect of solar radiation. Because most materials absorb radiation over the sensed parts of the EM spectrum, only fractions of the incoming radiation (typically, 1/20th (for water) to 4/5ths (sand) in the reflected region) are returned to the sensor (Short, 2009).

Absorption converts the incident radiation energy to heat at molecular level. It occurs at specific wavelengths, referred to as absorption bands. Particles such as gas molecules, dust and water molecules redirect the incident energy, resulting in scattering (Paltridge and Platt, 1976). The size of the particles establishes the type of scattering, whether Rayleigh (about 10-4 μm), Mie (comparable size to the radiation wavelength) or non-selective scattering (particles much larger than the wavelength) (Kempenners, 2007).

The absorption bands of the most important atmospheric gases for the range 400-2500 nm are depicted in Table 4.1 and graphically in spectra (Figure 4.12). The particular regions of the electromagnetic spectrum such as 0.9 μm, 1.1 μm, 1.4 μm and 1.9 μm wavelengths are almost opaque to the sensors. Regions that do not contain significant absorption features due to atmospheric gases are called transmission or atmospheric windows and these are the ones exploited by the remote sensing sensors (Lau, 2004).

Table 4.1 Atmospheric gases and corresponding wavelength absorption features (after Lau, 2004 and updated after Gao et al., 2009).

Gas	Absorption (μm)
H_20	0.94, 1.14, 1.38, 1.88 (Gao et al., 1993, 2009), 0.69, 0.72, 0.76 (Aspinall et al., 2002)
O_2	0.76, 0.6-1.3 (Gao et al., 1993, 2009)
CO_2	2.01, 2.08 (Gao et al., 1993), 1.6, 2.005, 2.055 (Aspinall et al., 2002)
O_3	0.6 Chappius band (Gao et al., 1993), 0.35, 9.6 (Aspinall et al., 2002)
N_2O	2.0-2.5
CO	2.0-2.5
CH_4	2.35 (Gao et al., 1993)

4.2 ATMOSPHERIC CORRECTIONS MODELS

Atmospheric removal is performed to correct the spectral data for solar irradiance and atmospheric gas effects (Goetz et al., 1985). The removal of atmospheric effects from IS data requires calibration/atmospheric correction. Calibration is a widely used term that refers to different levels of transformation from digital numbers (DNs) to reflectance. A full image calibration optimally includes the radiometric sensor calibration from DN values to at-sensor radiance, corrections for system distortions, transformation of the at-sensor radiance to apparent surface reflectance (atmospheric calibration) and solar and topographic correction to absolute surface reflectance (Schowengerdt, 1997; Jacobsen, 2001).

Atmospheric corrections of IS data are required particularly when the objectives are (Aspinall et al., 2002; Schaepman et al., 2009; Richter, 2010):

I. a quantitative analysis to derive a physical parameter,

II. analysis of the image with spectral libraries, usually measured in reflectance, including field spectra and,

III. change detection through multi-temporal analysis, involving sometimes multi-sensor data.

An example of a physical parameter to derive, I) is the determination of a pH value (e.g. Ong et al., 2003; Zabcic et al., 2005). In II), the data collected by IS sensors are not immediately comparable to laboratory or ground-based spectra, because the atmosphere alters the spectral signal reaching the sensor. Data collected using imaging spectrometers therefore must be converted from raw radiance values to atmospherically corrected

reflectance values to allow spectra to be compared with reference spectra in spectral libraries (Kruse 1994; Aspinall et al., 2002).

From sensors to atmosphere, conditions are different in multi-temporal acquisition data sets. Thus, to establish the change detection of a particular theme, in III), it is necessary to remove at least the atmospheric influence to obtain the signal of interest and make it comparable among imagery.

Even if it is feasible to analyse an IS image without atmospheric corrections, the distinctive absorption features and the overall view of the spectra can be advantageous when using reflectance data (Figure 2.2, Chapter 2). Plus, the full potential of IS can only be exploited when using physical based approaches and develop new knowledge about a study area (Ben-Dor et al., 2004; Richter, 2010).

However, in the case of one-off image analysis the results using radiance data can be acceptable. Nadeau et al., (2002) refer the similar results obtained in an arid environment when processing in 2050-2350nm either in at sensor radiance or surface reflectance.

The conversion of at sensor radiance to absolute or relative reflectance[1] can be obtained by different methods and models. These models are contained in one of the three types: I) Statistical or empirical models, II) Physical models and, III) Combined or mixed models of the previous two. An overview of these models and the main characteristics are summarised in Table 4.2.

The selection of one of the models is dependent of the objective of the work and the atmospheric and field data available. Aspinall et al. (2002) discriminated the requirements for atmospheric corrections based on the type of analysis of the IS data, whether is used a "top-down" or "bottom up" approach (Chapter 5). In the former, field mapping is used to train the imagery. The small geographic extent of the most IS data, reduces the potential for significant variations in atmospheric effects across the scene, while mapping field features directly to the image means that the classifying algorithm can incorporate atmospheric effects into the feature spectra as it searches the image to find similar features. Thus, a particular feature type will probably appear similar across the entire image and the atmospheric effects should not confuse the mapping process. In contrast, a "bottom up" approach typically uses ground-based or laboratory-based spectral libraries to identify key features, whereas atmospheric corrections are absolutely essential to match image spectra to library. It's worth noticing that in the case of S. Domingos the waste mining material mapping workflow, as depicted in Figure 3.9, encompasses both a "top-down" and a "bottom up" approach maximising advantages from both.

In both types of models, whether based on statistical or physical models, artefacts can be introduced, particularly in the ones that are statistically based when field spectral data is not used (Boardmann, 1998; Mustard et al., 2001; Ben-Dor et al., 2004). The latter authors concluded, through a literature survey, that users are now moving towards physical based model, rather than empirical-based methods, that are now more user-friendly and is installed in most of the common IS software providing reasonable results and do not require visiting the specific site.

Although some experiments have been conducted using statistical models, i.e. flat field and empirical line in the HyMAP™ data over S. Domingos test site, the results were not satisfactory probably due to the characteristics of field spectral data available and were abandoned. In fact, neither the measurements of the GER Mark V have high quality in the particular targets selected; neither the amount of spectral data collected was enough. The use of statistical models with no field measurements such as logarithmic residuals or IARR (Table 4.2) gave poor results, quite different from ground measurements, even if EFFORT polishing was used afterwards.

1 Ideally the calibration of IS data to absolute reflectance data should be done using onboard calibration is difficult and typically not available (Kruse, 2004). However, this is an extreme simplification of the reflectance quantities in optical remote sensing, as defined and detailed in Schaepman-Srub et al. (2006).

As referred by Van der Meer (2001), it should be noted that the empirical approaches only approximate the highly variable processes in time and space in the atmosphere controlling the transfer of radiance to and from the Earth´s surface to the sensor. Plus, the IS data due to its narrow bandwidths has the adequate conditions to perform an atmospheric correction based on physical models.

Table 4. 2 Examples of some atmospheric corrections models. Based on Aspinall et al., 2002; Shaw and Burke, 2003; Ben-Dor et al., 2004; Goetz, 2009 and Richter, 2010.

METHODS	DESIGNATION	PROCEDURE
STATISTICAL OR EMPIRICAL	FLAT FIELD CALIBRATION Requires an area of the image with known reflectance on the ground.	Divides the ground reference spectra into the image spectra for each band then uses the resultant ratios to calculate the relative reflectance
	INTERNAL AVERAGE RELATIVE REFLECTANCE (IARR) No field measurements required	An average spectrum is calculated from the entire scene; this is then used as the reference spectrum and divided into the measured spectrum at each pixel of the image to estimate relative reflectance.
	LOGARITHMIC RESIDUALS designed to remove solar Irradiance, atmospheric transmittance, instrument gain, topographic effects, and albedo effects from radiance data.	Creates a pseudo reflectance image that is useful for analyzing mineral-related absorption features. Log residuals calibration is similar to IARR calibration in that both tools use only in-scene statistics to produce a result.
RADIATIVE TRANSFER MODELS	ATmosphere REMoval (ATREM) program (Gao and Goetz 1990; Gao et al., 1992; Gao et al., 1993)	A three channel ratioing method uses the water vapour absorption bands to calculate the amount of water vapour for each pixel. This produces an image of water vapour concentrations. This image is used with transmittance spectra of atmospheric gases to produce scaled surface reflectance.
	MODerate resolution TRANsmission (MODTRAN) (Berk et al., 1998, 1999; Adler-Golden et al., 1998; Gastil and Melack 1998)	Similar to ATREM
	Fast Line-of-sight Atmospheric Analysis of Spectral Hypercubes (FLAASH) (Adler-Golden et al., 1999, Anderson et al.,2002)	Taking advantage of the fact that each pixel in a hyperspectral image contains an independent measurement of the atmospheric water vapour absorption bands (differential absorption) and uses an adjacency component.
	ATCOR (Richter, 2010)	Uses look-up tables derived from Modtran® 4 radiative transfer code. Different codes (ATCOR 2/3 e 4) optimised according to the origin of the image, spaceborne or airborne, and characteristics of the study area, if flat or mountainous.
COMBINED METHODS	ATREM and EP* Clark et al., (1995) *similar to Empirical Line	To correct model errors in ATREM by calculating normalization factors for one pixel and then applying them to the rest of the ATREM-corrected image.
	MODTRAN and EP (Goetz et al., 1998)	Ground measurements of spectral irradiance with MODTRAN to derive a model EP that did not require uniform ground targets of different reflectance.
	Empirical Flat Field Optimal Reflectance Transformation (EFFORT) Goetz et al., (1997), Boardman (1998)	Bootstraps a linear adjustment to apparent reflectance spectra to improve the accuracy of spectra from AVIRIS following calibration with ATREM.

4.2.1 PHYSICAL MODELS

Physical-based or radiative transfer models are based in image information and require also detailed information about atmosphere and the sun, the target area including mean elevation of the scene and location, image acquisition altitude, local visibility and exact acquisition times, and the definition of an atmospheric model (Ben-Dor et al., 2004; Goetz, 2009). These parameters are then input to the atmospheric model selected (e.g., mid-latitude summer) and used to compute the absorption and scattering characteristics of the atmosphere at the instance of remote sensing data capture, most notably an aerosol description (the visibility or optical depth, and, if possible, an aerosol "type") and the column water amount.

The scene information and spectral features of the water vapour absorptions are used to model the theoretical atmosphere at the time of flight, e.g. as in the ATREM code (Table 4.2). This method attempts to correct for

the solar irradiance atmospheric scattering and absorption as determined for the general conditions at the time of data acquisition. In this each pixel is examined for water vapour by analysing the bands at 0.94 μm and 1.14 μm due to atmospheric molecules (Rayleigh scattering) and aerosols to calculate the spatial variation of the atmospheric water content. The derived water vapour values are then used for modelling water vapour absorption effects in the entire 0.4-2.5 μm region. Other gasses (O_2, O_3, CH_4, CO, CO_2 and N_2O), which absorb incident radiation causing noise in the data (Table 4.1) are modelled using the inputted scene information. The transmittance spectra of the atmospheric gasses are derived using the Malkmus narrow band model (Malkmus, 1967) based on the HITRAN 92 (Rothman et al., 1992) database and the 5S (Simulation of the Satellite Signal in the Solar Spectrum) code (Tanré et al., 1986), which is used to model scattering effects (Kruse, 1994; Lau, 2004).

The effect of different methods for calibration and atmospheric correction on the characteristic spectral profile for materials is pronounced (Aspinall et al., 2002). This has been already verified in the case of statistical models when tested for S. Domingos study area. In the case of radiative transfer modelling, within the software available, two were used in the test site. One was HyCORR, which is a modified version of the ATREM (GAO et al., 1999). Groesel et al. (2002), tested both HyCORR and ATREM in vegetated Alpine environment and concluded that these two softwares provided similar results.

The other software used in S. Domingos is the FLAASH (Table 4.2), which is a MODTRAN4-based atmospheric correction software package developed jointly by the Air Force Phillips Laboratory, Hanscom AFB and Spectral Sciences, Inc. (Adler-Golden et al., 1999). One key feature of FLAASH is that it offers the option of correcting for light scattered from adjacent pixels into the field-of-view. Limited comparisons of retrievals with ATREM, ACORN, and FLAASH (Griffin and Burke, 2003; Kruse, 2004) have demonstrated that the derived surface reflectances from these algorithms are quite comparable (Gao et al., 2009).

An empirical Flat Field Optimal Reflectance Transformation TM (EFFORT) (Boardman, 1998) is a post correction program (Table 4.1) also implemented in ENVI (ITT, 2010) as FLAASH. This program determines and applies mild adjustments to ATREM (or similarly to HyCORR) apparent reflectance data so the spectra appear more like spectra of real materials, and improving the accuracy of the apparent reflectance without field measurements (Boardman, 1998) or optionally using it as reality boost spectra.

4.3 HYMAP™ (YEAR 2000 ACQUISITION)

As mentioned previously HyCORR and FLAASH software were both used in HyMAP™ data captured on the 21st of August 2000. The difference in the FLAASH corrected data compared to HyCORR is that local atmospheric data and a few tests with field spectra were undertaken to model the radiance data. Both corrections of the HyMAP™ data had a cross-track illumination correction and an EFFORT Polishing.

4.3.1 HYCORR CORRECTION

The HyMAP™ data delivered by HyVista Corporation (HVC) were in radiance (μW/cm^2 nm sr) calibrated data (at sensor) and apparent reflectance (scaled). Geo-correction files were also provided based on DGPS data flight (Chapter 3). The data were delivered as ENVI compatible files. An example of the radiance and apparent reflectance data set is depicted in Figure 4.2.

The HyCORR correction was undertaken by HyVista Corporation (HVC). The apparent reflectance data was obtained from calibrated data with HyCORR on its more advanced level, which consists of an ATREM pass followed by an EFFORT polishing pass to remove systematic ATREM errors (HVC, 2008).

The water vapour retrieval, during the HyCORR pass, can be seen as one band image (Figure 4.3). In this is depicted the amount of water vapour modelled for each pixel, where the highest values correspond to water dams and wet soils.

The EFFORT calculated gains and offsets are applied to atmospheric corrected apparent reflectance data. The data are used to generate "pseudo field" spectra by fitting each observed spectrum with a parametric model of Legendre polynomials. Gains and offsets for every band are calculated by comparing the modelled spectra to the data spectra, for pixels that are well-fit. A number of spectra are used that span the entire albedo range to give good leverage for the linear regression process, and the data values versus modelled values are fit with a line for every band. The slope and offset of this line are used to correct the apparent reflectance data for the error features (ITT, 2010). An example of part of this process is in Figure 4.4 where some spectra are shown with the model used (solid), and the final calibration spectral library (dotted).

Variations in brightness gradients across each fligthline direction remain after the application of HyCORR with EFFORT polishing. This is also evidenced in the water vapour column of Figure 4.3. To minimize the differences along track mean values were calculated showing the mean variation in the cross track direction and using a multiplicative correction method with a polynomial function, in this case of order 1, is fitted to the means to remove them.

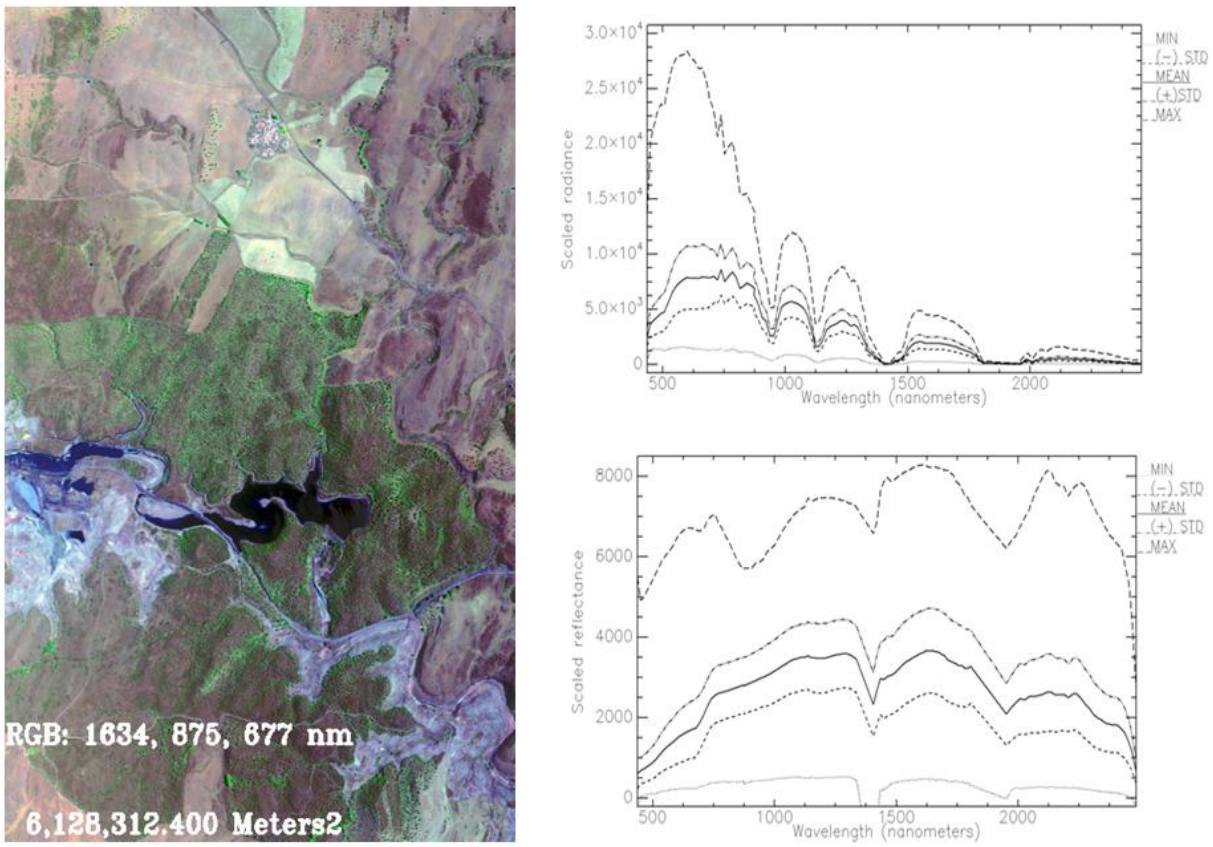

Figure 4.2 Image and spectral space of radiance and apparent reflectance data from HYCORR. Detail of fligthline 08 with HyMAP™ sensor (Achada do Gamo area, Figure 3.6).

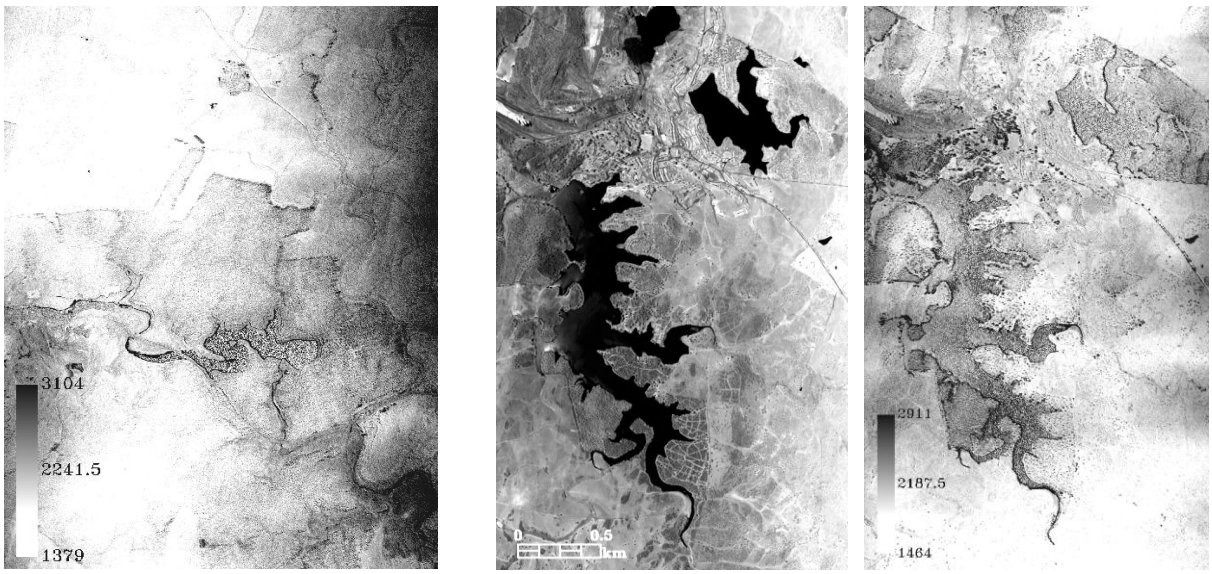

Figure 4.3 Spatial variation of water retrieval from HYCORR (results from Hyvista Corporation). Units are water vapour in atm-cm*1000. Examples of two fligthlines: left-area of 08 in Figure 4.2, centre-image space of 10, S .Domingos village area and, right-vapour water spatial distribution of centre.

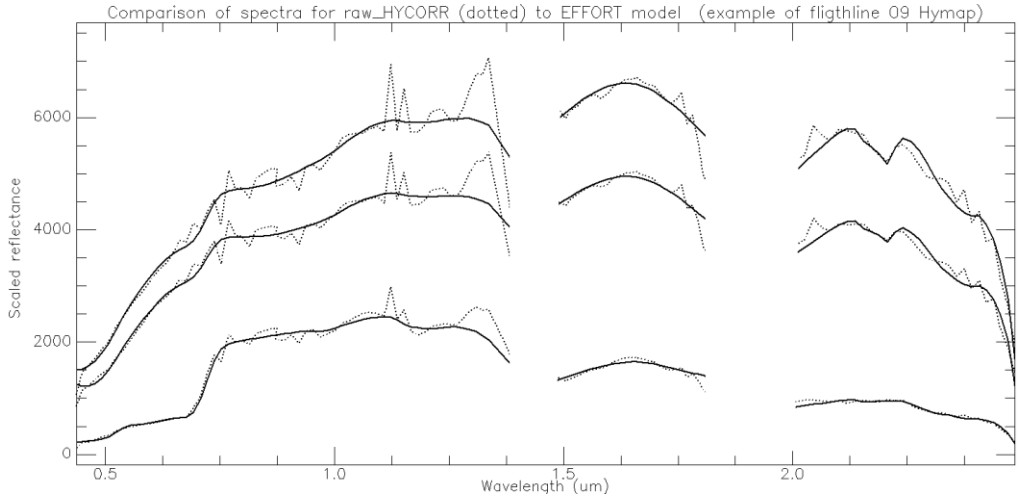

Figure 4.4 Spectra from final calibration from HYCOOR-EFFORT with the model used in to fit in EFFORT polishing data set. Results from Hyvista Corporation.

This procedure is implemented in ENVI software. To eight fligthlines, from 11 (North of open pit) to 04 (Pomarão Harbour), was applied the same procedure and were afterwards geocoded using geocorrection files provided by HVC.

The geocorrection files were obtained through geometric correction algorithms. The HyMAP™ system is mounted on a Zeiss SM2000 gyro-stabilised platform that provides 5 degrees of pitch and roll correction and 8 degrees of yaw correction. High quality DGPS integrated with a Boeing CMIGITS II GPS/INS inertial monitoring unit was used to provide sensor pointing data to precisely geocode the raw data. Geometric correction factors are provided to convert the data to map coordinates (HVC, 2008) in this case to UTM, WGS84, Zone 29N.

The fligthlines were mosaiced using a nearest neighbour resampling. In this it was considered the statistical areas overlapping regions with a final pixel size of 4.1m.

The global statistics of spectral data for the apparent reflectance mosaic is in Figure 4.5.

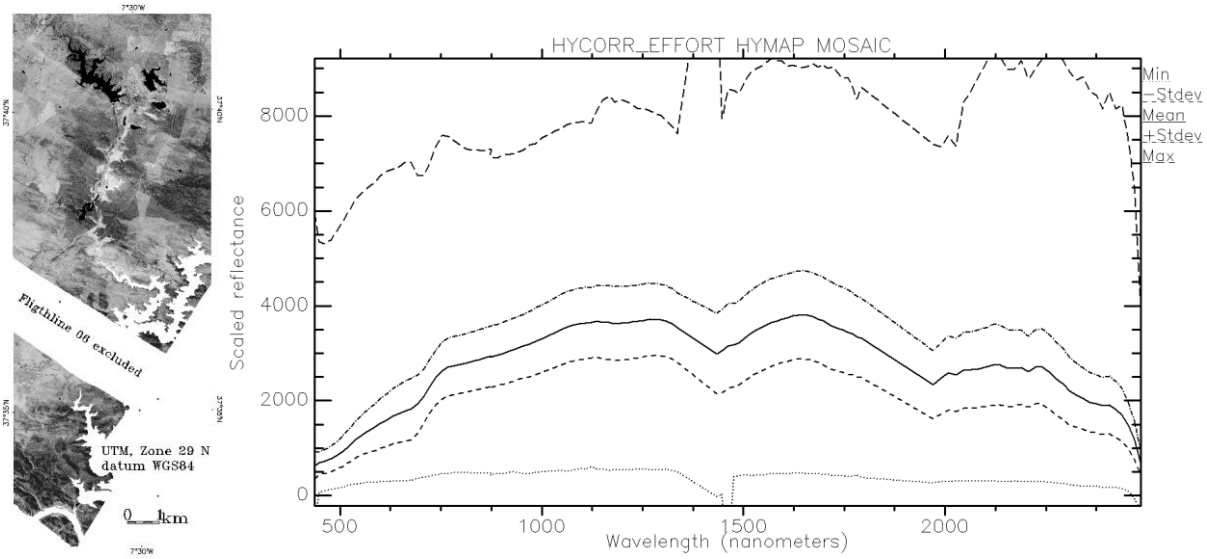

Figure 4.5 S. Domingos apparent reflectance mosaic with HyCORR atmospheric correction and EFFORT polishing (results from HyVista Corporation), with basic statistical spectral values.

In this statistical values fligthline 06 and water areas had been masked. This fligthline is excluded as result of low quality reported in the analysis in Chapter 3, particularly in the SWIR range.

The visible and near-infrared regions displayed smooth spectral features, which corresponded well to areas that contained vegetation and iron oxides.

4.3.2 FLAASH CORRECTION

The FLAASH algorithm operates on a pixel-by-pixel basis, taking advantage of the fact that each pixel in a IS image contains an independent measurement of the atmospheric water vapour absorption bands (differential absorption).

Details of the program are given in Addler-Golden et al. (1999); Anderson et al. (2002); Mattew et al. (2003) and in FLAASH 2009. A schematic flow of FLAASH is given in Shaw and Burke (2003). Below is described, as in FLAASH 2009, the main assumptions and operational mode of the program.

FLAASH starts from a standard equation for spectral radiance at a sensor pixel, L*, that applies to the solar wavelength range (thermal emission is neglected) and flat, Lambertian materials or their equivalents:

$$L^* = A\rho/(1-\rho eS) + B\rho e/(1-\rho eS) + L^*a \qquad (4.1)$$

where, ρ is the pixel surface reflectance,

ρe is a surface reflectance averaged over the pixel and a surrounding region,

S is the spherical albedo of the atmosphere,

L*a is the radiance backscattered by the atmosphere, and

A and B are coefficients that depend on atmospheric and geometric conditions but not on the surface.

Each of these variables depends on the spectral channel; the wavelength index has been omitted for simplicity. The first term in Eq. (4.1) corresponds to radiance that is reflected from the surface and travels directly into

the sensor. The second term corresponds to radiance from the surface that is scattered by the atmosphere into the sensor.

The distinction between ρ and ρe accounts for the adjacency effect (spatial mixing of radiance among nearby pixels) caused by atmospheric scattering.

The values of A, B, S and L*a are determined from MODTRAN4 calculations that use the viewing and solar angles and the mean surface elevation of the measurement, and they assume a certain model atmosphere, aerosol type, and visible range. The values of A, B, S and La are strongly dependent on the water vapor column amount, which is generally not well known and may vary across the scene. To account for unknown and variable column water vapour, the MODTRAN4 calculations are looped over a series of different column amounts, and then selected wavelength channels of the image are analyzed to retrieve an estimated amount for each pixel. Specifically, radiance averages are gathered for two sets of channels: an absorption set centered at a water band (typically 1130 nm) and a reference set of channels taken from just outside the band. A lookup table for retrieving the water vapour from these radiances is constructed. After the water retrieval is performed, Equation (4.1) is solved for the pixel surface reflectances in all of the sensor channels. The solution method involves computing a spatially averaged radiance image Le, from which the spatially averaged reflectance ρe is estimated using the approximate equation:

$$L_e \approx \left(\frac{(A + B)\rho_e}{1 - \rho_e S} \right) + L_a \qquad (4.2)$$

Spatial averaging is performed using a point-spread function that describes the relative contributions to the pixel radiance from points on the ground at different distances from the direct line of sight. For accurate results, cloud-containing pixels must be removed prior to averaging. The cloudy pixels are found using a combination of brightness, band ratio, and water vapor tests, as described by Matthew et al.(2000).

The FLAASH model includes a method for retrieving an estimated aerosol / haze amount from selected dark land pixels in the scene. The method is based on observations by Kaufman et al. (1997) of a nearly fixed ratio between the reflectances for such pixels at 660 nm and 2100 nm. FLAASH retrieves the aerosol amount by iterating Equations (4.1) and (4.2) over a series of visible ranges. For each visible range, it retrieves the scene-average 660 nm and 2100 nm reflectances for the dark pixels, and it interpolates the best estimate of the visible range by matching the ratio to the average ratio of ~0.45 that was observed by Kaufman et al. (1997). Using this visible range estimate, FLAASH performs a second and final MODTRAN4 calculation loop over water.

As inherent of any radiative transfer-based atmospheric correction algorithms, the FLAASH requires some atmospheric information, or if certain atmospheric absorption bands are present in the IS data. Figure 4.6 depicts the input data used to run the code. The parameters were selected according to the characteristics of the study area as well as local information as contained in Table 4.3.

The model atmosphere was set to mid-latitude summer, according to the closest latitude coordinates, as described in tables used in MODTRAN atmospheric models (FLAASH 2009), which rely on a seasonal-latitude surface temperature model.

Despite the air temperatures in the area considered, with an average of 25°C (Table 4.3), are closer to a tropical model atmosphere (27°C), however the water amount retrieval values are lower than expected values for a tropical model and closer to local pressure QFF. Local average pressure in 1019,85 HPa corresponds to 1039.99 cm, lower than the values estimated with mid-summer latitude atmospheric model with an average of 1267.60 cm calculated from the FLAASH results.

S. Domingos characteristically follows a rural aerosol model, i.e. regions of the atmosphere not impacted upon by urban or industrial processes. It is assumed to be composed of 70% water-soluble material (ammonium, calcium sulphate and organic compounds) and 30% dust-like particles.

For modelling the data set the FLAASH software admits some variability in the input parameters, which were tested in the HyMAP™ data. Part of this has been done through a trial-and-error method relatively to some of the variable parameters that were not precisely defined (Figure 4.6).

The most distinctive parameter when compared with similar algorithms is the possibility to consider an adjacency effect correction (Figure 4.6) that takes into account the spatial vicinity of pixels. In this case, in the Equation 4.1 $\rho \neq \rho e$.

Two examples are depicted in Figure 4.7 relative to fligthline 08 and 10. The effects of scattering are obviously more pronounced in the first bands of the visible spectrum, giving higher reflectance values with adjacency than without. After 780 nm the spectral average tends to be similar with or without adjacency correction and its inverted after 829 nm, i.e. the highest reflectance values are given without adjacency correction. This trend is similar for the SWIR range, whereas the overall reflectance spectra is similar but with higher values without adjacency correction. Another difference is detected on the column water vapour (Figure 4.7), where the amount of water is "shrinked" when using the adjacency effect (c).

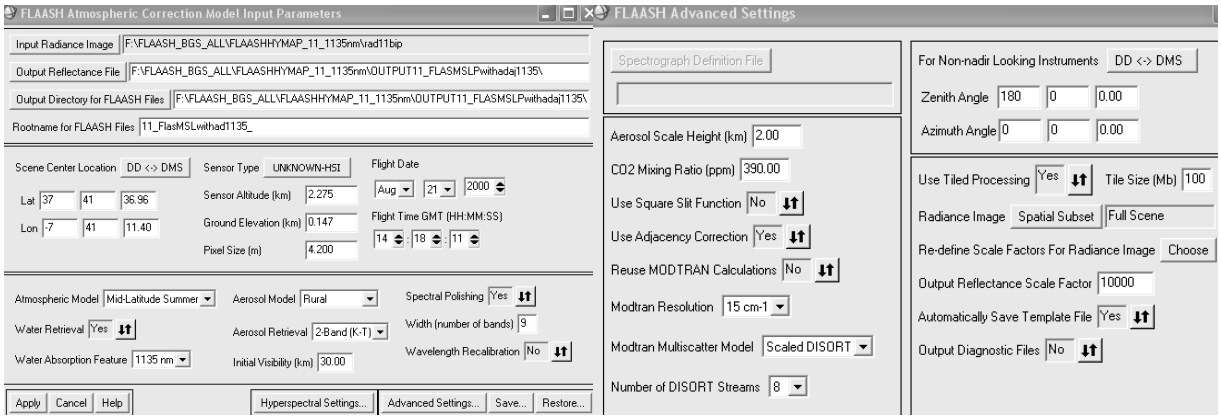

Figure 4.6 FLAASH used parameters for one of the S. Domingos fligthline.

Table 4. 3 Wheather conditions at the time of the flight (year 2000). Courtesy of BEJA AIRPORT BASE.

21-Aug-2000 Local time	Pressure QFF (HPa)	Air temperature (°C)	Relative Humidity %	Wind Direction°, average speed, Gust (kmh^{-1})	Nebulosity (x/8)	Visibility (km)
12:00 AM	1020.6	23.2	52	310, 13	2	30
1:00 PM	-	25.2	40	330, 22	2	30
2:00 PM	-	25.6	39	340, 17, 39	2	30
3:00 PM	1019.1	26.0	38	340, 19, 37	2	30

Especially under hazy conditions and when strong contrasts occur among the materials in the scene, the adjacency correction can result in significant reflectance errors at short wavelength. Although a few contrasts occur among materials in the scene, particularly between soils and water bodies, the haze is minor (Table 4.3) the case of the S. Domingos area, and the spatial component through adjacency correction is taken into account for the final reflectance spectral signal for all the fligthlines.

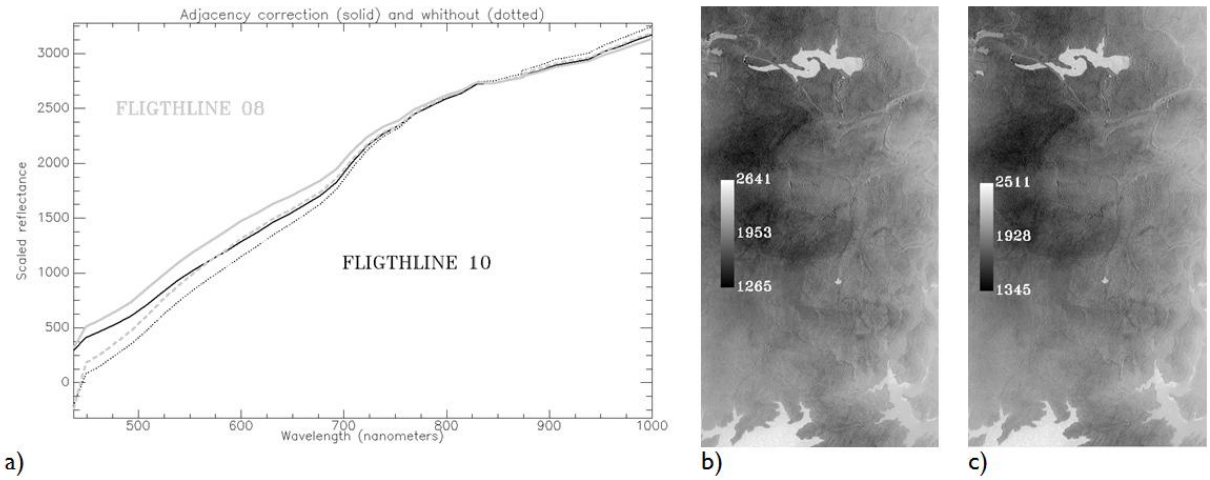

Figure 4.7 Effect of adjacency correction in FLAASH. Average spectral values for two fligthlines in a), and water vapour (cm) variations without, b) and with adjacency correction c), in fligthline 08 (Achada do Gamo).

Each fligthline was atmospherically corrected and afterwards was also corrected for illumination effects remaining, using a cross track calculation of multiplicative polynomial order 2 (Figure 4.8). This has been controlled and checked through across fligthline profiles and Minimum Noise Fraction (MNF) bands.

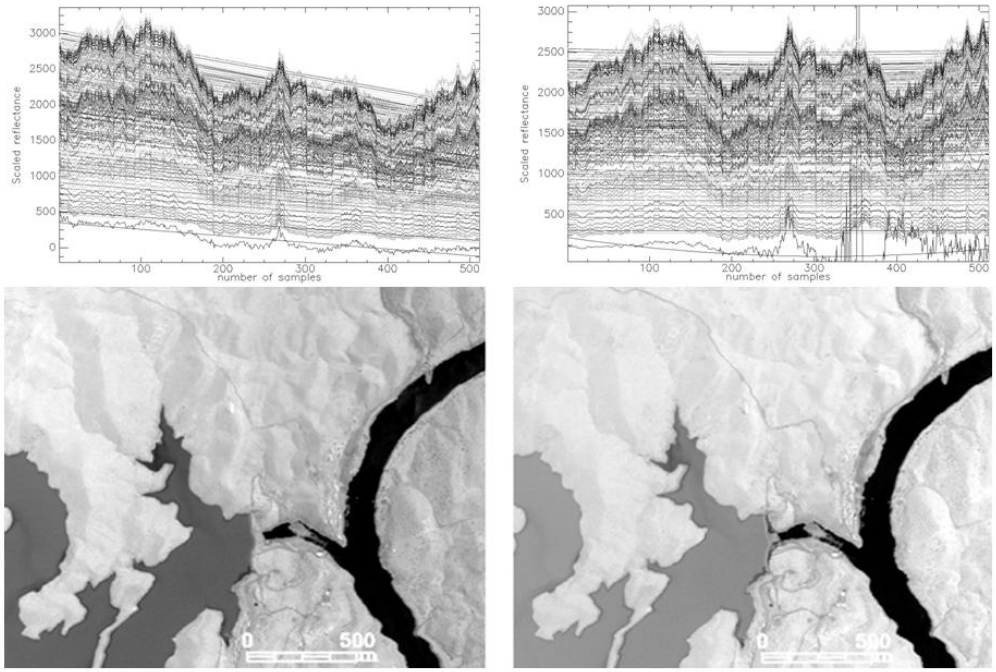

Figure 4.8 A multiplicative polynomial interpolation of order 2 on HyMAP™ data for Cross Track Illumination Correction: Upper-before (left) and after (right) illumination correction. Lower-equivalent Minimum Noise Fraction 1. Detail of flightline 04 encompassing the Pomarão harbour.

The average spectral values of reflectance of each fligthline were still very distinct from either field spectra either from equivalent average spectral values from HyCORR correction. An EFFORT polishing was then executed. The options using this code include the possibility to model the reflectance data using reality boost

spectra, and also selecting the spectral segments to do it. The degree of polynomial order to polish the data can also be variable according to each of the segments selected.

The wavelength range was also tested using different segments, but the results with higher similarity with HyCORR software were achieved using three wavelength segments separated by strong water vapour absorption bands, i.e. 1.4 μm and 1.9 μm. Detailing, the segments are 437-1323 nm, 1433-1805 nm and 1970-2485 nm.

It is generally accepted that using a few spectra characteristic of the area of interest as reality boost spectra produces better-fitting modelled spectra (ITT, 2010). Thus, a few local field spectra were tested.

Following recommendations from the Center for the Study of Earth from Space, in Thulin (2008), the selection of reality boost spectra should not be more than five because of the possible unpredictable interaction between them. With this assumption, the local field spectra selected was focused on our subject of interest, i.e. the wastes mining materials used in the MINEO project (Quental et al., 2002a, Appendix II). Two types of experiments were executed and within these particularly the ones related to Acid Mine Drainage (AMD). The latter are depicted in gray in Figure 4.9.

The targets PoS137, PoS138, PoS154, Tel181 and Sd246, named according to the spatial location (Figure 3.6), are general spectra within wastes, while the others have a more similar pattern. Further details of the type of sample and mineralogical correlation information of these spectra are given in Table 5.A.II (Chapter 5).

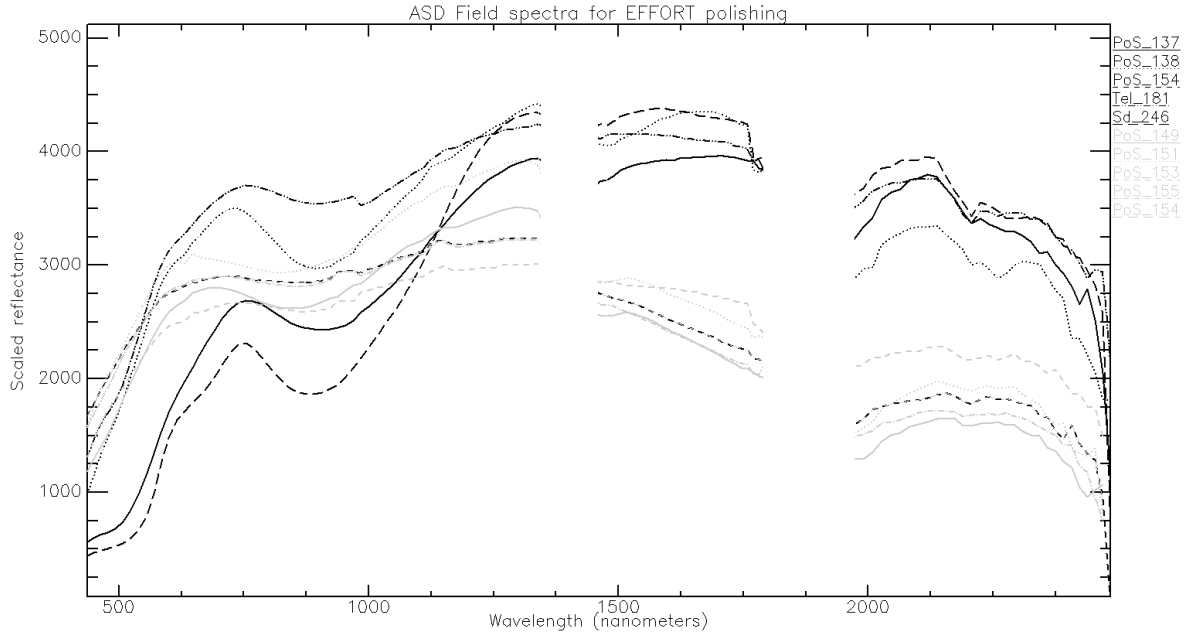

Figure 4.9 Input field spectra for EFFORT code from waste mining materials map (Appendix II). On gray the ones specifically related to low pH.

The Legendre polynomial order chosen was default 10 for the three segments selected, after some tests undertaken on different values ranging from 20 to 5. Using a polynomial of order 5 the final modelling gave a spectral signal extremely flattened, while using 20 gives steep slopes in the signal produced.

Each fligthline has been polished with these spectra, statistically checked and controlled with MNF for error detection.

The EFFORT Polishing is an important step in the final product, depending also on the options taken. In Figure 4.10 is shown an example of the variations of the spectral pattern when using different options concerning the introduction or not of field spectra.

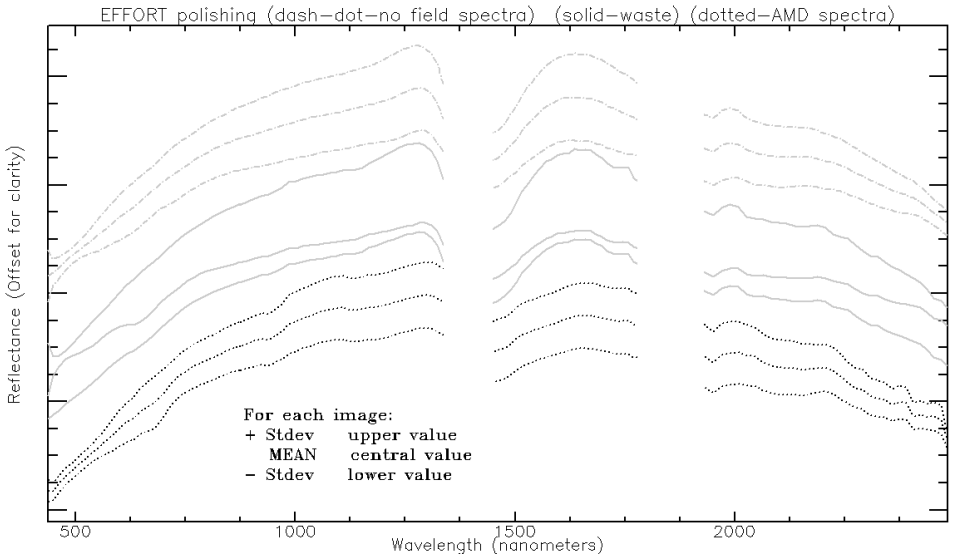

Figure 4.10 Effect of EFFORT comparing different options concerning use of boost spectra. Example of fligthline 08.

In this is depicted the variations respectively using EFFORT with no field data, with waste spectra and AMD related spectra. The waste spectra EFFORT modelled image comprehends a higher differentiation in data, according to the wider variable input spectra when compared to the more homogeneous AMD related spectra. A variation is detected with a peak at 1758nm possibly resulting from the spectrum PoS137 seen in Figure 4.9.

Thus, the possibilities of application of EFFORT, using different values of distinct parameters, play a key-role on the spectral response of the imaged target. Smoothing the signal or modifying the overall spectra implies modifications on the extraction of information from IS data. Despite the changes detected in the spectral average reflectance signal it is important to test exactly what are the direct implications when mapping an area with an AMD environment.

4.3.3 CONSEQUENCES OF EFFORT POLISHING IN IMAGE CLASSIFICATION

Although the extraction of information is dealt with in more detail in Chapter 5, the different data sets obtained with EFFORT Polishing correction were processed to assess the implications in the spectral response of the final classification of the area.

Following the first part of the methodology detailed in Section 5.2 with the multi-source spectral methodology, (Chapter 5), related to the extraction of information from HyMAP™ an automated hourglass was run (ITT 2010), creating an MNF transform, a PPI and extracting endmembers that where then used to map an area using the SAM algorithm. Due to its particular characteristics of very low pH in the dam and already known high acid generating potential of waste mining materials (Chapter 3, Figure 3.6, Figure 4.14) is shown a detail of Achada do Gamo area in Figure 4.11. In this, the different colours report to the spatial dispersion of distinct endmembers. In a), the data set does not have boost spectra and is based solely in image information, while in b) it corresponds to an AMD related spectra depicted in gray in Figure 4.9 and c) is a more general field spectra (black in Figure 4.9).

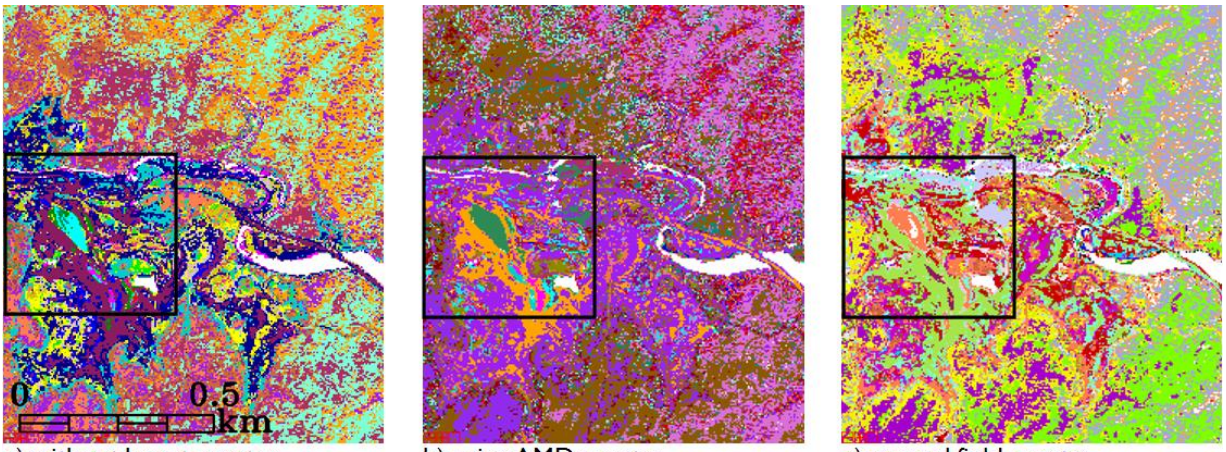

a) without boost spectra b) using AMD spectra c) general field spectra

Figure 4.11 Results of endmembers mapping (SAM) with different EFFORT options without and with spectra in Figure 4.9. Unclassified areas are white. Detail of Achada do Gamo area with shallow acidic dam (Figure 4.14) on the left centre side (dark square).

The EFFORT image without using boost field spectra provides higher variability when mapping using information extracted from the images, while when the EFFORT was executed using field spectra focused on specific targets of interest the information is more homogeneous. Unclassified areas increase from a)=5.2% to c)=6.8%. b) and c) reflect also the characteristics of the type of spectra, depicting b) homogeneous areas of AMD while c) shows different areas of general waste. The latter shows distinct areas of waste materials, namely hills of metallurgical slags, while in b) this is not discriminated.

It's worth noticing that the endmembers used to map the different EFFORT resultant images were controlled through the Pearson correlation matrix using mineralogical standard spectral libraries (methodology developed in Chapter 5) and gave consistent results indicating minerals such as copiapite, coquimbite and alunite at correlation ≥0.90 in the acidic dam area (Chapter 5).

This experiment using different EFFORT polishing conditions permits to conclude that constraining the image modelling using spectral signatures of a specific target of interest limits the extraction of information, if the objective is to increase the knowledge about an area when a resource such as IS data is available. Thus, the mosaic to be used in the next steps of processing in Chapter 5 will be the one polished solely using the image data leaving the use of field spectra to a further advanced phase of image processing.

4.3.4 COMPARISON OF HYCORR AND FLAASH RESULTS

The HyCORR correction was undertaken by HyVista Corporation (HVC), which is an ATREM based model. The other one was obtained using the FLAASH software, a MODTRAN based model, which optionally considers an adjacency effect. Results from FLAASH incorporate information concerning local atmospheric conditions and the EFFORT polishing as been previously tested using local field spectra. The average with respective standard + and - deviation are depicted in Figure 4.12. The upper image is the normal display of wavelength range, whilst the lower is a continuum removal, where the absorption features of reflectance spectra are compared from a common baseline, i.e. a convex hull fit over the top of a spectrum using straight-line segments that connect local spectra maxima (Chapter 2, Section 2.1.4).

While all the parameters were known using FLAASH, the same didn´t occur with HyCORR product delivered by HVC. The comparison of average values for both reflectance mosaics resulting from radiative transfer

modelling from HyCORR and FLAASH codes, show that the overall shape of average results is similar but presents some variability within the wavelength range.

The average amount of water retrieval is variable. In FLAASH the average values of all the fligthlines equals 1580 cm while in HYCORR the average value of water is 1650 cm.

Also the spatial distribution pattern is more consistent using FLAASH, i.e. more homogenous over water bodies. The use of adjacency correction certainly plays a role on this variation (Figure 4.7), and possibly the atmospherical model selected.

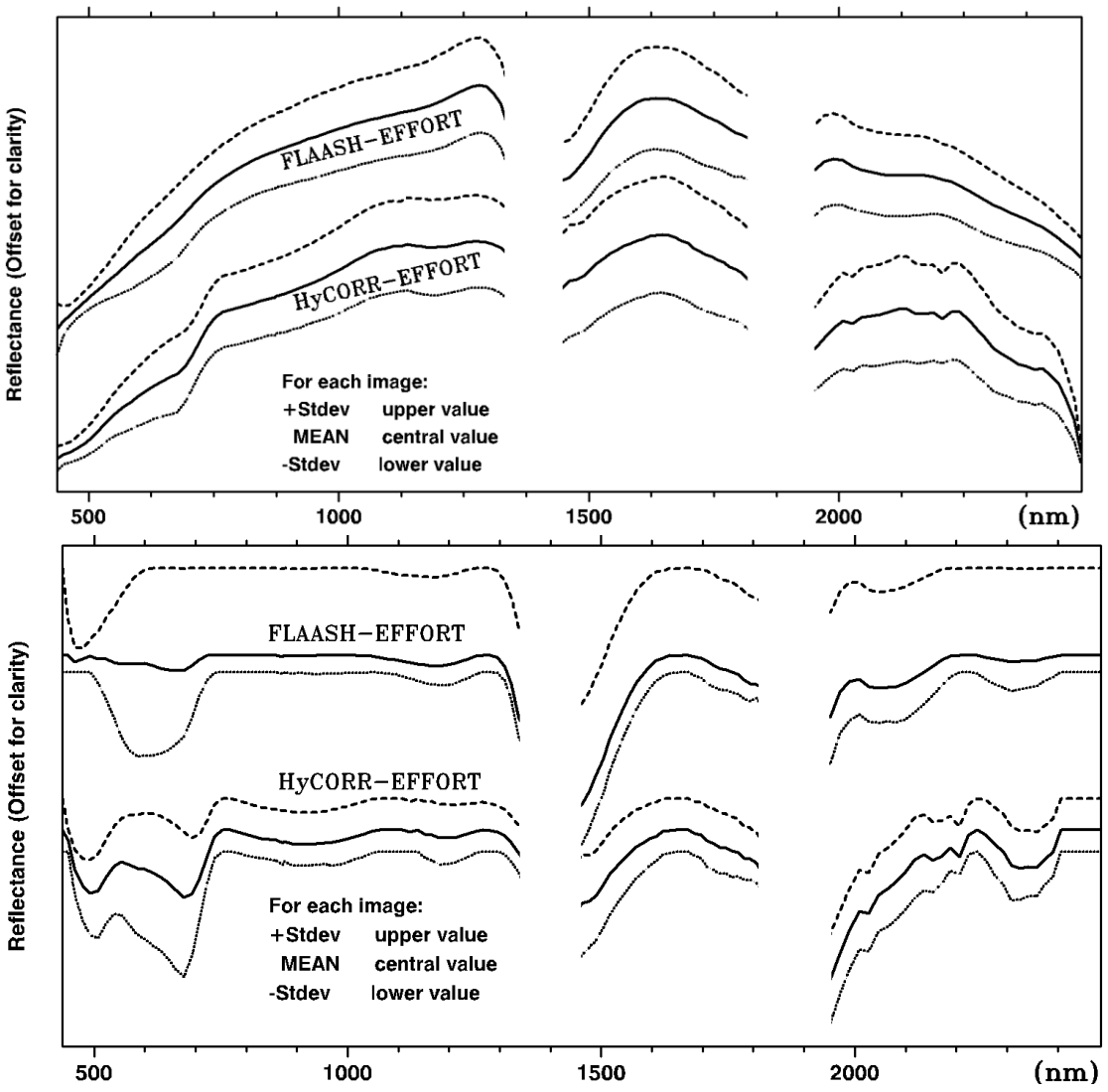

Figure 4.12 Average values (centre) and (+)(-) Stdv of HyCORR and FLAASH relative to the S. Domingos mosaics with EFFORT Polishing. Display, upper-normal, lower-continuum removed.

The overall average spectra are similar to what has already been partially depicted in Figure 4.10 for fligthline 08. Across the wavelength range the HyCORR corrected spectra delineates better the "red edge" feature of vegetation around 676-692 nm. The "red edge feature" is a sharp order of magnitude increase in leaf reflectance between approximately 680 and 750 nm wavelength. In this particular case, with the FLAASH correction this feature is greatly smoothed.

A slight absorption detected at 1122 nm in HyCORR also disappears. Another distinctive character is a broad shoulder with a peak at 1281nm wavelength when comparing FLAASH to the previous HyCORR atmospheric correction. In the segment corresponding to 1462-1793 nm, FLAASH delineates a more pronounced curve than using HyCORR. Absorption features at 2027, 2226 and 2391 nm in HyCORR, disapear in FLAASH. Most of these features are related to Al-OH bonds, while the latter (2391 nm) is possibly related to methane (CH_4). The wavelength range 2.0-2.5 um reflect the absorption features of CO, CO_2 and N_2O of atmospheric gases (Table 4.1).

Generically, considering average values, FLAASH-EFFORT whithout field spectra is smoother than the mosaic resultant from HyCORR-EFFORT. This can lead to a non-identification of a few minerals relevant for AMD detection (Chapter 5), if the average values are reflected in specific targets of interest.

In the absence of reliable reference data for validation of the reflectance data obtained (Chapter 3, Section 3.5.2.1) a local statistics is given for a few selected targets (Figures 4.13 and 4.14), adressing more or less invariant areas or of interest related to AMD detection. Both corrections are depicted, HyCORR-EFFORT corresponds to the lower values, whilst FLAASH-EFFORT corresponds to the upper values.

Generically, what is already detected in Figure 4.12 showing the FLAASH-EFFORT with a smoother spectral response is repeated for most of the local targets. An exception is the dark metallurgical slags target which

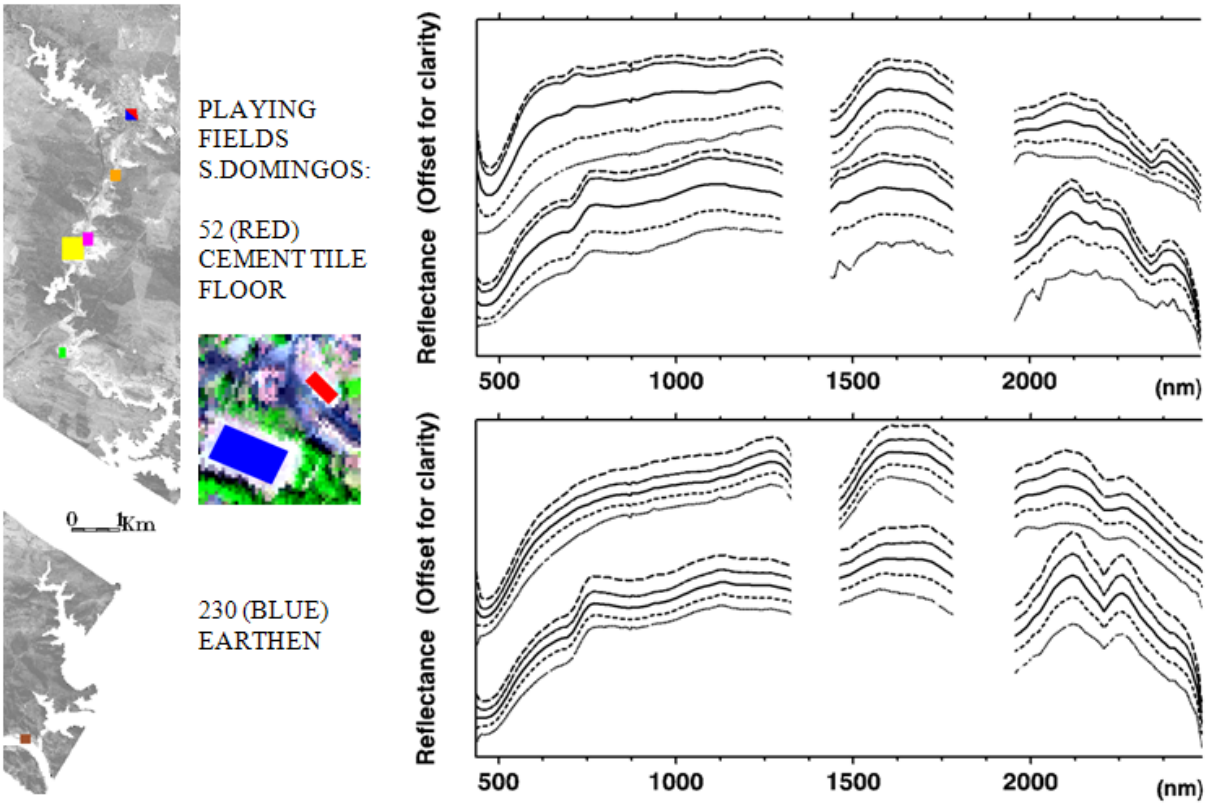

Figure 4.13 Local targets and respective HyCORR (five lower values) and FLAASH (five upper values) spectral values in S. Domingos HyMAP™ IS data. MAX-upper value, MIN-lower value, MEAN-central value with respective (-) and (+)standard deviation. Number-pixels of target. Left-global location.

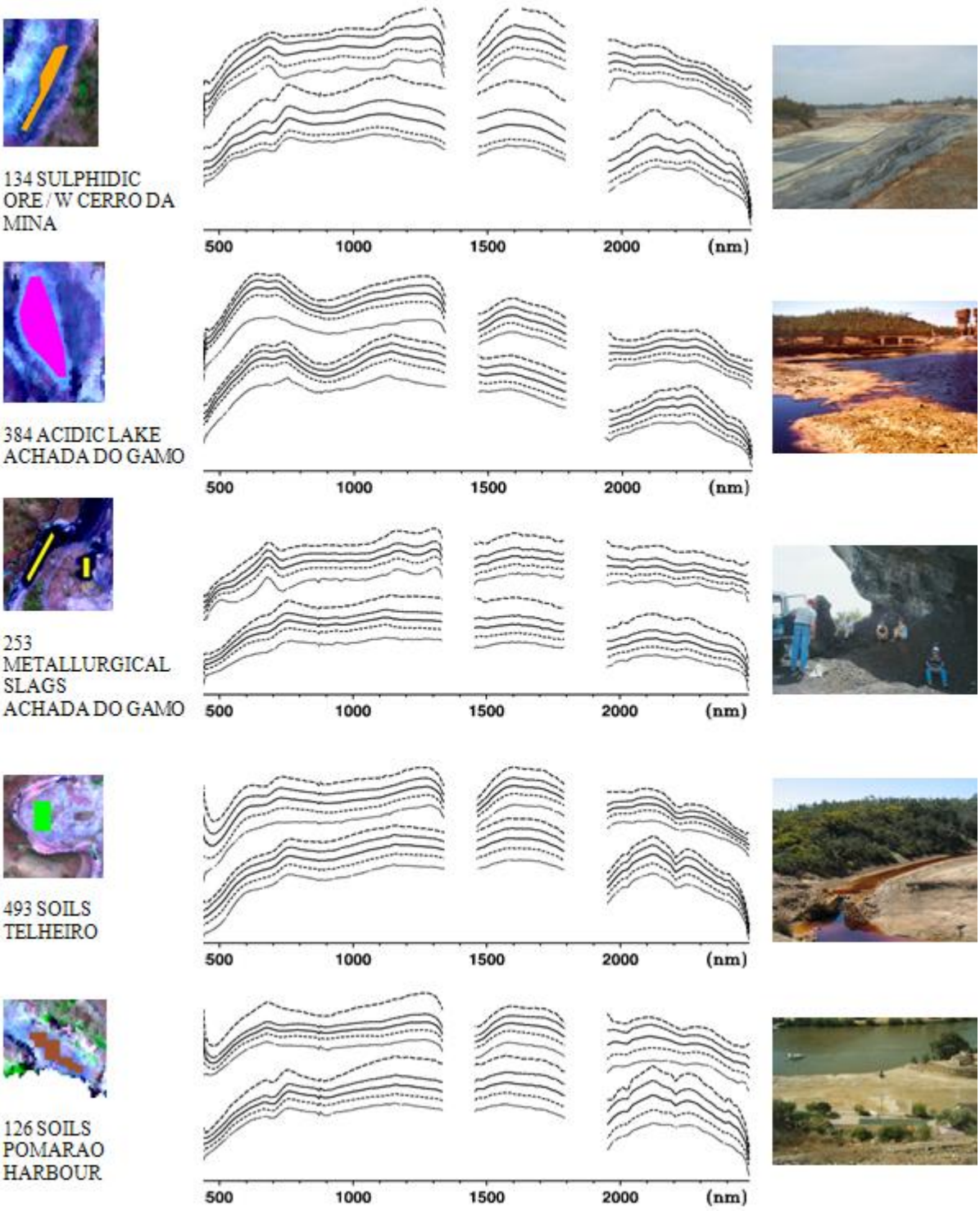

Figure 4.14 Cont. of Figure 4.13, where is the global location of local targets. HyCORR (five lower values) and FLAASH (five upper values) spectral response in S.Domingos HyMAP™ IS data. MAX-upper value, MIN-lower value, MEAN-central value. Number-pixels of target. Reflectance is offset for clarity.

appears with more peaks and absorption features across the wavelength range in FLAASH than in HyCORR. From the two playing fields is seen that the one with cement tile floor is more heterogeneous, with more

extreme values than the one with earthen materials for both corrections. This can possibly be explained by the dark and brigth areas that constitute the cement tile floor (Figure 3.13, Chapter 3).

There is a general pattern with a sligth absorption feature around 676-692 nm in FLAASH in which seems to be a shift when compared to the near values 692-707 nm verified in HyCORR, detected in most of the targets. This value around 692 nm appears to invert the upper or lower curve of the next wavelengths in the two corrections. It is unclear the origin of these features possibly combining vegetation and iron crystal field absorptions which occour in this wavelength range.

The absorption feature at 872 nm, connected with heamatite detection (Chapter 5) is more evidenced in HyCORR, in acidic lake and metallurgical slags targets being absent in some of FLAASH correction particularly in the average values. It appears in Pomarão harbour and Telheiro on both and its absent in sulphidic ore. On opposition, an absorption feature at 461 nm is more evident in sulphidic ore and acidic lake in FLAASH correction, while the metallurgical slags presents a depression at 448 nm. The other targets have an absorption feature at 477.

The absorption features in the segment 1951-2500 nm are more pronounced in the HyCORR then in the FLAASH correction. More specifically, the absorption feature at 2206 nm, i.e. related with Al-OH bond is smoother or inexistent in FLAASH correction. Another absorption feature that appear in HyCORR and is absent in FLAASH is at 2391 nm.

These variations highligth the effect of different atmospheric corrections in targets related with mining waste materials and related pollutants. This will be assessed at the IS methology developed in Chapter 5, considering the mineralogical information (Table 5. 1, Chapter 5) more in detail and based in classification results (Table 5.7).

4.4 SPECIM EAGLE-HAWK (YEAR 2007 ACQUISITION)

The SPECIM EAGLE-HAWK dataset shortens the spectral width to much lower values than the HyMAP™ dataset (Chapter 3, Table 3.4). Taking into account that one of the main objectives is the comparison with HyMAP™ for monitoring purposes related to AMD, the SPECIM EAGLE-HAWK has been spectrally resampled to ensure these parameters are consistent for both images.

This spectral resampling reduces the radiance mosaic from 489 to 124 bands (Figure 4.15), excluding the two last existing in HyMAP™ at 2470 and 2485 nm that are not reached by SPECIM EAGLE-HAWK wavelength range (Chapter 3, Table 3.4). When the wavelength is not the same is taken the band with the smallest spectral difference from above or below the exact value. The maximum difference value in equivalent spectral bands between the two datasets is 3.51 nm, namely at 2100 and 2309 nm of HyMap™ wavelength values.

The spectral resampling adds another important advantage by reducing the size of radiance mosaic from 24.6 to 5.45 Gigabytes, which leads to a significant decrease of the time required for data processing.

Another important step is to eliminate the gap between the EAGLE and HAWK sensors (Chapter 3, Figure 3.15). Thus, the wider EAGLE area capture is partially masked by the same Field of View (FOV) of the HAWK sensor.

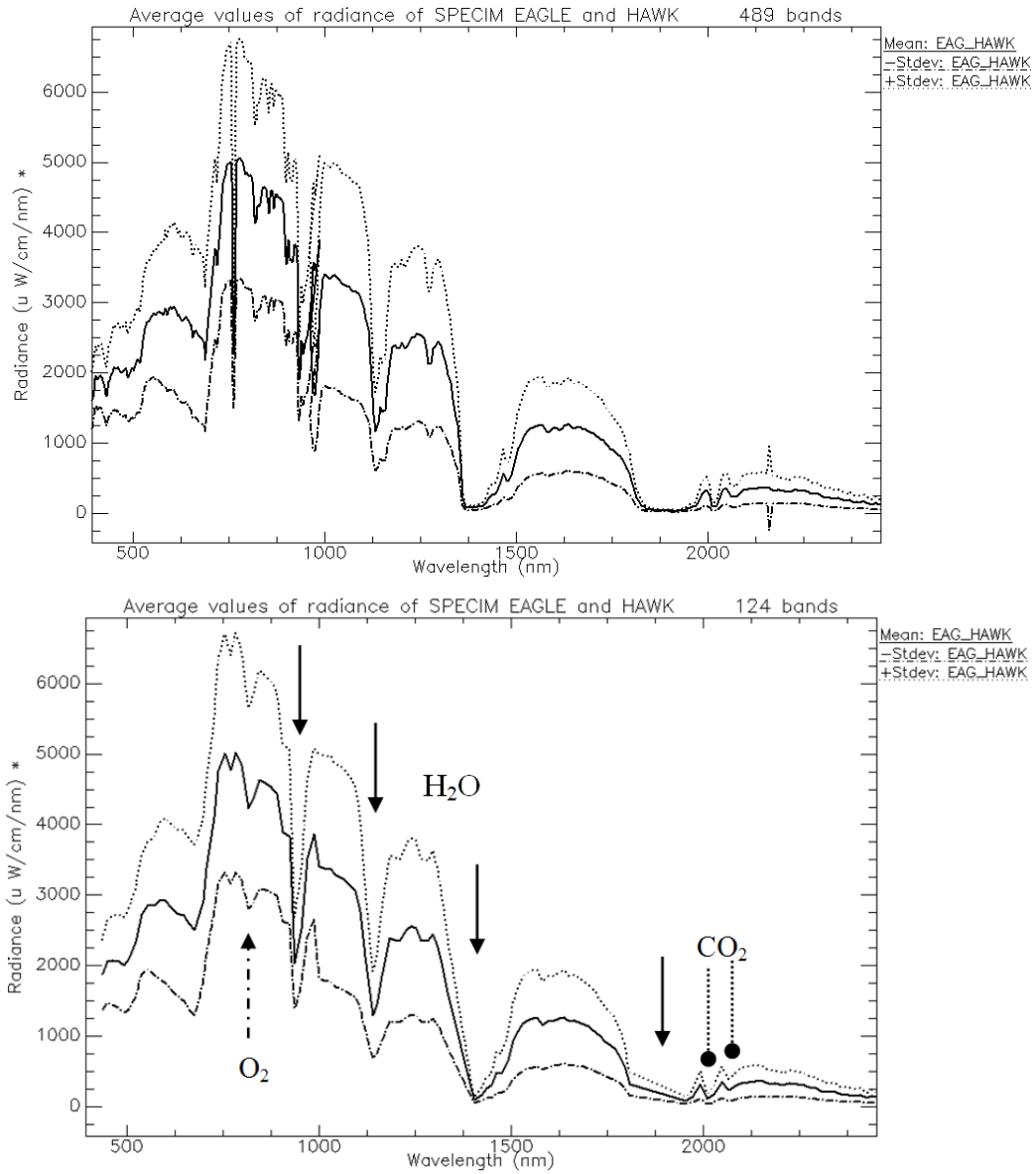

Figure 4.15 Effect on average scaled radiance values from spectral resampling from SPECIM EAGLE-HAWK (upper image) to the closest HyMAP™ bandwith (lower). Main absorption features from Table 4.1.

The fligthlines were mosaiced using the statistical areas overlapping regions and a nearest neighbour resampling.

4.4.1 FLAASH CORRECTION

The input parameters for FLAASH are depicted in Figure 4.16, with the local atmospheric conditions detailed in Table 4.4. The atmospheric model selected is still considered a mid-summer latitude model following temperature and latitude conditions as referred in FLAASH (2009). The overall average statistics for the mosaic is shown in Figure 4.17 as well as the final result using EFFORT polishing. The latter follows the same conditions as for the 2000 mosaic, i.e. using only image information and the three wavelength segments 437-1323nm, 1433-1805 nm and 1970-2451 nm.

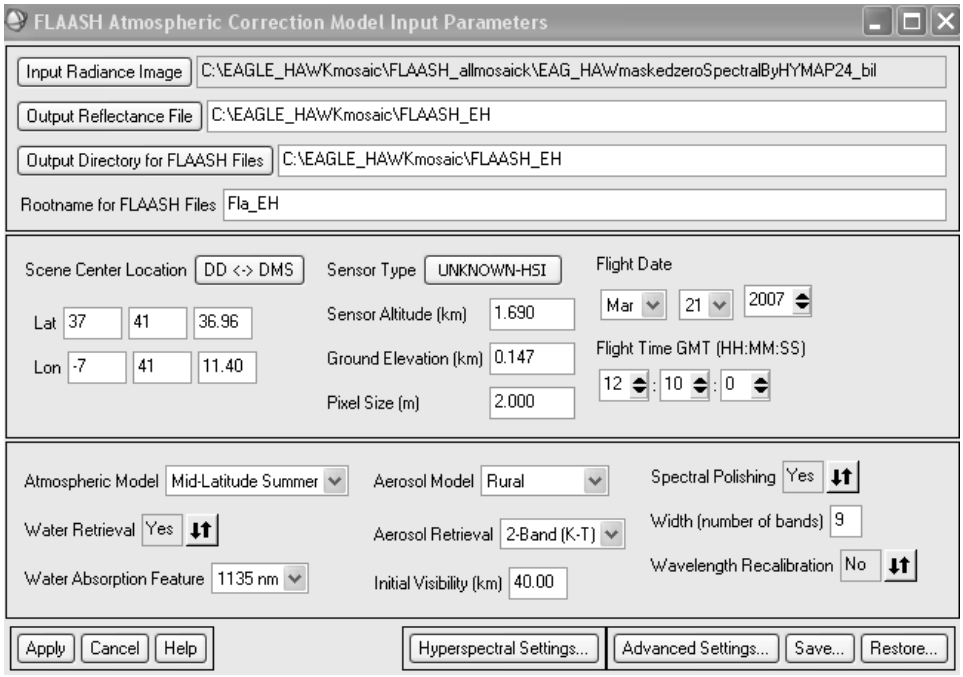

Figure 4.16 FLAASH used parameters for the S. Domingos mosaic of SPECIM EAGLE-HAWK. Advanced settings similar to Figure 4.6.

Table 4. 4 Wheather conditions at the time of the flight (year 2007). Courtesy of BEJA AIRPORT BASE.

21-March 2007 Local time	Pressure QFF (HPa)	Air temperature (°C)	Relative Humidity (%)	Wind Direction°, mean speed, Gust (kmh^{-1})	Nebulosity (x/8)	Visibility (km)
10:00 AM	1017.4	08.6	53	010, 24, 43	0	40
11:00 AM	1017.3	10.6	48	360, 26,46	1	40
12:00 AM	1017.1	11.6	44	360, 28, 46	1	40
01:00 PM	1016.7	12.2	41	360, 26, 48	1	40
02:00 PM	1016.3	13.0	41	360, 30, 48	1	40

Using the three wavelength segments the overall result of EFFORT application increased the values around 500 nm as well as on wavelengths after 2223 nm with a broad absorption feature centred at 2356 nm. A few absorption features appear between 437 and 700 nm after the EFFORT application, detailed in the following Section.

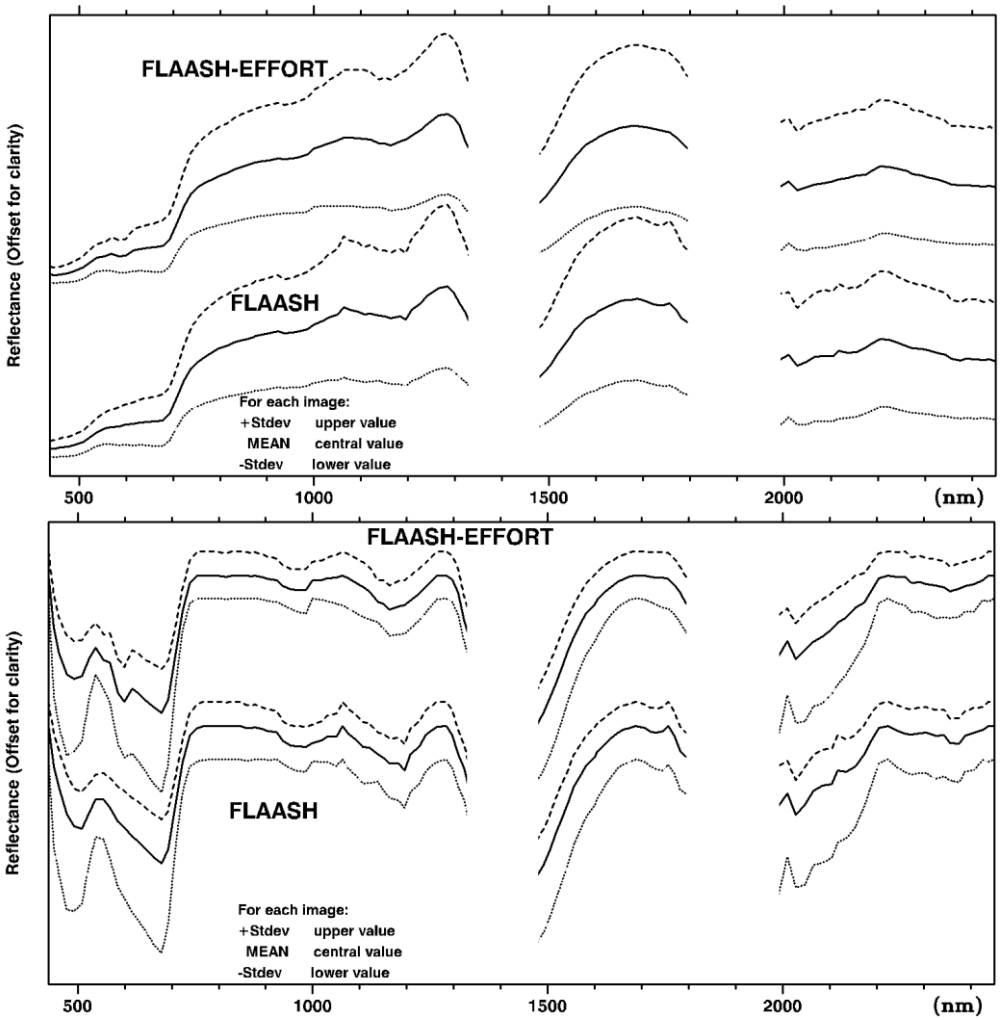

Figure 4.17 Average statistics for reflectance of SPECIM EAGLE-HAWK resultant from FLAASH software and also with EFFORT Polishing. Upper-normal display, lower-continuum removal.

4.5 2000 AND 2007 IMAGES COMPARISON

The overal average reflectance of mosaics of year 2000 in August and year 2007 in March depicts some significant changes, being the most evident related to seasonal vegetation (Figure 4.18). This is associated with the "red edge" feature of vegetation, sharply defined in the 2007 mosaic image.

The study of position and shifts of the red edge inflection point allows determination of variations of plant health levels and seasonal patterns among other type of information such as biomass, chlorophyl content and hydric status (Curran et al., 1990; Pu et al., 2003). The spectroscopic study of vegetation is beyond the scope of this thesis, although it constitutes a subject of interest for indirect determination of contamination related to mining environments as demonstrated by previous studies (Kuosmanen et al., 2002; Middleton et al., 2003). This is particularly relevant when there is no soil exposure, which is not the case of S. Domingos test site allowing waste or mineral mapping directly.

Other significant changes report to the flattened average spectral response from year 2000 compared with absorptions features clearly defined on SPECIM EAGLE-HAWK of year 2007, i.e. at 492, 599, 678, 985, 1138, 1163, 1990 and 2028 nm. Generally in the segment 1433-1805 nm there is a shift of the broader shape to the

higher wavelengths of 2007 average values data, while in the segment 2028-2450 nm the reflectance values increase from 2000 to 2007 dataset.

Concerning year 2000, with much more flattened average spectral features, absorption features appear at 461 nm, a very sligth at 872 nm as well as broad depression at 2028 nm.

The variations in spectral signatures throughout these years may also be established in a bigger scale if known supposedly unchangeable or more or less stable targets in terms of spectral behaviour are compared. In fact, research by Anderson and Milton (2006), indicate that even supposedly homogeneous artificial calibration targets, such as concrete and tarmac may not have a non-variant reflectance over time, through ageing and effects of atmospheric conditions. The variant conditions report essentially to seasonal biological growth over targets or humidity, but also to capture conditions such as different viewing angle and illumination geometry.

These conclusions can eventually be extended to other type of artificial targets such as cement tile floor, in Figure 4.13, corresponding to the red target (Figure 4.19). This target was lost to the HAWK sensor due to different Field Of View (FOV) of both sensors and windy conditions, as detailed in Chapter 3 in Section 3.6.

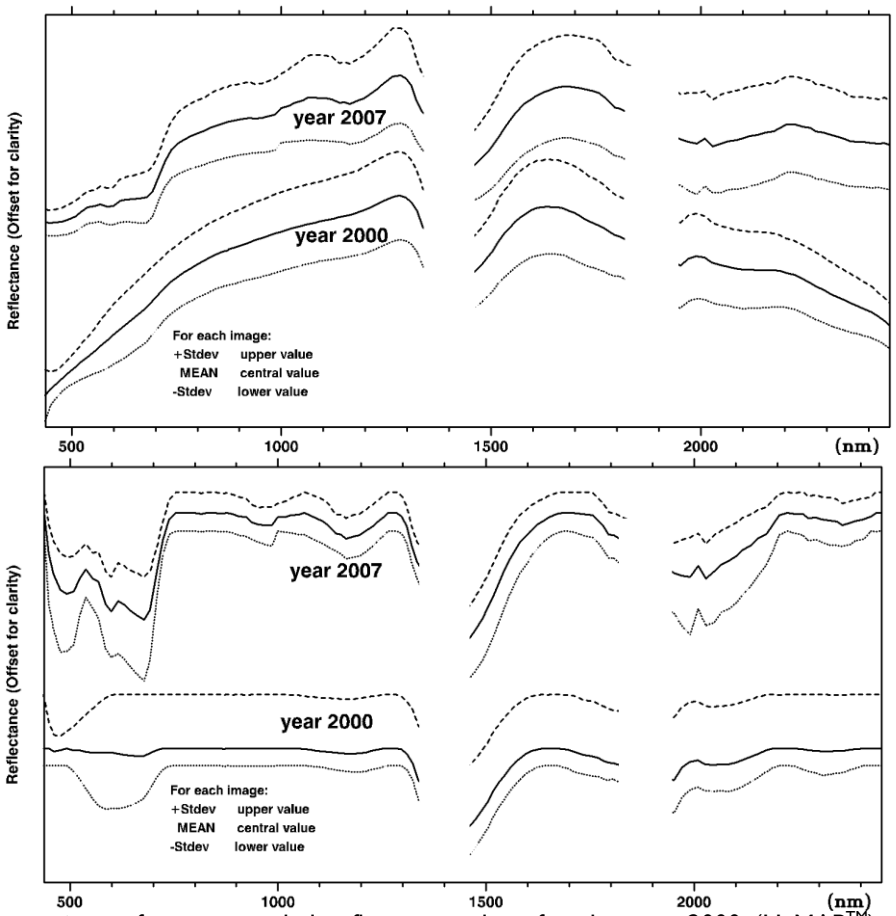

Figure 4.18 Comparison of average scaled reflectance values for the year 2000 (HyMAP™) and year 2007 (SPECIM EAGLE-HAWK). Both corrected with FLAASH and EFFORT Polishing. Upper- normal display, lower- continuum removal.

The reference targets are depicted in Figure 4.19. The purple square encompasses the red target, the playing field measurements of Figure 3.13 (Chapter 3), whereas the blue target was selected for intercomparison of 2000 and 2007 images without field measurements. The cyan rectangle depitcs the dark target of Figure 3.13 (Chapter 3) and seen as orange rectangle, where ASDField SpecPro measurements were undertaken.

The display of different spectra is according to the data available. In the case of the red target, is depicted part of the ASD field spectra measured in the available area and equivalent section of FLAASH-EFFORT correction from years 2000 and 2007. The pattern of these spectra are generically similar, although a broad depression in the EAGLE data delimited at 585-599 nm has no equivalent in either in HyMap™ 2000 nor in field spectra collected in 2007. The HyMap™ 2000 has higher reflectance values from 437 that decreases to 462 nm.

The orange target, i.e. plastic of water reservoirs, has 25 measurements and compared with SPECIM EAGLE HAWK there are significant changes in the spectral response in the EAGLE sensor with a strong decrease in the values, higher similarity in the wavelength range 1400-1600 nm and minor absorption changes in the 1990-2500 nm. Its noticeable that field spectra has wider variability then SPECIM EAGLE-HAWK. However, field spectra reports to very low reflectance values (Chapter 3, Figure 3.13).

The blue target for multitemporal image comparison has higher radiance values for HyMap™ 2000 than SPECIM EAGLE-HAWK, decreasing the difference to the highest wavelength range, whereas the scaled reflectance values in SPECIM EAGLE-HAWK increase, being more evidenced in the segment 1990-2500 nm and also with higher dispersion. An absorption feature at 1637nm is very clear in the 2007 image, possibly related to the CO_2.

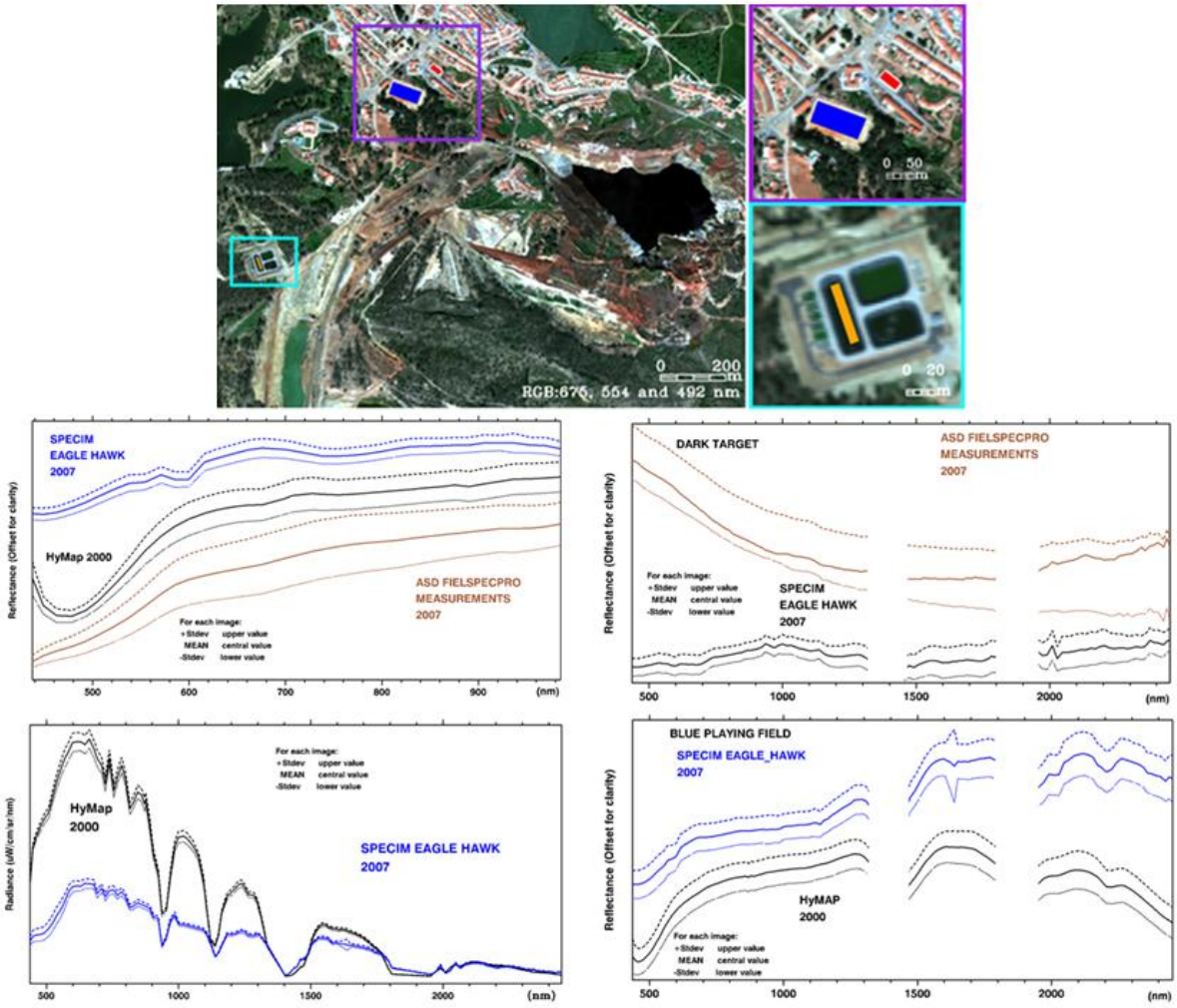

Figure 4.19 Targets for spectral comparison of reflectance of SPECIM EAGLE-HAWK with field measurements (brown spectra) (Chapter 3, Figure 3.13): red and orange. Target for inter images spectral comparison of 2000 and 2007 IS data: blue.

The difference in radiance values, higher in the VNIR in the HyMap™ can eventually be explained by different conditions of the soil. In this case, seasonal variations were expected due to different water content of the soil in the two datasets due to S. Domingos climate, with a dry and wet period (Chapter 3, Section 3.1) covered by the two IS datasets.

A more detailed aspect can be seen comparing some of the targets of the Figure 4.14, i.e. when they exist in the 2007 image, as depicted in Figure 4.20. In these targets the SPECIM EAGLE-HAWK presents the same pattern as already mentioned in the blue target of Figure 4.19. The reflectance values present equal or have higher variability to the targets but the Pomarão soil target (sienna). The highest variability is related to the yellow target corresponding to the metallurgical slag hills. These two targets have been artificially modified as detailed in Chapter 5, Section 5.3.

The general conclusion in the average comparison of global multitemporal data that there is an increase of reflectance values after 2028 nm is also reflected in the common targets of both datasets.

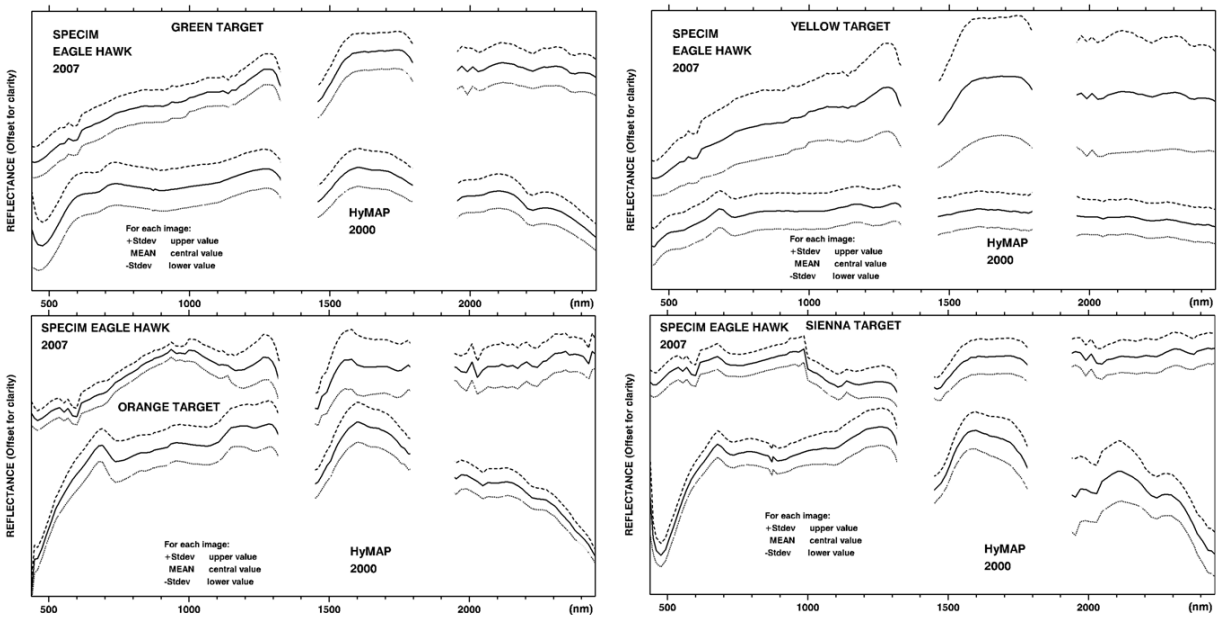

Figure 4.20 Spectral average values and standard deviation of similar targets by area of Figure 4.14. Upper spectra are from 2007 whilst lower are from 2000 IS data.

The differences reported in the average comparative values of the targets have to be taken into account. Despite the fact that they are from the same area, the spatial resolution is different from HyMap™(4.1 m) to SPECIM (2.0 m) or to ASDFieldSpecPro (20 cm).

This example shows that the multi-temporal analysis cannot be considered absolute with the available data set, and is at most qualitative. Thus, the more correct approach for the comparison of the two data sets is to consider it as evolutionary trends.

4.6 CONCLUSIONS

The target and the sensor are separated through the atmosphere that interferes with the signal received. Several methods have been developed to remove the atmospheric effects I) statistical or empirical, II) radiative transfer modelling, and III) a combination of the two previous. In II, the theoretical atmosphere at the time of data capture is retrieved according to meteorological data on a pixel-by-pixel basis. Then, the radiative transfer

equation is calculated given the aerosol and column water vapour and transformation to reflectance. Optionally, the reflectance can have a post-processing spectral polishing.

The fact that the physical based model is included in most of the common IS software providing reasonable results and do not require visiting the specific site determines that is becoming more used rather than empirical-based methods (Ben-Dor et al., 2004). Additionally, the latter only approximate the highly variable processes in time and space in the atmosphere controlling the transfer of radiance to and from the Earth´s surface to the sensor (Van der Meer, 2001). Plus, the full potential of IS can only be exploited when using physical based approaches and develop new knowledge about a study area (Ben-Dor et al., 2004; Richter, 2010).

The two IS data sets collected in the S. Domingos, i.e. the HyMAP™ (year 2000) and SPECIM EAGLE-HAWK (year 2007), were atmospherically corrected with a radiative transfer modelling using FLAASH software (ATREM based model), comparing in the case of HyMAP™, two different types of software (HyCORR, a MODTRAN based model). A post atmospheric processing was done using an EFFORT Polishing in the segments 437-1323 nm, 1433-1805 nm and 1970-2485 nm (2451 in the case of SPECIM EAGLE-HAWK).

For both 2000 and 2007 IS datasets, the FLAASH was run with an atmospheric model of a mid-latitude summer, using an adjacency effect which takes into account the spatial component by integrating reflectance from neighbourhood pixels, and local atmospheric information. Post atmospheric corrections were conducted with an EFFORT Polishing, in which were tested in the case of the 2000 IS data the effect of using local field spectra, specifically, of mining waste and Acid Mine Drainage (AMD), or without field spectra, to model the reflectance data. The findings of this experiment permits to conclude that constraining the image modelling using spectral signatures of a specific target of interest limits the extraction of information, if the objective is to increase the knowledge about an area when a resource such as IS data is available. Thus, the mosaic to be used in the next steps of processing in Chapter 5 will be the one polished using solely the image data leaving the use of field spectra to a further advanced phase of image processing.

Comparing both average reflectance mosaics of year 2000, the overall shape of results is similar but presents some variability within some segments of the wavelength range. The FLAASH-EFFORT is smoother than HyCORR-EFFORT and in some cases excludes absorption features, as the case of "red edge" feature. A distinctive character is a broad shoulder with a peak at 1281 nm wavelength in FLAASH-EFFORT. Also, in the segment corresponding to 1462-1793 nm, is delineated a more pronounced curve. In the wavelength range 2.0-2.5 um, absorption features related to Al-OH bonds, CH_4, CO, CO_2 and N_2O present in atmospheric gases disappear or are smoother in FLAASH-EFFORT.

More detailed comparisons in local targets related to more or less stable or supposedly invariant targets or focused in mining wastes and Acid Mine Drainage (AMD) show generally the same pattern as in the global average reflectance values, with an exception to the metallurgical slag hills that present higher variation in FLAASH than in HyCORR. A few other variations highlight the effect of different atmospheric corrections in targets related with waste mining materials and related pollutants. This will be assessed at the IS methodology developed in Chapter 5. Part of this is probably related to the adjacency correction which is absent in the HyCORR modelling, and possibly the atmospheric model selected. However, the fact that some input parameters in the HyCORR software were not known complicates the interpretation of the different results obtained when modelling with distinct software. The same applies to the EFFORT Polishing.

The SPECIM EAGLE-HAWK images captured in the year 2007 (March) were spectrally resampled to the HyMAP™ wavelength range and mosaic before the application of the FLAASH software and afterwards with EFFORT-Polishing.

The comparison of average reflectance of both datasets, of years 2000 and 2007, depicts the main trends in terms of spectral patterns. There are some significant changes in the global average spectral pattern, part of this related to seasonal vegetation, evidenced by the "red edge" feature. Other significant changes report to the

flattened average spectral response from year 2000 compared with absorptions features clearly defined on SPECIM EAGLE-HAWK of year 2007, i.e. at 492, 599, 678, 985, 1138, 1163, 1990 and 2028 nm. Generally in the segment 1433-1805 nm there is a shift of the broader shape to the higher wavelengths of 2007 average values data, while in the segment 2028-2451 nm the reflectance values increase from 2000 to 2007 dataset.

In a more detailed scale comparing local targets either with field spectra gathered simultaneously with the sensor as well as with 2000 IS data, there are some differences in which are not completely clear the reasons.

In fact, there are many factors that are involved between the two dataset capture, despite the different characteristics of both sensors. This include, but are not limited to; the seasonality corresponding to the wet period of the S. Domingos area in 2007 comparing to the dry period in 2000 and consequent effects in vegetation patterns, and the different viewing angle and illumination geometry.

Thus, the multitemporal analysis cannot be considered absolute with the available data set, and is at most qualitative. The more correct approach for the comparison of the two data sets is to consider it as evolutionary trends.

5. IMAGE PROCESSING TECHNIQUES OF IMAGING SPECTROSCOPY DATA

5.0 INTRODUCTION

In this Chapter the image processing techniques for the Imaging Spectroscopy (IS) data of the S. Domingos area are described. Additionally, some insights of the algorithms driven approaches (advantages and disadvantages of the algorithms used) are examined and discussed.

The algorithms developed for the test site are presented in the form of an article submitted to a peer-reviewed scientific journal, where the proposed methodology is tested using a 2000 flightline dataset acquisition for the S. Domingos area encompassing the open pit. This methodology relies in a multi-source spectral data to identify the materials related with the Acid Mine Drainage (AMD), deriving a map expressed in terms of mineralogical assemblages of spectral high correlation.

The methodology is then extended to the all IS dataset captured in 2000, introducing a few improvements to the multi-source mineralogical assemblages of high correlation. Following the differences established in function of the type of atmospheric corrections undertaken in Chapter 4, the methodology is applied to HyMap^{TM} data set, testing two atmospheric radiative transfer modelling using different software's, i.e. FLAASH and HYCORR, both with an EFFORT correction. Environmental consequences are drawn from the comparison of results obtained.

The SPECIM EAGLE-HAWK IS data set captured in year 2007 is processed for the common areas captured in year 2000, whereas the same multi-source spectral data methodology is applied and others.

The trends of environmental evolution related to Acid Mine Drainage (AMD) of the S. Domingos area is drawn from the comparison of the two multi-temporal maps, highlighting the main focus of environmental concerns.

5.1 TYPES OF MAPPING ALGORITHMS

When choosing a classifier according to the objective of the IS data analysis there are two main types of approaches based on pixel i.e. a full or sub-pixel techniques (Chapter 2, Section 2.1.4).

Another useful concept related to strategies of information processing and knowledge ordering is if it is a top-down or a bottom-up model, as referred in Chapter 4 in Section 4.2. The former may also be considered as a synonym of analysis or decomposition, whereas essentially the system under analysis is broken down to gain insight into its subsystems. A bottom-up approach is essentially gathering together systems to give rise to grander systems.

When strictly applied to image classification both types of models have requirements detailed in Chapter 4, Section 4.2 concerning atmospheric corrections, each with different advantages.

Concretely, in the case of bottom-up approach an atmospheric correction is required due to the use of field or laboratory spectra, while in the case of a top-down approach the atmospheric effects are already incorporated when searching for similar features across the image. Focusing strictly into the advantages of IS classification a bottom-up approach allows that the same spectral library to be extended over wide areas and across multiple images to identify specific feature types (Aspinall et al., 2002). The same authors also consider that IS imagery can sometimes provide the unique opportunity to take advantage of the strong points of both top-down and bottom-up approaches, while avoiding some of their pitfalls.

Due to the complexity of IS data, with very high spectral resolution and many contiguous bands, a mapping method that can combine approaches and concepts will potentially improve the final result. The methodology developed in the next Section takes into account a full pixel approach and both a top-down and a bottom-up concept, by combining different IS datasets. Specifically, the sequence of algorithms for extraction of endmembers is based in a top-down approach, while the integration of high correlation spectra of distinct origin correspond to a point dimension of IS data to expand to a whole IS image related to a bottom-up approach.

5.2. THE MULTI-SOURCE SPECTRAL METHODOLOGY

Adjacent bands in IS data are very highly correlated and the correlation tends to be higher than the spatial correlation (Zhang and Desai 2000). Thus, when processing these types of data, is expected that the correlations should be higher when considering a point dimension, i.e. a lab spectral analysis data, instead of spatial dimension i.e. a pixel.

The establishment of a quantitative link highlighting the relationship among multi-source spectral data is also an important contribution for validation issues, which have incremental difficulties when compared with multispectral data, as shown in Chapter 2, Section 2.1.4. Thus, if properly correlated through mathematical matrixes, it's a way to eliminate uncertainties during image processing and guarantee that the results obtained are similar when derived from different sources.

Other basis for the development of this methodology is that it encompasses both a full pixel as well as a sub-pixel component (Chapter 2, Section 2.1.4) as expressed in terms of mineralogical assemblages with high correlation. The full pixel approach is considered when extracting endmembers from the image, as well when using similarity measures to map the IS data. Thus it might be advantageous to consider a full pixel approach instead of an unmixing one. However, a sub-pixel concept is underlying once the spectra of different sources are expressed in terms of combinations of mineralogical correlations.

In the next Section this multisource spectral methodology is presented in the form of an article submitted to a scientific journal.

IDENTIFICATION OF MATERIALS RELATED TO ACID MINE DRAINAGE USING HYMAPTM IMAGERY AT S. DOMINGOS MINE AREA, SE PORTUGAL[1]

[1] Authors: Lídia Quental[a]; António Jorge Sousa[b] Stuart Marsh[c] Maria Manuela Abreu[d]

[l]Laboratório Nacional de Energia e Geologia, Tecnologia e Inovação, [b]Instituto Superior Técnico, Universidade Técnica de Lisboa (TULisbon), [c]British Geological Survey [d]Instituto Superior de Agronomia, Universidade Técnica de Lisboa (TULisbon)

ABSTRACT

Imaging spectroscopy (IS) can identify target materials at both mineralogical and geochemical level. Therefore, in environmental applications it can be used to assess contamination derived from mining activities, expressed as contamination pathways related to Acid Mine Drainage (AMD). This can be based on specific assemblages of mineralogical spectral libraries, which can indicate pH values at the time of their generation and the subsequent acid generating potential, or field spectral measurements as input data for mapping algorithms. This study presents a methodological approach developed to improve the results for mapping contamination pathways, by combining multi-source spectra at different scales. Besides the mineralogical libraries and field spectra mentioned, additional endmembers that are extracted from IS data are used, so as to highlight particular site phenomena otherwise undetected by the two previous approaches. The highly correlated spectra are then input to the Spectral Angle Mapper algorithm, to establish a map of local field spectra and also one derived from endmembers. The intersection of the two maps results in an improved map, assigned in terms of correlation ≥0.8 of mineralogical assemblages focused on AMD indicators. This methodology was tested in the abandoned S. Domingos Mine, in SE Portugal, Iberian Pyrite Belt, with AMD caused by long-term exploitation of Volcanogenic Massive Sulphide deposits. Data from the HyMap™ sensor covered the area and spectroradiometric measurements were undertaken and analysed for mineralogical and geochemical content. A fligthline containing the open pit was processed according to the aforementioned methodology, focusing directly on the target of interest and minimising errors. The final map displays the mineralogical assemblage correlations ≥0.8 of variable pH indicators, particularly isolating a low pH combination.

KEY-WORDS: Imaging spectroscopy, multi-source spectra, Pearson correlation matrix, Acid Mine Drainage, mineralogical correlation map.

5.A INTRODUCTION

Imaging spectroscopy (IS) or hyperspectral imaging sensors, characterized by high spectral resolution across a wide range of the electromagnetic spectrum, along with dedicated algorithms, enable the identification of the chemical or mineralogical composition of the imaged target. Thus, wide fields of application can take advantage of IS properties. Focusing on environmental concerns such as contamination related to mining areas, several studies have provided valuable information on mineralogical assemblages with the purpose of assessing (Swayze et al., 1996; 2000; Dalton et al., 1998) and monitoring (Ong et al., 2003; Zabcic et al., 2005) areas affected by Acid Mine Drainage (AMD) and consequent release of hazardous elements. Rather than using mineralogical assemblages contained in standard mineralogical spectral libraries, which are processed in the identifiable spectral range of the minerals searched, another possibility is to directly map the contaminants using spectral field signatures across the Visible, Near Infra-Red (VNIR) and Short Wave Infrared (SWIR) range, properly correlated with chemical field data (Kemper and Sommer, 2003; Ben-Dor et al., 2009).

The project "Assessing and Monitoring the Environmental Impact of Mining Activities in Europe Using Advanced Earth Observation Techniques" (MINEO; FP5 contract IST-1999-10337) also added a contribution to the environmental assessment and monitoring of mining areas, covering a diversity of mining environments and respective types of contamination (Chévrel et al., 2003, 2004). Specifically concerning the AMD environment, contamination mapping based on IS has been achieved using spectral data either of waste mining field materials (Quental et al., 2002a; 2003) or from mineralogical standard spectral libraries as developed by Clark et al. (1993) (Borguignon et al., 2003; Quental et al., 2003), and focused on their acid generating potential (Swayze et al., 1996; 2000; Montero et al., 2005). Thus, hot spot targets were highlighted for remediation purposes, and consequently, to minimise their impact on the surrounding environment.

These studies all take advantage of the fact that the occurrence of certain minerals indicates specific ranges of pH values. Waste mining materials with high sulphide content are considered a primary source of AMD (Singer and Stumm, 1970; Nordstrom and Alpers, 1999; Espãna et al., 2005). When in contact with water and oxygen the sulphides react to oxidize and generate an acidic leachate which contains dissolved trace elements and

sulphate. This acidic leachate is partly neutralised by hydrolysis reactions with the surrounding materials as the solution flows away from the active oxidation points leading to the accumulation of iron sulphates, oxyhydroxides and oxides in a spatial and temporal sequence that represents the buffering of the acidic solution as it moves away from its source (Swayze et al., 2000; Montero et al., 2005). Using IS principles it is possible to identify the unique spectral absorption characteristics of secondary iron minerals (Clark, 1999). Further details on the basis for spectral interpretation and mineral identification are given in Montero et al. (2005) and Crowley et al. (2003). Thus, the mineralogical mapping of an area based on specific minerals can indicate pH values at the time of their generation and subsequently the acid generating potential, providing valuable information for the prioritization of remediation procedures.

Nevertheless, both types of spectral datasets, i.e. reference spectra from the field or standard libraries, may present some drawbacks according to the nature of the problem considered and specifically concerning contamination mapping. When using mineralogical standard libraries to classify IS data, the spectra are measured in the laboratory in pure samples, not taking into account the highly complex mixtures of minerals under evolution in the natural environment. In fact, this procedure is suitable when pure materials, contained in the library, are on the ground, but in most real-world situations, since materials are both spatially and intimately mixed, only the strongest features are matched. Even if a few sites in a scene are pure materials, many others are mixtures of materials (Plaza et al., 2004, 2009; Chang, 2007). These mixtures of materials within a pixel can complicate the analysis of IS information, often masking the diagnostic spectral features of materials of interest and hampering their identification (Zhang et al., 2005).

Although field spectroradiometric measurements depict the local reality of the target at a given time, if this is not properly matched with mineralogical and geochemical analysis the derived classification may lack significant information and not take full advantage of IS's capabilities. Moreover, the spatial view provided by IS data and extraction of information through adequate algorithms, i.e. relevant endmembers as the "purest" spectrum or just a constituent part of a spectral mixture (Boardmann, 1995; Adams and Gillespie, 2008) that occur in a scene, can give further information about local spectral signatures that is only occasionally detected by the other two types of spectra. In fact, taking into account the real-world situations where materials are spatially or intimately mixed, the most widely used technique analyzing IS data is to determine endmember spectra directly from the image (Plaza et al., 2004). The extraction of endmembers from an image has benefits over the use of spectra measured in the field or laboratory. Library and field spectra are rarely acquired under the same conditions as airborne or satellite data and they may not adequately represent all important endmembers. On the other hand, field and laboratory spectra are usually collected from surfaces one wants to map, and thus, they have direct physical meaning for mapping purposes. Imagery may provide similarly meaningful endmembers that can be considered "pure", or relatively "pure", spectra (Rogge et al., 2007). Additionally, when using endmember spectra, this already takes into account the spectral pattern modeled by the atmospheric corrections, thus, information in the similar spectral and spatial data to be mapped.

In order to maximise the spectral information to environmentally assess mining areas using IS data, a new, hybrid methodology is applied to further discriminate materials according to their AMD potential. It relies on the use of multi-source spectra and the establishment of a quantitative link through correlation with mineralogical standard libraries of USGS (Clark et al., 1993). This methodology highlights: i) local field spectroradiometric characteristics assigned to known mineralogical content and, ii) information provided by meaningful hyperspectral image derived endmembers. The methodology is tested on the open pit area of the S. Domingos Mine located in the Iberian Pyrite Belt.

5.B METHODOLOGY

The methodological approach exploits the Pearson correlation coefficients among three types of spectral data with distinct origins: i) mineralogical standard library; ii) local field spectroradiometric measurements; and iii) endmembers derived from high spectral resolution images. This serves as a means to select spectra for contamination mapping of the IS data (Figure 5.A1).

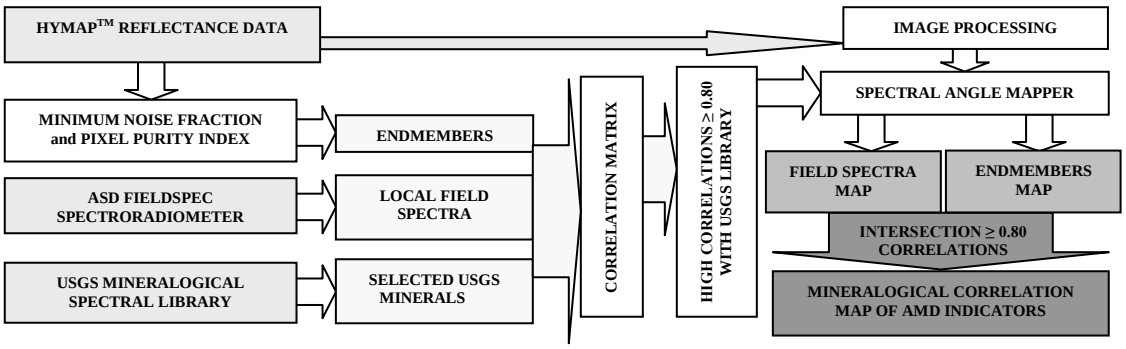

Figure 5.A 1 Methodological approach.

For i) the minerals selected according to their characteristics related to AMD are taken from the USGS mineralogical spectral library as developed by Clark et al. (1993) and implemented in ENVI 4.8 software (ITT, 2010). These spectra were measured on a custom-modified, computer-controlled Beckman spectrometer at the USGS Denver Spectroscopy Lab. Wavelength accuracy is in the order of 0.5 nm in the near-IR and 0.2 nm in the visible.

For ii) field spectra collected in the study area with a spectrometer contribute ground reference information. In this case the ASD FieldSpecPro spectrometer was used with spectral sampling varying from 1.4 nm to 2 nm and spectral resolution from 3 nm to 12 nm with wavelength accuracy of 1 nm.

For iii), among the different types of algorithms to extract endmembers from images , a sequence of a Minimum Noise Fraction (MNF) transform (Boardman et al., 1994) as modified from Green et al. (1988), Pixel Purity Index (PPI) (Boardman et al., 1995) and n-D visualiser were selected. These algorithms were implemented in ENVI software (ITT, 2010) and follow a protocol designated as Automated Spectral Hourglass, where the prediction of endmembers can be done in an automatic manner.

From the endmember spectra obtained, those not related to the mapping target, i.e. the AMD, are excluded, which encompasses vegetation patterns or errors in the image. Jointly with field spectra and the mineral spectral library, they are correlated through the Pearson correlation matrix according to the same wavelength values. In this case the ANDAD software (Sousa and Sousa, 2000) was used to do this. Establishing the correlation among these multi-source spectral data, i.e. i), ii) and iii), two features are highlighted, a) potentially relevant endmembers provided by a spatial spectral view, based on the IS images and, b) the relationship of field spectra of a specific area and their acid generating potential, based on mineralogical assemblages.

In order to improve the next steps of classification, only the spectra with the highest values, i.e. ≥0.80 assigned to USGS mineralogical spectral library and focused on AMD indicators are selected for the spatial mapping of IS image using the Spectral Angle Mapper (SAM) algorithm (Kruse et al., 1993). The SAM is an algorithm which is a physically-based spectral classification that uses an n-dimensional angle to match pixel spectra to reference spectra. The algorithm determines the spectral similarity between two spectra by calculating the angle between the spectra, treating them as vectors in a space with dimensionality equal to the number of bands. In this case, the angle between IS image and multi-source spectra are compared.

Two maps result from SAM, one from field spectral data and the other from endmembers, both being expressed in terms of correlations with the USGS mineralogical spectral library (Clark et al., 1993). Thus, each pixel of both maps is assigned to the minerals with correlation values ≥0.80, i.e. they are converted to the mineral correlation values established.

Performance is improved by eliminating pixels mapped only for one type of input spectra, so that the final map is the intersection of the two previous maps. For each input map, respectively derived from field spectra and from endmembers, the pixels containing the same assigned minerals are merged above the correlation threshold ≥0.80 and then intersected. This intersection is executed by combining pixels with identical mineral

assemblages above the threshold correlation value mentioned. In this way, the dispersion pattern of the most relevant minerals for the area, in particular the ones which indicate a low pH value and thus environmental hot spot targets, are highlighted.

5.C TEST SITE AND DATA SETS

5.C.1 Characteristics of the test site: S. Domingos Mine area

The now abandoned S. Domingos Mine (SD) is located within the Iberian Pyrite Belt, known worldwide as the Metallogenic Province for Volcanogenic Massive Sulphides (VMS) deposits within the Iberian Peninsula. The former mine, in southeastern Portugal close to the border with Spain, is approximately sixty kilometers SE of Beja. The mining activity started in pre-Roman and Roman times with the exploitation of Ag, Au and Cu in the gossan and afterwards in modern times, in the middle XIX century for Cu and S, secondarily for Au, Pb and Zn both in the gossan and VMS. Mining ceased in 1966 due to the exhaustion of the ore and production has been estimated at more than 25Mt (Carvalho, 1979), while waste mining materials are estimated to be in the range of several million tons.

Compatible with the volume of the ore extracted and processed, the AMD was intensive with effects that endure until today. The development of several mining infrastructures for exploitation, processing and transportation of the ore, including sulphur plants, facilitated the dispersion of mine waste materials and related pollutants, visible within an area of 50 km^2 (Quental et al., 2002a;b) (Figure 5.A.2).

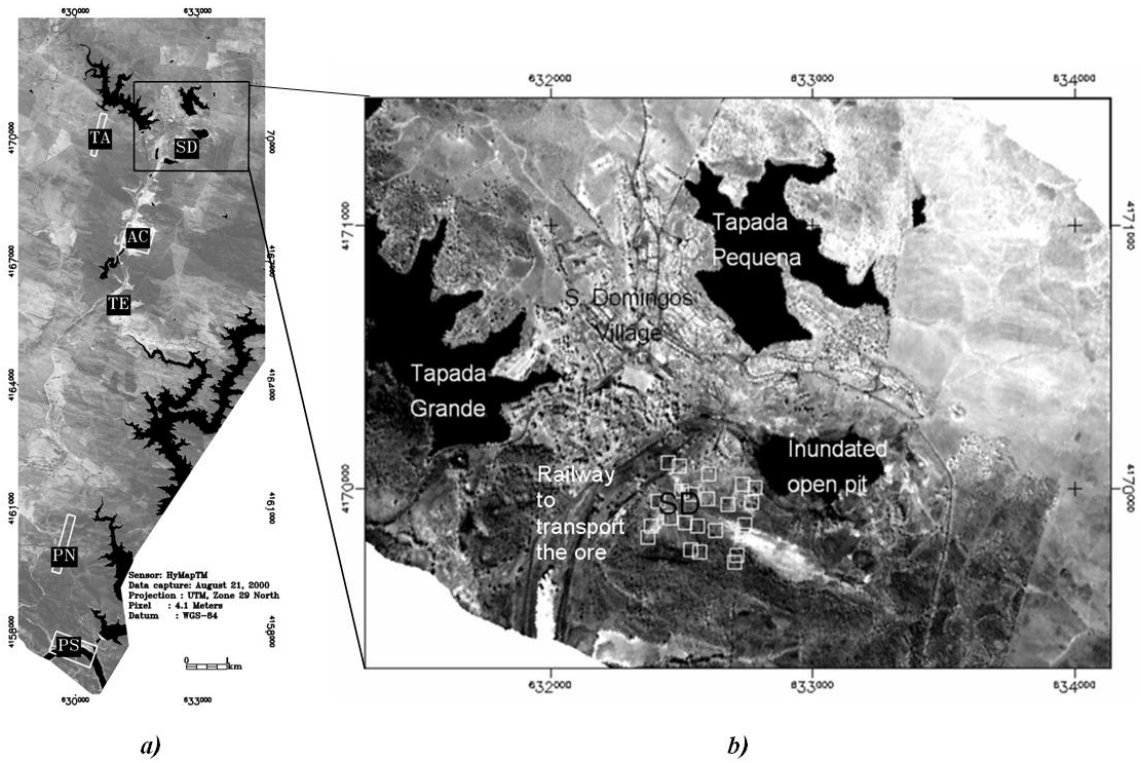

Figure 5.A.2. a) General view of the area related to mining activities and main subareas for data collection overlayed on geocoded and mosaiced fligthlines of the HyMap^{TM} sensor, b) fligthline of detailed study area with subset area and soil and spectra samples location (white squares, SD-S. Domingos).

No remediation measures have been applied to the area, allowing for a complex geochemical evolution under semiarid conditions. According to the Thornthwaite classification, the climate of the region is semiarid mesothermic, with no excess water and small thermal efficiency in the hot season, and it can be divided in two

distinct seasons, a wet period from November to March and a dry period from May to September. The annual average air temperature is 17.6 °C, and annual precipitation is 559 mm (Abreu et al., 2008).

5.C.2 Airborne hyperspectral data from HyMap™

The HyMap™ sensor owned by Hyvista Corporation (HVC), covers the spectral range 450 to-2500 nm, with a spectral bandwidth varying between 10-20 nm and with a signal to noise ratio better than 500/1 (Cocks et al.,1998). HVC used a Dornier 228 aircraft operated by the Deutsches Zentrum für Luft und Raumfahrt (DLR) to acquire HyMap data over the S. Domingos mining area on 21 of August 2000. The ground instantaneous field of view (GIFOV) for these data is 4.3 m. The dataset was provided as radiance by HVC, and also calibrated to reflectance using HyCorr software, which is a modified version of the ATmospheric REMoval (ATREM) (Gao et al., 1999) software with an Empirical Flat Field Optimal Reflectance Transformation™ (EFFORT) Polishing implemented in the ENVI software. The EFFORT as described by Goetz (1997) and Boardman (1998) is an analytical process that bootstraps a linear adjustment to apparent reflectance spectra to improve the accuracy of spectra following calibration with ATREM. This improves the comparison with library-based spectra, the basis of many of the image interpretation methods.

The fligthlines were geocoded in UTM, WGS84 datum using DGPS flight data. An overview of the area is given by the mosaiced fligthlines in Figure 5.A.2a, while the fligthline tested in this work encompasses the open pit is depicted in Figure 5.A.2b.

5.C.3 Field data

5.C.3.1 Spectroradiometric measurements

Field spectra were collected across the area with an ASD FieldSpec@Pro spectrometer, with wavelengths between 350-2500 nm. The collection was focused on selected targets depicted in Figure 5.A.2a) and named S. Domingos (SD), Tapada (TA); Achada do Gamo (AC); Telheiro (TE); Pomarão N (PN) and Pomarão S (PS). These subareas were selected inside of the main area of the airborne hyperspectral dataset capture, taking into account the diversity of geological features, mining aspects and environmental issues (Quental et al., 2002 a and b). Particular emphasis was given on supposedly contaminated targets, respectively SD, AC, TE and PS, while TA and PN are considered background areas. Based on the geochemical concentration of some of the targets, their field descriptions and spectral characteristics, 92 spectra were selected for this work.

5.C.3.2 *Soils and waste mining materials*

Soil and mine waste materials samples collected (Figure 5.A.2) for the contaminated subareas of SD presented high anomalies of several chemical elements such as As, Cu, Pb and S (Quental et. 2002a; b; Abreu et al., 2004). The other two contaminated subareas (AC and TE), presented high values mainly in As, Hg, Pb and Sb (Tavares et al., 2008; 2009).

X-Ray Diffraction analysis of the soil clay fraction (<2 μm) for the non-contaminated subareas of TA and PN (Figure 5.A.a) shows that the soils were mainly composed of mica, kaolinite, quartz, interstratified mica-vermiculite, berthierine, halloysite, hematite and vermiculite. In the contaminated subareas of SD, AC and TE soil clay fraction contained mica, kaolinite, hydroxy-interlayer Al/Fe vermiculite, quartz, goethite, hematite, and halloysite.

Jarosite, natrojarosite, anglesite and plumbogummite salts were identified in the materials of SD, TE and AC (contaminated subareas). Salt efflorescence, only recognised in AC and SD sub-areas, showed a mixture of complex hydrated sulphates of Pb, Cu, Zn, K, Al, As, Fe and Ca. A mixture of copiapite and rumerite has been recognised in AC. Alunite was also identified in SD.

Jarosite only occurred in soil samples with pH <4.2, whereas the hydroxy-interlayer Al/Fe vermiculite occurs in soil samples where pH lies between 3.5 and 6. This clay mineral does not occur in soils developed on dumps, which were not leached by acid waters (SD), even if the pH lies in the same range (Quental et al., 2002a).

5.D Results

5.D.1 Correlation matrix of spectral data

The ASD field spectra collected in the sub-areas were visually analysed, with the vegetation excluded. Selected minerals from the USGS spectral mineralogical library (Clark et al., 1993), taking into account global mineralogical field results for the area and AMD indicators, and extracted endmembers from Hymap™ also excluding vegetation and image errors, were correlated in ANDAD software (Sousa and Sousa, 2000) based on wavelength values. Excluding also noisy bands such as strong water vapour bands and a few others either from ASDFieldSpecPro or in Hymap™, the wavelength values used were the ranges 449-1337 nm, 1434-1782 nm and 1989-2470 nm corresponding to 118 bands.

Table 5.A.I presents the characteristics of the USGS spectral library minerals that have correlation ≥0.80 with the other two types of data, namely field spectral data and image endmembers (Table 5.A.II).

Examples in spectral space of the highest correlated minerals with low pH spectra are given in Figure 5.A.3.

Table 5.A.I Minerals from the USGS spectral library (Clark et al., 1993) presenting high correlations and with Correlation Matrix Name (CMN) adopted.

USGS Spectral library filename		CMN	USGS Spectral library filename		CMN
a-alunit	Ammonioalunite NMNH145596	aA	jarosit3	Jarosite GDS100 Na-Sy 90C	J3
a-jarosi	Ammonio-jarosite SCR-NHJ	aJ	jarosit4	Jarosite GDS101 Na-Sy 200	J4
a-smecti	Ammonio-Smectite GDS86	aS	jarosit5	Jarosite GDS24 Na	J5
alunite1	Alunite GDS84 Na03	A1	jarosit6	Jarosite JR2501 K	J6
alunite2	Alunite GDS83 Na63	A2	jarosit7	Jarosite NMNH95074-1 Na	J7
alunite3	Alunite GDS82 Na82	A3	jarosit8	Jarosite WS368 Pb	J8
alunite4	Alunite AL706 Na	A4	jarosit9	Jarosite SJ-1 H3O - 10-20%	J9
alunite5	Alunite HS295.3B	A5	kaolini1	Kaolinite CM9	K
Copiapit	Copiapite GDS21	Co	kaolini2	Kaolinite KGa-1 (wxyl)	K2
chlorit4	Chlorite SMR-13.c 45-60um	C4	kaolini3	Kaolinite KGa-2 (pxyl)	K3
chlorit5	Chlorite SMR-13.d 30-45um	C5	kaolini4	Kaolinite KL502 (pxyl)	K4
chlorit6	Chlorite SMR-13.e <30um	C6	kaolini5	Kaolinite GDS11 <63um	K5
Ferrihyd	Ferrihydrite GDS75	F	kaolini6	Kaolinite CM3	K6
goethit1	Goethite WS222	G1	kaolini7	Kaolinite CM5	K7
goethit2	Goethite HS36.3	G2	kaolini8	Kaolinite CM7	K8
goethit3	Goethite WS219	G3	illite1	Illite GDS4	I1
goethit4	Goethite WS220	G4	illite2	Illite IMt-1.a	I2
Hematit1	Hematite 2%+98%Qtz GDS76	H1	illite3	Illite IMt-1.b <2um	I3
Hematit2	Hematite GDS27	H2	illite4	Illite IL101 (2M2)	I4
Hematit3	Hematite GDS69.a 150-250u	H3	illite5	Illite IL105 (1Md)	I5
Hematit4	Hematite GDS69.b 104-150u	H4	Lepidocr	Lepidocrosite GDS80 (Sy)	L
Hematit5	Hematite GDS69.c 60-104um	H5	pyrite1	Pyrite HS35.3	Py1
Hematit6	Hematite GDS69.d 30-45um	H6	pyrite2	Pyrite S142-1	Py2
Hematit7	Hematite GDS69.e 20-30um	H7	pyrite3	Pyrite S26-8	Py3
Hematit8	Hematite GDS69.f 10-20um	H8	pyrite4	Pyrite S29-4	Py4
Hematit9	Hematite GDS69.g <10um	H9	pyrite5	Pyrite S30	Py5
Hematite	Hematite HS45.3	Ha	quartz2	GDS31 0-74um fr	Q2
Hematitb	Hematite WS161	Hb	quartz3	Quartz HS32.4B	Q3
Hematitc	Hematite FE2602	Hc	quartz4	Quartz GDS74 Sand Ottawa	Q4
Jarosit1	Jarosite GDS99 K-y 200C	J1	Sulfur	Sulfur GDS94	S
Jarosit2	Jarosite GDS98 K-Sy 90C	J2			

Table 5.A.II Minerals Correlation coefficients of field spectra (subareas of Figure 5.A.2. a) and endmembers expressed in USGS spectral library minerals following CMN nomenclature of Table 5.A.I.

FIELD SPECTRA	**≥0.90**	**0.80≤N<0.90**
TE-73	J(3,8)	J(2,4,5,6,7,9),Q(3,4), G(3,4),H1,L
TE-90	L,G3,J(2,3,6,7,8,9)	G(1,4),I(1,5).J(1,4,5),F,H1
TE-92	J(2,3,6,8,9)L	G(1,3,4),J(1,4,5,7),I1,F,H1
PN-103	G(1,3,4),I5,J8,H(1,2),Q4,L,F	J(3,4,5,6,7),H(a,b,c,8,9),Q(2,3),I1,C(5,6),Py2
PN-103-6	G(1,3,4),H(1,2)J8	F,J(3,5,6,7),I1,Q(2,3),H(a,b,c,9),C6
PS-137	L,G(1,3,4,H(1,2),Q4,J(6,7,8),I5	F,J(2,3,4,5,9),Q(2,3),I1,H(a,b,c,9),C6,Py2
PS-138	J(2,3,9)	aJ,J(1,6)
PS-149	Co,A3	A(1,2,4,5,6)aA,aI,aS,I4,K(3,4)
PS-151	Co,A3	A(a,1,2,4,5,6),aI aS,I4,K(3,4,6)
PS-152	A(1,3,5,),Co,aI	I4,A(a,2,4,6),S,K(1,2,3,4,5,6,7)
PS-154	A(1,3,5),Co,aI	I4,A(a,2,4,6),S,K(1,2,3,4,5,6,7)
PS-155	A(1,3,5),Co,Ai	A(a,2,4,6),I4,aS,K(1,2,3,4,5,6,7)
PS-157	J(2,3,9)	J(a,1,4,6,5,7,8),L,G3
PS-158	J(2,3,4,6,8)	J(1,5,7,9),L,H1,G(1,3,4),I1,Q4
PS-163	L	J(2,3,4,5,6,7,8,9)G(1,3,4),H(1,2),I1,F,Q4
PN-175	F,G(1,3,4),I(1,5),J(6,7,8),L	C(4,5,6),H(1,2),J(2,3,4,5),Py2,Q(2,3,4)
PN-176	F,G(1,3,4),H(1,2),I5,J8,L,Q(3,4)	C6,H(a,b,c,8,9),I1,J(6,7),Py2,Q2
AC-203		A(a,1,3),aS,Co,I, K(2,3,6,7)
SD-210	F,G(1,3,4),H(b,c,1,2,9),I5,J8,L,Py2,Q4	C6,H(a,3,4,6,7,8),J(3,4,5,6,7),Q(2,3),Py5
SD-212	F,G(1,3,4),H(1,2),I5,J8,L,Q4	C6,H(a,b,c,8,9),I1, J(2,3,4,5,6,7,9), Py2,Q(2,3)
SD-225		Co,A(a,1,3)
SD-246	F,G(1,3,4),H(1,2),I5,J(6,7,8),L	C6,H(b,c,3,8,9),I1, J(2,3,4,5,9),Py2, Q(2,3,4)
SD-248	F,G(1,3,4),G(3,4),H(c,1,2),I5,J(7,8),L,Q4	C6,H(b,3,7,8,9),I1, J(2,3,4,5,6,9),Py2, Q(2,3)
ENDMEMBERS	**>=0.90**	**0.80=<N<0.90**
# A		aS,Co,aA,A3
# B		J(2,3,9),I1
# C	A(1,3),Co	A(a,2,4,5,6),aI,as,I4,K(3,4,6,7)
# D		J(2,9)
# E	A(1,3,5,6)Co, aI	A(a,2,4),aS,I4, K(1,2,3,4,5,6,7)
# F		aJ,J(2,3,9),Q1
# G		F,G(3,4),H1,I1,J(2,3,6,7,8,9),L,Q4
# H		J(2,3,9), Aj

It is clear that relevant spectra related to AMD may present a relatively flat pattern and not sharp absorption features that can be easily identified. The minerals spectra themselves are rather flat, as well as the signatures of most mixed materials either from image or from field spectra, which determined the use of the entire above mentioned wavelength range.

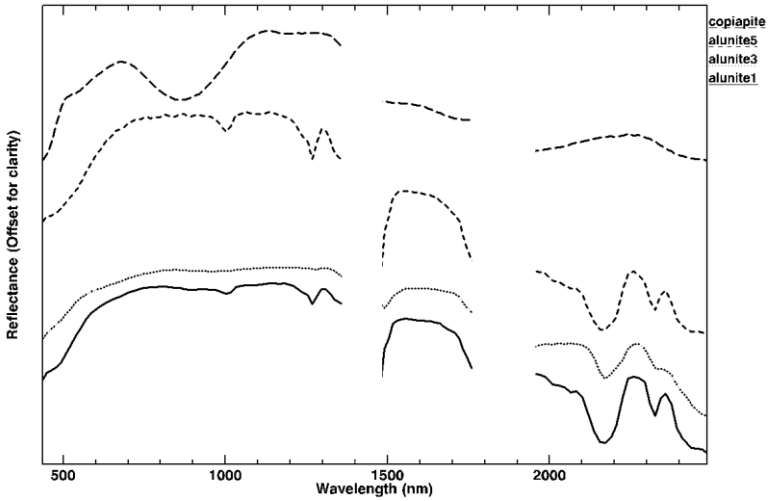

a) USGS spectral library (Clark et al., 1993).

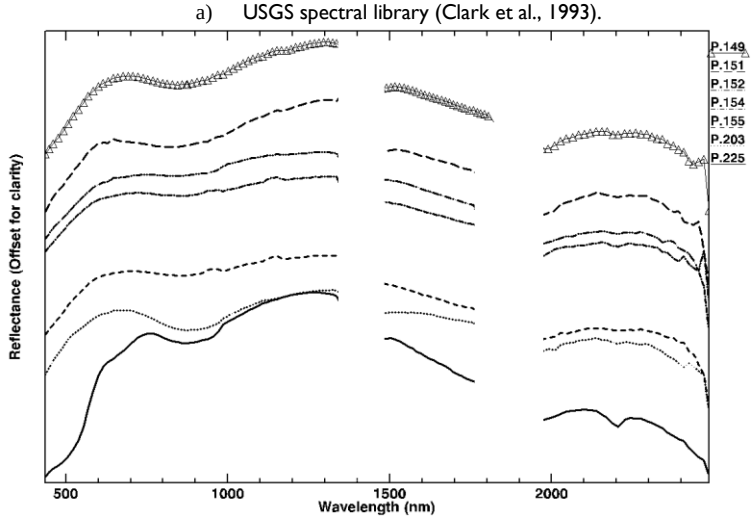

b) ASD FieldSpecPro.

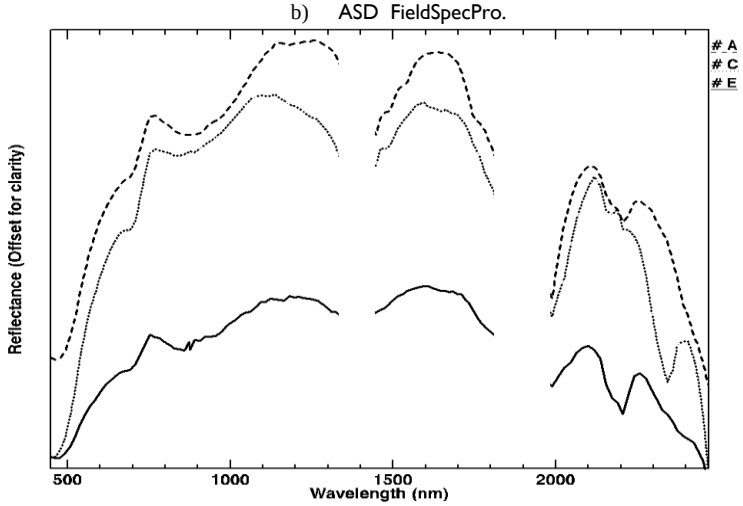

c) Endmembers.

Figure 5.A.3. Examples of low pH minerals spectra from laboratory measurements (a), the high correlated field spectra (b) and image derived endmembers (c).

5.D.2 Spectral Angle Mapper (SAM)

The SAM inputs the highly correlated spectra with USGS library expressed in Tables 5.A.I and 5.A.II, using a standard 0.1 radians angle [2].

This algorithm produces the two intermediate maps (Figure 5.A.1) of spatial distribution of spectra that each have high correlations with the USGS spectral library minerals (Table 5.A.II): in Figure 5.A.4 depicts the pattern of field spectra, while Figure 5.A.5 shows the pattern of the endmembers extracted from the HyMap™ image.

Further details are given in both about % of classified classes and also the statistical parameter coefficient[3] of variation (CV), in order to compare the homogeneity of the classes. The intersection of the two maps is done by assigning each pixel to classes according to the value of correlation of mineralogical assemblages, after Table 5.A.II. The final map is depicted in Figure 5.A.6. In this, each of the minerals discriminated in the subtypes in Table 5.A.II, e.g. J1 (jarosite 1) or J2 (jarosite 2) is summarised in just one type (jarosite). This is done to facilitate the comprehension of the spatial dispersion pattern of minerals over the area. For the intersection, only correlations ≥0.80 are considered and it is focused on minerals that are connected to the acid producing capabilities (red-yellow classes) or not (orange-brownish classes). The averages of the final classes are depicted in Figure 5.A.6. The minerals in brackets refer to non-acid generating minerals present in the correlation matrix in field and image endmember spectra. An exception to this is the quartz and illite in the jarosite class, due to the fact that it reports only to the image endmember class. This has been maintained, as neither of the two minerals are as clearly environmental indicators as the different iron secondary minerals.

Details of the three maps are given in Table 5.A.III, considering the area occupied and the CV.

Table 5.A.III Detail of input spectra, areas and correlation coefficients of the intermediate and final maps.

MAPS / CLASSES	ASD FIELD			ENDMEMBERS			MINERALOGICAL CORRELATION		
	Spectra (Table 5.A.II)	Area (m²)	CV	Spectra (Table 5.A.II)	Area (m²)	CV	Spectra	Area (m²)	CV
Copiapite -alunite (I,S,K)	P(149,151, 152,154,155, 203,225)	36,369.8	0,482	#(A,C,E)	219,439.3	0,301	Intersection of correlation minerals	2,237.3	0,399
Jarosite (I, qz)	P138	203,186.6	0,286	#(B,D, F, H)	1,742,848.9	0,231		21,855.2	0,379
				# G	355,858.5	0,243			
FGHIJL (qz)	P(90,92, 163)	731,242.5	0,196					202,742.9	0,219
SUM		970,798.9			2,318,146,70			226,835.40	

[2] Referred as the cosine in ENVI (ITT, 2010) and not the inverse as formally defined (Chang, 2007).

[3] Coefficient of variation (CV) = σ/aver, whereas σ = standard deviation and aver = average of data distribution.

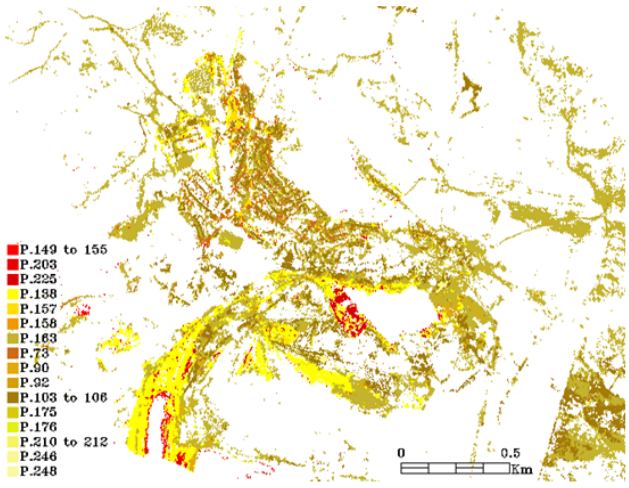

Field Spectra	%	CV	Field spectra	%	CV
Unclassified	79.348				
TE-73	0.809	0.244	PS-155	0.005	0.339
TE-90	0.381	0.189	PS-157	0.282	0.241
TE-92	0.129	0.222	PS-158	0.014	0.199
PN-103	0.040	0.162	PS-163	11.319	0.194
PN-103-6	1.700	0.173	PN-175	0.018	0.167
PS-137	1.926	0.233	PN-176	0.011	0.185
PS-138	3.286	0.286	AC-203	0.049	0.224
PS-149	0.016	0.151	SD-212	0.056	0.116
PS-151	0.002	0.238	SD-225	0.441	0.487
PS-152	0.019	0.548	SD-246	0.070	0.129
PS-154	0.057	0.596	SD-248	0.020	0.135

Figure 5.A.4 Spectral Angle Mapper algorithm of field spectra of Table 5.A.II, and details of % and coefficient of variation of each class. Red-yellow-brown colors show increase of pH values based on minerals associations.

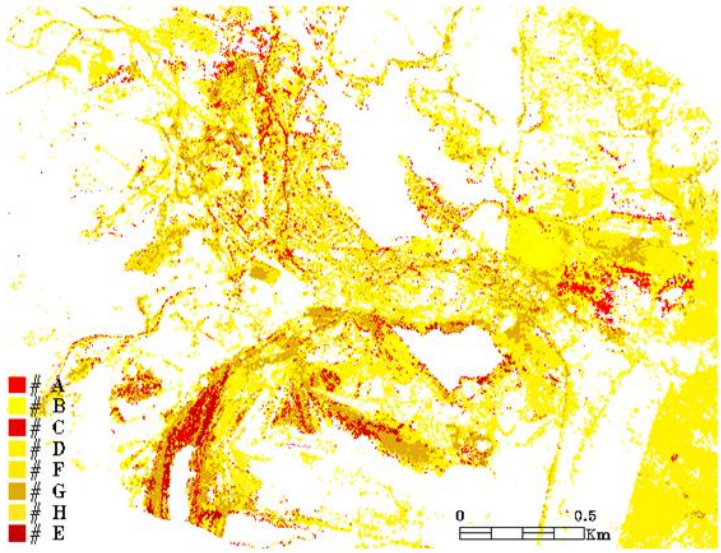

Endmember spectra	%	CV
Unclassified	62.499	-
# A	1.494	0.246
# B	8.231	0.251
# C	1.397	0.294
# D	16.094	0.179
# E	0.659	0.299
# F	3.154	0.232
# G	5.756	0.243
# H	0.716	0.404

Figure 5.A.5 Spectral Angle Mapper algorithm of endmembers extracted from the image. Legend key for minerals correlations in Table 5.A.II, and details of % and coefficient of variation of each class. Red-yellow-brown colours show increase of pH values based on mineral associations.

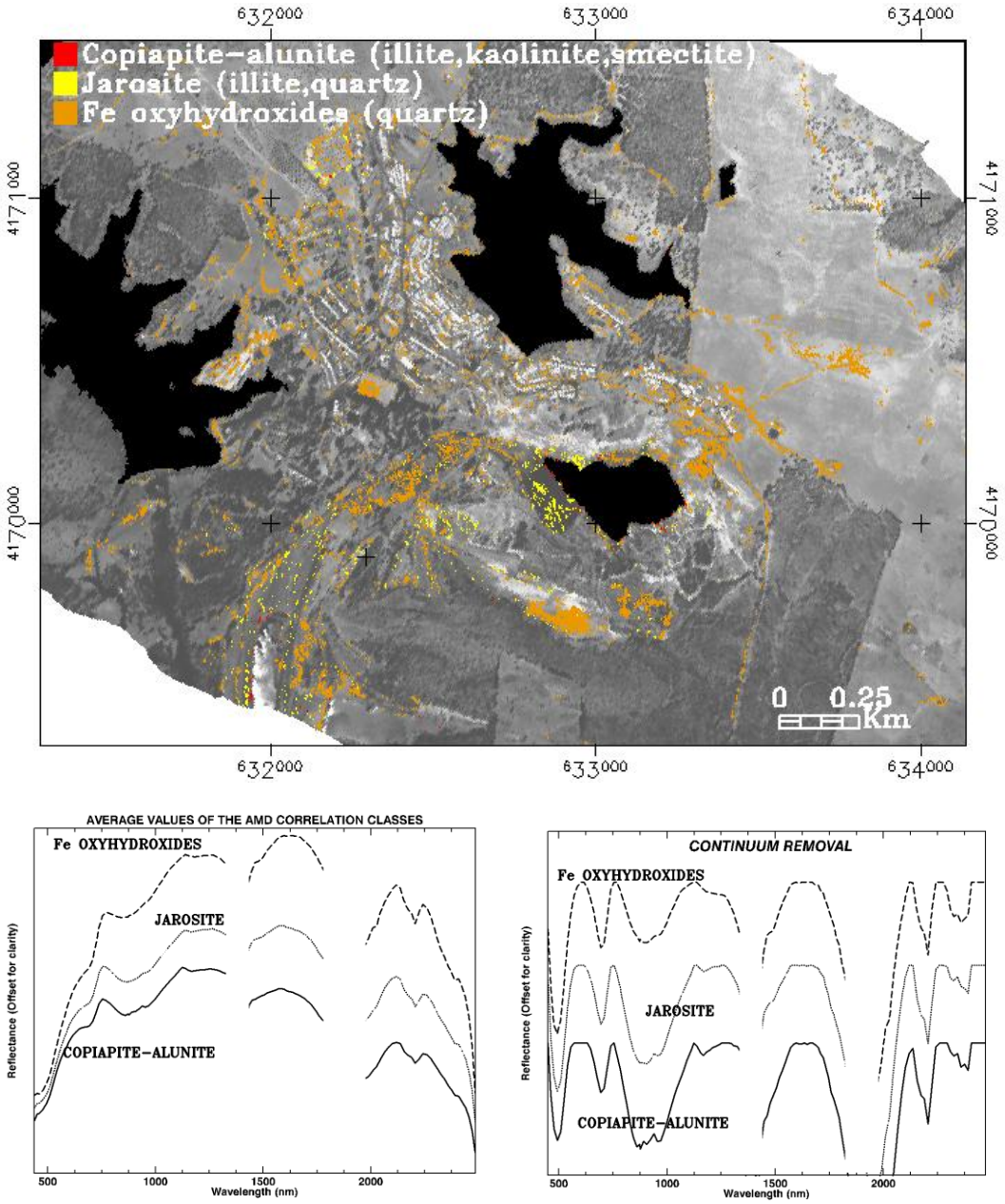

Figure 5.A.6 Mineralogical correlation (≥0.80) map of AMD with increasing pH from red through yellow to brown classes and average spectra (normal-left and continuum removal-right) of the classes obtained.

5.E Discussion

5.E.1 Correlation Matrix

Values from Table 5.A.II show that correlations ≥0.80 are achieved, according to what is expected from IS data characteristics, where the adjacent bands are very highly correlated and this correlation tends to be higher than the spatial correlation (Zhang and Desai, 2000).

Considering ASD field spectra measurements, from the 92 spectra selected 23 present high correlations with the USGS library. From the 96 image endmembers extracted from Hymap™, 20 spectra present also a very high correlation with the USGS library, but 10 of them are related solely to minerals not relevant for the objective of the work (e.g. quartz, and a-smectite) that do not indicate acid generating potential or buffering capacity. Two more were excluded due to the fact that copiapite and alunite were below 0.80 correlation values. Thus, only 8 spectra directly related to the acid generating potential remain for further processing.

It is also observed that the correlation of the USGS spectral library minerals with field spectral measurements indicate a much higher global correlation, namely ≥0.90, when compared with the global correlation of endmembers derived from the hyperspectral image, and also show a much greater variability of minerals. In contrast, only two correlations ≥0.90, can be detected on the correlation of the USGS spectral library minerals and image endmembers and the mineralogical diversity is much lower. This is thought to be explained by the large pixel dimensions, when compared to a much more localised point measurement of field spectra, and also by the effect of the atmospheric corrections undertaken in smoothing the signal with an EFFORT polishing (Section 5.C.2). It must also be stressed that the higher variability expressed in the X-Ray Diffraction results (Section 5.C.3.2) without equivalent available data on spectral libraries, implies a higher mineral complexity in the target analysed.

These mineralogical assemblages provide indications about pH values at the time of the minerals' formation. The accumulation of specific types of minerals is a function of the pH values and the chemical content of leachates. Copiapite [$Fe^{2+}Fe^{3+}4(SO_4)_6(OH)_2$•$20(H_2O)$] and jarosite [$KFe_3(SO_4)2(OH)_6$] form at pH values <3, and precipitate near sources of acidity that are also sources of iron and trace elements (Nordstrom and Alpers, 1999; Smith et al., 2006). However, jarosite may also precipitate at higher pH values of waters, i.e. 3.8 as referred in Bigham et al. (1996). Goethite [α-FeOOH] forms at pH values generally less than 6 from the dissolution of previous minerals, including early-formed goethite, and so precipitates farther from contaminant sources. Hematite [α-Fe_2O_3] accumulates even farther from the sources of acidity, after forming in a pH dependent process that may involve the dehydration and transformation of earlier precipitates, such as those of goethite and ferrihydrite (Montero et al., 2005). The latter usually occurs at pH 6.5 or higher (Bigham et al., 1996).

The mineralogical correlations obtained highlight the mineralogical assemblage of copiapite and types of alunite, whether with the presence of a-smectite, illite or kaolinite (Table 5.A.II), and the exclusion of any other iron secondary minerals, in particular of jarosite.

Although copiapite and jarosite appear as the minerals with the lowest pH values in the sulphide oxidation pathway (Nordstrom and Alpers, 1999; Smith et al., 2006), this split appears to confirm a higher pH precipitation value for jarosite, suggesting a threshold of pH values detectable in the spectral data. The correlation values (Table II) are only above ≥0.90 for the endmembers for this specific copiapite-alunite assemblage. This assemblage equates in the previously reported field spectra mapping (Quental et al., 2002a; 2003) to the class defined as mixed sulphur materials, corresponding to high acid producing material.

Using detailed information about the type of mineralogical spectral library allows further environmental knowledge of the minerals present to be extracted, e.g. type of goethites or jarosites. This can serve as environmental indicators, based on the mineral´s capabilities to sequester hazardous elements, as in the case of jarosite and lead. Once such elements are in the form of stable minerals it significantly reduces their spread in soils and rivers (Silva and Figueiredo, 2010). As an example, the correlation with USGS "Jarosite WS368 Pb" contains Pb. However, in this test fligthline, this was only verified at point spectra level, i.e. at field measurements and endmembers, but is not seen in the image scale final map.

5.E.2 HyMap™ mapping

Comparing the maps derived from field spectra (Figure 5.A.4) with the map derived from image endmembers (Figure 5.A.5), the spatial pattern is quite distinct. The field spectra map a smaller area than the endmembers,

even if the number of ASD spectra is higher (23) than the endmembers input spectra (8). Although both maps have a low coefficient of variation (CV<1), implying low variability data and probably absence of anomalous data, this value tends to be lower in most of the endmember classes. The variability already detected at a mineralogical level in the Pearson correlation matrix for field and endmember spectra is translated to the image mapping. While the field spectra map depicts as a major pattern several secondary iron mineral assemblages, implying a high but unclear pH value (FGHIJL class, Table 5.A.III), the endmembers maps show the major areas connected to environmental indicators such as jarosite. In fact, in the field map the mapped areas increase from low to higher pH classes, i.e. copiapite-alunite to jarosite and mixed secondary Fe minerals classes in the ASD field map, while in the endmembers map the major areas are covered by jarosite. The final AMD correlation map follows the same distribution pattern as the ASD field map except that, in the case of jarosite class, the CV is higher than from both input maps (CV=0.399), possibly due to a very small intersection area with wider variability.

The final AMD mineralogical correlation map shows the copiapite-alunite dispersion surrounding acidic water dams, i.e. the inundated open pit, following the railway path and the southern dams. A few other pixels from this class were detected west of the north end of Tapada Pequena, in connection with jarosite class, as well as in the border of the Tapada Grande and Tapada Pequena dams (Figure 5.A.2b). To the south of the open pit, waste piles also contain a few pixels of copiapite-alunite.

The jarosite (illite, quartz) class is concentrated in the waste materials of the open pit, to the west, and northwest in a more acidic area connected with the geological background materials. This class also depicts a more dispersed pattern in the village, where part of the ground is composed of waste materials, and also following the railway path. This shows that the dispersion of hazardous materials is not limited to the areas of exploitation but has been spread out by activities undertaken over long periods of time, including the use of these materials for construction purposes, as is the case for the Tapada Pequena and Tapada Grande water dams.

The occurrence of a large area, i.e. 21,855m^2 (Table 5.A.III), with only jarosite as a secondary iron mineral is very significant because it seems to extend the pH threshold to limits higher than 3.5, as previously suggested by Montero et al. (2005), if applied to this test site. This is supported by field data, where jarosite occurs in soil samples with pH values up to 4.2. Also, work by Hammerstrom et al. (2005) seems to imply a precipitation of jarosite not under very low pH waters, but driven instead by potassium availability.

From the spectral point of view, the average values do not display significant changes among the three types of classes (Figure 5.A.6), slightly improving when a continuum removal is applied. In fact, many of the minerals of the three classes have a broad spectral absorption feature associated with Fe^{2+} or Fe^{3+} (Crowley et al., 2003), so a continuum removal facilitates the comparison. From these, the copiapite-alunite class displays sharper absorption features, exclusively occurring at 859, 875, 902 and 953 nm wavelengths. These values differ from the copiapite (434, 547, 883, 914, 2205, 2295, 2400, 2440 nm) as well as from the alunites in USGS libraries of Clark et al. (1993).

The reasons for the absence or shifts in the absorption features may be primarily related to the fact that the classes obtained are mixtures, instead of pure materials as depicted in the USGS spectral libraries. The grain size may also contribute to this variation in spectral absorption features.

All three AMD correlation classes depict strong absorption features at 492, 692 and 2206 nm. Shared smaller features are present at 2326 and 2391 nm, while a small feature at 1168 nm is depicted for both copiapite-alunite and jarosite classes. The feature at 2358 nm is absent from the jarosite class.

The AMD correlation map indicates an increasing pH value at the time of their formation, from the copiapite-alunite to the iron oxy-hydroxides minerals classes.

5.E.3 Advantages of the method employed

Classical validation techniques may not be appropriate when applied to Imaging Spectroscopy, as the imagery is at times able to map the environment with greater accuracy than can be obtained by field crews or maps produced by various methods other than remote sensing (Jacquez et al., 2002; Aspinall et al., 2002; Foody, 2008). This is particularly relevant when the objective is mineralogical or chemical mapping, when ground reference data collection must deal with significant scaling from field ground reference points to pixel sized image samples and most often with mixed pixels. The multi-source methodology tested makes a contribution to resolving this issue by using different spectral data sources that are highly correlated. Each source contributes with a different component to the final mapping. The field spectral data provides validation by ground reference data, while the endmembers from the image provide a spatial view with contiguous spectral data and the USGS spectral library ties the results to known mineralogy. The extraction of endmembers, as detailed in Section 5.B, has benefits over the use of spectra measured in the field or laboratory.

The Pearson Correlation matrix using multi-source spectral data, i.e. image endmembers, field spectra and standard libraries has two major benefits: i) it provides mineralogical information to unknown spectra, and ii) it selects information from amongst a huge amount of spectral data, focusing on the subject of interest (in this case AMD) by using the most relevant mineral assemblages. Thus, the required input spectra for mapping are minimized and correspond only to highly correlated spectra.

In i), a lot of information is retrieved concerning the mineralogical content, which is coherent with field descriptions and with chemical analysis. Using detailed information about the type of mineralogical spectral library allows the extraction of further environmental knowledge of the minerals present, e.g. the type of goethites or jarosites.

The fact that two types of maps are produced, i.e. field spectra and endmembers, and the final map is expressed in terms of mineralogical assemblages' intersection', contributes also to a better result, as contributions to the final result have come from two types of mapping.

Finally, this methodology overcomes some of the difficulties encountered in previous studies, whereby image results are difficult to reconcile with field data, or have obscure mineralogical meaning, by minimising the gap among different spectral data, i.e., field (ASD FielsSpecPro), laboratory measurements (USGS standard libraries) and airborne images (HyMap^{TM}) data.

5.F Conclusions and final remarks

The methodology applied provides a simple way of taking advantage of multi-source spectral data, highlighting and focusing immediately on the target of interest, whether for environmental or for exploration purposes. The USGS mineralogical spectral library (Clark et al., 1993) provides the link depicting the mineralogical assemblages contained in field spectra and image endmembers. This allows a focusing directly on the target of interest, by selecting the high correlations of specific, relevant mineral assemblages. The quantitative correlation established to link these distinct spectral sources minimises the errors related to anomalous data. It is also a way of using ground reference data for improving the results of IS mapping, by creating two different types of maps, and using solely the identical classified pixels in both mapping outputs, i.e. image endmember and field spectra.

In this specific test site, by detailing the mineralogical spectral content of the data it has been possible to detect the exclusivity of an AMD signature based on mineralogical assemblages of copiapite with alunites, whether accompanied with a-smectite, illite or kaolinite, whereas jarosite was completely split into another class. This suggests that a significant pH threshold has been detected spectrally, extending the range of potential applications for IS data. In this specific test site, detailing the mineralogical spectral content of data has been possible to detect the exclusivity of an AMD signature based on mineralogical assemblages of copiapite with alunites, whether accompanied with a-smectite, illite or kaolinite, whereas jarosite was completely split into another class. This appears to suggest a pH threshold detected spectrally.

Acknowledgements

The data set was collected in the framework of the MINEO project in the 5th FP (IST-1999-10337) of EU. We are grateful to Dr. Hartmut Mollat from BGR, responsible for the field spectroradiometric measurements as well as for his suggestions, during data capture.

This work was partially funded through Foundation for Science and Technology of Portugal (Grant BD/17257/2004).

Published with the approval of the Executive Director, British Geological Survey.

5.2.1. HYMAP™ MOSAIC

To the Hymap™ mosaic gathered as described in Chapters 3 and 4, i.e. with two different atmospheric corrections HyCORR (undertaken by Hyvista Corporation) and FLAASH both with EFFORT Polishing, is applied the multi-source spectral methodology as contained in the previous Section. Further minor improvements were incorporated in the multisource spectral methodology, namely;

I. the use of USGS 2007 (Clark et al., 2007) spectral library, instead of the USGS 1993 (Clark et al., 1993) implemented in the ENVI software

II. introduction of two other secondary Fe minerals in USGS libraries (Table 5.A.I) related to AMD (Coquimbite -GDS22 W1R1Bc AREF- and Schwertmannite BZ93-1 W1R1Bb AREF), designated in the Correlation Matrix Name (CMN, Table 5.I, as Cq and Sc respectively)

III. changes in the wavelength range used due to the importance of some bands, i.e. introduction of 434 nm, but also for compatibility with SPECIM EAGLE-HAWK sensor (exclusion of 2470 and 2485 nm). The 118 bands are contained in these wavelength ranges: 434-1324 nm, 1448-1970 nm and 1989-2454 nm

IV. in order to improve the final maps, only the spectra having correlations ≥0.90, instead of ≥0.80 are selected for further processing, as a way to highlight the dominant spectral features of a pixel. Nevertheless, the HyMap™ mosaic is also mapped at ≥0.80 spectra correlation to check the utility for environmental assessment purposes.

5.2.1.1 HyCORR with EFFORT correction

The dataset for the Pearson correlation matrix is n=251, containing 70 USGS minerals, 91 ASD field spectra and 90 endmembers. From the output of the matrix are excluded the spectra which correlation with USGS minerals are <0.90, as well as the ones not containing any environmental indicator related to AMD, i.e. only quartz, a-smectite, illite, kaolinite or alunite. With these criteria the ASD data were reduced to 67 field spectra and the endmembers to 36. In Tables 5.1 and 5.2 are depicted the spectra correlations, respectively from ASD field and endmembers, that were captured in the next step when using the Spectral Angle Mapper (SAM) and excluded the ones containing less than 30 pixels.

A few changes are reported compared to ASD field spectra correlations shown in the previous Section, part due to the improvements above mentioned. From the same field set, few spectra are excluded and others absent in the previous section, once not captured by SAM, appear in these correlations. Some modifications in the correlation value also occur, as the changes in the wavelength range increase the correlation with copiapite to ≥0.90, instead of <0.90 previously detected, e.g. AC-203 spectrum (Table 5.A.2 and Table 5.1). The

suggestion in Section 5.E.1that the separability of jarosite from the mineralogical assemblage of Copiapite-Alunites (a-Smectite, illite or/and kaolinite) is possibly related to a pH threshold, is corroborated by integration of the coquimbite mineral to this assemblage. This mineral is often associated with copiapite and is also indicative of very low pH. The assemblage coquimbite-copiapite has been also reported in a similar environment within Iberian Pyrite Belt, typical of the banks of the stream affected by AMD (Ferreira da Silva et al., 2009).

Other type of information, such as the one reported in PS-164 to PS-166 field spectra (Table 5.1) indicate a correlation ≥0.90 with Jarosite 8 (Table 5.A.I) and Schwertmannite, revealing the capture of hazardous elements like Pb, as described in Silva and Figueiredo (2010). Although depicted at this level of correlation, this class is not isolated at the threshold ≥0.90 for the endmembers mapping and thus not intersected in the final classes following this methodology.

The SAM results for each of the input spectra are depicted in Table 5.3, excluding broad classes with a high dispersion such as Schwertmannite, while other identical minor mineralogical assemblages are not intersected by both maps.

Table 5.1 Correlation coefficients of field spectra used expressed in USGS spectral library minerals following CMN nomenclature of Table 5.A.1.

ASD Field Spec Pro		
n=57	≥0.90	0.80≤N≤0.90
TE-67	J(2-3-6-8) Sc	G(1-3-4) H1 I5 J(1-4-5-7-9) L Q(3-4)
TE-71	J(2-3-9)	G3 J(a-1-4-6-7-8) L Sc
TE-84	H1 J(2-3-8) Sc	G(1-3-4) H(a-2) I5 J(4-6-7-9) L Q(3-4)
TE-85	H1 Sc J(3-6-8) Q4 J6	F G(1-3-4) H(a-2) I5 J(2-4-5-7-9) L Q(2-3)
TE-90	G(3-4) J(2-3-6-7-8) L Sc	F G1 H(1-2) I(1-5) J (1-4-5-9) Q4
TE-92	J(2-3-6-8-9) L Sc	F G(1-3-4) H1 I1 J(a-1-4-5-7)
PN-97	F G(3-4) H1 J8 L Sc	G1 H(a-c-2) I(1-5) J(2-3-4-5-6-7-9) Q(3-4)
PN-98	G(3-4) H1 J8 L Sc	F G1 H(a-c-2) I(1-5) J(2-3-4-5-6-7-9) Q(3-4)
PN-99	G(3-4) J8 L Sc	F G1 H(a-1-2) I(1-5) J(2-3-4-5-6-7-9) Q(3-4)
PN-100	G3 L Sc	F G(1-4) H(1-2) I(1-5) J(2-3-6-7-8-9) Q(1-4)
PN-103	F G(1-3-4) H(1-2) I5 J(7-8) L Q4 Sc	C(1-5-6) H(a-b-c-3-7-8-9) I1 J(3-4-5-6) Py2 Q(2-3)
PN-105	G (1-3-4) H(1-2) I5 J8 L Q4 Sc	C6 F H(a-b-c-9) I1 J(2-3-4-5-6-7) Py2 Q(2-3)
PN-106	G(1-3-4) H(1-2) I5 J8 L Q4 Sc	C6 F H(a-b-c-9) I1 J(3-4-5-6-7) Py2 Q(2-3)
PN-107	G(3-4) H1 J8 L Q4 Sc	F G1 H(a-b-c-2) I(1-5) J(2-3-5-6-7) Q(2-3)
PN-111	Sc	F G(1-3-4) H(a-1) I1 J(2-3-6-7-8-9) L Q(1-4)
PN-112	Sc	F G(1-3-4) H(1-2) I(1-5) J(2-3-4-5-6-7-8-9) L Q(1-4)
PS-137	F G(1-3-4) H(1-2) I5 J(6-7-8) L Q4 Sc	C6 H(a-b-c-9) I1 J(2-3-4-5-9) Py2 Q(2-3)
PS-138	J(a-2-3-9)	J(1-4-6) L Sc
PS-143	J(2-3-6-8) Sc	F G(1-3-4) H1 I(1-5) J(1-4-5-7-9) L Q4
PS-146	J(2-3-9) Sc	G(3-4) H1 I1 J(a-1-4-5-6-7-8) L
PS-147	J(2-9)	J(a-1-3-4-6) Sc
PS-149	A3 Co	A(a-1-4-5-6) aS Cq I(a-4) K(3-8)
PS-151	A3 Co	A(a-1-2-4-5-6) aS Cq I(a-4) K8
PS-152	A(1-3-5) Co	A(a-2-4-6) aS Cq I(a-4) K(2-3-4-5-6-7-8)
PS-154	A(1-3-5) Co Cq	A(a-2-4-6)aS I(a-4) K(2-3-4-6-7-8)
PS-155	A(1-3-5) al Co Cq	A(a-2-4-6) aS I4 K(3-4-6-7-8)
PS-156	A(1-3-5) Co Cq	A(a-2-4-6) aS I(a-4) K(2-3-4-5-6-7-8)
PS-157	J(2-3-6-9)	G3 J(a-1-4-5-7-8) L Sc
PS-158	J(2-3-4-6-8) Sc	G(1-3-4) H1 I5 J(1-5-7-9) L Q(3-4)
PS-163	G3 J8 L Sc	F G(1-4) H(1-2) I(1-5) J(2-3-4-5-6-7-9) Q4
PS-164	J8 Sc	G(1-3-4) H1 I1 J(2-3-4-5-6-7-9) L Q(3-4)
PS-165	J8 Sc	G(1-3-4) H(a-1) I1 J(2-3-4-6-7-9) L Q(3-4)
PS-166	J8 Sc	F G(1-3-4) H1 I(1-5) J(1-2-3-4-5-6-7-9) L Q(3-4)
PN-169	Sc	F G(1-3-4) H(a-1-2) I(1-5) J(2-3-6-7-8-9) L Q(1-3-4)
PN-171	G(3-4) H1 J8 L Sc	C6 F G1 H(a-2) I(1-5) J(2-3-4-5-6-7) Q(2-3-4)
PN-172	Sc	G(3-4) H(a-1) J(2-8) L Q(1-4)
PN-174	C6 F G(1-3-4) H(1-2) I5 J(7-8) L Py2 Q(2-3-4) Sc	C(1-3-4-5) H(b-c-7-8-9) I1 J(4-5-6) Py(4-5)
PN-175	J8 F G(1-3-4) I(1-5) J(5-6-7) L Sc	C(1-4-5-6) H(b-1-2) J(2-3-4) Py2 Q(2-3-4)
PN-176	F G(1-3-4) H(1-2) I5 J8 L Q(2-3-4) Sc	C6 H(a-b-c-3-8-9) I1 J(6-7)Py2
TE_181	J(2-3)	H1 J(a-6-8-9) L Sc
TE_182	J2 Sc	G3 H(a-1) J(3-6-8-9) L Q4
TE_183	J(2-3-8) Sc	G(3-4) H(a-1) J(4-6-7-9) L Q(3-4)
TE_191	J3	H1 J(a-2-4-6-8-9) L Q(3-4) Sc
TE_192	J(2-3)	J(a-1-4-6-8-9) Sc
AC-203	Co	A(a-3) aS K(3-8)
AC-206	Co	A(a-1-3) aS K8

(Cont.)

(Cont.)ASD Field Spec Pro		
n=57	≥0.90	0.80≤N≤0.90
SD-210	F G(1-3-4) H(b-c-1-2-9) I5 J(7-8) L Py2 Q(2-4) Sc	C6 H(a-3-4-6-7-8) I1 J(2-3-4-5-6) Py5 Q3
SD-212	F G(1-3-4) H(c-1-2) I5 J8 L Q4 Sc	C6 H(a-b-3-7-8-9) I1 J(2-3-4-5-6-7-9) Py2 Q(2-3)
SD-215	H1 Q4 Sc	F G(1-3-4) H(a-b-c-2) I(1-5) J(3-6-7-8) L Q(2-3)
SD-216	Sc	F G(3-4) I1 J(2-9) L Q1
SD-217	G4 H1 Q4 Sc	F G(1-3) H(a-2) I(1-5) J(2-3-6-7-8) L Q3
SD-218	H1 Q4 Sc	F G(1-3-4) H(a-c-2) I(1-5) J(2-3-6-7-8) L Q(1-3)
SD-226	G4 Sc	F G(1-3) H(a-b-c-1-2) I(1-5) J(6-7-8) L Q(3-4)
SD-236	Sc	F G(1-3-4) H(a-1-2) I1 J(2-3-6-8-9) L Q(1-4)
SD-237	J8 G(1-3-4) H1 J6 L Q(3-4) Sc	F H(a-b-c-2) I(1-5) J(2-3-4-5-7-9) Py2 Q2
SD-246	F G(1-3) H(c-1-2) I5 J(7-8) L Q4 Sc	C6 H(b-3-7-8-9) I1 J(2-3-4-5-6-9) Py2 Q(2-3)
SD-248	F G(1-3-4) H(c-1-2) I5 J(7-8) L Q4 Sc	C6 H(a-b-3-7-8-9) I1 J(2-3-4-5-6-9) Py2 Q(2-3)
Cq=Coquimbite Sc= Schwertmannite		

Table 5.2 Correlation coefficients of endmember spectra used expressed in USGS spectral library minerals following CMN nomenclature of Table 5.A.1.

Hycorr-EFFORT mosaic endmembers		
n=36	≥0.90	0.80≤N≤0.90
6	J(2-9) Sc	G(3-4) H1 J(3-6-8) L
9	H1 J8 Q4 Sc	F G(1-3-4) H(a-2) I5 J(2-3-6) L Q(2-3)
11	H1 J8 Q4 Sc	F G(1-3-4) H(a-b-c-2) I5 J(2-3-6-7) L Q(2-3)
12	A(1-5) Co	A(2-3-6) Cq I(a-4)
13	Sc	F G(1-3-4) H(1-2) I1 J(2-3-6-7-8-9) L Q4
19	G(3-4) J(2-8) L Sc	F G1 H(1-2) I(1-5) J(3-4-5-6-7-9) Q4
22	G(1-4) H(b-c-1-2) I5 J8 Q(2-3-4) Sc	C6 F G3 H(a-3-7-8-9) J(6-7) L Py2
23	I1 Sc	F G(3-4) J(6-7-8) L
24	H(a-1) I5 J8 Q(2-3-4) Sc	F G(1-3-4) H(b-c-9-2) J6 L Py2
25	H(a-1) Q(3-4) Sc	F G(1-3-4) H(b-c-2-9) I5 J8 L Py2 Q2
29	G(1-3-4) H(1-2) I5 J8 L Q4 Sc	C6 F H(a-b-c-3-8-9) I1 J(2-3-6-7) Py2 Q(2-3)
35	Sc	F G(1-3-4) H1 I1 J(2-3-6-8-9) L
36	Sc	F G(1-3-4) H1 I1 J(2-3-4-6-7-8-9) L Q(3-4)
39	G3 J(2-9) L Sc	F G(1-4) H1 I1 J(3-4-6-7-8)
41	H(a-1) Q4 Sc	G(1-3-4) H(b-c-2) I5 J(2-3-6-8) L Q(2-3)
44	H1 J8 Q(3-4) Sc	F G(1-3-4) H(a-b-2) I5 J(2-3-6-7) L Q(2-3)
54	A(1-3) Co	A(a-2-4-5-6) aS Cq I(a-4) K(1-2-3-4-5-6-7-8)
56	L Sc	F G(1-4) H(1-2) I1 J(2-3-4-6-7-8-9) Q4
60	F G(1-3-4) H(b-c-1-2-9) I5 J8 L Q4 Sc	C6 H(3-4-6-7-8) I1 J(5-6-7) Py(2-5) Q(2-3)
64	J2 Sc	G(3-4) H1 J(a-3-4-6-7-8-9) L
65	H(a-1)	G(3-4) J8 L Q(3-4) Sc
66	I1 Sc	F G(1-3-4) H(1-2) I5 J(2-6-7-8) L Q4
68	Sc	F G(1-3-4) H(a-1-2) I(1-5) J(2-3-6-8) L Q(3-4)
70	H1 Q4 Sc	G(1-3-4) H(a-2)I5 J(2-3-6-8) L Q3
72	G(3-4) L Sc	G(1-3-4) H(a-2)I5 J(2-3-6-8) L Q3
73	F G(1-3-4) H2 J(6-7-8) L Sc	C6 H(b-c-1-9) I(1-5) J(2-3-4-5-9) Py2 Q4
75	J(2-9)	G3 J(a-3) L Sc
79	G(1-3-4) H(b-1-2) I5 J8 L Q(3-4) Sc	C6 F H(a-c-3-8-9) I1 J(2-3-6-7) Py2 Q2
85	A(1-3-5) Co	A(a-2-4-6) aS Cq I(a-4) K(2-3-4-6-7-8)
86	G(1-4) H(1-2) I5 J8 Q(3-4) Sc	C6 F G3 H(a-b-c-8-9) I1 J(3-6-7) L Py2 Q2
91	Sc	F G(1-3-4) H1 I1 J(2-3-6-7-8-9) L Q4
94	Co	A(a-1-3-5-6) aS I4 K(3-8)
101	Sc	F G(1-3-4) H(a-1) I1 J(2-3-6-7-8-9 L Q(3-4)
111	F G(3-4) I1 J7 L Sc	C6 G1 H(1-2) I5 J(2-3-4-5-6-8-9)
114	F G(1-3-4) H2 J8 L Sc	H(b-c-1-9) I(1-5) J(2-3-4-5-6-7-9) Py2 Q4
115	G(1-3-4) H(1-2) I5 J8 L Q4 Sc	C6 F H(a-b-c-8-9) I1 J(2-3-6-7) Py2 Q(2-3)
Cq=Coquimbite Sc= Schwertmannite		

Table 5. 3 Intermediate and final mineralogical correlation ≥ 0.90 maps of AMD for S. Domingos area with a HyCORR-EFFORT correction. Spectra number reports to Tables 5.1 (ASD field) and 5.2 (endmembers).

MAPS / CLASSES	ASD FIELD			ENDMEMBERS			MINERALOGICAL CORRELATION ≥0.90		
	Spectra	Area (m²)	CV	Spectra	Area (m²)	CV	Spectra	Area (m²)	CV
Copiapite-alunite (Coquimbite) (I,S,K)	149-151-152 154-155-203-206	108,996.04	0.22	#(12-85 54-94)	102,759.53	0.30	Intersection of correlation minerals	78,368.22	0.22
Jarosite (I, Qz)	138-147-157-181	1,015,828.25	0.23	#(75)	24,004.68	0.22		7,127.44	0.20
Goethite-Jarosite-Lepidocrocite-Schwertmannite (G-J-L-Sc)	90-99-163	466,830.49	0.18	# (19-39)	15,263.48	0.16		7,648.55	0.15
Goethite-Lepidocrocite-Schwertmannite (G-L-Sc)	100	804,543.37	0.18	# (72)	2,723.22	0.12		1,798.67	0.12
SUM		2396,198.14			144,750.90			94,942.88	

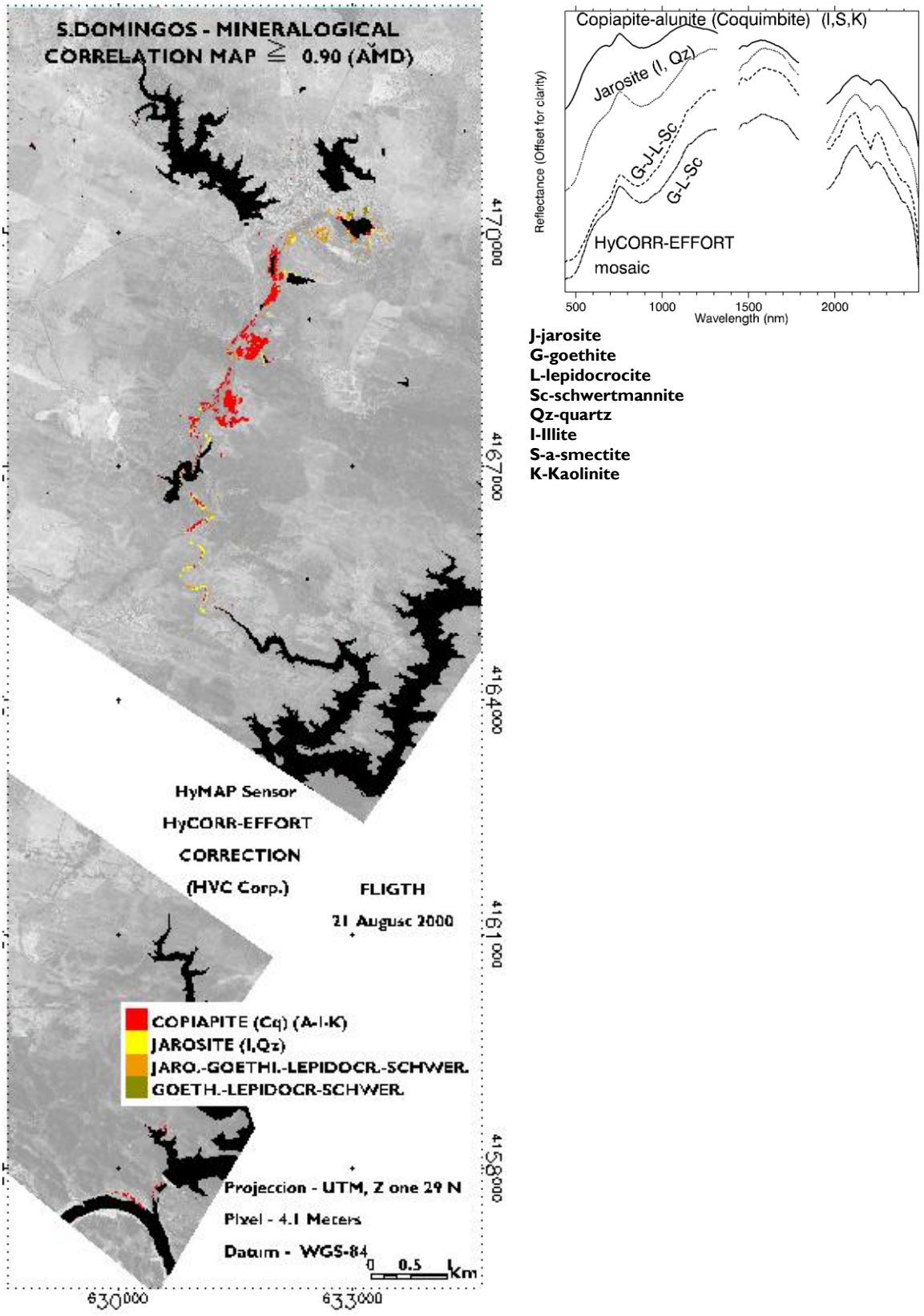

Figure 5. 1 Mineralogical correlation ≥0.90 maps for S. Domingos area with an HyCORR-EFFORT correction (Hyvista Corporation). Rigth-average spectra of the classes.

5.2.1.2 FLAASH with EFFORT correction

The dataset for the Pearson correlation matrix is n=251, containing 70 USGS minerals, 91 ASD field spectra and 65 endmembers. The criteria applied for selection of spectra to the result of the correlation matrix is the same as in the above section with HyCORR correction mosaic. Thus, the ASD data are reduced to 67 field spectra (enclosed in Table 5.1) and the endmembers to 14 (Table 5.4). This is significantly less than the endmembers selected with the HYCORR-EFFORT correction (n=36). The SAM results for this mosaic are expressed in Table 5.5, whilst the final map generated by intersection is in Figure 5.2.

Table 5. 4 S. Domingos mosaic FLAASH-EFFORT correction derived endmembers - Correlation coefficients of endmember spectra used expressed in USGS spectral library minerals following CMN nomenclature of Table 5.A.1.

FLAASH-EFFORT MOSAIC endmembers		
N=14	≥0.90	0.80≤N≤0.90
77	A(1-3-5) Co	A(2-4-6) al aS Cq I(a-4) K(3-4-6-8)
79	H1 J8 Q4 Sc	G(1-3-4) H(a-b-c-2) I5 J(2-3-6-7) L Q(2-3)
57	F G(3-4) I1 I5 J8 L Sc	C6 G1 H(1-2) J(2-3-4-5-6-7-9) Q(2-3-4)
62	Sc	F G(1-3-4) H1 I(1-5) J(2-3-6-7-8-9) Le Q(3-4)
65	G(1-4) H(1-2) J8 Q4 Sc	F G3 H(a-b-c-9) I(1-5) J(2-3-6-7) L py2 Q(2-3)
72	H(1-2) J8 Q(3-4) Sc	F G(1-3-4) H(a-b-c-9) I5 J(6-7) L py2 Q2
75	H(a-1) Q4 Sc	F G(1-3-4) G(3-4) H(b-c-2-9) I5 J(6-7-8) L Q(2-3)
44	G(1-4) H(1-2) H2 I5 J8 Q4 Sc	C6 F G3 H(a-b-c-3-8-9) J(2-3-6-7) L py2 Q(2-3)
49	G(1-4) H(1-2) J8 Q4 Sc	F G3 H(a-b-c-8-9) I5 J(2-3-6-7) L py2 Q(2-3)
51	Sc	F G3 I1 J8 L
54	H1 Q4	G(1-3-4) H(a-2) I5 J(2-3-6-7-8) L Q(2-3) Sc
11	F G(1-3-4) H(b-c-1-2-9) I5 J8 L py2 Q4 Sc	C(5-6) H(3-4-6-7-8) I1 J(3-4-5-6-7) py5 Q(2-3)
14	G(3-4) L Sc	F G1 H(1-2) I(1-5) J(2-3-4-5-6-7-8-9) Q4
23	A(1-3-5) a-l Co	A(2-4-6) Cq I4 K(1-4-6-8)

Cq=Coquimbite Sc= Schwertmannite

Table 5. 5 Intermediate and final Mineralogical correlation ≥ 0.90 maps of AMD for S. Domingos area with an FLAASH-EFFORT correction. Number of spectra reported to Table 5.1 (ASD field) and Table 5.4 (endmembers).

MAPS / CLASSES	ASD FIELD			ENDMEMBERS			MINERALOGICAL CORRELATION ≥0.90		
	Spectra	Area (m²)	CV	Spectra	Area (m²)	CV	Spectra	Area (m2)	CV
Copiapite-alunite (Coquimbite) (I,S,K)	149-151-154-155-203-206	58,280.27	0,19	(#77 #23)	24,307.260	0,18	Intersection of correlation minerals	14,137.21	0.15
Heamatite-Jarosite-Quartz-Schertwanite (H-J-Q-Sc)	85	69,374.87	0,20	#79-72	276,995.180	0,21		41,789.66	0,19
Goethite-Lepidocrocite-Schwertmannite (G-L-Sc)	100	560,193.25	0,21	#14	206,645.330	0,23		99,128.57	0.19
H-Q-Sc	215-218	65,037.89	0,35	#75	21,062.930	0,31		8,892.49	0.34
SUM		752,886.28			529,010.700			163,947.93	

5.2.1.3 Comparison of classification results in HyMap™ mosaics

The individual maps of both atmospheric corrections show some variability in the intermediate steps before the final merging, as depicted in Table 5.6. The FLAASH mosaic maps less area either using ASD input either endmembers spectra. The global mapping results per area indicate that the HyCORR-EFFORT mosaic presents a broader mapping area from ASD field map while this is significantly less for the endmembers extracted from the image. In the FLAASH-EFFORT mosaic both types of input spectra are more balanced and the final

intersection map covers a broader area, i.e. 163,947.93m^2 compared to the cover area of the 94,942.88m^2 from the HyCORR-EFFORT mosaic.

Table 5. 6 SAM intermediate maps classification results for HYCORR and FLAASH corrected mosaics showing the ASD and endmembers input spectra. Classes containing less than 30 pixels were excluded.

S.DOMINGOS MOSAIC-HYCORR CORRECTION SAM-ASD SPECTRA			SAM-ENDMEMBERS			S.DOMINGOS MOSAIC-FLAASH CORRECTION SAM-ASD SPECTRA			SAM-ENDMEMBERS		
CLASSES n=52	Pixels	%	CLASSES N=36	Pixels	%	CLASSES n=48	Pixels	%	CLASSES n=14	Pixels	%
Unclass.	1484006	38,909	Unclass.	2121409	55,621	Unclass.	1987953	51,050	Unclass.	3020354	77,559
TE-67	169	0,004	#6	84	0,002	TE-67	268	0,007	#77	1244	0,032
TE-84	350	0,009	#9	3267	0,086	TE-71	92	0,002	#79	11583	0,297
TE-85	4893	0,128	#11	1179	0,031	TE-84	614	0,016	#57	94586	2,429
TE-90	1432	0,038	#12	54	0,001	TE-85	4127	0,106	#62	534185	13,717
TE-92	102	0,003	#13	342894	8,990	TE-90	101	0,003	#65	6303	0,162
PN-97	1255	0,033	#19	741	0,019	TE-92	503	0,013	#72	4895	0,126
PN-99	3461	0,091	#22	141	0,004	PN-97	381	0,010	#75	1253	0,032
PN-100	47859	1,255	#23	579	0,015	PN-98	245	0,006	#44	440	0,011
PN-103	778	0,020	#24	659	0,017	PN-99	925	0,024	#49	47	0,001
PN-105	1058	0,028	#25	38	0,001	PN-100	33325	0,856	#51	187894	4,825
PN-106	56	0,001	#29	1506	0,039	PN-105	289	0,007	#54	18953	0,487
PN-107	6959	0,182	#35	2561	0,067	PN-106	4143	0,106	#11	57	0,001
PN-111	25800	0,676	#36	916	0,024	PN-107	8567	0,220	#14	12293	0,316
PN-112	50073	1,313	#39	167	0,004	PN-111	3316	0,085	#23	202	0,005
PS-137	3691	0,097	#41	883	0,023	PN-112	296	0,008	SUM	3894289	100,000
PS-138	22851	0,599	#44	887	0,023	PS-137	554	0,014			
PS-143	118	0,003	#54	4727	0,124	PS-138	12896	0,331			
PS-146	3336	0,087	#56	246822	6,471	PS-143	231	0,006			
PS-147	25482	0,668	#60	57	0,001	PS-146	1762	0,045			
PS-149	317	0,008	#64	164860	4,322	PS-147	21878	0,562			
PS-151	27	0,001	#65	78962	2,070	PS-149	255	0,007			
PS-152	309	0,008	#66	105498	2,766	PS-151	63	0,002			
PS-154	893	0,023	#68	131815	3,456	PS-154	453	0,012			
PS-155	218	0,006	#70	680	0,018	PS-155	389	0,010			
PS-156	259	0,007	#72	162	0,004	PS-157	772	0,020			
PS-157	77	0,002	#73	420	0,011	PS-163	1338	0,034			
PS-158	52	0,001	#75	1428	0,037	PS-164	4566	0,117			
PS-163	22878	0,600	#79	1443	0,038	PS-165	31408	0,807			
PS-164	501	0,013	#85	735	0,019	PS-166	13113	0,337			
PS-165	1073	0,028	#86	1904	0,050	PN-169	140174	3,600			
PS-166	29909	0,784	#91	432775	11,347	PN-171	10662	0,274			
PN-169	249372	6,538	#94	597	0,016	PN-172	1504420	38,633			
PN-171	32272	0,846	#101	155023	4,065	PN-175	670	0,017			
PN-172	1666026	43,681	#111	71	0,002	PN-176	87	0,002			
PN-174	72	0,002	#114	1341	0,035	TE_181	6122	0,157			
PN-175	970	0,025	#115	6788	0,178	TE_182	35720	0,917			
PN-176	4164	0,109	SUM	3814073	100,000	TE_183	1310	0,034			
TE_181	12018	0,315				TE_191	1325	0,034			
TE_182	59847	1,569				TE_192	17686	0,454			
TE_183	3219	0,084				AC-203	2167	0,056			
AC-203	4408	0,116				AC-206	140	0,004			
AC-206	53	0,001				SD-215	1711	0,044			
SD-210	29	0,001				SD-217	32249	0,828			
SD-212	69	0,002				SD-218	2158	0,055			
SD-215	991	0,026				SD-226	2165	0,056			
SD-216	380	0,010				SD-236	141	0,004			
SD-217	38665	1,014				SD-237	406	0,010			
SD-218	537	0,014				SD-248	30	0,001			
SD-236	72	0,002				SUM	3894166	100,000			
SD-237	231	0,006									
SD-246	159	0,004									
SD-248	238	0,006									
SUM	3814034	100,000									

Specifically concerning the most important class of very low pH, i.e. the Copiapite (Cq) Alunite (I,K) class is substantially reduced both at endmembers and field spectra in the FLAASH mosaic. This class diminishes from 6484 pixels in HyCORR to 3467 in FLAASH in ASD mapping, while in the endmembers this is reduced from 2442 pixels to 1446 in FLAASH. The final class Co(Cq)(Alunite, kaolinite, illite) of the mineralogical correlations ≥0.90 is of 78,368.216 m^2 in HyCORR and of 14,137.210 m^2 in FLAASH.

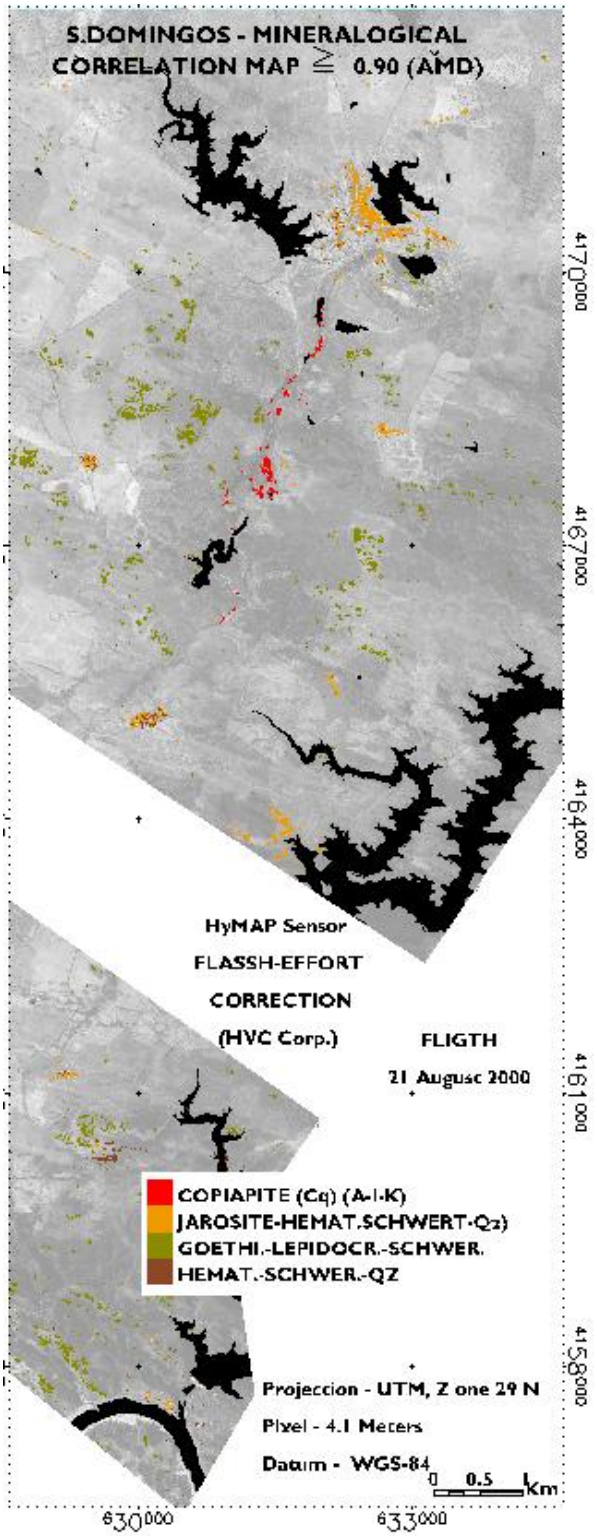

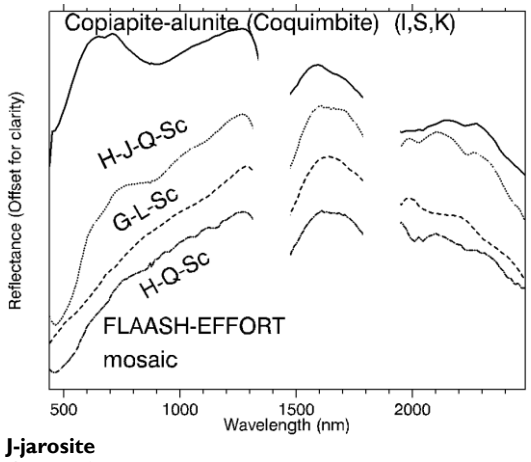

J-jarosite
G-goethite
H-heamatite
L-lepidocrocite
Sc-schwertmannite
Q-quartz
I-Illite
S-a-smectite
K-Kaolinite

Figure 5. 2 Mineralogical correlation ≥0.90 maps for S. Domingos area with a FLAASH-EFFORT correction. Rigth-average spectra of the classes.

Although the general pattern displayed by Copiapite (Cq)-Alunite class is similar, in the FLAASH mosaic this disappears when there is not a considerable spatial dispersion, e.g. over the village and surrounding the open pit. A possible explanation is given by the effect of water removal (Chapter 4) in the FLAASH mosaic eliminating the possibility of identification and also by the less pronounced spectral response effect due to polishing and possibly enough to justify the disappearance of the Jarosite class at this correlation level.

Spectrally is shown in Figure 5.3 the average values of the classes obtained in both mosaics.

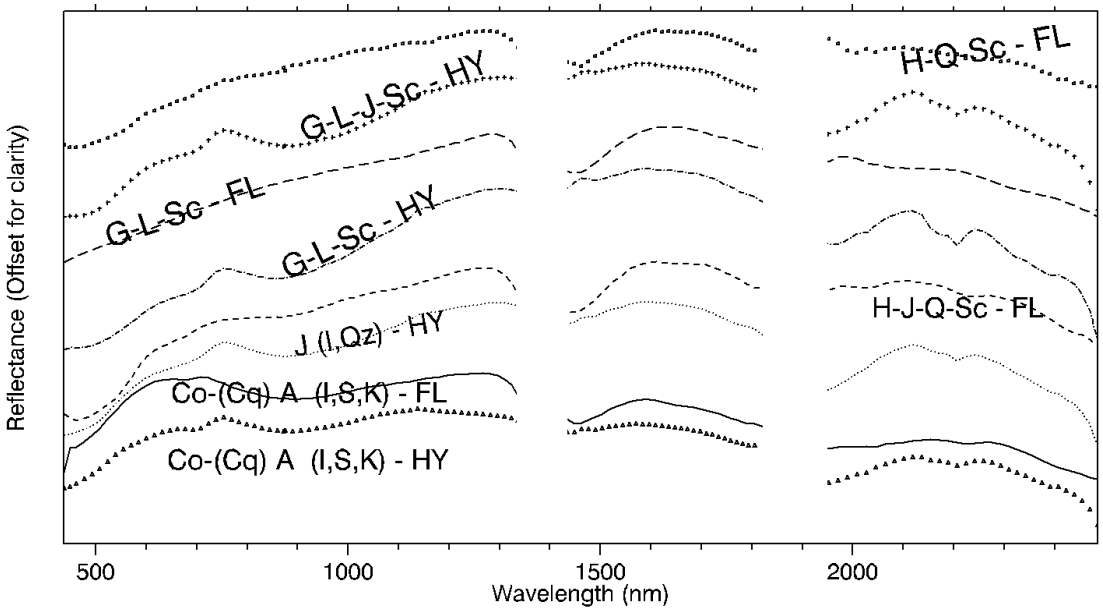

Figure 5. 3 Average spectral values of classes from both mosaics. Hy-HyCORR and FL-FLAASH correction. Co-copiapite, Cq-coquimbite, A-alunite; J-jarosite, G-goethite, H-heamatite, L-lepidocrocite, Sc-schwertmannite, Q-quartz I-Illite, S-a-smectite and K-Kaolinite.

The most important class concerning the AMD detection, the Co-(Cq)-A-(I,S,K), is spectrally very similar on both mosaics, whilst the G-L-Sc is much more flattened in the FLAASH mosaic, following the general conclusions in Chapter 4. Within the HyCORR classes the one containing jarosite (G-J-L-Sc) is similar to the one without jarosite (G-L-Sc) and the Jarosite (I, Qz) class is not strikingly different in the average spectral patterns.

It's important to remark whereas the AMD signature indicates the very low pH as copiapite/coquimbite together with alunite, illite, or kaolinite of high correlation ≥ 0.90, constitutes the only secondary iron minerals. By contrast although identified at this correlation level by only one secondary iron minerals, e.g. Jarosite (I,Qz) contains others at a lower correlation level. The Jarosite (I, Qz) class in the HyCORR mosaic is accompanied by other minerals such as heamatite and lepidocrocite at a lower correlation level, i.e. from ≥ 0.80 to <0.90.

The importance of information derived from very high correlation coefficients is to depict the essence of similarity at pixel level and draw a global picture of the area. Considering the different mapping results in function of the different atmospheric corrections is important to see if the threshold correlation values are lowered what the implications are. This is relevant in terms of quantitative environmental assessment, if following this methodology.

Following the same methodology for mapping but using input spectra of endmembers and ASD field at correlation level ≥ 0.80, the results are displayed in Table 5.7 just for the low pH class. This mapping includes the endmembers that were excluded in the previous mapping at ≥ 0.90 mineralogical correlation in both mosaics. The results show a wider dispersion in the HyCORR mosaic for the final map (Figure 5.4).

As expected the CV is higher than with the correlation level at 0.90 (Table 5.3 and 5.5), although minor in the FLAASH mosaic.

Table 5. 7 Classification results from SAM for both HYCORR and FLAASH corrected mosaics at correlation level 0.80 for low pH class.

HyCORR EFFORT MOSAIC CORRELATION ≥0.80								
MAPS / CLASSES	ASD FIELD			ENDMEMBERS			MINERALOGICAL CORRELATION ≥0.80	
	Spectra	Area (m²)	CV	Spectra	Área (m²)	CV	Área (m²)	CV
Copiapite (Coquimbite) -alunite (I,S,K)	136-149-150-151-152-154-155-156-193-194-203-204-205-206-225	290,695.316	0,37	#(12-17-27-33-49-51-54-74-76-83-85-94)	261,059.287	0,38	225,724.669	0,36
FLAASH-EFFORT MOSAIC CORRELATION ≥0.80								
MAPS / CLASSES	ASD FIELD			ENDMEMBERS			MINERALOGICAL CORRELATION ≥0.80	
	Spectra	Area (m²)	CV	Spectra	Área (m²)	CV	Área (m²)	CV
Copiapite (Coquimbite) -alunite (I,S,K)	136-149-150-151-152-154-155-156-193-194-203-204-205-206-225	180,001.480	0,22	#(19-21-23-29-38-66-67-77)	38,125.080	0,25	23,853.390	0,17

From this it can be observed that the lowest pH class is mapped differently at 0.80 mineralogical correlations following the same variations as depicted in mapping at 0.90 correlations. The area covered by this class in FLAASH mosaic is about 62% of the HyCORR mosaic for the ASD field map, 15% of the endmembers map and 11% in the final intersection map. Thus, as already seen in the 0.90 correlation the atmospheric corrections are a key-issue in constraining the mapping results, when applying this methodology. From this, the ASD field spectra mapping in area shows more similarities in both mosaics, and seems a more independent measure of the reality with less effect in function of the different atmospheric corrections.

In Figure 5.4 is depicted the spatial dispersion of low pH class Copiapite (Coquimbite)-alunite (I,S,K) for both mineralogical correlation mapping at 0.80 and 0.90 levels, while the equivalent average spectra are depicted in Figure 5.5.

Despite the differences in the coverage area of both mosaics it's important to notice that the correlations values input spectra are very high and there is convergence in the areas mapped. The FLAASH-EFFORT mosaic depicts a more discrete pattern but the changes are also less than in the HyCORR-EFFORT when comparing threshold correlation values of 0.80 and 0.90. These results highlight the consequences of the different type of atmospheric corrections undertaken.

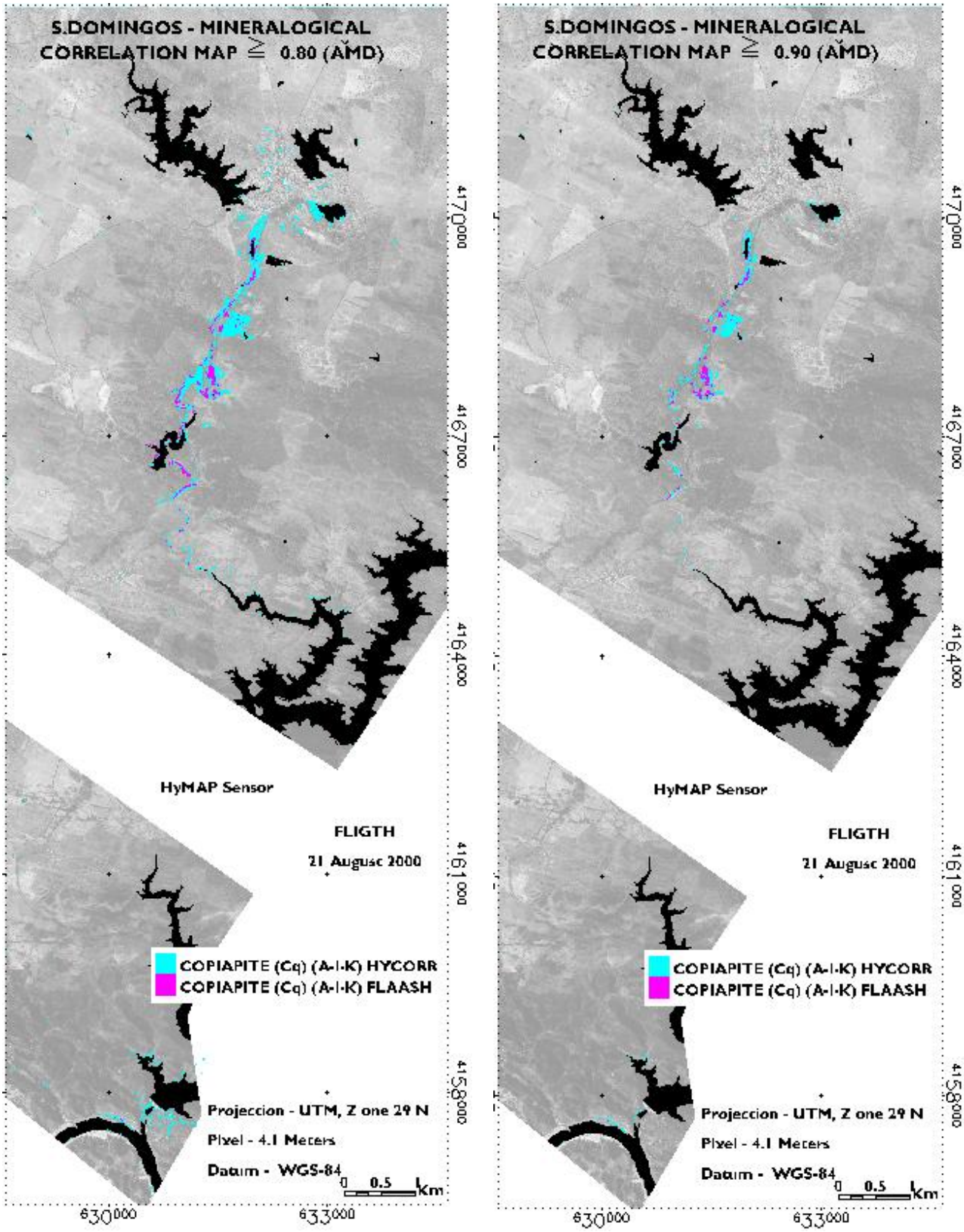

Figure 5. 4 Low pH delineation [Copiapite (Coquimbite)-Alunite (I,S,K)] at 0.80 (left) and 0.90 (right) levels for both HyCORR-EFFORT (cyan) and FLAASH-EFFORT (magenta) mosaics.

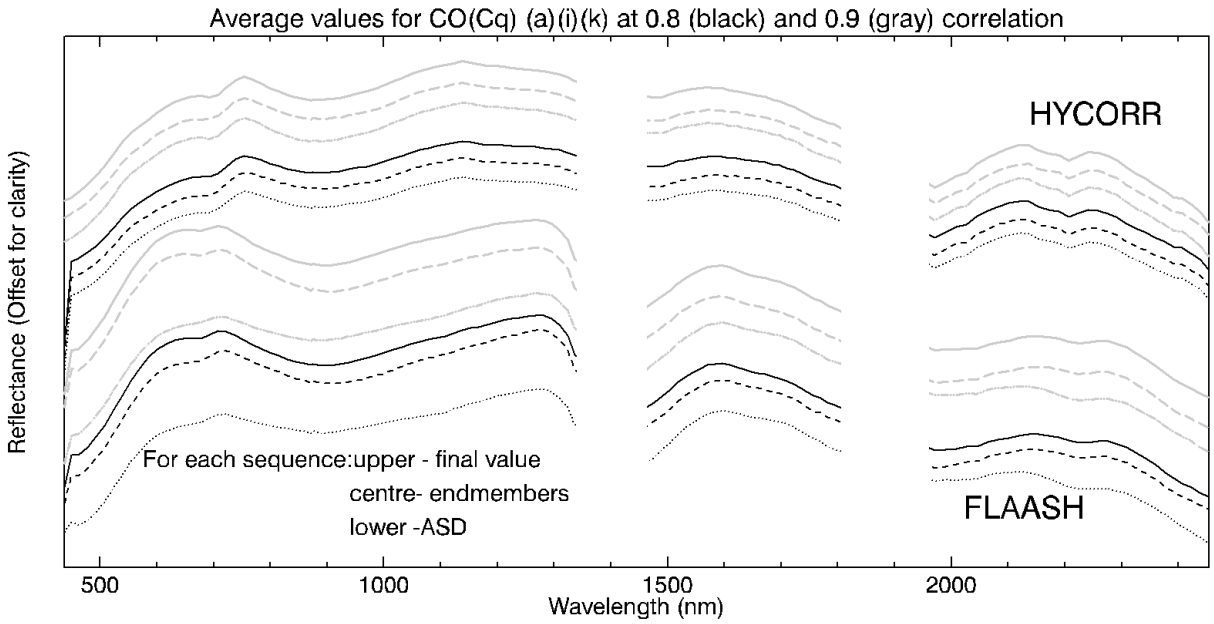

Figure 5. 5 Comparison of average spectra for ASD, endmember and final map for both HyCORR (upper sequence) and FLAASH (lower sequence) mosaics for low pH delineation [Copiapite (Coquimbite)-Alunite (I,S,K)] at 0.80 (black) and 0.90 (gray) correlation levels.

Comparing the HyCORR mosaic mineralogical correlation map at ≥ 0.80 with the spatial pattern depicted on the test fligthline in Section 5.2, shows that there are substantial changes between them. Several factors can explain these differences including but not limited to: variations applied in the global mosaic processing such as new wavelength range, introduction of other minerals and different endmembers in the correlation matrix, or even the cross track illumination correction in the pre-processing steps as described in Chapter 4. Considering the number of input ASD spectra, in the fligthline containing the open pit for the Copiapite–alunite class is 7, whilst the endmembers are 3. In the whole HyCORR mosaic these numbers are 15 and 12, respectively (Table 5.A.II, and Table 5.7), thus increasing the probability of being captured by SAM, even if the angle used is the same.

5.2.2. SPECIM EAGLE HAWK MOSAIC

The multi-source spectral methodology as undertaken in year 2000 IS data is also applied to year 2007 IS data from SPECIM EAGLE-HAWK sensor. However, when extracting endmembers from the mosaic, through an Automated Spectral Hourglass, there is a general lack of spectral information. Valuable spectra, i.e. excluding vegetation and error spectra, are reduced and using these input spectra to the SAM algorithm only 1% of the image is mapped. Difficulties when extracting endmembers can be related to spectra spiking and faulty channels. Spiking may have been increased possibly due to spectral sub setting undertaken as described in Chapter 4.

There are other possible contributions. The stripping problem typical of the pushbroom sensors, as referred in Chapter 3 (Figure 3.16), were investigated but did not yield meaningful results, although some tests of illumination correction across the fligthline were undertaken. The situation is complex as also contains to the continuous stripping aligned with the fligthline direction a smoother stripping across track direction. Controlling through MNF factors the results of the corrections using polynomials were not satisfactory and were abandoned. Plus, these variation along and across the fligthline do not exactly match each of the MNF factors.

For the extraction of endmembers other algorithms, such as Sequential Maximum Angle Convex Cone (SMACC) (ITT, 2010) were tested and reasonable results obtained. However, the conditions to retrieve spectral information from the mosaic would have to be substantially different from the ones used in year 2000.

Other possibilities were then considered in order to have a common factor for multi-temporal comparison: a) to map the area using the input data, i.e. both endmembers and field spectra used for the generation of mineralogical correlation map (Figure 5.2), but adding input spectra for 0.80 correlation (Table 5.7) and b) to map the area using the ASD FieldSpec field measurements gathered simultaneously with 2007 IS acquisition. This last possibility is based on the characteristics of field spectra as more independent information than image endmembers, as obtained with HyMap™ data in the previous Section.

In a) the resultant map using SAM, maps approximately 10% of the input data, either from ASD or from endmembers using correlations at 0.80. However, the low pH signature of copiapite-coquimbite (A-I-K) class, is not detected when using endmembers, whilst the ASD contained in the same class maps solely a very small area surrounding an acidic dam downwards from the open pit to Achada do Gamo (AG) subarea and in the sulphide ore pile to south. In b) the results obtained are described in next section.

5.2.3 COMPARISON OF SPECIM EAGLE HAWK AND HYMAP™ MOSAICS

SAM using ASD field spectra (year 2007)

As referred in Chapter 3, the objective of 2007 ASD field spectra collection was to provide calibration targets measurements during the overfligth as well as to depict materials signature whose previous known spectral response indicated a low pH value. These spectra have been collected essentially at the sulphur plant area (AG) and surrounding the open pit (SD) in previous collection points or nearby that indicated already a very low pH.

In the case of the Pomarão harbour measurements were not taken, because the pavement was being modified with dark slags materials from AG area. Using the same input minerals of USGS (Clark et al., 2007) spectral library as in the Pearson correlation matrix for the HyMap™ mosaic the results show mainly materials related to copiapite-coquimbite (A-I-K). This spectral pattern is depicted in Figure 5.6, with variable correlation values, as well as others corresponding to jarosite. Examples of the classes are observed; although they are not exclusive, i.e. spectral measurements in visually similar materials may belong to different classes at this correlation level.

Using the ASD 2007 input spectra with correlations ≥0.80, containing the ones in Figure 5.6 and others, the SAM maps 0.7% of SPECIM EAGLE-HAWK mosaic. The two classes related with AMD gives a copiapite-(Coquimbite) alunite class with an area of 1,378.420 m² and a jarosite class with 2,286.160 m². The major mapped areas correspond to the acidic dam downward from open pit to Moitinhos and the sulphidic ore pile between the two, as detailed in Figure 5.7. AG, the most contaminated area, and also part of TE as referred in Chapter 3 (Figure 3.15), were lost for the HAWK sensor and therefore not processed in the whole mosaic.

A few other points appear to the south in the Pomarão Harbour area and to the north near the easterm margin of the open pit.

The common factor between the two multi-sensor and multitemporal images, being the same set of ASD field spectra collected in 2007 is inputted to the HyMap™ mosaic with HycORR-EFFORT correction for SAM algorithm. The result is shown in Figure 5.8 and is compared with the one obtained using ASD field spectra collected in 2000 with a similar mineralogical content. The most mapped area for the ASD field spectra 2007 was shown in Figure 5.7.

The most evident variation is a wider area covered by the copiapite-coquimbite class in the 2000 map, as expected. In fact, these efflorescent salts appear during the dry season, diminishing or disappearing during the rainy season. However, derived from the Pearson correlation matrix and as depicted in Figure 5.6, the spectra

identify the materials far behind the visible colour. It is also noticed in the 2007 map, the appearance of jarosite class, mostly nearby the former, indicating the presence of a more stable mineralogical form.

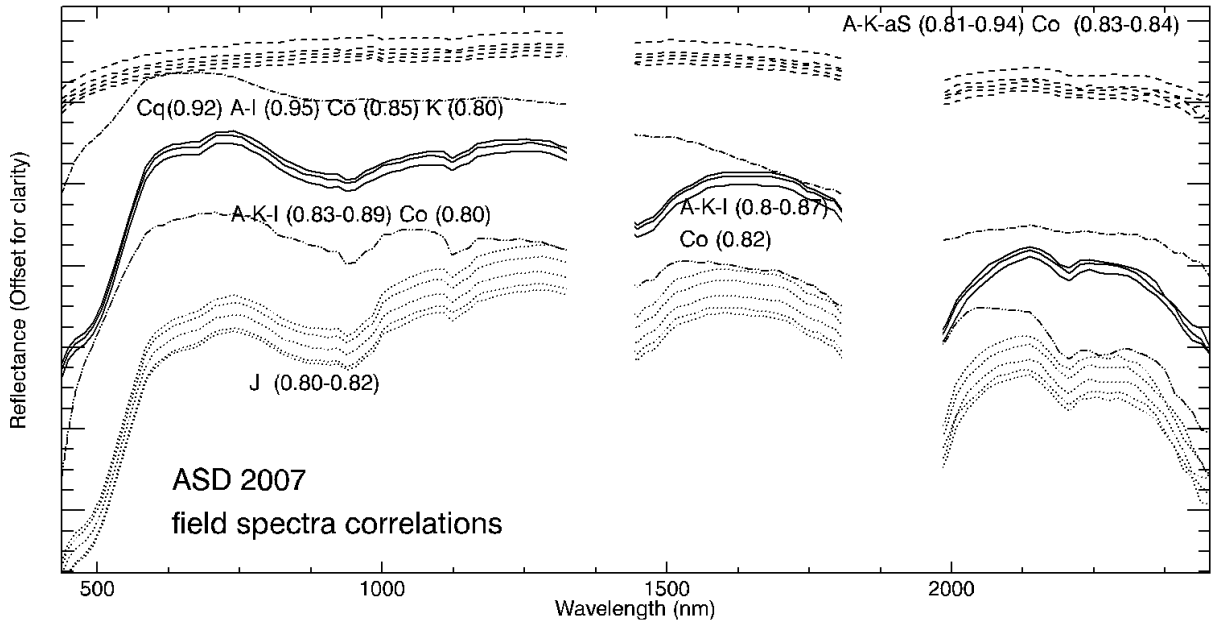

Cq(0.92)A-I(0.95)Co(0.85)K(0.80)
S. Domingos

A-K-aS(0.81-0.94)Co(0.83-0.84)
Achada do Gamo

*mixture (≥0.67) (≤0.81) of Co-Cq-A-I-K-Py Achada do Gamo

Figure 5. 6 Upper-Spectral patterns from field data in 2007 and information derived from the correlation matrix with USGS 2007 mineralogical spectral library. J-jarosite, Co-copiapite, Cq-coquimbite, aS-a-smectite, I-Illite K-Kaolinite, A-alunite and Py-pirite. Lower-materials in which measurements were obtained, *not captured at image level.

The map using ASD (2000) with a similar mineralogical correlation matrix corresponding to copiapite-(Cq)-(A-I-K) at correlation level 0.80, covers an area of 180,001.480 m² (Table 5.7) while the map using ASD (2007) correspond to 84,184.476 m². This comparison allows for the visualisation of the behaviour of multi-temporal similar mineralogical correlations, although the number of input spectra is distinct. The spatial pattern is different, once in the ASD 2000 data, the area is more concentrated along the open pit and surrounding the village, as well as in the Pomarão Harbour, while the area using ASD 2007 data is spread throughout other small villages, marking the railway track after Telheiro and with a broader dispersion in the Pomarão harbour. Also, downstream from the Telheiro area near the Chança dam there is a significant increase in this low pH class mapping. Even with a similar mineralogical correlation, the mapping results using different ASD input spectra show some discrepancies, which in this case were not eliminated by other type of input spectra. Remark on the final mapping at 0.80 correlations using the ASD 2000 spectra, the area is substantially reduced to 23,853.390 m² when intersected with the endmembers mapping.

In the same Figure 5.8 another comparison is done using the ASD 2007 as input spectra in the HyCORR-EFFORT corrected mosaic, testing in this case a different atmospheric correction. The results show again a different response, whether the ASD 2007 spectra are less spread than the ASD 2000. Details are given about the areas covered with ASD 2000 and 2007 in Table 5.8.

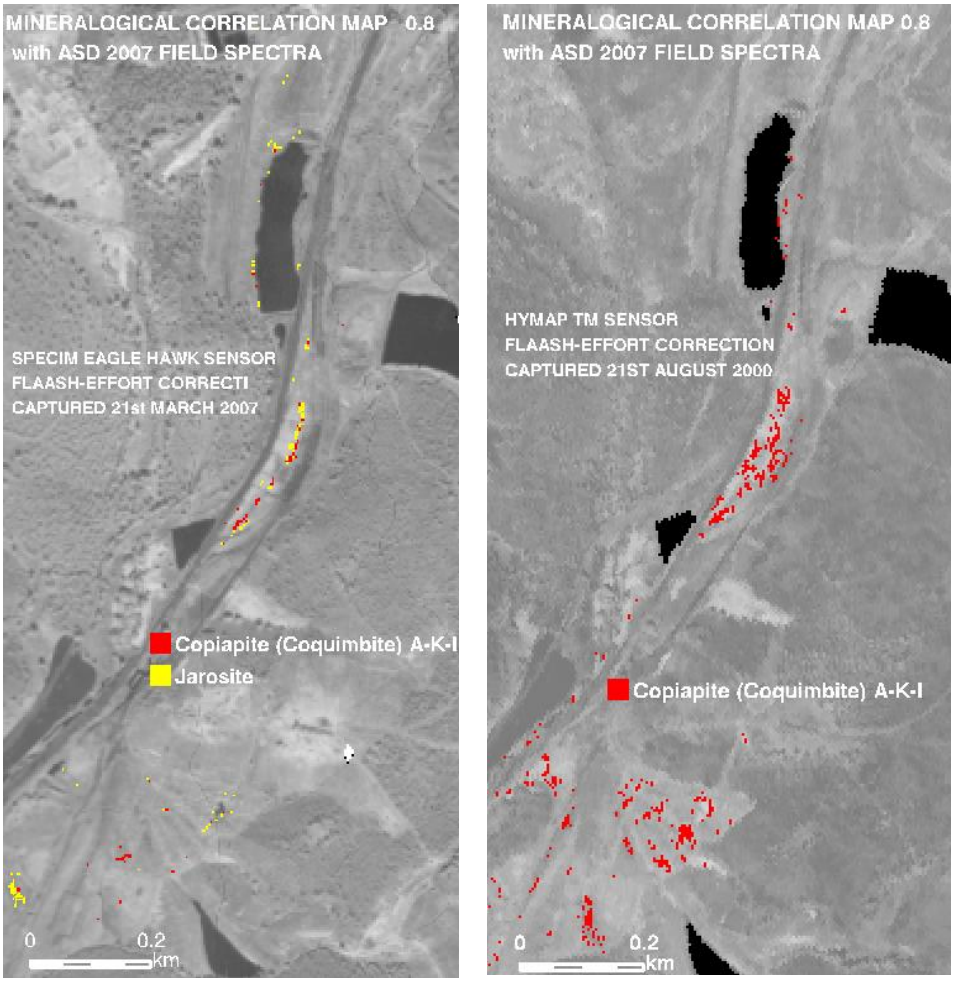

Figure 5. 7 Mineralogical correlation ≥0.80 map of subset area of Figure 5.4 using solely ASD field spectra collected in 2007. Left-Specim EAGLE HAWK (year 2007), and right-HyMap™ (year 2000).

Table 5. 8 Classification results from SAM using ASD field spectra for both HYCORR and FLAASH corrected mosaics at correlation level 0.80 for low pH class.

FLAASH-EFFORT MOSAIC CORRELATION ≥0.80				
MAPS / CLASS	ASD FIELD 2000	spectra n=15	ASD FIELD 2007	spectra n=13
	Area (m2)	CV	Área (m2)	CV
Co-Cq-A (I,S,K)	180,001.480	0,22	84,184.480 Meters²	0,32
HyCORR EFFORT MOSAIC CORRELATION ≥0.80				
MAPS / CLASS	ASD FIELD 2000	spectra n=15	ASD FIELD 2007	spectra n=13
	Area (m2)	CV	Área (m2)	CV
Co-Cq-A (I,S,K)	290,695.316	0,37	15,213.049	0,34

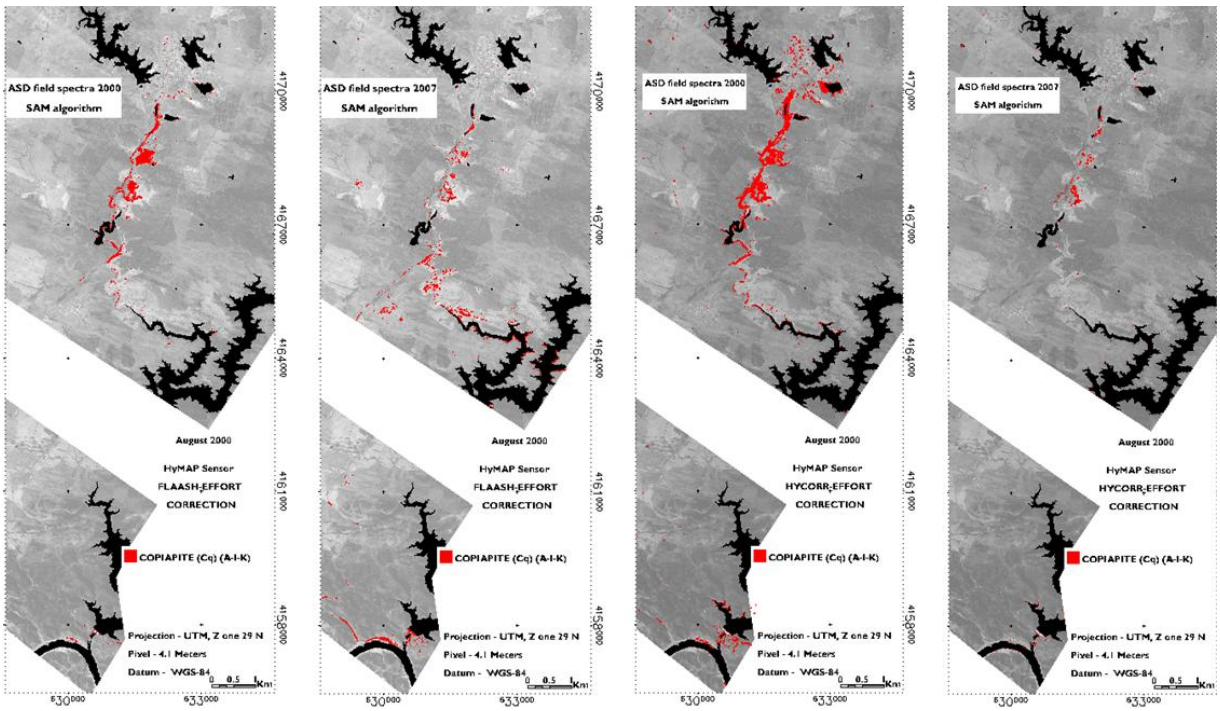

a) b) c) d)

Figure 5. 8 Comparison of SAM algorithm in IS 2000 with FLAASH-EFFORT (a and b) and HYCORR-EFFORT(c and d) mosaics using input ASD spectra collected in 2000 (a and c) and in 2007 (b and d) assigned to mineralogical correlation at mineralogical ≥0.80 with USGS mineralogical spectral library.

For multi-temporal comparison the images of interest are in Figure 5.8 a) and b) where the 2000 and 2007 ASD field spectra can be seen. The 2007 input spectra show a wider dispersion particularly south of TE and in the Pomarão harbour following the railway track, while the ASD 2000 maps show a broader area south of the open pit encompassing Moitinhos and AC. However, further environmental considerations have to be considered carefully. In fact, the patterns are distinct if using only one type of input spectra as seen in the analysis of 2000 HyMap^{TM} data, whether with HyCORR-EFFORT or with FLAASH-EFFORT polishing.

From the images in Figure 5.8 it is important to see that the maps obtained cannot be based solely in one type of input spectra. For example, from the two mosaics, the HyCORR-EFFORT covers the largest area with the ASD 2000, whilst with the ASD 2007 is the smaller. Again, this shows that the HyCORR-EFFORT presents more extreme results in function of the input spectra as already seen when using the multi-source methodology. In this case it is a trade-off between spectral homogeneity and mineralogical differentiation, which is seen by a generally lower value of Coefficient of Variation (CV) in the classes, obtained using FLAASH-EFFORT correction, as well as less spatial differentiation when using different mineralogical correlation threshold values (i.e. 0.90 or 0.80).

The selection of a full pixel methodology has its advantages according to what has been described in Section 5.1. As seen in Chapter 2, Section 2.1.4, the SAM algorithm presents some difficulties when the targets are small and encompass mixed pixels, whereas for the detection of the target is required a larger angle. The use of a standard angle has been the way to have a balanced result, neither losing too many targets neither having too many commission errors in classification. However, as in this case the input spectra are already concentrated in the target of interest should be tested with smaller detection angle.

5.3. ENVIRONMENTAL MONITORING OF S. DOMINGOS AREA

ASSESSMENT

In the waste mining materials map as established in Quental et al. (2002a), Appendix II, using ASD field spectra, the AMD has been detected through the most acidic class, i.e. designated as *mixed sulphur materials*. Other classes were based in the chemical content of the materials measured and defined as *contaminated soils and sediments*. This map was transformed in more effective mineralogical information based on the correlation matrix from contiguous spectral bands using multi-source spectral data.

From the previous classification, some input field spectra were excluded and others appear depending also on the threshold value selected, i.e. ≥0.80 or ≥0.90.

A low pH class <3 based in the mineralogical assemblage of copiapite, coquimbite, alunite, illite and kaolinite was determined from the multi-source spectral methodology, from which most of the previous *mixed sulphur materials* spectra were enclosed.

This signature excludes any other type of secondary iron minerals and is then the basis to attribute a clear pH value. Although usually assigned the same pH value to jarosite s.s., this class appears isolated in correlation matrix and in the HyCORR-EFFORT mosaic. Field data analysis seems to attribute a higher pH value in S. Domingos, whereas jarosite occurred in soil samples with pH values up to 4.2. Other classes indicate a mixture of secondary iron minerals and the establishment of pH values are more imprecise, being difficult to establish differences among few other classes such as G-L-J-Sc or G-L-Sc. Thus, the environmental concerns are focused in the more extreme class of low pH.

Derived from the maps obtained with the multisource spectral methodology the pH<3 spatial pattern is variable depending either on the threshold value or on the atmospheric corrections undertaken (Figure 5.1, 5.2. and 5.4). Nevertheless, the general trends are: I) surrounding the open pit, II) in the village spread mostly by construction materials, III) downward south of the open pit surrounding the acidic dams and following the pathway to Moitinhos where remain the cementation tanks, IV) AG where is located the sulphur plants, V) the pathway to TE encompassing more acidic dams, VI) downward to Chumbeiro where the S. Domingos river joins with the Chança river and VII) the railway linking the TE to the Pomarão harbour, and the harbour itself with a more less pronounced influence on the eastern side of the Chança river in the Spanish border.

This pattern indicates the spread of hazardous materials over all the area during the mine exploitation and afterwards by the use of mining waste materials, especially as pavements and construction.

MONITORING

The IS data gathered in year 2007 (March, wet season) of part of the same areas obtained in year 2000 (August, dry season) contains differences at several levels as referred to in Chapters 3 and 4, that confines the multi-temporal assessment to a mere trend due to the uncertainty associated with the results obtained.

The climate highly controls the precipitation and dissolution of efflorescent sulphates retaining hazardous elements like Cu and Pb in more or less stable minerals, e.g. jarosites, and releasing others such as Zn (Figueiredo et al., 2007) or spreading them when are solubilised. The cycling of metals and acid by the precipitation and dissolution of efflorescent salts is an important process at mine sites (Hammarstrom et al., 2005).

Coquimbite also appears when copiapite is dehydrated (Jamieson *et al*., 2005). The change, observed in Achada do Gamo, from coquimbite to copiapite must occur when the solid, in contact with the oxidizing normal atmosphere, is submersed by the saturated lake water that has a pH and an electric potential that falls inside the iron(II) ions stability field. This efflorescent assemblage of minerals is only observed during the summer (dry and hot season) once they dissolve with the first rains (Abreu et al., 2010).

The fact that the correlation matrix attributes very high values of sulphate minerals to materials a priori not identified as such, as depicted in Figure 5.6, seems to indicate that even in a different season the equivalent chemical content of these efflorescent salts can be detected.

The spatial dispersion of low pH class is lower than the one obtained with the same set of field spectra collected in 2007 for the IS data of year 2000. The same focus of copiapite-coquimbite-alunites appears surrounding the acidic dam south of the open pit as depicted in Figure 5.7 and jarosite appears nearby. In the Pomarão harbour, the pattern is very discrete, but a few spots appear in the borders of the platform as well as in the Chança dam. This can be explained by the new coverage of waste materials spread throughout the harbour simultaneously with IS data capture, covering the more acidic materials (Figure 5.8).

Figure 5. 9 Left-the Pomarão harbour with a set of temporary structures and new coverage of waste materials, in March 2007. Rigth-detail of old materials at the border of the new coverage.

However, as referred previously, for the differences reported in the images remains the doubt if the results achieved translate a temporal change, particularly taking into account that the IS data collected in 2000 was in the hot season and 2007 in wet season, or are connected to multi-sensor IS data differences. The several steps to minimise the differences for multi-sensor comparison may have introduced limitations on the 2007 IS data, and consequently in the capability to discriminate materials.

5.4. CONCLUSIONS

A multi-source spectral methodology was developed for the S. Domingos mine area, establishing a quantitative link among multi-source spectral data through correlation matrixes. From these multi-source spectral data at different levels, i.e. derived from image endmembers, field spectral measurements and from mineralogical spectral libraries (Clark et al., 1993, 1997), the high correlations established related to AMD are selected and are inputted to SAM algorithm generating two different maps in function of either field spectra or endmembers spectra. Each map is converted to high spectral correlations of mineralogical assemblages and the final map is the intersection of the two previous. The improved map is focused in low pH (<3) class corresponding to the mineralogical assemblage of copiapite-coquimbite-alunite-illite-kaolinite.

Through the application of this methodology combining different input spectra several aspects were highlighted:

I. the screening information obtained over unknown spectra by assigning it to the mineralogical components and focusing directly on the thematic target of interest, in this case AMD

II. the importance of local field spectral measurements in a different scale depicting in the image a local field reality

III. the importance of having information at image level through the endmembers, derived from the same scale as the area to map

IV. the differences in mapping results obtained by independent sources (b and c), which are minimised by conveying solely the common high mineralogical correlations at each pixel and its contribution to validation issues

The application of the multi-source spectral methodology in the S. Domingos area was undertaken generating two maps of mineralogical correlation ≥0.90 of low pH, using the HyCORR-EFFORT and FLAASH-EFFORT mosaics. The two maps show considerable differences in the area mapped and the mineralogical correlation classes are also different. The HyCORR-EFFORT depicts a jarosite class, whilst in the FLAASH-EFFORT the jarosite is enclosed within another mineralogical correlation class. The low pH class covers different areas in both, being of 78,368.216m^2 in HyCORR-EFFORT and 14,137.210 m^2 in FLAASH-EFFORT. Lowering the correlation threshold value to ≥0.80, the values increase to 225,724.669 m^2 and 23,853.390 m^2 respectively.

The areas mapped show in a general way, at its maximum spatial extension, depending on the correlation threshold and atmospheric corrections, low pH in the following areas: I) surrounding the open pit, II) in the village spread mostly by construction materials, III) downward south of the open pit surrounding the acidic dams and following the pathway to Moitinhos where remain the cementation tanks, IV) AG where is located the sulphur plants, V) the pathway to TE encompassing more acidic dams, VI) downward to Chumbeiro where the S. Domingos river connects with the Chança river and VII) the railway linking the TE to the Pomarão harbour, and the harbour itself with a more less pronounced influence on the eastern side of the Chança river in the Spanish border.

The variations are less pronounced in FLAASH-EFFORT, and are seen as a trade-off between spectral homogeneity and mineralogical differentiation in the two mosaics. The SAM algorithm shows also sensitiveness to the input spectra, reason why there is a need to control with another type of mapping to ensure that the results are intersected by both.

The multi-source spectral methodology was tested in SPECIM EAGLE-HAWK of year 2007, but the retrieval of information was very low, possible due to the pre-processing and atmospheric corrections in order to minimise the differences to the HyMap^{TM} data captured in year 2000. As a common factor for comparison of the multitemporal data, the ASD field spectra gathered in 2007 and at mineralogical correlation ≥0.80 was inputted to the SAM algorithm to map both 2000 and 2007 data. The results show the occurrence of low ph<3 in 2007 data south of the open pit in the acidic dam and at Moitinhos as well as a few pixels at the Pomarão harbour. In 2000, the similar areas mapped are broader. Due to the differences established in both mosaics, this comparison is merely a trend, remaining uncertain the seasonal changes according to different time of data capture, with visually strong evidences during the dry season with efflorescent salts.

From the processing of the IS data of the S. Domingos area following this methodology it can be concluded that the capability of mapping with high mineralogical correlations shows different results in function of the pre-processing and atmospheric corrections undertaken. The need of having multi-source spectral data is a pre-requisite in order to minimise deviations according to the full pixel algorithm used and as contribution for validation. Field spectral data reveal its importance as bridging the gap among local field information, laboratory spectral libraries and image scale.

Monitoring with IS data is itself a challenging task due to different viewing angle and illumination conditions particularly in the case of airborne capture. Adding to this, a multi-sensor approach complicates the system with different technical specifications. Furthermore, in the case of the S. Domingos area, seasonal variations have chemical/mineralogical implications in the AMD detection.

6. FROM AIRBORNE HYPERSPECTRAL TO SPACEBORNE MULTISPECTRAL SENSORS MAPPING RESULTS

6.0 INTRODUCTION

The high spectral resolution of imaging spectroscopy (IS) allows very detailed mapping concerning several properties of interest of the image targeted, as already illustrated in the previous chapters.

However, constraints in data capture such as high cost for aircraft and mobilization in a scientific environment and restricted windows of opportunities for campaigns (Chapter 2, Section 2.1.5; Holzwarth and Heldens, 2006; Reunsen et al., 2007), have implications on the use of IS data on a routine basis.

A way to partly overcome this is to use a spaceborne platform to carry an IS sensor instead of an airborne platform. In this way the routine acquisition of dataset and consequently the development of cost-effective monitoring systems based on IS is greatly facilitated.

Specifically concerning Acid Mine Drainage (AMD) detection it is important to see what can be translated from mapping results achieved using airborne IS datasets versus spaceborne IS datasets. Ideally, to compare both airborne and spaceborne datasets, they should be captured in a time frame close to each other to avoid both physical and/or chemical changes in the target analysed.

In the absence of a spaceborne IS data for the case study of the S. Domingos area, the multispectral image (MSI) Landsat Enhanced Thematic Mapper Plus (ETM+) acquired in the same period (August 2000) with 17 days apart of the airborne IS data is compared with the HyMap^{TM} mosaic.

The MSI is processed using FLAASH for the atmospheric corrections as the same way for the HyMap^{TM} data collected in 2000 (Chapter 4). The image is primarily processed as obtained in the waste mining materials map (Quental et al., 2002a; Appendix II) and afterwards using the same methodology as developed in Chapter 5.

6.1. AIRBORNE VERSUS SPACEBORNE IMAGES

When comparing airborne vs. spaceborne IS data acquisition, the latter is more advantageous when related to time consuming procedures and financial issues associated with providing data on a regular basis. However, it has a lower spatial resolution and signal-to-noise ratio (SNR). In fact, an electro-optical imaging system contains certain limitations based on the law of conservation of energy, where the amount of energy emanating from the surface per unit area and per unit wavelength is finite. Consequently, this generates a "trade-off space" among

spatial, spectral and noise components of an imaging system (Landgrabee, 1978). These physical limitations imply that even if the spectral resolution is similar for airborne and spaceborne IS sensors, e.g. many bands, variations exist on space and noise components.

Thus, detailed studies on a large scale necessarily require an airborne dataset acquisition. This limitation makes the use of a spaceborne IS sensor more suitable for studies at regional scale with a large resolution size i.e. only coarse features can be observed in the image, instead of the small resolution size achievable by airborne IS platform adequate for detailed local studies.

Literature research comparing IS airborne and spaceborne case studies in order to define what could be the major problems when tackling concrete applications of the IS data, are mainly focused on Hyperion sensor (Chapter 2, Section 2.1.3). A few authors such as Kruse et al. (2002; 2003) and Kuosmanen et al. (2005) report to the low signal to noise ratio (SNR) when comparing Hyperion either with HyMap™ or with AVIRIS. However, they also consider that the main outline or basic classes of thematic mapping is achieved and that spaceborne IS has potential.

In the absence of a spaceborne IS image for S. Domingos, is compared what can be translated from IS airborne (Hymap™) AMD mapping results to a spaceborne MSI. The main characteristics of both sensors are in Table 6.1.

Table 6. 1 Comparison of airborne HyMap™ with spaceborne Landsat ETM+.

Sensors	Flying height	Spectral range (μm)	Spectral resolution	Spatial resolution (m)	SwathWidth (km)	Number of bands	SNR	Scanner
HyMap™	2.2 km	0.437-2.285	10-20 nm	4.3	~2.5	126	~500:1	whiskbroom
Landsat ETM+	705km orbit	0.45-2.35*		30.0, 15.0 (Pan)	185	7*	Moderate	

*excluded thermal band

The objective in this chapter is two-fold:

I. To evaluate what are the capabilities of IS and MSI data in discriminating and mapping waste mining materials related to AMD surface materials, changing spatial and spectral resolution and,

II. To quantify in terms of area what is given by the AMD hot spots on both datasets.

This can clarify at what level MSI data can be applied to AMD detection facilitating the development of EO monitoring systems related to AMD. If satisfactory, the advantage is the possibility to extend the mapping to a regional scale, e.g. to the whole Iberian Pyrite Belt.

For comparison of both datasets, MSI and IS were standardized concerning spectral resolution, as well as calibration issues and classification methods. The general procedures were conducted as depicted in the flowchart in Figure 6.1.

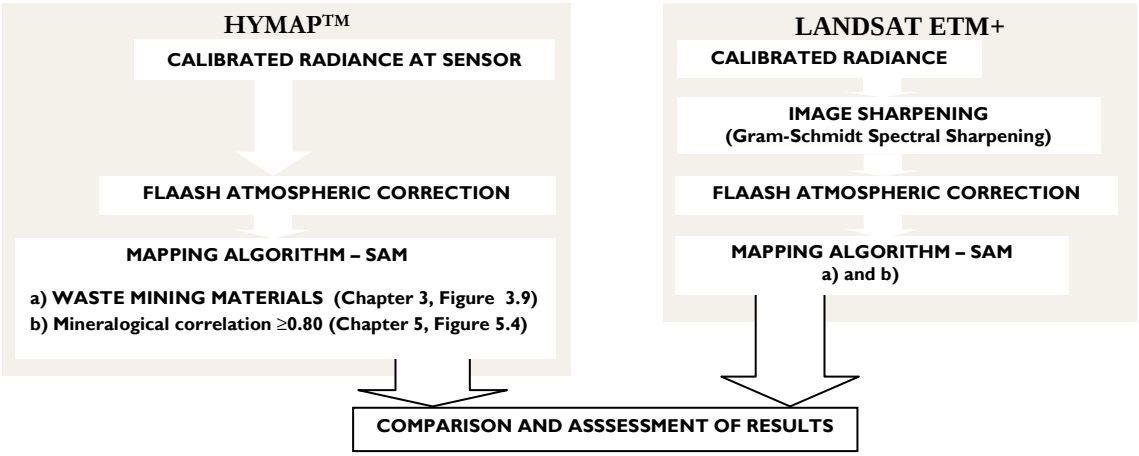

Figure 6. 1 Airborne IS and spaceborne multispectral procedures for mapping AMD.

6.2. MULTISPECTRAL DATA LANDSAT ETM+

6.2.1 RADIANCE DATA

The Landsat ETM+ was captured on the 4th August 2000 (L71203034_03420000804) for the S. Domingos study area. The VNIR-SWIR data, as well as the panchromatic image, given in digital numbers, were calibrated to radiance using details from the FAST files and WEB retrieval information using the ENVI software calibration capabilities. The sun elevation angle was 60.4 and the sun azimuth angle was 127.0. The data capture started at 10:59:38.71 GMT and finished at 11:00:05.69 GMT.

In order to increase the spatial resolution of the Landsat ETM+ from 30 m to 15 m, an image sharpening algorithm was used. The Gram-Schmidt Spectral Sharpening (GSSS) algorithm (Laben and Brower, 2000) sharpens low resolution multispectral data using panchromatic high spatial resolution data. Synthesizing the GSSS, in the first step a panchromatic band is simulated from the lower spatial resolution spectral bands. Second, a Gram-Schmidt transformation is performed on the simulated panchromatic band and the spectral bands, where the simulated panchromatic band is employed as the first band. Third, the high spatial resolution panchromatic band is swapped with the first Gram-Schmidt band. Finally, the inverse Gram-Schmidt transform is then applied to form the pan-sharpened spectral bands (ITT, 2010). An underlying assumption of these algorithms is that one can accurately estimate what the panchromatic data would look like using lower spatial resolution multispectral data.

The resultant image is valid if the main characteristics of the multispectral data are maintained. The statistics after the application of GSSS algorithm on the Landsat ETM+ L71203034_03420000804 is depicted in Table 6.2 for the multispectral data and the pan-sharpened results. Some variation is observed on the maximum and minimum values, being higher on the sharpened image, although the general pattern is maintained.

The correlation among some of the spectral bands shows slight variations, in the order of 1%, when comparing both datasets. This is negligible, and considering that the spatial resolution increases two-fold, is worth using it, especially when comparing to a much smaller spatial resolution of the airborne data (Table 6.1).

In Figure 6.2 shows a detail of the Landsat ETM+ of the transformation on the image, with increased visual discrimination of previously indiscernible features for the area.

Table 6. 2 a) Basic statistics for the Landsat ETM+ (calibRad-30 m) and the sharpened image (GSSS-15 m). b) Correlation matrix for the same dataset.

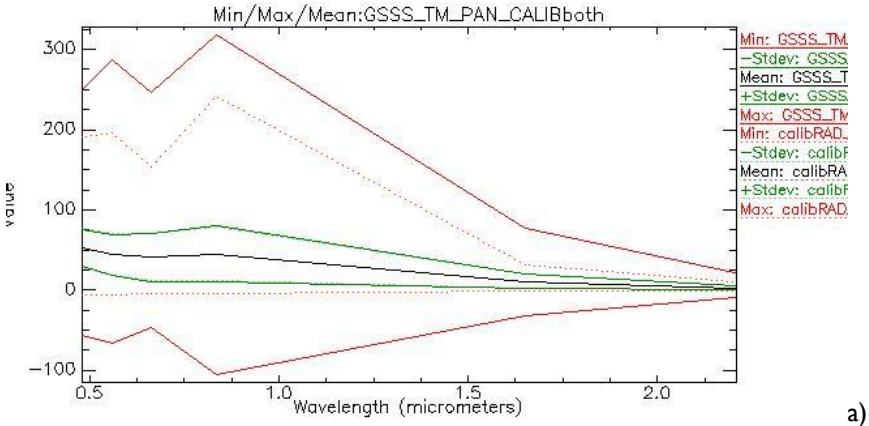

a)

b)

Multispectral Landsat ETM+ (different value for GSSS)						
Correlation	b 1	b 2	b 3	b 4	b 5	b 7
b 1	1.00	0.93	0.81	0.73	0.71	0.72
b 2	0.93	1.00	0.97	0.89	0.89	0.90
b 3	0.81	0.97	1.00	0.91	0.94	0.95
b 4	0.73	0.89	0.91	1.00	0.95	0.92
b 5	0.71	0.89	0.94	0.95	1.00	0.98
b 7	0.72	0.90	0.95	0.92	0.98	1.00

Pan-sharpened (GSSS algorithm)						
Correlation	b1	B2	b3	b4	b5	b7
b 1	1.00	0.92	0.80	0.72	0.70	0.71
b 2	0.92	1.00	0.97	0.90	0.90	0.91
b 3	0.80	0.97	1.00	0.92	0.95	0.96
b 4	0.72	0.90	0.92	1.00	0.95	0.92
b 5	0.70	0.90	0.95	0.95	1.00	0.98
b 7	0.71	0.91	0.96	0.92	0.98	1.00

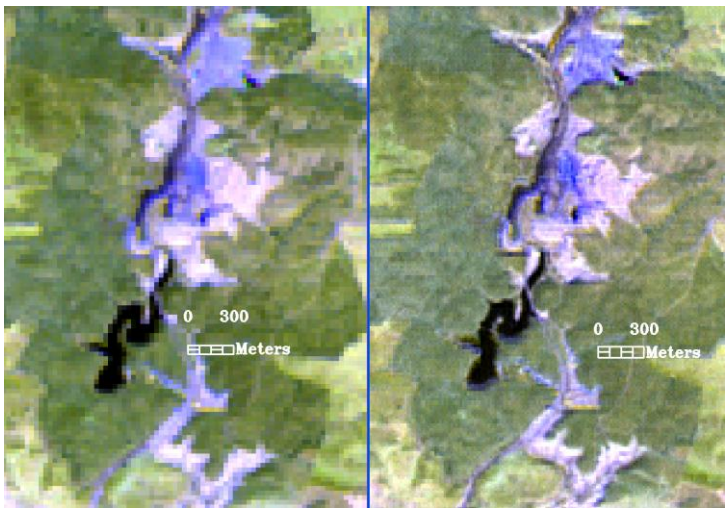

Figure 6. 2 Increased visual discrimination in a detail of Landsat ETM+ at Achada do Gamo by sharpening. Left-original multispectral (30 m pixel) and right-multispectral sharpened with panchromatic (15 m pixel) using Gram-Schmidt Spectral Sharpening algorithm. RGB: 751.

6.2.2 APPARENT REFLECTANCE DATA (FLAASH)

The image pan–sharpened in the previous Section (6.2.1) was the input for the atmospherical corrections using a radiative transfer model. The corrections were conducted in the *Fast Line-of-sight Atmospheric Analysis of*

Spectral Hypercubes (FLAASH) module of the ENVI software (ITT, 2010) as described in Chapter 4. According to the characteristics of the area and time of data capture, the atmospheric model used was a mid-latitude summer and the aerosol model rural, adequate to the area of analysis. The characteristics of the image after atmospherical corrections are in Table 6.3.

Table 6. 3 a) FLAASH average spectral values for sharpened Landsat ETM+, b) covariance and correlation.

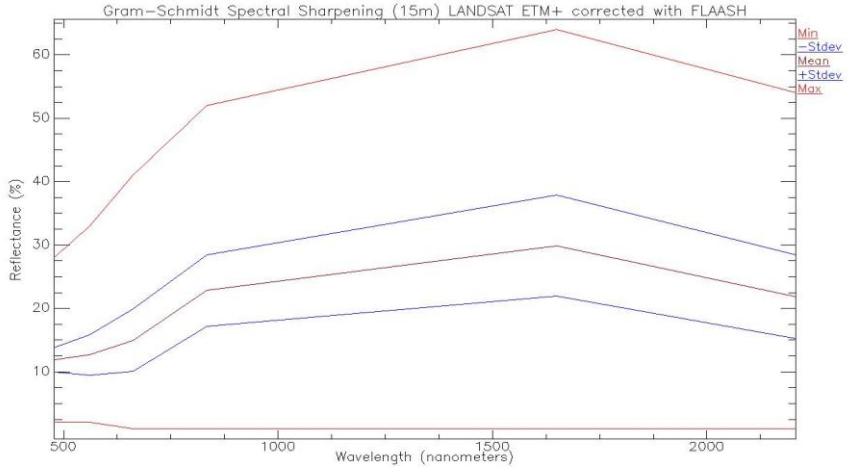

a)

b) Covariance	B1	B2	B3	B4	B5	B6
B1	3.87	6.05	8.86	9.01	11.77	10.11
B2	6.05	10.51	15.52	15.56	20.71	17.78
B3	8.86	15.52	24.51	24.81	33.93	28.47
B4	9.01	15.56	24.81	31.73	38.49	29.41
B5	11.77	20.71	33.93	38.49	63.31	50.38
B6	10.11	17.78	28.47	29.41	50.38	43.92

Correlation	B1	B2	B3	B4	B5	B6
B1	1	0.95	0.91	0.81	0.75	0.77
B2	0.95	1	0.97	0.85	0.8	0.83
B3	0.91	0.97	1	0.89	0.86	0.87
B4	0.81	0.85	0.89	1	0.86	0.79
B5	0.75	0.8	0.86	0.86	1	0.96
B6	0.77	0.83	0.87	0.79	0.96	1

6.2.3 WASTE MINING MATERIALS MAPPING

The image processing as detailed on Chapter 3 in Figure 3.9 using an IS mosaic also with a radiative transfer modelling, is tested with the Landsat ETM+ images corrected with FLAASH in the previous Section.

The first part of the methodology using information derived solely on the image, using an Authomated Hour Glass sequential combination of algorithms in ENVI, generates seven endmembers. The Spectral Angle Mapper (SAM) algorithm using a standard maximum angle of 0.1 gives a pattern of the contamination area similar to the one obtained using a calibrated Landsat ETM+ as undertaken in Quental et al. (2002a). However, it is not possible to clearly exclude some classes for the next step of the classification without avoiding a mismatch with potential areas of interest. This is due to low number of endmembers which stems from the fact of the low spectral discrimination that these images contain.

For the next step of the classification through the SAM algorithm, the input spectra are the ASD field measurements displayed on Figure 6.3a), which were resampled to the spectral range of Landsat ETM+ (Figure 6.3b). The radian angle was the standard 0.1.

Thus, the next step using field spectral measurements is conducted without masking, making redundant this step in the multispectral classification, as expected due to the low spectral resolution.

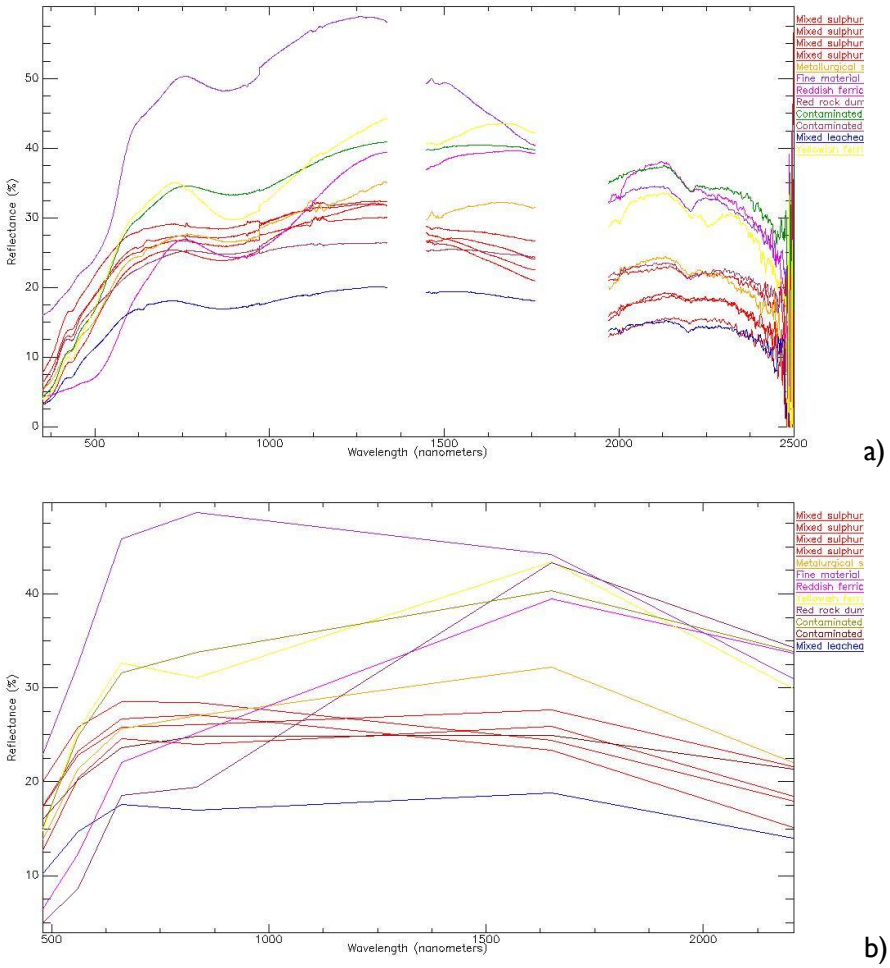

Figure 6. 3 a) ASD field spectra measurements, and b) Resampling of a) to Landsat ETM+ spectral range.

The results are depicted in Figure 6.4 c) and d), respectively, the distribution of classes in percentage and the spatial mapping.

Focused already on a few selected spectra from previous hyperspectral data classification, the mapping shows the dispersion of the different type of spectra concentrated on the areas mostly controlled by the AMD, assessed mainly by the spectra of the mixed sulphur materials. Specifically for this class, although the name is the same, the spectra are inputted to the classifier individually into four spectra, 150, 152, 153 and 154. The distribution shows 3, 45, 1293 and 564 pixels, respectively, for the mixed sulphur materials classes, which present high similarity (Figure 6.5).

It is worth noticing that the comparison between the maps generated by the endmembers or the field spectra, the discrimination appears to be higher using the latter. Again, as observed in IS imaging processing in Chapter 5, Section 5.2, the field spectra seem to play also a key-role when processing MSI as a more independent source of input data.

a)

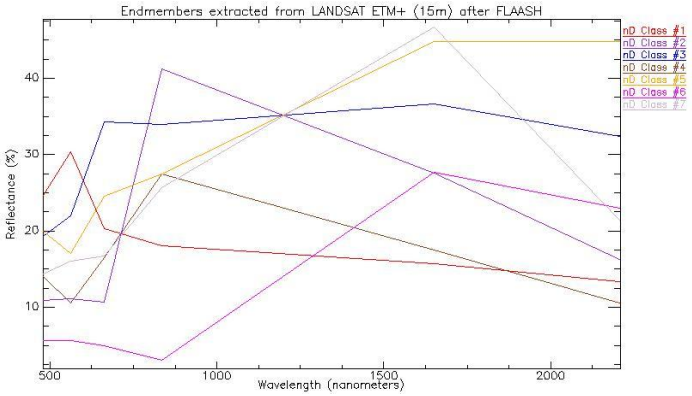

c)

Class Name	Meters²	Pct
Unclassified	152,887,050.0000	97.13%
MIXED SULPHUR M	428,400.0000	0.27%
METALLURGICAL S	348,300.0000	0.22%
FINE MATERIAL A	16,200.0000	0.01%
REDDISH FERRICR	63,675.0000	0.04%
YELLLOWISH FERR	11,925.0000	0.01%
CONTAMINATED SOILS AND SEDIMENTS	2,956,725.0000	1.88%
CONTAMINATED SOILS WITH SHALE FRAGMENTS	665,550.0000	0.42%
MIXED LEACHEATE	26,775.0000	0.02%

b)

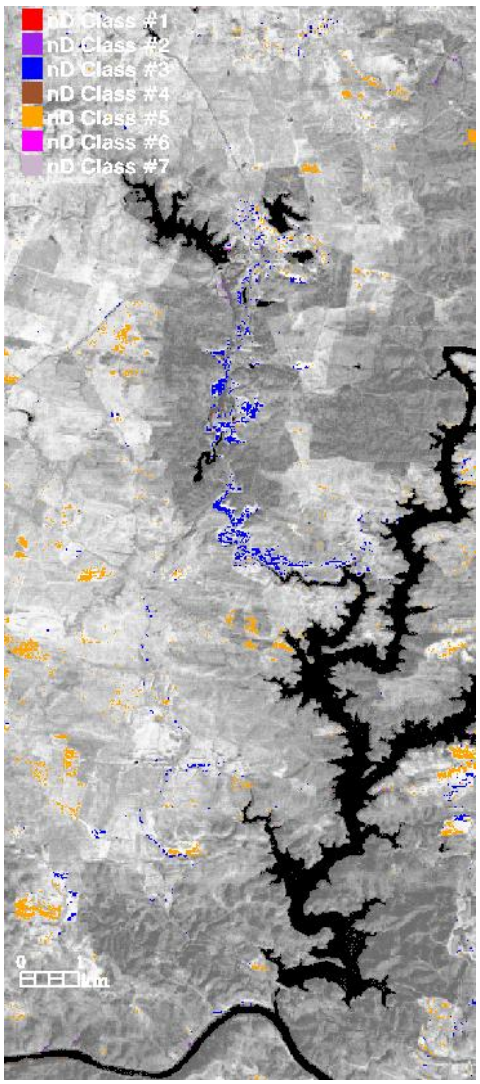

d)

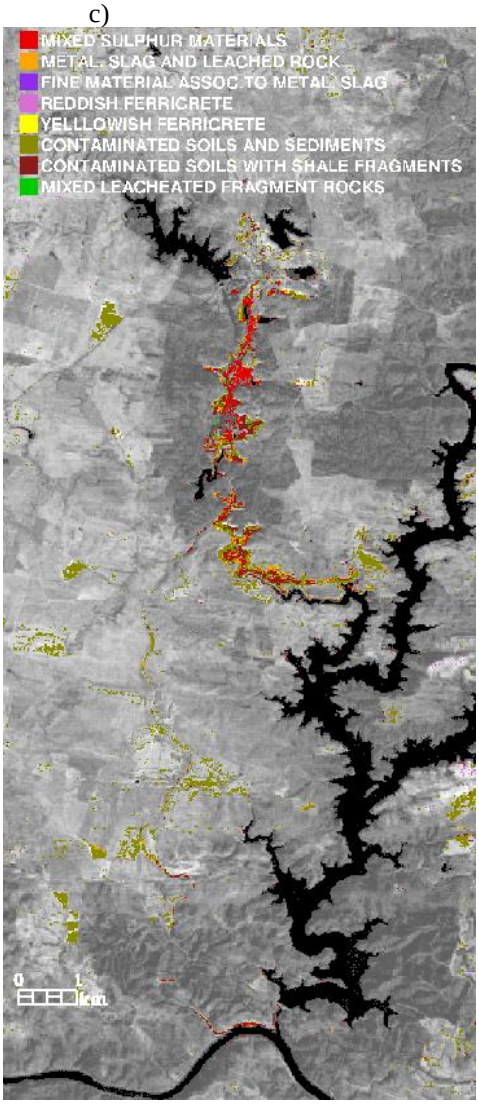

Figure 6. 4 a) Endmembers extracted from pan-sharpened Landsat ETM+ image (15 m pixel) and SAM (0.10 radian) with the same endmembers b). c) and d) SAM (0.10 radian) classification results using ASD field spectra.

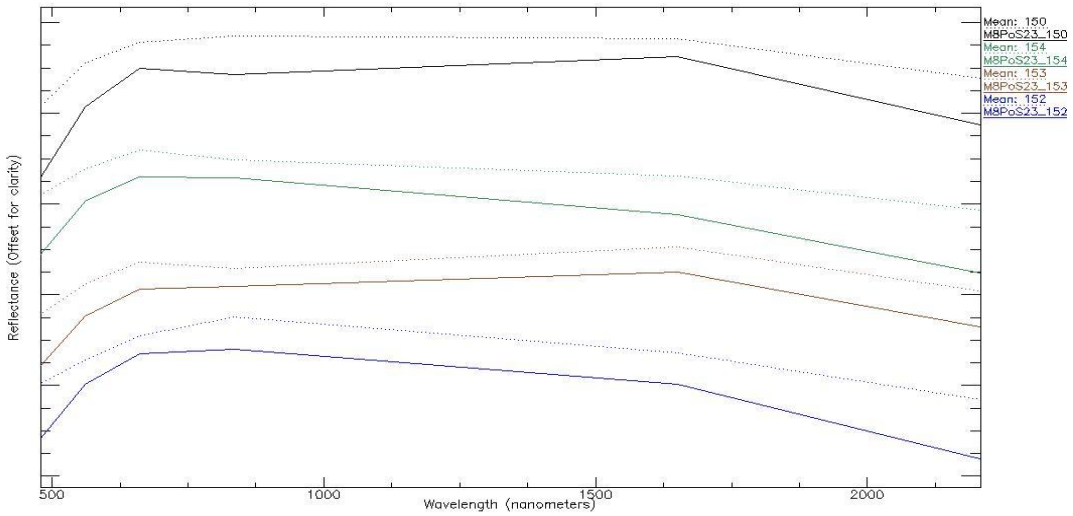

Figure 6. 5 Comparison of field spectra of mixed sulphur materials (solid) and average of SAM results of Figure 6.4d)(dotted).

To evaluate post classification results and compare relative distributions of spectral data from thematic classes per band, the statistical parameter coefficient of variation (CV) (Chapter 5, Section 5.2) was calculated for each class. Generally, a value of CV<1 means: distribution has low data variability and probably absence of anomalous data; 1<Cv> 1– existence of variability on data distribution; Cv > 2– high data variability, presence of outliers. The results obtained for Landsat ETM+ pan-sharpened image are all below 1, as depicted in Figure 6.6.

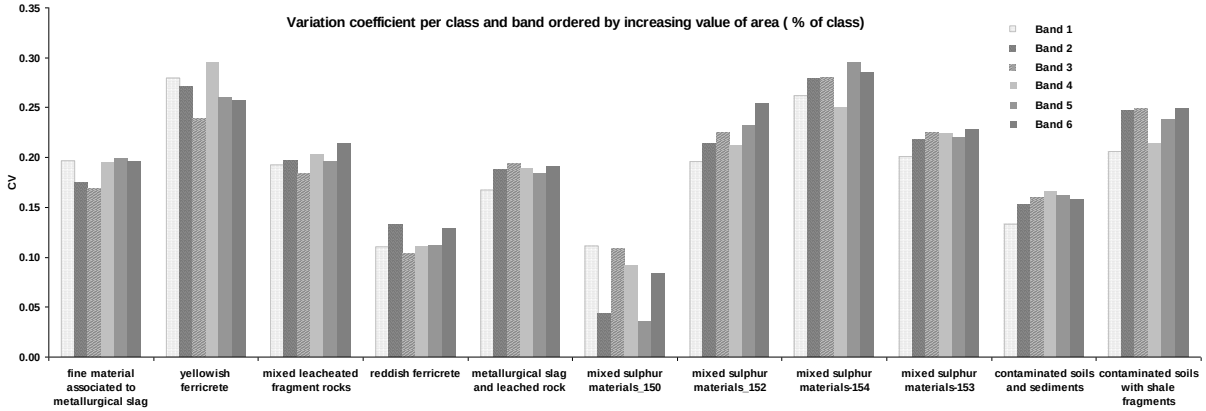

Figure 6. 6 Coefficient of variation per class.

To evaluate post classification results and compare relative distribution of spectral data from thematic classes per band, the statistical parameter coefficient of variation (CV) (Chapter 5, Section 5.2) was calculated for each class per band. In average, class material types present a CV value around 0.19, much lower than 1, which means that classified features are represented by homogeneous pixel spectral values, with low variability and probably without anomalous spectral data. Ordered by average of bands in each class, from the highest CV (0.28) to the lowest (0.08) the classes are as following: mixed sulphur materials-154 (0.28) > yellowish ferricrete (0.27)> contaminated soils with shale fragments (0.23)> mixed sulphur materials-152(0.22) > mixed sulphur materials-153(0.21) > mixed leached fragment rocks (0.20) > fine material associated to metallurgical slag(0.19) > metallurgical slag and leached rock (0.18)> contaminated soils and sediments(0.16) > reddish ferricrete (0.12) > mixed sulphur materials-150(0.08). However, the latter present's high homogeneity reports only to three pixels.

The highest CV value is 0.29, for band 5 of the class mixed sulphur materials-154 with an average for all bands of 0.28, and the band 4 (0.29) of the class yellowish ferricrete with an average value of 0.27. Although the CV values are the highest, they are still quite far from the value 1, thus being considered as robust results in this case.

The Root Mean Square (RMS) error for the classes shows quite high residuals, increasing the uncertainty about the match of the spectra. Within the classes of interest there seems to have some mismatch with much flattened spectral signatures, namely water with mixed sulphur materials or fine material associated to metallurgical slag. An RMS error shows that the deviation is high. In order to minimise the RMS, a trial with a Spectral Angle Mapper (SAM) using different smaller angles was undertaken. The smallest angle giving significant results is 0.05 radians. The results for the latter show that the RMSe is only minimized for few spectra, respectively 152 and 153. However, by minimising the angle it is observed that the mixed sulphur materials are the remaining last classified signature, which shows the strength of the association of the low pH signature with spectral data.

Comparing results of mining waste materials, with an AMD signature given by mixed sulphur materials and also by fine materials associated to metallurgical slag, both at MSI and IS data (undertaken in a FLAASH-EFFORT mosaic) the area covered is 444,600.00m^2 and 87,327.950 m^2 respectively. However, one of the mixed sulphur spectrum, 153, has a copiapite-coquimbite correlation below 0.80 and constitutes the major coverage of this class in MSI. If it is excluded from mapping, the AMD signature diminishes to 166,050.000 m^2, and in IS data to 48,564.090 m^2, more similar to a final copiapite-coquimbite(I-S-K) assemblage of low pH. Thus, even when the spectral resolution is low it is essential to have previous knowledge of correlation of mineralogical assemblages in order to select the adequate spectra. This is only achievable with high spectral resolution data.

6.2.4 MINERALOGICAL CORRELATION MAPPING

The same set of input either of endmembers and ASD spectra as used in the mineralogical correlation map in Chapter 5 (Table 5.7) (Table 6.4) has been resampled to the MSI wavelength. From these input spectra, the ones depicted in Table 6.4 are mapped in Figure 6.7, and spatially on Figure 6.8.

In the endmembers are only mapped 161 pixels corresponding to class #23 and #77 (Table 6.4). By contrast, the ASD field spectra are high, mapping 763 pixels. The final intersection area related to low pH class shows great similarity with the results obtained both spatially (Figures 5.7 and 6.7) and per m^2 (Table 6.4). The CV does not show strong differences, being more evident and higher in the final map of the Landsat ETM+.

Table 6. 4 Classification results from SAM in Landsat ETM+(upper) using the input spectra as in HyMap™ correlation level 0.80 for low pH class (lower).

LANDSAT ETM+	FLAASH-EFFORT Correction CORRELATION ≥0.80							
MAPS / CLASSES	ASD FIELD			ENDMEMBERS			MINERALOGICAL CORRELATION ≥0.80	
	Spectra	Area (m²)	CV	Spectra	Área (m²)	CV	Área (m²)	CV
Copiapite (Coquimbite) -alunite (I,S,K)	136-149-150-151-152-154-155-156-193-194-203-204-225	418,275.000	0,27	#(23-77)	36,225.000	0,24	29,700.000	0,24
HyMapTM FLAASH-EFFORT MOSAIC CORRELATION ≥0.80								
MAPS / CLASSES	ASD FIELD			ENDMEMBERS			MINERALOGICAL CORRELATION ≥0.80	
	Spectra	Area (m²)	CV	Spectra	Área (m²)	CV	Área (m2)	CV
Copiapite (Coquimbite) -alunite (I,S,K)	136-149-150-151-152-154-155-156-193-194-203-204-205-206-225	180,001.480	0,22	#(19-21-23-29-38-66-67-77)	38,125.080	0,25	23,853.390	0,17

Spectral average values and standard deviation are in Figure 6.7, for both individual mapping of ASD and endmember spectra as well as the average value given by IS data in Chapter 5.

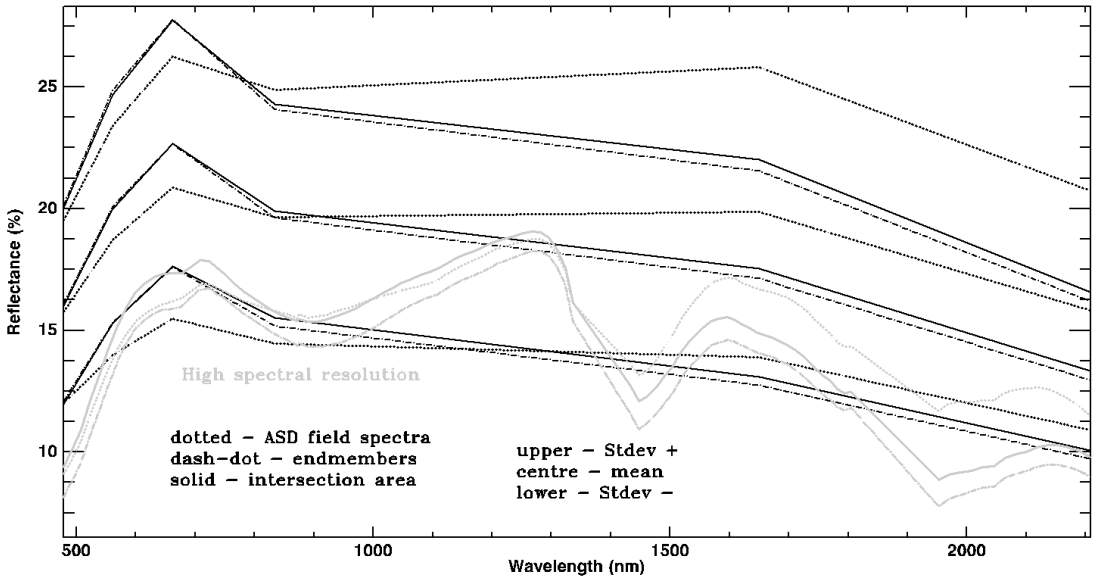

Figure 6. 7 Average spectral patterns and standard deviation of multispectral low pH map (black) compared with average results obtained with hyperspectral data (gray)(Chapter 5).

The spatial dispersion obtained shows that is possible to broadly outline the low pH AMD minerals on Landsat ETM+ in a similar way as achieved with the HyMap^{TM} (Chapter 5, Figure 5.4), although spatial variations exist particularly south of the open pit southwards to the acidic dam. Despite these local differences, it's worth noticing that these results are based in the input spectra of IS data with their differentiation capabilities achieved by mineralogical correlation, focusing in the high correlation of minerals associated with low pH values. If the results are obtained without this mineralogical correlation providing further knowledge about the input spectra the uncertainty increases, already in a broad outline (Figure 6.7). This similarity between IS and MSI diminishes when just using field spectra as can be observed in the waste mining materials map both in IS and MSI (Chapter 3 and Section 6.2.3). Also, when the field spectra are assigned to mineralogical correlation and set to high values, i.e. ≥0.80, the low pH signature is quite distinct, as seen in the end of the previous Section (6.2.3).

Kruse and Perry (2007), when extending the IS signatures to regional mapping using IS data conclude that the mapping should be conducted using spectral measurements, instead of mineralogical mapping with much lower discriminating capability when using multispectral dataset. This has already been done even when mapping IS data, relying instead on all spectrum mineralogical correlation knowledge to assign low pH values.

The low spectral and spatial resolution is also seen in the requirements of less input spectra to map similar areas of this specific mineralogical associated related to low pH (Table 6.4).

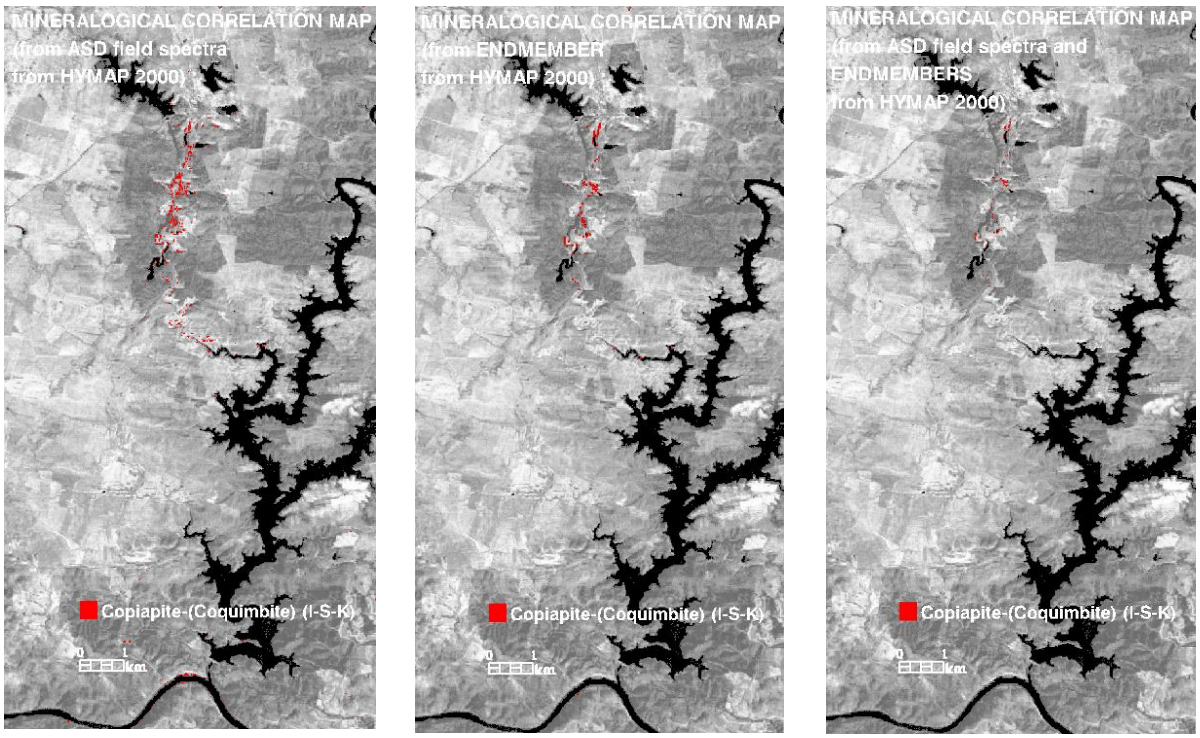

Figure 6. 8 SAM results of sharpened Landsat ETM+ for input spectra of Table 6.4 at mineralogical correlation ≥0.80. Left-from ASD field spectra, centre-endmembers and right-intersection of previous.

6.3. CONCLUSIONS

To evaluate what are the capabilities of IS (HyMap™) and MSI (Landsat ETM+) data in discriminating and mapping waste mining materials related to AMD surface materials, the images were processed to generate two maps:

I. Waste mining materials map related to AMD using field spectra (Chapter 3, Figure 3.9, Appendix II)

II. Mineralogical correlation map ≥0.80 AMD (Chapter 5, Figure 5.4).

To diminish the spatial differences the MSI, captured 17 days apart from the IS, was sharpened to 15 m and atmospherically corrected using FLASSH. All input spectra were resampled to the MSI wavelength range.

In I), the results depict a broader outline than with the IS waste mining materials map, with coherent CV classes, although with RMSe with high residuals. In area, the low pH classes assigned to the classes mixed sulphur materials and fine material associated to metallurgical classes covers 444,600.00m^2 and 87,327.950 m^2 in IS (conducted in the FLAASH-EFFORT mosaic). This value decreases to 166,050.000 m^2 and to 48,564.090 m^2 if further mineralogical correlation information is added and set to high values i.e. ≥0.80. This demonstrates that even if the spectral resolution is lower than IS, the final product of AMD mapping is quite different if knowledge derived from high spectral resolution data is considered to select the input spectra.

In II), comparing the two maps, i.e. endmembers and field spectra, generated before the final intersection, the dispersion is higher in the latter (Figure 6.8), as already observed in IS mapping (Table 6.4). The final map of copiapite-coquimbite (I-S-K) assemblage of low pH covers an area of 29,700.000 m^2 closer to the area derived for the same class in IS data, i.e. 23,853.390 m^2. It is important to notice that this similarity of results is achieved by resampling information from field spectroscopic data, images of high spectral resolution and with additional knowledge derived from the correlation matrix. Thus, when applied to the S. Domingos test site the mapping

results from IS can be translated to MSI data, with a relative certainty. This highlights the importance of IS data in developing knowledge that decreases the uncertainty about mapping results.

Another important point concerns the specificities of an AMD signature, with a strong association of the mineralogical assemblages and the spectral data, remaining one of the last classes to disappear when the angle of the mapping algorithm is minimised. This imply that the conclusions reported to AMD signature when extending to MSI mapping results should be carefully considered when the thematic target is different.

Although the ability to identify spectral signatures of specific materials is highly dependent both upon the spectral and the spatial resolution of the data, in this case a specific signature of target of interest has been isolated, i.e. the AMD. This allowed achieving similar mapping results, even if the spectral width and spatial resolution changed from 126 to 6 bands and from 4.1 m to 15 m respectively in IS and MSI data.

With the results obtained, there is potential to extend the AMD to a regional scale, e.g. the whole of the Iberian Pyrite Belt, which has a strong environmental footprint derived from long term mining activity.

7. CONCLUSIONS

7.1. CONTRIBUTION FOR THE USE OF IMAGING SPECTROSCOPY (IS)

IS allows to map surfaces at a mineralogical and/or chemical level with a non-destructive character. The spectral response given by an IS sensor allows the expansion of a point spectroscopy to a spatial dimension providing the capability of gather spectral information over wide areas. The absorption features obtained by an IS sensor facilitates the quantitative and qualitative characterization of both the surface and the atmosphere.

This capability adds more complexity to the regular image processing chain. A few constraints occur presently related with IS data accuracy and validation processes as well as lack of agreed standards (Holzwarth and Heldens, 2006; Reunsen et al., 2007). Particularly in the case of application of classical validation or accuracy assessment to IS data, limitations are reported to the fact that IS may map the environment with greater accuracy than can be obtained by field crews or maps produced by other methods then remote sensing (Aspinall et al., 2002; Jacquez et al., 2002; Foody, 2008).

A way to minimise the uncertainty about the thematic maps obtained, i.e. in this case assign mineralogical associations to each pixel related to Acid Mine Drainage (AMD), is to use multi-source data correlated quantitatively and combine different mapping results.

7.1.1 THE MULTI-SOURCE SPECTRAL METHODOLOGY

The multi-source spectral methodology improves the final mapping results by eliminating uncertainties at two levels. The first level is at the input data and establishes a quantitative link among multi-source spectral data through correlation matrixes. From these multi-source spectral data at different levels, i.e. derived from image endmembers, field spectral measurements and from mineralogical spectral libraries (Clark et al., 1993), the high correlations related to AMD environmental minerals indicators are selected and are inputted to SAM algorithm generating two different maps in function of either field spectra or endmembers spectra. Each map is converted to high spectral correlations of mineralogical assemblages.

The second level is to consider only the intersection area of both maps in function of mineralogical assemblages. The final map is focused in a low pH (<3) class corresponding to the mineralogical assemblage of copiapite-coquimbite-alunite-illite-kaolinite-smectite.

Through the application of this methodology combining different input spectra further significant contributions have been added with respect to the use of IS applied to mining environments and in particular, within the study area, has highlighted:

I. the screening information obtained over unknown spectra by assigning it to the mineralogical components and focusing directly on the thematic target of interest, in this case AMD.

II. the importance of local field spectral measurements with higher radiometric and SNR and spectral resolution than the image scale, depicting in the image a local field reality.

III. the importance of having information at image scale through the endmembers, derived from the same scale as the area to map

IV. the differences in mapping results obtained by independent sources (II and III), which are minimised by conveying solely the common high mineralogical correlations at each pixel and its contribution to validation issues.

7.1.2 ASSESSMENT AND MONITORING OF AMD IN THE S. DOMINGOS STUDY AREA

The multi-source spectral methodology was applied in the S. Domingos study area revealing an exclusive low pH (<3) mineralogical assemblage, whereas jarosite is not contained at high correlation level. This methodology was applied both with different correlation thresholds, i.e. at ≥0.80 and ≥0.90, and with different software for the atmospheric corrections using a radiative transfer modelling (FLAASH and HYCORR with EFFORT polishing) in the case of IS year 2000 (HyMap^{TM}).

From this we concluded that the spatial dispersion based on mineralogical correlation minerals of low pH is variable, either as a function of the atmospheric corrections undertaken or the threshold of correlation selected.

The areas mapped show in a general way, at its maximum spatial extension, depending on the correlation threshold and atmospheric corrections, pH<3 in the following areas: I) surrounding the open pit, II) in the village spread mostly by construction materials, III) south of the open pit surrounding the acidic dams and following the pathway to Moitinhos where the cementation tanks remain, IV) Achada do Gamo where the old sulphur plants are located, V) the pathway to Telheiro encompassing more acidic dams, VI) from Telheiro to southward to Chumbeiro where the S. Domingos river meets with the Chança river and VII) the railway linking Telheiro to the Pomarão harbour, and the harbour itself with a more less pronounced influence on the eastern side near the Spanish border.

The variations in mapping result compared with HyCORR-EFFORT are less pronounced using FLAASH-EFFORT, and are seen as a trade-off between spectral homogeneity and mineralogical differentiation in the two mosaics.

From the input spectra to mapping algorithms, the local ASD field spectra maps wider areas than the endmembers and shows less differentiation in function of the different atmospheric corrections conducted in the IS mosaic. Thus, field spectra can be considered as a more independent source of information, which is coherent with a smaller field-of-view and less influence of illumination conditions when measured. Nevertheless, the broader area mapped shows the need of having multi-source spectral data in order to minimise deviations according to the full pixel algorithm used and as contribution for validation.

The application of the same methodology to the SPECIM EAGLE-HAWK of year 2007 was not efficient. A common factor for multi-temporal comparison was to map with the ASD field spectra gathered in 2007 and at mineralogical correlation ≥0.80 was inputted to the SAM algorithm to map both 2000 and 2007 data.

The results show the occurrence of low pH (<3) in 2007 data south of the open pit in the acidic dam and at Moitinhos as well as a few pixels at the Pomarão harbour more or less accompanied by the jarosite class. In 2000 the similar areas mapped are broader.

However, the mapped areas cannot be addressed in a quantitative way but merely as an evolutionary trend, due to the differences established in both mosaics (see Chapter 4). These differences occur both at global statistics and specific targets of interest and reasons for this include, but not limited to: the seasonality corresponding to the wet period of the S. Domingos area in 2007 comparing to the dry period in 2000 and consequent effects in vegetation patterns, and the different viewing angle and illumination geometry of multi-sensor data capture.

Monitoring with IS data is itself a challenging task particularly in the case of airborne capture. Adding to this, a multi-sensor approach complicates the system with different technical specifications. Furthermore, in the case of the S. Domingos area, seasonal variations have chemical/mineralogical implications in the AMD detection.

7.1.3 FROM AIRBORNE HYPERSPECTRAL TO SPACEBORNE MULTISPECTRAL SENSORS MAPPING RESULTS

To evaluate what are the capabilities of IS (HyMap^{TM}) and MSI (Landsat ETM+) data in discriminating and mapping waste mining materials related to AMD surface materials, the MSI sharpened and atmospherically corrected was processed to generate two maps:

I. Waste mining materials map related to AMD using field spectra (Chapter 3, Figure 3.9)

II. Mineralogical correlation map ≥0.80 AMD (Chapter 5, Figure 5.4).

In I), the results depict a much broader outline than with the IS waste mining materials map, with coherent CV classes, although with RMSe with high residuals. In II), comparing the two maps, i.e. endmembers and field spectra, generated before the final intersection, the dispersion is higher in the latter (Figure 6.8), as already observed in IS mapping (Table 6.4). The final map of copiapite-coquimbite (A-I-S-K) assemblage of low pH covers an area closer to the area derived for the same class in IS data.

It's important to notice that this similarity of results is achieved by resampling information from field spectroscopic data, images of high spectral resolution and with additional knowledge derived from the correlation matrix. Thus, when applied to the S. Domingos test site the mapping results from IS can be translated to MSI data, with a relative certainty. This highlights the importance of IS data in developing knowledge that decreases the uncertainty about mapping results.

Another remark should also be done concerning the specificities of the AMD signature, with a strong association of the mineralogical assemblages and the spectral data on this test site. This implies that the conclusions reported to AMD signature when extending to MSI mapping results should be carefully considered when the thematic target is different.

Although the ability to identify spectral signatures of specific materials is highly dependent upon both the spectral and spatial resolution of the data, in this case it has been isolated a specific signature of target of interest, i.e. the AMD. This allowed achieving similar mapping results, even if the spectral width and spatial resolution changed from 126 to 6 bands and from 4.1m to 15m respectively in IS and MSI data.

With the results obtained there is potential to test the extension of the AMD spectral signatures to a regional scale, e.g. at Iberian Pyrite Belt scale where a strong environmental footprint derived from long term mining activity is inevitably observed.

7.1.4 GOVERNMENTAL POLICIES RELATED TO MINING ENVIRONMENTS

Imaging Spectroscopy is an appropriate method to comply with the demand of environmental data as set by legal requirements of current European Directives, by minimizing costs of density sampling and analysis. These include the Soil Policy Development and Soil Strategy from DG ENV, in particular soil monitoring, and the

directive 2006/21/EC on the management of waste from extractive industries, as well as the Integrated Pollution Prevention and Control directive (IPPC, 2008/1/EC).

The results obtained in S. Domingos using a multi-source methodology delineated in areas of pH<3. The generation of metal-laden effluents of low pH, if not carefully managed can contaminate soils, surface water courses and groundwaters and have a derived impact on ecosystems. The AMD is more evident in old mining areas due to the different environmental concept at the time and technological issues, which were not able to prevent or control the associated damage.

When considering environmental assessment the critical areas for safety protection and remediation measures should take no risks and should be assigned to a low correlation threshold, in this case pH<3 map with mineralogical correlation ≥0.80. Again, the lack of standards in IS appears relevant, when the maps are different in function of the atmospheric corrections undertaken.

Relatively to the monitoring capabilities of IS data, they have a few limitations. Airborne capture remains difficult and many times dependent of the aircraft's ability to fly, sensor availability and atmospheric conditions amongst others. In this case the data capture in 2007 was in a different season than the recommended for monitoring purposes.

However, the fact that IS methodology and results were translated to a contemporary MSI image generating a similar map of pH<3 opens perspectives for the routine use of spaceborne MSI but with less uncertainty relying on IS knowledge (see below Section 7.2.4).

Another possibility as IS as a component of cost-effective monitoring systems (Section 7.2.5) is the use of field spectroradiometer.

7.2. FORWARD DEVELOPMENTS

7.2.1 PRE-PROCESSING

The removal of atmospheric effects, a key factor that controls all subsequent image processing (Chapters 4 and 5), has been dealt here through physical models, i.e. radiative transfer modeling, and some tests conducted using statistical models. However, "noise" in IS images may not be removed completely, depending on the model(s) used and of the conditions of dataset capture. Part of this noise can be identified through its spatial structure and thus be filtered using geostatistical methods.

In order to remove noise, a methodology was partially tested with the HyMap™ data (Quental et al., 2007), following the steps: I) A multivariate statistical analysis using a compression algorithm Minimum Noise Fraction (MNF); II) Factorial Kriging in the most relevant MNF bands to detect multiple scales of spatial variability and filter the noise, III) An inverse MNF transform of the noise-whitened factors.

The component II) yields high complexity in the case of IS images in function of the options taken on the order used in the image processing chain. Thus, it is essential to identify the origin of distinct noises prior to removing them from the images. In the lack of adequate validation spectra to support the options taken and combined with the technical issues derived from the high data volume characteristic of these images, these tests were abandoned.

It remains as a methodology to be further exploited taking into account the sensitiveness of spectral response of IS data, where sometimes the limits of noise and information are doubtful. This methodology can be particularly relevant in the case of SPECIM EAGLE HAWK, where a different type of spatial noise was detected.

7.2.2 SPECIM EAGLE-HAWK

For multi-sensor monitoring purposes, the SPECIM EAGLE HAWK data was spectrally resampled, when possible, to the HyMap™ data spectral resolution, to ensure these parameters were consistent for both images. Thus, a considerable amount of spectral information, i.e. corresponding to 19,15 Gbytes, was not processed, and can aid in adding more detail on the characterization of the S. Domingos area when using its full spectral extension. This can give a more accurate time point when processed in all its spectral extension and resampled afterwards for monitoring purposes.

Additionally, other spectral data, e.g. field and mineralogical libraries, has detailed spectral resolution to be combined in the correlation matrix and depict the variations when accounting with more absorption features.

Modifications on the input bands for the correlation matrix, conducted in this thesis, demonstrated that variations in the results can be significant, e.g. in the case of low pH environmental mineralogical indicators such as copiapite and coquimbite. Additionally, it can also detail what were the implications on the signal obtained when spectrally sub setting the SPECIM EAGLE HAWK data.

7.2.3 SPECTROSCOPY

Field spectral data revealed its importance as reference data and bridging different scale levels, i.e. laboratory, field and airborne spectral data. Establishing a quantitative link when correlated with mineralogical libraries facilitates the use of field spectroscopy for AMD assessment. As stated by Montero et al. (2005) field spectroscopy can also configure a quick way and cost effective method for AMD assessment.

Laboratory studies using spectral measurements of field materials concerning low pH minerals, can contribute to further comprehension of the evolution of waste mining materials in dry and wet seasons. In fact, the cycling of metals and acid by the precipitation and dissolution of efflorescent salts is an important process at mine sites (Hammarstrom et al., 2005). The pollutants content, e.g. Pb and As in these materials can also be exploited in terms of absorption features supported by other analytical methods.

7.2.4 FROM AIRBORNE TO SPACEBORNE AMD DETECTION

The similarity of mapping results of pH<3 obtained when translating the IS (HyMap™) mapping conditions (i.e. field spectra and endmembers correlated) degraded spectrally for a sharpened MSI (Landsat ETM+), highlights the following:

I. depicts the potential to test the extension of the AMD spectral signatures to a regional scale. This can be relevant for areas within the same Metallogenic Provinces, e.g. the Iberian Pyrite Belt, where a strong environmental footprint derived from long term mining activity is observed.

II. if at some stage of a mine life cycle there is IS information validated by mapping results when translated to MSI in a close time gap, it can lead to the extension of this knowledge to a multi-temporal MSI. This can in fact contribute to monitoring capability concerning mining areas, with routine data acquisition in a cost effective way.

Relative to the mineralogical correlation of low pH(<3) remains to be tested the translation of this spectral signature from IS airborne to IS spaceborne.

REFERENCES

Abreu, M.M, Batista M.J, Magalhães M.C, Matos J.X, (2010).Acid Mine Drainage in the Portuguese Iberian Pyrite Belt. In Brock C. Robinson (Ed.), *Mine drainage and Related problems*. Nova Science Publishers, Inc. NY.70p.

Abreu, M. M., Tavares, M.T., Vairinho, M. M., Joaquim, C., Quental, L. (2004).Geoquímica comparada dos solos da área mineira de São Domingos, Alentejo: fundo geoquímico versus zona de exploração. *Revista de Ciências Agrárias*, 27 (1),301-313.

Abreu, M. M., Tavares, M.T.Batista, M.J.(2008). Potential use of Erica andevalensis and Erica australis in phytoremediation of sulphide mine environments: São Domingos, Portugal.*Journal of Geochemical Exploration* 96 (2008) 210–222.

Adams J.B. Gillespie A.R (2008). Remote sensing of landscapes with spectral images: a physical modeling approach.362p. Cambridge University Press.

Adler-Golden, S.M. (1998).MODTRAN cloud and multiple scattering upgrades with application to AVIRIS. *Remote Sens. Environ.*, 65:367-375.

Adler-Golden, S.M.,Matthew, M.W.,Bernstein,L.S.,Levine,R.Y.,Berk,A.,Richtsmeier,S.C., Acharya, P.K., Anderson, G.P., Felde, G., Gardner,J., Hike, M., Jeong, L.S., Pukall, B., Mello, J., Ratkowski, A., Burke, H.(1999). Atmospheric correction for shortwave spectral imagery based on MODTRAN4.SPIE Proc. Imaging Spectrometry,3753:61-69.

Allan, J.C. (1965). A Mineração em Portugal na Antiguidade. *Bol.Minas*, Lisboa 2(3), pp. 139-175.

Anderson GP, Felde GE, Hoke ML, Ratkowski AJ, Cooley TW, Chetwynd Jr. JH, J. Gardner A, Adler-Golden SM, Matthew MW, Berk A, Bernstein LS, Acharya PK,. Miller DP, Lewis PE (2002)MODTRAN4-based atmospheric correction algorithm: FLAASH (fast line-of-sight atmospheric analysis of spectral hypercubes). Proc. SPIE, Vol. 4725, 65.

Anderson K, Milton EJ (2006).On the temporal stability of ground calibration targets: implications for the reproducibility of remote sensing methodologies.*International Journal of Remote Sensing*,V. 27, Number 16, 2006 , pp. 3365-3374(10) Taylor and Francis Ltd

Asmat, A. , Atkinson, P. M., Foody, G. M.(2010) 'Geostatistically estimated image noise is a function of variance in the underlying signal', *International Journal of Remote Sensing*, 31: 4, 1009-1025.

Aspinall RJ, Marcus WA, Boardman J (2002).Considerations in collecting, processing, and analyzing high spatial resolution and hyperspectral images in analyses and forecasts. Journal of Geographical Systems 4:15–29

Atkinson, P.M., Sargent, I.M.J., Foody, G.M., Williams, J. (2005).Interpreting image-based methods for estimating the signal-to-noise ratio. *International Journal of Remote Sensing*, 26, (20), 5099-5115.

Ball, D.W.(2007).The Electromagnetic Spectrum: a History.*Spectroscopy*, 22 (3), 14 – 20.

Ball, D.W. (1995). Defining Terms. *Spectroscopy,* 10, 16-18.

Barriga, F., Carvalho, D. (1983).Carboniferous volcanogenic sulfide mineralizations in South Portugal (Iberian Pyrite Belt). In: Sousa M. J. L., Oliveira, J. T., Eds., The Carboniferous of Portugal. *Memórias dos Serviços Geológicos de Portugal*, v. 29, pp.99-113.

Bateson, A., Curtiss, B. (1996). A method for manual endmember selection and spectral unmixing. *Remote Sens. Environ.*, 55, 229−243.

Batista, M.J.(2000).Environmental State of the Portuguese Test Site. S. Domingos Mine:Past and Present. Report for European Comission (http://www.brgm.fr/mineo/IGM_test_site.pdf).

Ben-Dor E. , N. Goldshalager, O. Braun , B. Kindel , A.F.H.Goetz , D. Bonfil , M. Agassi, N. Margalit , Y. Binayminy, A. Karnieli (2004).Monitoring of Infiltration Rate in Semiarid Soils using Airborne Hyperspectral Technology *International Journal of Remote Sensing* 25:1-18

Ben-Dor, E., Kindel, B. , Goetz, A.F.H. (2004). Quality assessment of several methods to recover surface reflectance using synthetic imaging spectroscopy data. *Remote Sens. Environ.*, 90, 389-404.

Ben-Dor, E.; Chabrillat, S.; Demattê, J.A.M.; Taylor, G.R.; Hill, J.; Whiting, M.L.; Sommer, S. (2009). Using Imaging Spectroscopy to study soil properties. *Remote Sens. Environ.*, V.113, Supplement 1, Imaging Spectroscopy Special Issue, pp S38-S55.

Berk A, Bernstein LS, Anderson GP, Acharya PK, Robertson DC, Chetwynd JH, Adler-Golden SM (1998) MODTRAN cloud and multiple scattering upgrades with application to AVIRIS. Remote Sens. Environ. 65:367–375

Berk A, Anderson GP, Bernstein LS, Acharya PK, Dothe H, Matthew MW, Adler-Golden SM, Chetwynd JH Jr, Richtsmeier SC, Pukall B, Allred CL, Jeong LS, Hoke ML (1999).MODTRAN4: Radiative transfer modeling for atmospheric correction. AVIRIS 1999,Proceedings, JPL, California. 7 pp

(http://makalu.jpl.nasa.gov/docs/workshops/99_docs/6.pdf)

Berman, M., Kiiveri, H., Lagerstrom, R., Ernst, A., Dunne, R., Huntington, J. F. (2004). ICE: A statistical approach to identifying endmembers in hyperspectral images. *IEEE Transactions on Geoscience and Remote Sensing*, 42, 2085−2095.

Bigham,J. M., Schwertmann,U. S., Traina,J., Winland, R. L. , Wolff,M. (1996). Schwertmannite the chemical modeling of iron in acid sulfate waters. *Geochimica et Cosmochimica Acta*, V. 60, No. 12, pp. 2111-2121.

Bird A. C., Taylor J. C., Brewer T. R.(2000). Mapping national park landscape from ground, air and space. *International Journal of Remote Sensing*, 21:2719–2736.

Boardman, J.W. (1993). Automating spectral unmixing of AVIRIS data using convex geometry concepts. *Summaries of the Fourth Annual JPL Airborne Geoscience Workshop.* Jet Propulsion Laboratory, Pasadena, CA, pp. 11-14.

Boardman J. W., Kruse, F. A. (1994). Automated spectral analysis: A geologic example using AVIRIS data, North Grapevine Mountains, Nevada. Proceedings, Tenth Thematic Conference on Geologic Remote Sensing, San Antonio, TX, 9-12 May 1994, pages I-407 - I-418.

Boardman JW (1998a). Post-ATREM polishing of AVIRIS apparent reflectance data using EFFORT: a lesson in accuracy versus precision. AVIRIS 1998 *Proceedings,* JPL, California. (http://makalu.jpl.nasa.gov/docs/workshops/98_docs/7.pdf)

Boardman, J. W., (1989b). Inversion of imaging spectrometry data using singular value decomposition.*Proceedings* IGARSS'89, 12th Canadian Symposium on Remote Sensing, v. 4., pp. 2069-2072.

Boardman, J. W., Kruse, F.A., (1994).Automated spectral analysis: a geological example using AVIRIS data, north Grapevine Mountains, Nevada.*Proceedings, ERIM Tenth Thematic Conference on Geologic Remote Sensing*, Environmental Research Institute of Michigan, Ann Arbor, MI, pp. I-407 - I-418.

Boardman, J. W., Kruse, F. A., Green, R. O., (1995). Mapping target signatures via partial unmixing of AVIRIS data: in Summaries, Fifth JPL Airborne Earth Science Workshop, JPL Publication 95-1, v. 1, pp. 23-26.

Boardman, J. (1998) Post-ATREM polishing of AVIRIS apparent reflectance data using EFFORT: a lesson in accuracy versus precision, in: Summaries of the Seventh Annual JPL Airborne Geoscience Workshop, Pasadena, CA.

Borel C.C., Gerst S.A.W. (1994). Nonlinear spectra mixing models for vegetative and soil surfaces. *Remote Sens. Environ.*, 47:403-416.

Bourguignon, A., Quental, L., Cottard, F., Hosford, S., Chevrel, S.(2003). Hyperspectral Investigations of Mining-Related Contaminated Areas: Acid Mine Drainage Mineral Identification Comparison Between Field and Airborne Data (Sao Domingos Mine, Southeast Portugal), 3rd EARSel Workshop on Imaging Spectroscopy, DLR, Munich, Germany.

Bunsen, R. , Kirchhoff, G. (1863) Untersuchungen über das Sonnenspektrum und die Spektren der Chemischen Elemente. Abh. kgl. Akad. Wiss., 1861.

Burns, R., (1993). Mineralogical Applications of Crystal Field Theory, Second Edition, Cambridge University Press, Cambridge, 551p.

Campbell, J.B.(2007).Introduction to Remote Sensing. 4th edition ISBN 9780415416887. Taylor & Francis. 546 p.

Carvalho, D. (1979).Geologia, metalogenia e metodologia da investigação de sulfuretos polimetálicos do sul de Portugal. Comunicações dos Serviços Geológicos de Portugal, t. 65, pp.169-191.

Chang, C (2007).*Hyperspectral Data Exploitation: Theory and Applications.* 440p. ISBN: 978-0-471-74697-3. Willey.

Chevrel S, Kuosmannen V, Belocky R, Tapani T, Mollat H, Quental L, Vosen P, Schumacher V, Kuronen E, Aastrup P (2002). Hyperspectral Airborne Imagery For Mapping Mining-Related Contaminated Areas In Various European Environments – First Results Of The Mineo Project. *Proceedings of the 5th Airborne Remote Sensing Conference and Exibition* (IARSC).

Chevrel S. (2003a): Airborne Hyperspectral Campaign for Investigation of Mining-Related Impacts in Various Vegetated European Environments The European RDT Project MINEO. 3rd EARSel Workshop on Imaging Spectroscopy, DLR, Munich, Germany.

Chevrel S, Kuosmanen V, Groesel K, Marsh S, Tukiainen T, Schaeffer U, Quental L, Vosen P, Loudjani P, Kuronen E, Aastrup P.(2003b). Remote-sensing monitoring of environmental impacts. *Mining Environmental Management*, Vol.11, Nb 6 November, pp 19-23.

Chevrel S., Kuosmanen, V., Groesel, K., Marsh S., Tukainen, T. Schaeffer, U., Quental, L., Vosen, P., Loudjani, P. , Astrup.P. (2004) .Hyperspectral Remote-Sensing Assessment Of Mining-Related Environmental Impacts - Examples From The Mineo Project. Abstracts Of The 32nd International Geological Congress, 247-1 Url: Http://Www.32igc.Org/Scientific_Session_Warning.Htm Available On January 2009.

Chevrel, S. (2005). MINEO two years later - did the project impulse a new era in imaging spectroscopy applied to mining environments? In: *Proceedings of the 4th Workshop on Imaging Spectroscopy*

Chevrel, S., Kuosmanen, V., Groesel, K., Marsh, S.H., Tukiainen, T., Schaeffer, U., Quental, L., Vosen, P., Loudjani, p., Kuronen, E. , Aastrup, P. (2003). Remote sensing monitoring of environmental impacts. *Mining Environmental Management*, 11(6), 19-23.

Chudnovsky A. ; Ben-Dor E. (2008). Application of visible, near-infrared, and short-wave infrared (400-2500 nm) reflectance spectroscopy in quantitatively assessing settled dust in the indoor environment. Case study in dwellings and office environments. *Science of the Total Environment*, Vol 393/2-3 pp 198-213.

Clark, R.N., Gallagher, A.J., and Swayze, G.A.,(1990).Material absorption band depth mapping of imaging spectrometer data using the complete band shape least-squares algorithm simultaneously fit to multiple spectral features from multiple materials: in *Proceedings of the Third Airborne Visible/Infrared Imaging Spectrometer (AVIRIS) Workshop*, JPL Publication 90-54, pp. 176-186.

Clark, R.N., Swayze, G.A. (1991).Mapping with imaging spectrometer data simultaneously fit to multiple spectral features from multiple materials: in *Proceedings of the Third Airborne Visible/Infrared Imaging Sepctrometer (AVIRIS) Workshop*, JPL Publication 91-28, pp. 2-3.

Clark, R. N., Swayze, G. A., Gallagher, A. J., King, T. V. V., Calvin, W. M., (1993). The U. S. Geological Survey, Digital Spectral Library. Version 1: 0.2 to 3.0 microns. U.S. Geological Survey Open File Report 93-592, 1340 pages.

Clark, R. N., Swayze, G. A., (1995).Mapping minerals, amorphous materials, environmental materials, vegetation, water, ice, and snow, and other materials: The USGS Tricorder Algorithm. In Summaries of the Fifth Annual JPL Airborne Earth Science Workshop, JPL Publication 95-1, v. 1, pp. 39 - 40.

Clark, R. N. (1999). Chapter 1: Spectroscopy of Rocks and Minerals, and Principles of Spectroscopy, in *Manual of Remote Sensing,* V3, Remote Sensing for the Earth Sciences, (A.N. Rencz, ed.) John Wiley and Sons, New York, p 3- 58.

Clark, R. N., G. A. Swayze, K. E. Livo, R. F. Kokaly, S. J. Sutley, J. B. Dalton, R. R. McDougal, C. A. Gent (2003) Imaging spectroscopy: Earth and planetary remote sensing with the USGS Tetracorder and expert systems, *J. Geophys. Res*., 108(E12).

Clark, R.N., Swayze, G.A., Wise, R., Livo, E., Hoefen, T., Kokaly, R., Sutley, S.J.(2007). USGS digital spectral library splib06a: U.S. Geological Survey, Digital Data Series 231, http://speclab.cr.usgs.gov/spectral.lib06

Cocks T., R. Jenssen, A. Stewart, I. Wilson, T. Shields (1998).The HyMap Airborne Hyperspectral Sensor: The System, Calibration and Performance. Proc. 1st EARSeL Workshop on Imaging Spectroscopy (M. Schaepman, D. Schläpfer, and K.I. Itten, Eds.), 6-8 October 1998, Zurich, EARSeL, Paris, p. 37-43.

Cope, M.; Delpy, D. T. Med. Biol., Eng. Comput. 1988, 26, 289-294p.

Congalton RG , Green K (2009) Assessing the accuracy of Remotely Sensed Data:Principles and Pratices. 2nd Edition. Taylor & Francis. 200p.

Congalton, R. (2005). Thematic and Positional Accuracy Assess¬ment of Digital Remotely Sensed Data. 2005 Proceedings of the Seventh Annual Forest Inventory and Analysis Symposium 149-155p.

Cope, M.; Delpy, D. T. Med. Biol., Eng. Comput. 1988, 26, 289-294p.

Cotton C., Tongue R. (2001), BGS test site report.

Crowley J. K., Zimbelmand R.(1997). Mapping hydrothermally altered rocks on Mount Rainier, Washington, with airborne visible/ infrared imaging spectrometer (AVIRIS) data. *Geology* 25, 559–562.

Crowley, J. K., Clark, R. N.(1992) AVIRIS study of Death Valley evaporite deposits using least squares band-fitting methods: in Summaries of the Third Annual JPL Airborne Geoscience Workshop, JPL Publication 92-14, v. 1, p. 29-31.

Crowley J. K., Hubbard B. E., Mars J. C.(2003). Analysis of potential debris flow source areas on Mount Shasta, California, by using airborne and satellite remote sensing data, Remote Sens. Environ., Volume 87, Issues 2-3, Pages 345-358, ISSN 0034-4257.

Crowley,J.K., Williams.D.E., Hammarstrom, J.M., Piatak , N., Ming Chou, I, Mars,J.C. (2003). Spectral reflectance properties (0.4–2.5 μm) of secondary Fe-oxide, Fe-hydroxide, and Fe-sulphate-hydrate minerals associated with sulphide-bearing mine wastes.Geochemistry: Exploration, Environment, Analysis; v. 3; no. 3; p. 219-228; DOI: 10.1144/1467-7873/03-001.

Curran PJ, Dungan JL , GHGLZ HL (1990). Exploring the relationship between reflectance red edge and chlorophyll content in slash pine.Tree Physiology 7, 33-48. Heron Publishing – Victoria Canada.

Dalponte, M.; Bruzzone, L.; Vescovo, L.; Gianelle, D. (2009) The role of spectral resolution and classifier complexity in the analysis of hyperspectral images of forest areas. *Remote Sens. Environ. 113*, 2345-2355.

Dalton, J.B., King, T.V.V., Bove, D.J., Kokaly, R.F., Clark, R.N., Swayze, G.A., (1998). Mapping of acid-generating and acid buffering minerals in the Animas watershed by AVIRIS spectroscopy. Proc. 7th AVIRIS Earth Sci.

Workshop, JPL, vols. 97-21, 4 pp.

Davies T. (1998) The history of near infrared spectroscopic analysis: Past, present and future "From sleeping technique to the morning star of spectroscopy". *Analusis* 26, 4, 17-19pp

Dell`Indice, F. (2010). Improving quality of imaging spectroscopy data. Phd Dissertation, Univeristat Zurich. 144p.

Ditmann C., Vosen P (2002). MINEO Central environment test site Contamination /impact mapping and modelling. Final report for EC.72p.

Dold, B., 1999. Mineralogical and geochemical changes of copper flotation tailings in relation to their original composition and climatic setting—implications for acid mine drainage and element mobility. Terre Environ. 18, 1–230.

Dópido,I.,Villa A.,Plaza,A.,Gamba,P.(2011). A COMPARATIVE ASSESSMENT OF SEVERAL PROCESSING CHAINS FOR HYPERSPECTRAL IMAGE CLASSIFICATION:WHAT FEATURES TO USE? . *Proceedings of 3rd Workshop on Hyperspectral Image and Signal Processing (WHISPERS): Evolution in Remote Sensing, Lisbon*, Portugal, 6-9June.4p.

Du, P. Tan, K. Su, H. (2009). Feature extraction for target identification and image classification of OMIS hyperspectral image. *Mining Science and Technology*, 19, Issue 6, 835-841pp. ISSN 1674-5264, DOI: 10.1016/S1674-5264(09)60152-6.

Durucan, S. Korre,A., Munoz-Melendez, G. (2006). Mining life cycle modelling: a cradle-to-gate approach to environmental management in the minerals industry. *Journal of Cleaner Production*,14,1057-1070 pp.

Dzombak D.A., Ghosh R.S. Wong-Chong G.M.(2006) Editors, Cyanide in Water and Soil, CRC Press, Boca Raton (2006).

EC-DG (2008): Communication of the Commission (COM 699) "The raw materials initiative – meeting our critical needs for growth and jobs in Europe", European Commission (DG Enterprise) Brus¬sels 2008

ECPMM (2009). Environmental Code of Practice for Metal Mines. Environment Canada © Her Majesty the Queen in Right of Canada, represented by the Minister of the Environment, 2009. ISBN 978-1-100-11901-4.108pages

Elachi, C.(1987). Introduction to the Physics and Techniques of Remote Sensing. Wiley Interscience, New York. ISBN 0471848107, 413 p.

Elachi, C; Van Zyl, J. (2006). Introduction to the Physics and Techniques of Remote Sensing. Wiley Interscience, John Wiley and Sons, Inc. New York, 2nd edition. 552p. Online ISBN: 9780471783398

Espãna, J.S., Pamo, E.L., Pastor, E.S., Andrés, J.R., Rubí, J.M (2005). The natural attenuation of two acidic effluents in Tharsis and La Zarza-Perrunal mines (Iberian Pyrite Belt, Huelva, Spain).Environ Geol 49: 253–266

Farmer, V.C., (1974). The Infra-Red Spectra of Minerals, (V.C. Farmer, ed.) Mineralogical Society, London, 539pp.

Ferreira da Silva E., Bobos I., MatosJ. X, Patinha C., Reis A. P., E. Cardoso Fonseca, (2009).Mineralogy and geochemistry of trace metals and REE in volcanic massive sulfide host rocks, stream sediments, stream waters and acid mine drainage from the Lousal mine area (Iberian Pyrite Belt, Portugal) *Appl. Geochem.* 24, 383.

FIGUEIREDO M.O., PEREIRA da SILVA T., MIRÃO J.P. (2007). How does the uptake of lead along acid mine drainage processes affect the chemical exergy of jarosite in Exergetic Life Cycle Assessment (ELCA)? IEEES-3, 3rd Internat. Energy, Exergy & Environment Symposium,CD-ROM, 4 pp., Edt. A.F. Miguel et al. (ISBN 978-989-95091-1-5).

FLAASH (2009). Atmospheric Correction Module:QUAC and FLAASH User`s Guide. Version 4.7. ITT Visual Information Solutions. 2009 Edition.

Fleming C., Marsh S., Noy D., Newsham N. (2003).MINEO Western European test site.Contamination/impact mapping and modelling – Final report.

Foody, G. (2008). Harshness in image classification accuracy assessment. *International Journal of Remote Sensing* V.29, Issue 11, pp3137-3158

Fraunhofer, J. (1817) Bestimmung des Brechungs- und Farbenzerstreuungs-Vermögens verschiedener Glasarten, in Bezug auf die Vervollkommnung achromatischer Fernrohre, Vol. 56, pp. 264-313. Gilberts Annalen der Physik. Goetz, A.F.H., Vane, G., Solomon, J.E., , Rock, B.N. (1985) Imaging spectrometry for earth remote sensing. Science, 228, 1147.

Gaffey, S.J., L.A. McFadden, D. Nash, C.M. Pieters (1993).Ultraviolet, Visible, and Near-infrared Reflectance Spectroscopy: Laboratory spectra of Geologic Materials, in *Remote Geochemical Analysis: Elemental and Mineralogical Composition* (C. M. Pieters, and P.A.J. Englert, eds.), Cambridge University Press, Cambridge, 43-78pp.

Gao, B.-C., Goetz, A. F. H. (1990). Column atmospheric water vapor and vegetation liquid water retrievals from airbourne imaging spectrometer data. *Journal of Geophysical Research-Atmospheres*, 95(D4), 3549-3564.

Gao, B.-C., Goetz, A. F. H., Wiscombe, W.J.(1993).Cirrus cloud detection from airborne imaging spectrometer data

using the 1.38 micron water vapour band. *Geophysical Research Letters*, 20(4), 301-304.

Gao, B.-C., Montes, M. J., Davis, C. O., Goetz, A. F. H., (2009). Atmospheric correction algorithms for hyperspectral remote sensing data of land and ocean, *Remote Sens. Environ.,* 113, S17– 5 S242227

Gao, B.-C.; Hiedebrecht, K. B., , Goetz, A. F. H.(1999).Atmosphere Removal Program. (ATREM) User's Guide version 3.1 pp.101.

Gaspar, O. (1998).História da Mineração dos Depósitos de Sulfuretos Maciços Vulcanogénicos da Faixa Piritosa Portuguesa. *Boletim de Minas*,V35,N4 Lisboa.

Gastil, M., Melack J. M. (1998). Improved atmospheric correction for AVIRIS spectra from inland waters. In Green, R. O. (ed.), Summaries of the Seventh JPL Airborne Earth Science Workshop. JPL Publication 97-21, Vol. 1. Jet Propulsion Laboratory, Pasadena, CA: 141–145.

Gillis, D., Bowles, J. (2004).Target detection in hyperspectral imagery using demixed spectral angles. In Lorenzo Bruzzone (Ed.), Proceedings of SPIE. Image and Signal Processing for Remote Sensing IX, vol. 5238, pp. 244–254).

Goetz A.F.H., Rowan L.C., Kingston M.J. (1982).Mineral identification from orbit: Initial results from the shuttle multispectral infrared radiometer, Science **218** pp. 1020–1024.

Goetz A.F.H, Boardman JW, Kindeland B, Heidebrecht KB (1997) Atmospheric corrections: On deriving surface reflectance from hyperspectral imagers. *Proceedings* SPIE, 3118, pp 14–22.

Goetz A.F.H, Heidebrecht K.B, Kindell B, Boardman J.W (1998) Using ground spectral irradiance for model correction of AVIRIS data. AVIRIS 1998 Proceedings, JPL, California. 10 pp (http://makalu.jpl.nasa.gov/docs/workshops/98_docs/22.pdf)

Goetz, A.F.H, G. Vane, J.E. Solomon, , B.N. Rock, (1985) Imaging Spectroscopy for Earth Remote Sensing, *Science*, v. 228, pp. 1147-1153.

Goetz, A.F.H. (2009).Three decades of hyperspectral remote sensing of the Earth: A personal view. *Remote Sens. Environ.* 113 S5–S16.

Gove PB (1976). Webster's 3rd New International Dictionary of the English Language Unabridged: G.&C. Merriam Company, Springfield, MA, p 2662

Gowen, A.A. O'Donnell, C.P. Cullen, Downey, P.J. Frias,J.M. (2007). Hyperspectral imaging - an emerging process analytical tool for food quality and safety control, *Trends in Food Science & Technology*, V.18, Issue 12, pp 590-598, ISSN 0924-2244, DOI: 10.1016/j.tifs.2007.06.001.

Gray, N.F.(1997).Environmental impact and remediation of acid mine drainage: a management problem. *Environmental Geology* V.30, Numbers 1-2 / March.

Green, A. A., Berman, M., Switzer, P., , Craig, M. D. (1988).A transformation for ordering multispectral data in terms of image quality with implications for noise removal: IEEE Transactions on Geoscience and Remote Sensing, v. 26, no. 1, p. 65-74.

Griffin M. K., Burke H. K., (2003).Compensation of hyperspectral data for atmospheric effect. *Lincoln Laboratory Journal*, vol. 14, no. 1, pp. 29–54

Grimalt O, Ferrer M., Macpherson E. (1999) The mine tailing accident in Aznalcóllar. *Sci Total Environ* 242 (1999), pp. 3–11

Grösel K, Belocky R, (2002). MINEO Alpine environment test site Contamination /impact mapping and modelling – Final report for EC.51p.

Grove, C. I., Hook, S. J., Paylor, E. D. 1992, Laboratory reflectance spectra for 160 minerals 0.4 - 2.5 micrometers. JPL Publication 92-2.

Guanter, L. Ritcher, R., Moreno, J. (2006) Spectral calibration of hyperspectral imagery using atmospheric absorption features. *Applied Optics,* Vol. 45, 2360-2370pp.

Guelman, M., Ortenberg, F. (2009): Small Satellite's Role in Future Hyperspectral Earth Observation Missions. *Acta Astronautica*, 64(11-12), pp. 1251-1262.

Hammarstrom, JM, Seal II, RR, Meier, AL, Kornfeld, JM. (2005). Secondary sulfate minerals associated with acid drainage in the eastern US: recycling of metals and acidity in surficial environments. Chemical Geology, 215, 407-431.

Harsanyi, J. C., Chang, C. (1994). Hyperspectral image classification and dimensionality reduction: an orthogonal subspace projection approach. IEEE Transactions on Geoscience and Remote Sensing, 32, 770– 785.

Henkle W. R., John T. W. Hyde C. C.(1993).Geochemical and geophysical signatures at three precious metals exploration targets in Nevada. *Journal of Geochemical Exploration* 47, 29–43.

Holzwarth S; Heldens (2006).HYRESSA AM5 Report AM5: SWOT and User Needs workshop. HYperspectral REmote Sensing in Europe – specific Support Actions. HYRESSA, Deliv.No: D3.EC

Hunt G.R.(1977).SPECTRAL SIGNATURES OF PARTICULATE MINERALS IN THE VISIBLE AND NEAR INFRARED *Geophysics* 42, 501 (DOI:10.1190/1.1440721

Hunt, G.R. (1980). Electromagnetic radiation: the communication link in remote sensing. In: B.S. Siegal and A.R. Gillespie, Editors, *Remote Sensing in Geology*, John Wiley, NYpp. 5–45.

Hunt, G.R. (1982). Spectroscopic properties of rocks and minerals, in *Handbook of Physical properties of rocks*, Volume I, (R. S. Carmichael, ed.) CRC Press, Boca Raton, 295-385.

Hunt, G.R., Salisbury, J.W., (1970), Visible and near infrared spectra of minerals and rocks. I. Silicate minerals, Mod. Geology 1, 283-300.

Hunt, G.R., Salisbury, J.W.(1971) Visible and near infrared spectra of minerals and rocks. II. Carbonates, Mod. Geology 2, 23-30.

Hutsinpiller A. (1988). Discrimination of hydrothermal alteration mineral assemblages at Virginia City, Nevada, using the airborne imaging spectrometer. Remote Sens. Environ.s 24, 53–66.

HVC (2008). Hyvista Corporation data products.9p. http://www.hyvista.com/wordpresshvc/wp-content/uploads/2008/08/hvc_data_products.pdf. Assessed 11th of June 2010.

Ifarraguerri, A., Chang, C. I.(1999).Multispectral and hyperspectral image analysis with convex cones. *IEEE Transactions on Geoscience and Remote Sensing*, 37, 756−770.

ITT (2010). ENVI Users Guide: Version 4.8. ITT Visual Information Solutions.

Itten, K. I., Dell'Endice, F., Hueni, A., Kneubühler, M., Schläpfer, D., Odermatt, D., Seidel, F., Huber, S., Schopfer, J., Kellenberger, T., Bühler, Y., D'Odorico, P., Nieke, J., Alberti, E., Meuleman, K. (2008). APEX - the Hyperspectral ESA Airborne Prism Experiment. *Sensors*, 8, 6235-6259; doi:10.3390/s8106235

Jacquez, M., Marcus, W.A., Aspinall R.J., Greiling, D.A.(2002).Exposure assessment using high spatial resolution hyperspectral (HSRH) imagery. *Journal of Geographical Systems*, Vol.4, Number 1, Pages 1-14

Jamieson, HE, Robinson, C, Alpers, CN, McCleskey, RB, Nordstrom, DK, Peterson, RC (2005).Major and trace element composition of copiapite-group minerals and coexisting water from the Richmond mine, Iron Mountain, California. *Chemical Geology*, 215, 387–405.

Jolliffe, I.T., 2002. Principal Component Analysis, second edition, New York: Springer-Verlag New York, Inc.

Kaufman, Y. J., D. Tanre´, L. A. Remer, E. Vermote, A. Chu, and B. N.Holben (1997).Operational remote sensing of tropospheric aerosol over land from EOS moderate resolution imaging spectroradiometer, *J.Geophys.Res*., 102, 17,051– 17,067.

Kempeneers, P.(2007) Information Extraction from Hyperspectral Images Applied to Vegetation. PhD thesis, unpublished data. Universiteit Antwerpen. Belgium. 170p.

Kemper T., Sommer S.(2003). Mapping and monitoring of residual heavy metal contamination and acidification risk after the Aznalcóllar mining accident (Andalusia, Spain) using field and airborne hyperspectral data. In M. Habermeyer, A. Müller, & S. Holzwarth (Eds.), Proceedings of 3rd EARSEL Imaging Spectroscopy, Herrsching, Germany, May 13–16 2003,. CD-ROM ISBN 2-908885-56-5, pp 333-343.

Khorram S., Biging G. S., Chrisman N. R., Colby D. R., Congalton R. G., Dobson J. E., Ferguson R. L., Goodchild M. F., Jensen J. R., Mace T.H.(1999). Accuracy assessment of remote sensing-derived change detection. American Society for Photogrammetry and Remote Sensing Monograph Series, p 64.

Kramer,H.(2009). Earth Observation History on Technology Introduction. 857p http://www.eoportal.org/documents/kramer/History.pdf Assessed January 2010

Kruse, F. A., Lefkoff, A. B., Boardman, J. B., Heidebrecht, K. B., Shapiro, A. T., Barloon, P. J., Goetz, A. F. H. (1993) "The Spectral Image Processing System (SIPS).

Kruse, F. A. (1995).Mapping spectral variability of geologic targets using Airborne Visible/Infrared Imaging Spectrometer (AVIRIS) data and a combined spectral feature/unmixing approach.*Proceedings, AeroSense'95,* SPIE, 17-21 April 1995, Orlando, Florida.

Kruse F. A. (2002).Comparison of AVIRIS and Hyperion for Hyperspectral Mineral Mapping. 11th JPL Airborne Geoscience Workshop, 4-8 March, Pasadena, California.

Kruse F.A. (2003).Mineral mapping with AVIRIS and EO-1 Hyperion, Proceedings Of The 12th JPL Airborne Geoscience Workshop, Jet Propulsion Laboratory, Pasadena, CA (2003), pp. 149–156.

Kruse, F. A., Boardman, J. W., Livo, K. E. (2004).Using Hyperspectral Data for Urban Baseline Studies, Boulder, Colorado," *Proceedings 13th JPL Airborne Geoscience Workshop*, 31 March – 2 April 2004, Pasadena, CA, Jet Propulsion Laboratory Publication 05-3,CD-ROM.

Kruse, F. A., Perry, S. L.(2007).Regional Mineral Mapping By Extending Hyperspectral Signatures Using Multispectral Data.*Proceedings, IEEE AeroSpace Conference*, 3 - 10 March 2007, Big Sky, Montana, On CD-ROM, IEEE Catalog Number 07TH8903C, ISBN: 1-4244-0525-4.

Kruse, F.A., Taranik, J.V., Calvin, W.M., Michaels, J., Littlefield, E.F., Coolbaugh, M., Martini, B.A (2011).

Characterization of hydrothermal systems using simulated HyspIRI data. IEEE Aerospace Conference.

Kuosmanen, V., Arkimaa, H., Helminen, T., Hyvönen, E., Kuronen, E., Laitinen, J., Lerssi, J., Middleton, M., Rainio, H., Ruohomäki, T., Räisänen, M., Saarelainen, J., Sutinen, R. (2002). MINEO Boreal environment test site, Finland. Contamination /impact mapping and modelling – Final report. 86 pages.

Kuosmanen V, Laitinen J Arkimaa H (2005). A COMPARISON OF HYPERSPECTRAL AIRBORNE HYMAP AND SPACEBORNE HYPERION DATA AS TOOLS FOR STUDYING THE ENVIRONMENTAL IMPACT OF TALC MINING IN LAHNASLAMPI, NE FINLAND. Proceedings of 4th EARSeL Workshop on Imaging Spectroscopy. New quality in environmental studies. © EARSeL and Warsaw University, Warsaw 2005 Zagajewski B., Sobczak M., Wrzesień M., (eds)

Laben, C.A. Brower, B.V, (2000). Process for Enhancing the Spatial Resolution of Multispectral Imagery Using Pan-Sharpening, US Patent 6,011,875.

Landgrebe, D.A. (1978). The Quantitative Approach to Remote Sensing: Concept and Rationale. In Swain, P.H. and Davis, S.M., editors, Remote Sensing: The Quantitative Approach. pages 1-20, McGraw-Hill Inc., New York.

Larsen (1997). A 3-D Contextual Classifier. Proceedings of the 7th Scandinavian Conference on Image Analysis (SCIA'97).Michael Frydrych, Jussi Parkkinen, Ari Visa (Eds).pp 9-12.

Lau, IC (2004). Regolith-landform and mineralogical mapping of the White Dam Prospect, eastern Olary Domain, South Australia, using integrated remote sensing and spectral techniques (http://hdl.handle.net/2440/37972). Thesis. Assessed online January2010.

Lillesand, T.M., Kiefer R.W., Chipman J.W. (2004*). Remote sensing and image interpretation*, 5th ed., Wiley. ISBN 0-471-15227-7.

Lorchert G.(1999).Mapping hydrothermal alterations from AVIRIS data using spectral analysis tools and spectral libraries. Proceedings of the 13th Applied Geological Remote Sensing Conference, I-359–362

Lottermoser, Bernd G (2007). *Mine wastes: characterization, treatment and environmental impacts*. 2nd edition, Springer 304 p.

Jacquez, G. M., Marcus, W.A, Aspinall, R. J., Greiling, D.(2002).Exposure assessment using high spatial resolution hyperspectral (HSRH) imagery. *Journal of Geographical Systems* 4(1):1-14.

Malkmus, W.(1967).Random Lorentz band model with exponential tailed S line intensity distribution function. *Journal of the Optical Society of America*,57, 323-329.

Mars, JC, Crowley, JK (2003). Mapping Mine Wastes and analysing areas affected by selenium-rich water runoff in southeast Idaho using AVIRIS imagery and digital elevation data. *Remote Sens. Environ.,* 84, 3, pp422-436.

Marsh S.H. (2000).The MINEO Project: Earth Observation of mine pollution in Europe. GRSG Newletter, issue 28, pp30-32.

Martín,G., Plaza J., Plaza, A.(2011).ON THE INCORPORATION OF SPATIAL INFORMATION TO ENDMEMBER IDENTIFICATION ALGORITHMS WITHOUT THE PURE PIXEL ASSUMPTION. *Proceedings of 3rd Workshop on Hyperspectral Image and Signal Processing (WHISPERS): Evolution in Remote Sensing, Lisbon*, Portugal, 6-9June.4p.

Martínez P, Aguilar PL, Perez R.M. Plaza A (2002).Systolic S.O.M. Neural Network for Hyperspectral Image Classification. In: Series in Machine Perception and Artificial Intelligence - Vol. 49.Neural Networks and Systolic Array Design. David Zhang & Sankar K Pal (Eds). ISBN: 978-981-02-4840-6, pp. 193-204.

Mason, Barry (1878). Portugal-Notice sur la Mine de Pyrite Cuivreuse de S.Domingos. Lallemant Frères, Imprimeurs, Lisbonne, 35pp.

Matos J X, Soares S, Cardoso C (2006). Caracterização geológica-geotécnica da corta da mina de S. Domingos, Faixa Piritosa Ibérica. 10° Congresso Nacional de Geotecnia, pp. 2-3.

Matthew MW, Adler-Golden SM, Berk A, Felde G, Anderson GP, Gorodetzkey D, Paswaters S, Shippert M (2003) Atmospheric Correction of Spectral Imagery: Evaluation of the FLAASH Algorithm with AVIRIS Data. SPIE 5093.

Maxwell, J.C.(1873).A Treatise on Electricity and Magnetism Clarendon Press, Oxford.

McCloy K. R.(2006). Resource management Information Systems: Remote Sensing, GIS and Modelling. CRC Press, Taylor & Francis Group, Boca Raton, FL, USA.

Middleton M., Hyvönena E., Arkimaa H., Helminen T., Laitinen J., Kuosmanen V., Räisänen M-L., Timonen M. R. Sutinen (2003) Analysis of hyperspectral airborne HyMap data for vegetation mapping around Lahnaslampi talc mine, Finland. 3rd EARSEL Workshop on Imaging Spectroscopy, Herrsching

MINEO Consortium (2003). Final Report - Section 6: Detailed report.Report for the EC of the MINEO project, 47p.

Montero, I. (2002) MULTI-PLATFORM VIS/SWIR HYPERSPECTRAL APPROACH TO THE STUDY OF ACID

MINE DRAINAGE FROM SMALL ABANDONED MINES.Denver Annual Meeting (October 27-30, 2002) paper No. 242-12 Session No. 242 Remotely Sensed Data for Geologic and Environmental Studies

Montero, IC, Brimhalla, G.H., Alpers, C.N., Swayze, G.A. (2005). Characterization of waste rock associated with acid drainage at the Penn Mine, California, by ground-based visible to short-wave infrared reflectance spectroscopy assisted by digital mapping. *Chemical Geology,* 215,453– 472, Elsevier.

Mustard J F, M I Staid, , W J Fripp, (2001). A semianalytical approach to the calibration of AVIRIS data to reflectance over water application in a temperate estuary. *Remote Sens. Environ.,* 75: 335-349.

Nadeau, C., Neville, R.A., Staenz, K., Owneill, N.T., Royer, A.(2002). Atmospheric effects on the classification of surface minerals in an arid region using Short-Wave Infrared (SWIR) hyperspectral imagery and spectral unmixing technique. *Canadian Journal of Remote Sensing* 28, pp. 738–749.

Nascimento, J. M. P., Dias, J. M. B. (2005). Vertex component analysis: a fast algorithm to unmix hyperspectral data. *IEEE Transactions on Geoscience and Remote Sensing*, 43, 898−910.

Newton, I. (1704) Opticks: Or, a Treatise of the Reflexions, Refractions, Inflexions and Colours of Light Sam Smith and Benj. Walford, London.

Nordstrom, D.K., Alpers, C.N.(1999) Geochemistry of acid mine waters. In: Plumlee, G.S., Logsdon, M.J. (Eds.), The Environmental Geochemistry of Mineral Deposits: Part A. Processes, Techniques, and Health Issues, Rev. Econ. Geol., vol. 6A, pp. 133–155.

Oliveira, J.T.,Silva, J. B. (1990).Notícia Explicativa da Carta Geológica à escala 1:50000. Folha 46-D-Mértola. Serviços Geológicos de Portugal.

Oliveira, J.T.; Matos, J.X. (2004).O caminho de ferro da Mina de S. Domingos ao Pomarão: um percurso geo-educacional na Faixa Piritosa Ibérica. XXIV Encontro Prof. Geociências APG, 19pp.

Olyphant, G.A., Bayless, G.R., Harper, D., 1991. Seasonal and weather-related controls on solute concentrations and acid drainage from a pyritic coal-refuse deposit in southwestern Indiana, USA. J. Contam. Hydrol. 7, 219–236.

Ong, C., Cudahy, T.J. Swayze, G., (2003a).Predicting Acid Drainage Related Physicochemical Measurements Using Hyperspectral Data, *Proc. 3rd EARSeL Workshop on Imaging Spectroscopy*, Herrsching, 13-16th May 2003, pp 363-369.

Ong C., Swayze G., Clark R. (2003b).An investigation of the use of the Tetracorder Expert System for multi-temporal mapping of Acid Drainage- related minerals using Airborne Hyperspectral Data. Proceedings of 3rd EARSEL Imaging Spectroscopy, Germany, pp 357-362.

Paltridge G.W., Platt C.M.R. (1976).Radiative Processes in Meteorology and Climatology. Elsevier Scientific Pub Co.Amesterdam, the Netherlands.

Pinet PC, Kaufmann C, Hill J.(2006). Imaging spectroscopy of changing Earth's surface: a major step toward the quantitative monitoring of land degradation and desertification. Internal Geophysics (Applied Geophysics) C. R. *Geoscience* 338 (2006) 1042–1048p

Plaza A., Martinez P., Gualtieri J.A., Perez R.M.(2001). Spatial/Spectral Identification of Endmembers from AVIRIS Data Using Mathematical Morphology. *Proceedings of the Tenth JPL Airborne Earth Science Workshop*, JPL Publication 02-1, pp. 309-320.

Plaza A , Martínez P, Gualtieri,JÁ, Pérez R (2002). Automated Identification of Endmembers from Hyperspectral Data Using Mathematical Morphology.Image and Signal Processing for Remote Sensing VII, Sebastiano Bruno Serpico, Editor, *Proceedings of SPIE* Vol. 4541 © 2002 SPIE

Plaza A, Martinez P, Perez R, Plaza J (2004). A new approach to mixed pixel classification of hyperspectral imagery based on extended morphological profiles, *Pattern Recognition*, V37, Issue 6, Pages 1097-1116, ISSN 0031-3203, DOI: 10.1016/j.patcog.2004.01.006.

Plaza A., Plaza J, Cristo A.(2008). Morphological feature extraction and spectral unmixing of hyperspectral images. *A. IEEE International Symposium on Signal Processing and Information Technology (ISSPIT'08), Sarajevo, Bosnia & Herzegovina.*

Plaza A., Benediktsson J. A., Boardman J., Brazile J., Bruzzone L., Camps-Valls G., Chanussot J., Fauvel M., Gamba P., Gualtieri A., Marconcini M., Tilton J. C., Trianni G.(2009) Recent advances in techniques for hyperspectral image processing," Remote Sens. Environ., vol. 113, Supplement 1, pp. S110–S122.

Plaza J., Hendrix E.M.T., Garcia I., Martin G. Plaza A.(2011). On Endmember Identification in Hyperspectral Images without Pure Pixels: A Comparison of Algorithms. *Journal of Mathematical Imaging and Vision,* accepted for publication

Pu R, Gong P, Biging G, Larrieu M (2003). Extraction of red edge optical parameters from Hyperion data for estimation of forest leaf area index. IEEE Transactions on Geoscience and Remote Sensing, Vol.41 n4.

Quental L, Brito G (2002). MINEO S.DOMINGOS AMD WASTE MATERIAL (SAM). Appendix 6.1. MINEO FINAL REPORT

Quental L. Bourguignon A., Batista M.J., Brito G., Abreu M.M., Vairinho M., Sousa A.J., Cottard F. (2002a).MINEO Southern environment test site. Contamination/impact mapping and modelling – Final report for European Comission. 71p.

Quental,L. Abreu, M.M, Oliveira, V. Sousa, P., Batista, M.J., Brito, G.,Vairinho, M. Sousa, J. e Martins, L. (2002b). Imagens Hiperespectrais Para Avaliação E Monitorização Ambiental Em Áreas Mineiras: Resultados Preliminares Do Projecto Mineo Na Mina De São Domingos, Alentejo. In Actas do Congresso Internacional sobre Património Geológico e Mineiro.Museu do Instituto Geológico e Mineiro. Brandão, J. (ed.) Lisboa, ISBN 972 98469-8-7. pp 583-595.

Quental,L., Bourguignon, A., Cottard,F., Brito,MG., Abreu,MM., Sousa, AJ, Vairinho M. (2003a). Use Of Airborne Hyperspectral Imagery For Contamination Mapping At São Domingos Mine, Iberian Pyrite Belt,Southeast Portugal. *Proceedings of 4th European Congress on Regional Geoscientific Cartography and Information Systems*, Vol. II pp.698-9

Quental L., Brito M.G., Sousa A.J., Abreu M.M.,.Tavares T, Vairinho M. (2003b). Hyperspectral data to assess mining-related contaminated areas (S.Domingos Mine, Iberian Pyrite Belt, Southeast Portugal).*Proceedings Of The 2nd Mine-Water Interdisciplinary Network Europe (M-Wine) Workshop*. Editors: LMP Martins & DPS de Oliveira. Instituto Geológico e Mineiro, Alfragide (Lisbon), Portugal. CD-Rom. 30 June

Quental, L., Fleming, C., Marsh, S., Sousa, AJ. (2007) Acid mine drainage detection using hyperspectral tools: examples from two European mining areas. GRSG Newsletter Issue 46, June 2007,pp 14-16.

Quental, L., Sousa, A., Marsh, S. (2007) Hyperspectral image filtering and implications for environmental spectra related to mining contamination: example from the S.Domingos Mine, SE Portugal. In *10th Intl. Symposium on Physical Measurements and Spectral Signatures in Remote Sensing (*eds M.E. Schaepman, S. Liang, N.E. Groot, and M. Kneubühler), *Intl. Archives of the Photogrammetry, Remote Sensing and Spatial Information Sciences*, Vol. XXXVI, P21. ISPRS, Davos.

Quental, L., Sousa, A.J., Marsh, S. (2011) Low pH detection in SPECIM EAGLE-HAWK using field spectra at S. Domingos Mine, SE Portugal: preliminary results. *Proceedings of 3rd Workshop on Hyperspectral Image and Signal Processing (WHISPERS): Evolution in Remote Sensing, Lisbon*, Portugal, 6-9June.4p.

Räisänen M-L., Timonen M., Sutinen R. (2003).Analysis of hyperspectral airborne HyMap data for vegetation mapping around Lahnaslampi talc mine, Finland. *3rd EARSEL Workshop on Imaging Spectroscopy*, Herrsching.

Randeberg, LL; Larsen, EP, Svaasand, LO (2010). Characterization of vascular structures and skin bruises using hyperspectral imaging, image analysis and diffusion theory. *Journal of Biophotonics*, V3, 1-2, 53-65p.

Rego, M. (1996). Mineração no Baixo Alentejo. Câmara Municipal de Castro Verde.

Reusen I, Holzwarth S, Nieke J, Kooistra L , Malthus T, Chabrillat S, Kaufmann H, Gomez-Sanchez JA, Homolova L, Itten K, Malenovsky Z, Meuleman K, Miguel E, Mottus M, Mueller A, Pellikka P, Schaepman M (2007) TOWARDS AN IMPROVED ACCESS TO HYPERSPECTRAL DATA ACROSS EUROPE (HYRESSA) *Proceedings 5th EARSeL Workshop on Imaging Spectroscopy*. Bruges, Belgium, April 23-25 2007, 13p.

Riaza A., García-Meléndez E., Mueller A. (2009) SPECTRAL IDENTIFICATION OF PYRITE MUD WEATHERING PRODUCTS: A FIELD AND LABORATORY EVALUATION. EARSEL proceedings p3011-3017.

Riaza, A., Ong, C. and Müller, A., 2007. Pyrite mine wastes hyperspectral monitoring as a tool to detect Climate Change, *Proceedings 10th Intl. Symposium on Physical Measurements and Signatures in Remote Sensing*, ISPMSRS07, WG VII/1, March 12-14, 2007, Davos, Switzerland, pp. 228-233.

Richards, J.A., and Jia, X. (1999). *Remote Sensing Digital Image Analysis, an Introduction*. Third Edition. Springer-Verlag: Berlin.

Richter, N., Staenz, K., Kaufmann, H. (2008) Spectral unmixing of airborne hyperspectral data for baseline mapping of mine tailings areas. *International Journal of Remote Sensing* Vol. 29, No. 13, 10 July 2008, 3937–3956

Richter, R. (2010). Atmospheric / Topographic Correction for Satellite Imagery (ATCOR-2/3 User Guide, Version 7.1. 165p.

Roberts, D.A., Dennison, P., Ustin, S., Reith, E., Morais, M. (1999).Development of a Regionally Specific Library for the Santa Monica Mountains Using High Resolution AVIRIS Data. Summaries of the Eighth JPL Airborne Earth Science Workshop.

Rogge D.M. Rivard B. Zhang J. Sanchez A., Harris J., Feng J. (2007). Integration of spatial–spectral information for the improved extraction of endmembers. *Remote Sens. Environ.* 110 (2007) 287–303

Rothman L. S. et al., "The HITRAN molecular database—Editions of 1991 and 1992," *J. Quant. Spectrosc. Radiat. Transf*., V. 48, nos. 5/6, pp. 469–507, 1992.

Sabins, F.(1999). Remote sensing for mineral exploration. *Ore Geology Reviews* 14,157–183pp.

Santos Oliveira, J. M. (1998) – Algumas reflexões com enfoque na problemática dos riscos ambientais associados à actividade mineira. Estudos, Notas e Trabalhos do InstitutoGeológico e Mineiro, T. 39, pp. 3-25.

Schaepman, M.E., Green, R.O., Ungar, S.; Boardman, J., Plaza, A.J., Gao, B.C., Ustin, S., Miller, J., Jacquemoud, S., Ben-Dor, E., Clark, R., Davis, C., Dozier, J., Goodenough, D, Roberts, D., Goetz, A.F.H. (2006).The future of imaging spectroscopy - Prospective technologies and applications. In: *Proceedings 2006 IEEE International Geoscience and Remote Sensing Symposium.* - Denver: IEEE p. 2005-2008.

Schaepman, M.E., Wamelink, G.W.W., van Dobben, H., Gloor, M., Schaepman-Strub, G., Kooistra, L., Clevers, J.G.P.W., Schmidt, A., Berendse, F. (2007). River Floodplain Vegetation Scenario Development using Imaging Spectroscopy and Ecosystem Models. *Photogrammetric Engineering and Remote Sensing,* 73, 1179-1188

Schaepman, M. Ustin, M. Plaza,A., S., Painter, T. Verrelst, J., Liang, S (2009).Earth system science related imaging spectroscopy—An assessment. Remote Sens. Environ. 113, S123–S137

Schaepman-Strub, G., Schaepman, M.E., Painter, T.H., Dangel, S., Martonchik, J.V. (2006). Reflectance quantities in optical remote sensing – definitions and case studies. Remote Sens. Environ., 103, 27-42

Schott, J.R. (1997). Remote Sensing: The Image Chain Approach. Oxford University Press, New York.

Schläpfer D. (2006). Parametric Geocoding, PARGE User Guide, Version 2.3, ReSe Applications Schläpfer & Remote Sensing Laboratories University of Zurich, PDF/CDROM edition, Wil SG, pp. 195.

Scott K.M., Yanf K., HuntingtonJ. F.(1998).The application of spectral reflectance studies of chlorites to exploration. CSIRO Exploration and Mining Report 545R.

Sequeira (1884).Notícia sobre o estabelecimento de S.Domingos.Revista de Obras Públicas e Minas,14,15, 1883,1884.

Shaw GA , Burke HK (2003). Spectral Imaging for Remote Sensing LINCOLN LABORATORY JOURNAL, VOL14, n1.

Short, N. (2009).The Remote Sensing Tutorial, NASA Reference Publication 1078 and Library of Congress Catalog Card No. 81-600117; http://rst.gsfc.nasa.gov/ accessed December 2009

Singer, P.C., Stumm, W. (1970). Acidic mine drainage: the rate-determining step. Science, 167, pp. 1121–1123.

Silva, J. B., Oliveira, V., Matos, J. , Leitão, J. C. (1997) – Field Trip #2, Aljustrel and the Central Iberian Pyrite Belt. Geology and VMS Deposits of Iberian Pyrite Belt. Barriga and Carvalho, Eds., Guidebook Series, V. 27, 192p.

Silva, T.,Figueiredo, M.O.(2010).Secondary iron sulphates in AMD: a minerochemical analysis on jarosite supporting the valorization of its geoenvironmental contribution. Vol. 12, EGU2010-8973, EGU General Assembly 2010.

Singer, P.C.,Stumm, W. (1970). Acidic mine drainage: the rate-determining step. Science, 167, pp. 1121–1123.

Smith, AM, Hudson-Edwards, C.A, Dubbin, W.E, , Wright, K (2006). Dissolution of jarosite [KFe3(SO4)2(OH)6] at pH 2 and 8:Insights from batch.experiments and computational modelling. Geochimica et Cosmochimica Acta 70, 608–621

Smith, AM, Hudson-Edwards, C.A, Dubbin, W.E, Wright, K (2006). Dissolution of jarosite [KFe3(SO4)2(OH)6] at pH 2 and 8:Insights from batch.experiments and computational modelling. Geochimica et Cosmochimica Acta 70, 608–621

Sousa, P. and Sousa, A.J. (2000) Sistema ANDAD, CVRM-Centro de Geosistemas, IST, Lisbon.

Stehman, S.V., Czaplewski R.L. (1998). Design and analysis for thematic map accuracy assessment: Fundamental principles. Remote Sens. Environ., 64:331-344.

Steiniger, H, 2003, Die SWOT analyse, edditrex coop. (http://www.edditrex.de/scripts/consulting/swot_analyse.pdf#search=%22henny%20steiniger%20swot%20analyse%22 , 8/17/2006)

Stuffler, T., Hofer, S., Leipold, M., Förster, K.-P., Sang, B., Schubert, J., Penné, B., Kaufmann, H., Müller, A., Chlebek, C. (2009).*EnMAP – Space Segment – Instrument and Mission Parameters*. In: EARSeL SIG-IS Workshop; Tel Aviv, Israel.

Swayze, G. A., and R. N. Clark (1995). Spectral identification of minerals using imaging spectrometry data: evaluating the effects of signal to noise and spectral resolution using the Tricorder Algorithm: in Summaries of the Fifth Annual JPL Airborne Earth Science Workshop, JPL Publication 95-1, p. 157-158.

Swayze, G. A., Clark R.N., Pearson R.M., Livo K.E. (1996). Mapping Acid Generating Minerals at the California Gulch Superfund Site in Leadville, Colorado using Imaging Spectroscopy, In Summaries of the Sixth annual JPL Airborne Earth Sciences Workshop, R.O: Green (ed.), JPL Publication 96-4, March 4-8.

Swayze, G.A., Smith, K.S., Clark, R.N., Sutley, S.J., Pearson, R.M., Vance, J.S., Hageman, P.L., Briggs, P.H., Meier, A.L., Singleton, M.J., , Roth, S. (2000) Using imaging spectroscopy to map acidic mine waste, Environmental Science and Technology, 34, p. 47-54.

Tamstorf, M. Aastrup, P,Tukinainen, T (2002). MINEO Arctic environment test site Contamination /impact mapping and modelling – Final report for EC.59p.

Tanre, D., Deroo C., Duhaut P., Herman M., Morcrette J. J., Perbos J., Deschamps P.Y.(1990).Description of a computer code to simulate the satellite signal in the solar spectrum: The 5S code. *Int. J. Remote Sens.,* 11 (4), 659–668.

Tavares, M.T, Abreu, M.M, Vairinho, M.M., Sousa, A.J., Quental, L.(2009). Comportamento geoquímico de alguns elementos vestigiais na envolvente das Minas de S. Domingos, Alentejo: áreas da Tapada e do Telheiro. Rev. de Ciências Agrárias, **32**,1, p.182-194. ISSN 0871-018X.

Tavares, M.T., Sousa ,A.J. Abreu, M.M. (2008).Ordinary kriging and indicator kriging in the cartography of trace elements contamination in São Domingos mining site (Alentejo, Portugal).*Journal of Geochemical Exploration* 98 (2008) 43–56.

Thulin SM (2008) Hyperspectral Remote Sensing of Temperate Pasture Quality. PhD thesis. RMIT University Melbourne.

Tiess, G.(2009). European Technology Platform on Sustainable Mineral Resources – Key Areas for Research for the Future.*BHM Berg- und Hüttenmännische Monatshefte, V.154,12.* Springer Wien. pp567-571

Tompkins, S., Mustard, J.F., Pieters, C.M., Forsyth, D.W.(1997). Optimization of endmembers for spectral mixture analysis. *Remote Sens. Environ.*, 59, 472−489.

Van der Meer, F.D., de Jong, S.M. (2001). Imaging spectrometry: basic principles and prospective applications. Dordrecht etc., Kluwer Academic, 2001. *Remote sensing and digital image processing,* 4. pp. 403 Van der Meer + one CD-ROM. ISBN: 1-4020-0194-0.

Vane G., Green R.O., Chrien T.G., Enmark H.T., Hansen E.G., Porter W.M., (1993).The Airborne Visible/Infrared Imaging Spectrometer (AVIRIS), *Remote Sens. Environ.* **44**, pp.117–126.

Vane G., Goetz A.F.H., Wellman J.B. (1983) Airborne imaging spectrometer: a new tool for remote sensing, *IEEE Transactions on Geoscience and Remote Sensing* **GE–22** pp. 546–549.

Villa, A. Li, J., Plaza, A., Bioucas-Dias J. (2011).A NEW SEMI-SUPERVISED ALGORITHM FOR HYPERSPECTRAL IMAGE CLASSIFICATION BASED ON SPECTRAL UNMIXING CONCEPTS. *Proceedings of 3rd Workshop on Hyperspectral Image and Signal Processing (WHISPERS): Evolution in Remote Sensing, Lisbon*, Portugal, 6-9June.4p

Walder, I.,Schuster, P.(1998).Acid Rock Drainage. In: SARB Consulting, Inc. Environmental geochemistry of ore deposits and mining activities. *Short course Notes*, Albuquerque, New Mexico.

Webb, J. (1958). Observations on the geology and origin of the S. Domingos Pyrite deposits, Portugal. Com. Serv. Geol. Portugal, Lisboa. T. 42, pp.129-143.

Wetzel D.L. (1983) Anal. Chem. 55, 1165A.

Williams, PA. (1990). Oxide Zone Geochemistry. Chichester, England: Ellis Horwood Limited.

Winter M.E. (1999).N-FINDR: An algorithm for fast autonomous spectral end-member determination in hyperspectral data, *Proceedings of the SPIE Imaging Spectrometry* V, San Diego, CA.

Yang, K., Huntington, J.F., Boardman, J.W., Mason, P.(1999).Mapping hydrothermal alteration in the Comstock mining district, Nevada, using simulated satellite-borne hyperspectral data *Australian Journal of Earth Sciences* 46, 915–922pp.

Zabcic, N., Ong, C., Mueller, A., Rivard, B. (2005). Mapping Surface pH Using Airborne Hyperspectral Imagery at the Sotiel-Migollas Mine, Spain. *Proceedings of 4th EARSeL Workshop on Imaging Spectroscopy*. New quality in environmental studies. Zagajewski B., Sobczak M., Wrzesień M., (eds)©EARSeL and Warsaw University, Warsaw.

Zhang Y., Desai D.(2000).Hyperspectral image compression based on adaptive recursive bidirection prediction/JPG. *Pattern Recognition*, 33, 1851-1861p.

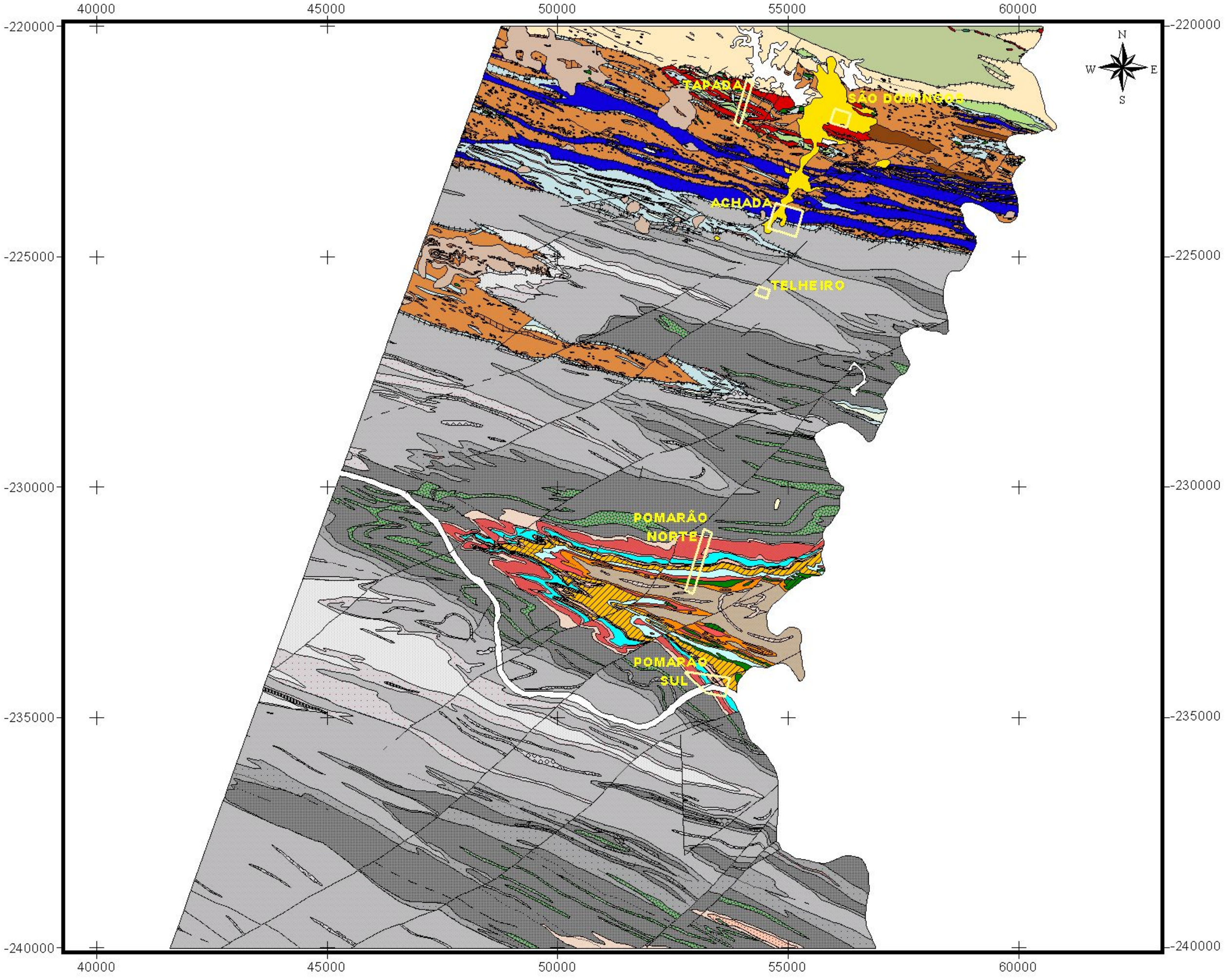

1:135 000 Scale

0 1.35 2.7 4.5 Km

LEGEND

COVER DEPOSITS

Quaternary
- Taillings and smelting products
- Fluvial terraces A
- Fluvial terraces A'

Pliocene
- Red sands and siltstones

UNCONFORMITY

CARBONIFEROUS — Upper Visean — Baixo Alentejo Flysch Group — Mértola Formation

M3 Member
- Mértola Formation M3 member
- M3 - pelites, greywackes and conglomerates
- M3 - thin bedded interbedded turbidites

M2 Member
- Mértola Formation M2 member
- M2 - thin bedded interbedded turbidites
- M2 - thin bedded interbedded turbidites
- M2 - intercalated coarser-grained greywackes
- M2 - thin bedded interbedded turbidites

M1 Member
- Mértola Formation M1 member (B1)
- M1 - pelites and thin bedded greywackes
- M1 - dominant classic turbidites
- M1 - pelites, greywackes and conglomerates
- M1 - thin interbedded turbidites

M0 Member
- Mértola Formation M0 member (B0)
- M0 - thin interbedded turbidites

CARBONIFEROUS — Tournaisian to Mid Visean — Pyrite Belt

Freixial Formation
- Freixial Formation

Volcano-Sedimentary Complex
- CVS - shales, siliceous shales, tuffites, siltstones
- CSV - jaspers, cherts
- CVS - "borra de vinho" purple and green shales
- CVS - fine grained acid tuffs
- CVS - spilites, diabases, and purple tuffs
- CVS - spilites, diabases, intermediates to basic porphyries
- CVS - rhyolites, rhyodacites, tuffs and aglomerates
- CSV - intrusive diabases
- CSV - microgranites and andesites

UPPER DEVONIAN — Middle-Upper Famennian — Pyrite Belt

Phylite-Qzite Formation
- Phylite - Quartzite Formation
- PQ form - bioturbated phylites, siltstones, quartzites

Pulo do Lobo Antiform
Chança Group
- Represa Formation (RF)
- RF - rare tufites
- Gafo Formation (GF)
- GF - intrusive diabases
- GF- acidic porphyries

UPPER DEVONIAN — Famennian ? — Pyrite Belt

Barranco do Homem Formation
- Barranco do Homem Formation

Pomarão
- Aguia Formation
- Touril Formation (T0) - Achada Mina member
- T0 - Corte Machado member
- T0 - Corte Machado member
- T0 - Varjotas member
- T0 - black shales member
- Cerqueirinha Formation

- Eira Garcia member - siltstones and dark shales
- Eira Garcia member - siltst. and dark shales interc. of qzites
- Nascedios member (NM)
- NM - dark shales with lenticular limestones

FAULTS
- Fault
- Thrust Fault
- Inferred Fault
- Overthrust

MINISTÉRIO DA ECONOMIA

INSTITUTO GEOLÓGICO E MINEIRO

DEPARTAMENTO DE GEOLOGIA

GEOLOGICAL MAP OF PORTUGAL

Sheet 46-D MÉRTOLA (partial)

MINEO São Domingos
AMD waste material
(Spectral Angle Mapper)

Map produced in September 2002

IGM

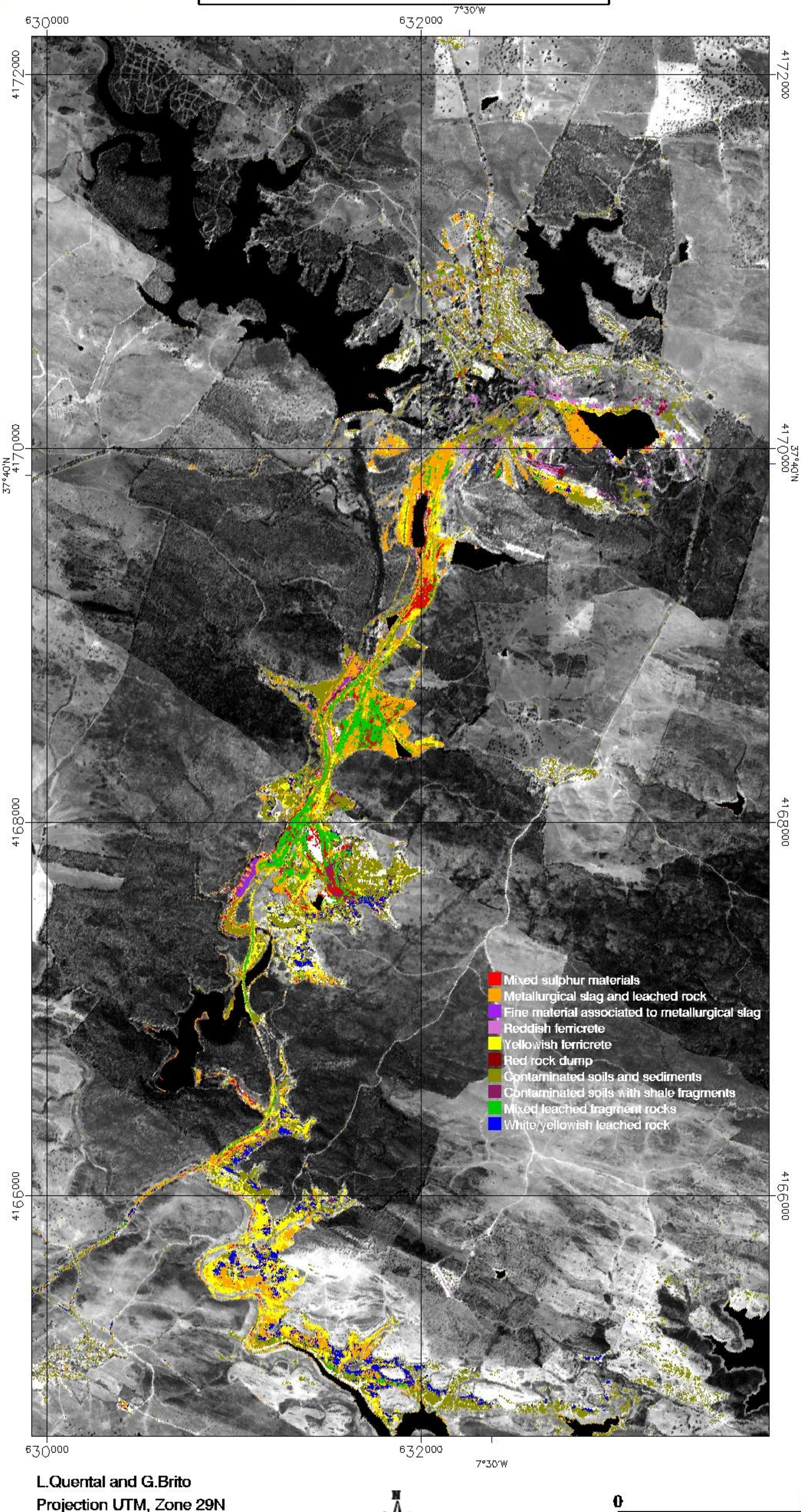

L.Quental and G.Brito

Projection UTM, Zone 29N

Pixel size:4.1 Meters

Datum: WGS-84

Ellipsoid: WG 84

N W E S

0 1 Km

MINEO São Domingos
AMD waste material
(Spectral Angle Mapper)

Map produced in September 2002

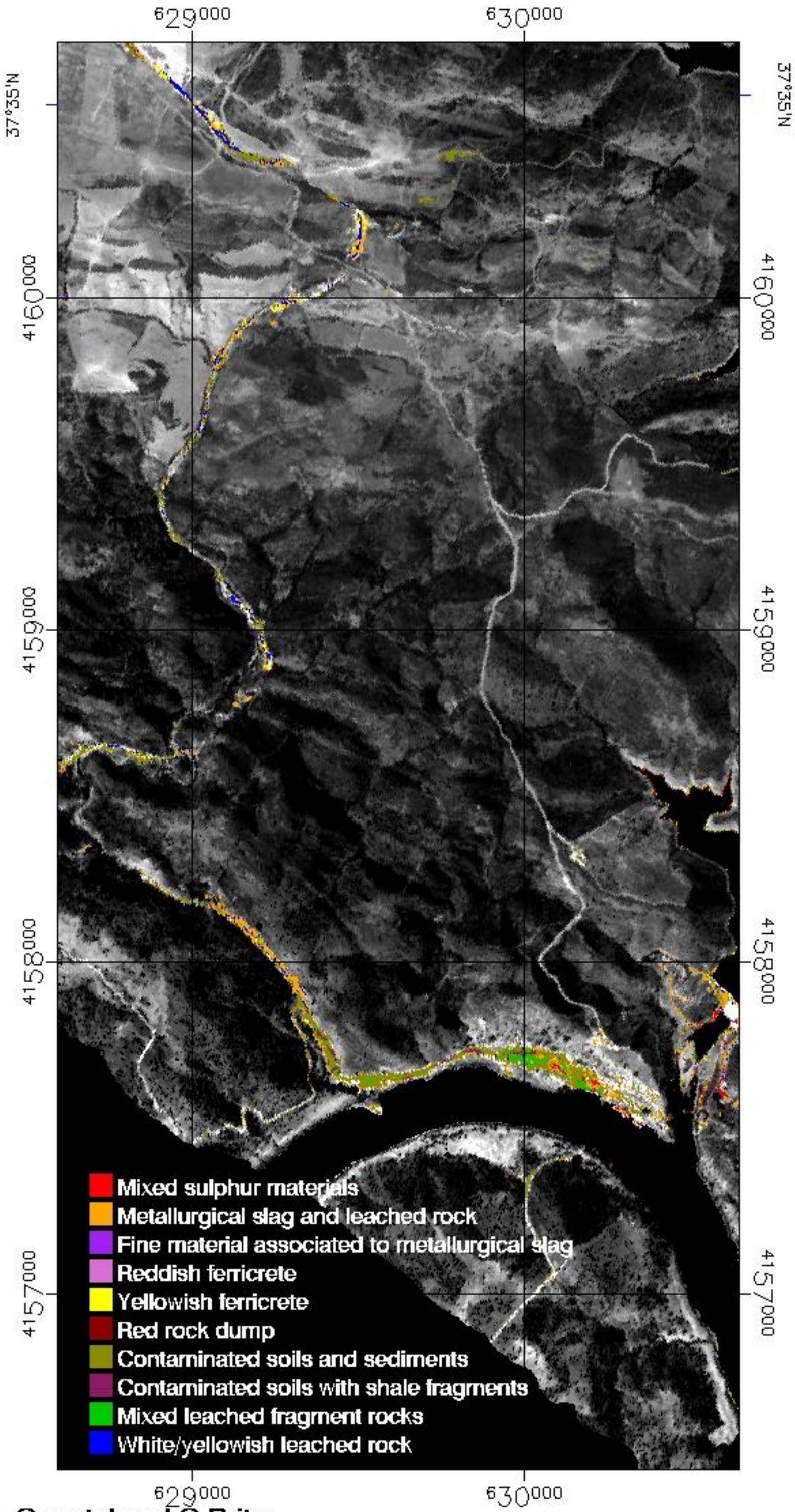

L.Quental and G.Brito

Projection UTM, Zone 29N

Pixel size: 4.1 Meters

Datum: WGS-84

Ellipsoid: WG 84

N W E S

0 0.5 km